

AD-762 939

LINE-OF-SIGHT WIDEBAND PROPAGATION

Phillip A. Bello, et al

CNR, Incorporation

Prepared for:

Rome Air Development Center
Advanced Research Projects Agency

April 1973

DISTRIBUTED BY:

NTIS

National Technical Information Service
U. S. DEPARTMENT OF COMMERCE
5285 Port Royal Road, Springfield Va. 22151

RADC-TR-73-167
Final Technical Report
May 1973



AD 762939

LINE-OF-SIGHT WIDEBAND PROPAGATION

CNR, Incorporated

Sponsored by
Defense Advanced Research Projects Agency
ARPA Order No. 2154

Approved for public release;
distribution unlimited.

The views and conclusions contained in this document are those of the authors and should not be interpreted as necessarily representing the official policies, either expressed or implied, of the Defense Advanced Research Projects Agency or the U. S. Government.

Reproduced by
NATIONAL TECHNICAL
INFORMATION SERVICE
U S Department of Commerce
Springfield VA 22151

Rome Air Development Center
Air Force Systems Command
Griffiss Air Force Base, New York



UNCLASSIFIED

Security Classification

DOCUMENT CONTROL DATA - R & D

(Security classification of title, body of abstract and indexing annotation must be entered when the overall report is classified)

1. ORIGINATING ACTIVITY (Corporate author) CNR, Inc 381 Elliot Street Newton Upper Falls, MA 02164		2a. REPORT SECURITY CLASSIFICATION Unclassified	
		2b. GROUP	
3. REPORT TITLE Line-of-Sight Wideband Propagation			
4. DESCRIPTIVE NOTES (Type of report and inclusive dates) Final Report (31 Jul 1972 - 6 Apr 1973)			
5. AUTHOR(S) (First name, middle initial, last name) Phillip A. Bello Joseph K. DeRosa Charles J. Boardman			
6. REPORT DATE April 1973		7a. TOTAL NO. OF PAGES 375 377	7b. NO. OF REFS 44
8a. CONTRACT OR GRANT NO. F30602-73-C-0013		9a. ORIGINATOR'S REPORT NUMBER(S)	
b. PROJECT NO. 2154			
c. Program Code Number 2G10		9b. OTHER REPORT NO(S) (Any other numbers that may be assigned this report)	
d. ARPA Order Number 21540001		RADC-TR-73-167	
10. DISTRIBUTION STATEMENT Approved for public release; distribution unlimited.			
11. SUPPLEMENTARY NOTES Monitored by Peter Edraos, RADC/DCID Griffiss AFB NY 13441 Telephone (315) 330-7583		12. SPONSORING MILITARY ACTIVITY Defense Advanced Research Projects Agency 1400 Wilson Blvd Arlington, VA 22209	
13. ABSTRACT This study investigates the limitations on the use of wideband pseudo-noise carriers imposed by the tropospheric propagation medium in the 4-10 GHz band. In addition channel measurement experiments are specified to check the analytical results. A detailed examination is given of the effects of refractive layers, volume scattering, surface scattering and reflection, and the frequency selectivity of the atmospheric constituents. The refractive layers, which are found to produce discrete multipath with multipath spreads from less than a nanosecond to tens of nanoseconds, are found to be the most serious source of system degradation. However, it is shown that a coherence bandwidth limitation, as such, does not exist in the 4-10 GHz band for the use of wideband pseudo-noise carriers. The effect of discrete multipath on the error rate performance of a representative pseudo-noise carrier data transmission modem is investigated. Also a two-correlator anti-multipath modem is investigated as a means to counteract the discrete multipath and is found to improve performance. For channel measurements, a pseudo-noise probing signal and a single time-multiplexed correlation demodulation is found to be the most economical for providing the essential data for channel parameter extraction and stored channel simulations.			

DD FORM 1 NOV 65 1473

181

UNCLASSIFIED

Security Classification

UNCLASSIFIED

Security Classification

14

KEY WORDS

LINK A

LINK B

LINK C

ROLE

WT

ROLE

WT

ROLE

WT

Microwave Line-of-Sight Communication

Tropospheric Propagation

Atmospheric Refraction

Digital Data Transmission

ib

UNCLASSIFIED

Security Classification

LINE-OF-SIGHT WIDEBAND PROPAGATION

Phillip A. Bello
Joseph K. DeRosa
Charles J. Boardman

Contractor: CNR, Incorporated
Contract Number: F30602-73-C-0013
Effective Date of Contract: 31 July 1972
Contract Expiration Date: 30 April 1973
Amount of Contract: \$44,000.00
Program Code Number: 2G10

Principal Investigator: Phillip A. Bello
Phone: 617 969-1690

Project Engineer: Henry J. Bush
Phone: 315 330-7583

Contract Engineer: Peter N. Edraos
Phone: 315 330-7583

Approved for public release;
distribution unlimited.

This research was supported by the
Defense Advanced Research Projects
Agency of the Department of Defense
and was monitored by Peter N. Edraos
RADC (DCID), GAFB, NY 13441 under
Contract F30602-73-C-0013.



PUBLICATION REVIEW

This technical report has been reviewed and is approved

Peter N. Edraos
PETER N. EDRAOS

RADC Project Engineer

TABLE OF CONTENTS

<u>Section</u>		<u>Page</u>
1	INTRODUCTION AND PROGRAM SUMMARY	1-1
	1.1 Summary	1-1
	1.2 Contents of Report	1-5
2	SYSTEM FUNCTION MODELING OF RCV CHANNELS	2-1
	2.1 System Functions for Time-Variant Channels	2-1
	2.2 The Structure of System Function Models Corresponding to Frequency-Selective Propagation Effects	2-8
	2.3 Characterization of RCV PN Carrier Channels	2-12
3	CHANNEL MODELING	3-1
	3.1 Methods of Approach	3-1
	3.2 Tropospheric Refraction Channel	3-5
	3.2.1 Propagation Modeling	3-11
	3.2.1.1 Physical Basis for Layers	3-11
	3.2.1.2 Refractive Index Structures	3-12
	3.2.1.3 Radio Propagation in the Presence of Layers	3-14
	3.2.1.3.1 Geometric Optics for RCV Applications	3-14
	3.2.1.3.2 Flat Earth	3-16
	3.2.1.3.3 Spherical Earth and the Modified Index	3-18
	3.2.1.3.4 Signal Strength	3-22
	3.2.2 System Function Characteristics	3-28
	3.2.2.1 Earth Shadowing in the Standard Atmosphere	3-29
	3.2.2.2 Single Stratified Layer Above Terminals	3-35
	3.2.2.3 Single Stratified Layer Below Terminals	3-58
	3.2.2.4 Single Stratified Layer Between Terminals	3-81
	3.2.2.5 Multilayer Profile	3-86

TABLE OF CONTENTS (Continued)

<u>Section</u>	<u>Page</u>
3.3 Volume Scattering Channel	3-92
3.3.1 Propagation Modeling	3-92
3.3.2 System Function Characteristics	3-98
3.3.2.1 Atmospheric Turbulence	3-98
3.3.2.2 Hydrometeors	3-113
3.4 Atmospheric Filter Characteristics	3-119
3.5 Surface Scatter and Reflection Channel	3-127
3.5.1 Propagation Modeling	3-127
3.5.2 System Function Characteristics	3-137
4 PERFORMANCE EVALUATION	4-1
4.1 Method of Approach	4-1
4.2 Effect of Multipath on RCV Spread Spectrum Receiver	4-3
4.3 System Analyzed	4-12
4.4 Formulation of Tracking Analysis	4-16
4.4.1 General Formulation	4-16
4.4.2 Two-Path Formulation	4-18
4.4.3 Solutions in the Fixed Phase Case	4-19
4.4.4 Solutions for Varying Phase	4-26
4.5 Error Probability Calculation	4-27
4.5.1 General Formulation	4-27
4.5.2 Two-Path Formulation	4-30
4.6 A Two-Channel Receiver	4-32
5 CHANNEL MEASUREMENTS	5-1
5.1 A Rational Approach to Modem Development	5-1
5.2 A Look at RCV Channel Measurement Needs	5-7
5.3 Comparison of Measurement Techniques	5-10
5.3.1 General Considerations in the Selection of Probing Techniques	5-10
5.3.2 Comparison of Matched Filter and Correlation Techniques	5-13
5.4 Use of Magnavox Frequency-Hopping PN Modem for Channel Probing	5-24
5.4.1 Description of Operating Modes to Use	5-25
5.4.2 Channel Measurement and Recording	5-29
5.4.3 Channel Parameter Extraction	5-34

TABLE OF CONTENTS (Continued)

<u>Section</u>	<u>Page</u>
6 CONCLUSIONS AND RECOMMENDATIONS	6-1
Appendix A SYSTEM MODEL FOR LINEAR CHANNELS USING PN CARRIERS	A-1
Appendix B EFFECT OF PROBABILITY DISTRIBUTION OF FREQUENCY HOPS ON CORRELATION FUNCTION OF PN CARRIER	B-1
Appendix C CALCULATIONS OF VARIANCES OF NOISE TERMS	C-1
Appendix D THE EQUATIONS OF GEOMETRIC OPTICS	D-1
Appendix E THE DIRECT PATH	E-1
Appendix F CALCULATIONS FOR SINGLE STRATIFIED LAYER ABOVE TERMINALS	F-1
Appendix G ANALYSIS OF MATCHED FILTER AND CORRELATION TECHNIQUES	G-1
Appendix H CALCULATIONS FOR SINGLE STRATIFIED LAYER BELOW TERMINALS	H-1
Appendix I CALCULATIONS FOR MULTILAYER PROFILE	I-1
Appendix J DEFINITION OF SPECULAR AND DIFFUSE COMPONENTS	J-1
Appendix K INTEGRAL FORMULATION OF THE SPECULAR COMPONENT	K-1
Appendix L CALCULATIONS FOR SURFACE SCATTER AND REFLECTION CHANNEL	L-1
Appendix M CALCULATION OF CORRELATION FUNCTIONS	M-1

LIST OF ILLUSTRATIONS

<u>Figure</u>		<u>Page</u>
2.1	System Model Block Diagram for Ground-RCV Configuration	2-2
2.2	General Structure of System Functions for Frequency Selective Tropospheric Propagation Effects	2-9
2.3	Signal Processing Operations of an RCV Link Including Pseudo-Noise Carrier Modulation and Demodulation	2-13
2.4	Illustration of Effect of Tropospheric Channel Multipath on PN Carrier System	2-16
2.5	PN Autocorrelation Functions for Uniform and Raised Cosine Tapered Frequency Hop Probabilities	2-19
3.1	Classification of Propagation Effects According to Their Potential Effect on High Baud Rate PN Systems	3-2
3.2	Typical Refractivity Profile	3-13
3.3	Horizontal Variation of N-Profile	3-15
3.4	Flat Earth Geometry	3-17
3.5	Spherical Earth Geometry	3-19
3.6	Effect of Earth-Flattening Coordinate Transformation on Ray Trajectories	3-23
3.7	Modified Radius of Curvature Versus Refractivity Gradient	3-24
3.8	Intensity Law	3-25
3.9	Geometry of Earth Shadow Zone	3-30

LIST OF ILLUSTRATIONS (Continued)

<u>Figure</u>		<u>Page</u>
3.10	Shadow Region in Standard Atmosphere	3-32
3.11	Transmitter Height Necessary to Clear Earth Surface as a Function of Range and Elevation Angle	3-34
3.12	Maximum Height of Layer Above Terminals to Allow Refractive Multipath	3-37
3.13	Multipath Delay Profile for Single Layer 600 Feet Above Terminals	3-46
3.14	Multipath Delay Profile for Single Layer 300 Feet Above Terminals	3-47
3.15	Multipath Delay Profile for Single Layer 200 Feet Above Terminals	3-48
3.16	Multipath Delay Profile for Single Layer 100 Feet Above Terminals	3-49
3.17	Normalized Curves of Amplitude Versus Range	3-51
3.18	Multipath Delay Profiles for Single Layer Just Above Terminals	3-54
3.19	Magnitude of Time-Variant Impulse Response $h(t_0, \epsilon)$	3-57
3.20	Ray Trajectories as a Function of Layer Height	3-62
3.21	Initial Ray Angle Vs. Range Case I: Nominal Conditions	3-64
3.22	Relative Power Vs. Relative Delay Case I: Nominal Conditions	3-66
3.23	Fading Record on Hawaii Experimental Link at 10 GHz	3-68
3.24	Initial Ray Angle Vs. Range Case II: Thin Layer Below Terminals	3-70

LIST OF ILLUSTRATIONS (Continued)

<u>Figure</u>		<u>Page</u>
3.25	Relative Power Vs. Relative Delay Case II: Thin Layer Below Terminals	3-71
3.26	Initial Ray Angle Vs. Range Case III: Layer of Steep N-Gradient Below Terminals	3-73
3.27	Initial Ray Angle Vs. Range Case IV: Thin Layer of Steep N-Gradient Below Terminals	3-75
3.28	Relative Power Vs. Relative Delay Case IV: Thin Layer of Steep N-Gradient Below Terminals	3-76
3.29	Ray Tracing for Measured N-Profile	3-79
3.30	Ray Trajectory for Layer Between Terminals	3-82
3.31	The Location of the Earth Shadow Zone With a Layer in the Standard Atmosphere	3-85
3.32	Initial Angle Vs. Range Diagram for Multilayer Profile	3-88
3.33	Delay Profile for Multilayer Refractive Index Structure	3-90
3.34	Measurement of RMS Index of Refraction	3-96
3.35	Frequency Correlation Function and Delay Power Spectrum for Volume Scattering Channel	3-109
3.36	Atmospheric Absorption by the 1.35 cm Line of Water Vapor and the 0.5 cm Line of Oxygen	3-124
3.37	Specular Scattering Coefficient Vs. Apparent Surface Roughness	3-128
3.38	Specular Delay as a Function of Height and Range	3-129
3.39	Elevation and Grazing Angles as a Function of Height and Range	3-130

LIST OF ILLUSTRATIONS (Continued)

<u>Figure</u>		<u>Page</u>
3.40	Doppler Shift as a Function of Elevation Angle	3-132
4.1	Error Probability for Coherent Detection of Spread-Spectrum Binary PSK Data; Two-Path Channel Model, Delay Difference $t_d = 0.0$ Chip, Various Relative Amplitudes α	4-4
4.2	Error Probability for Coherent Detection of Spread-Spectrum Binary PSK Data; Two-Path Channel Model, Delay Difference $t_d = 0.25$ Chip, Various Relative Amplitudes α	4-5
4.3	Error Probability for Coherent Detection of Spread-Spectrum Binary PSK Data; Two-Path Channel Model, Delay Difference $t_d = 0.50$ Chip, Various Relative Amplitudes α	4-6
4.4	Error Probability for Coherent Detection of Spread-Spectrum Binary PSK Data; Two-Path Channel Model, Delay Difference $t_d = 0.75$ Chip, Various Relative Amplitudes α	4-7
4.5	Error Probability for Coherent Detection of Spread-Spectrum Binary PSK Data; Two-Path Channel Model, Delay Difference $t_d = 1.0$ Chip, Various Relative Amplitudes α	4-8
4.6	E/N_0 Required to Give Error Probability of 10^{-4}	4-11
4.7	Simplified Block Diagram of RCV Spread Spectrum Receiver	4-13
4.8	Code and Carrier Tracking Loops of a Spread-Spectrum Receiver	4-14
4.9	Open Loop Error Voltage, $\alpha=0.7$, $t_d=1.2$ Bits, $\theta_m=0$	4-21
4.10	Open Loop Error Voltage, $\alpha=0.7$, $t_d=1.2$ Bits, $\theta_m=0$	4-22

LIST OF ILLUSTRATIONS (Continued)

<u>Figure</u>		<u>Page</u>
4.11	Code Loop Tracking Error as a Function of Multipath Delay, for Fixed Multipath Phase ($\alpha=0.7$)	4-24
4.12	Open Loop Error Voltage, $\alpha=0.7$, $t_d=0.5$, $\theta_m=\pi$	4-25
4.13	Varying-Phase Solution for $\alpha=0.7$, $t_d=0.5$ Bits	4-28
4.14	Reference Extraction for Two-Channel Detection (Data Feedback not Shown)	4-33
4.15	Two-Channel Combining and Detection	4-35
4.16	Calculated Error Probabilities for Various Receivers; Multipath Delay Difference $t_d=0.5$ Chip, Relative Amplitude $\alpha=0.7$	4-38
4.17	Performance as a Function of t_Δ ($\alpha=0.7$, $t_d=0.5$, $E/N_0=10.5$ dB)	4-40
4.18	Calculated Error Probabilities for Various Receivers; Multipath Delay Difference $t_d=0.5$ Chip, Relative Amplitude $\alpha=0.9$	4-41
4.19	Performance as a Function of t_Δ ($\alpha=0.9$, $t_d=0.5$, $E/N_0=11$ dB)	4-42
4.20	Calculated Error Probability for Various Receivers; Multipath Delay Difference $t_d=0.5$ Chip, Relative Amplitude $\alpha=1.0$	4-44
4.21	Performance as a Function of t_Δ ($\alpha=1.0$, $t_d=0.5$, $E/N_0=13$ dB)	4-45
5.1	Utilization of Channel Measurements in Modem Development	5-2
5.2	Simplified Block Diagram for Matched Filter Techniques: Low Pass Sampling	5-15

LIST OF ILLUSTRATIONS (Continued)

<u>Figure</u>		<u>Page</u>
5.3	Periodic Pulse Response of Baseband Time-Variant Channel	5-17
5.4	Simplified Block Diagram for Matched Filter Technique: Band-Pass Sampling	5-20
5.5	Simplified Block Diagram for Low Pass Correlation Technique	5-21
5.6	Simplified Block Diagram for Band-Pass Correlation Technique	5-22
5.7	Simplified Block Diagram for Multiplexed Band-Pass Correlation Technique	5-23
5.8	Synthesizer Functional Diagram	5-26
5.9	Frequency-Hopping Pattern for Probing Signal	5-27
5.10	Synchronizer Functional Diagram	5-30
5.11	Measurement and Recording of Transfer Function Amplitude Samples	5-31
5.12	Received Frequency Hop Patterns for Multipath Conditions	5-33
A.1	Idealized Signal Processing Operations in a Linear Channel With PN Carrier Modulation and Demodulation	A-2
A.2	Equivalent Channel Filter for Data Signal	A-4
E.1	The Direct Path	E-2
F.1	Geometry of Single Stratified Layer Above Terminals	F-2
F.2	Solutions for (k_T, k_R)	F-10
G.1	Options for Incorporation of Terminal Filters	G-4

LIST OF ILLUSTRATIONS (Continued)

<u>Figure</u>		<u>Page</u>
G.2	Basic Elements of Channel Measurement for Matched Filter and Correlation Techniques	G-6
H.1	System Geometry for Layer Below Terminals	H-2
I.1	Piecewise Linear m-Profile	I-2
I.2	Ray Trajectory in the i'th Layer	I-4
J.1	The Specular and Diffuse Components	J-2
J.2	The Discrete Specular Component	J-4
K.1	Geometry of Surface Scattering	K-2
L.1	Specular Point Geometry	L-2
L.2	Flat Earth Approximation	L-5
M.1	Receiver Pulse Shapes	M-2
M.2	The Correlation Function $R(t)$	M-6
M.3	The Correlation Function $S(t)$	M-7

LIST OF TABLES

<u>Table</u>		<u>Page</u>
3-1	Typical Multipath on Ground-Air Links	3-6
3-2	Typical Multipath on Air-Air Links	3-7
3-3	Typical <i>Earth Shadow</i> Regions on Ground-Air Links	3-10
3-4	Multilayer Refractive Index Profile	3-87
3-5	Summary of Multipath for Multilayer Profile	3-91
3-6	Summary Comments on Computationally Useful Propagation Models and Gross System Function Characteristics for Homogeneous Isotropic Refractive Index Fluctuations (Propagation Medium-Limited Rather Than Antenna-Limited Propagation Assumed)	3-104
3-7	Value of Λ_0 In Meters as a Function of Path Distance and Carrier Frequency	3-107
3-8	Rain Scattering Cross Sections/ m^3 at 4 and 10 GHz	3-117
3-9	Received Scatter/Direct Path Power Ratios P_0 Due to Rain for 100 Mile Path, 3' and 30' Antenna Dishes, at 4 and 10 GHz	3-118
3-10	Antenna Beamwidth Necessary to Discriminate Against Specular Ground Multipath	3-13
3-11	Summary of Reflection Coefficients	3-136
5-1	Sequential Hopping Sequences	5-28

SECTION 1
INTRODUCTION AND PROGRAM SUMMARY

The effort reported here supports the Department of Defense program to provide an anti-jam protected multiple-access command-and-control communications system for remote-controlled-vehicle (RCV) applications. Such protection requires pseudo-noise (PN) carriers of wide bandwidths. This study investigates the limitations on the use of wide-band PN carriers imposed by the tropospheric radio propagation medium in the 4 - 10 GHz band for air-ground and air-air paths. In addition, channel measurement experiments are specified to check the analytical results.

The method of approach for meeting the program objectives involves modeling the relevant propagation effects to develop multipath fading system-function models of RCV communication links as a function of system parameters. These models combined with appropriate signal-processing models of the terminal equipment allow a determination of data transmission error rate and thus provide the basis for a determination of the limitations on the use of high baud rate PN carriers imposed by the propagation medium.

In Section 1.1 below a concise summary is presented of the results of the study. Following this summary the organization of the report is outlined in Section 1.2.

1.1 Summary

An appropriate system function model of an RCV propagation channel consists of the cascade of two "filters." The first filter characterizes the frequency selective effects of the complex refractive index of the atmosphere (rain, water vapor, and

oxygen). The second filter is a time-variant linear filter having, under appropriate atmospheric conditions, the structure of an essentially discrete set of delayed paths whose amplitudes, phases, and relative delays are slowly time-varying. Around each of these paths there exists a low-level continuously distributed multipath due to scattering. The second filter structure characterizes the effects of refractive layers, atmospheric turbulence, surface scattering and reflection, and discrete reflections.

It is shown in this report (Section 3.4) that the frequency selectivity of the first filter, the atmospheric filter, produces no limitation on the use of wide-band PN carriers in the 4 - 10 GHz band. The coherence bandwidth, W_{coh} , of the second filter, which may be called the "multipath" filter, is given by some small fraction of the reciprocal of the multipath spread between the first and latest arriving paths. In Section 3.2 this multipath spread is computed to range from less than a nanosecond to tens of nanoseconds which leads to values of W_{coh} as small as a few MHz. At first glance it might be supposed that a PN carrier data transmission system will suffer increasing degradation as the bandwidth of the PN carrier increases beyond W_{coh} , because this is just what happens with conventional data transmission systems. However it is shown in Section 2 that for the discrete multipath structures present in RCV channels, just the opposite will occur. The PN correlation process in the receiver allows the rejection of multipath components which differ from the desired path by more than a time duration equal to the duration of the autocorrelation function of the PN signal. The individual paths are extremely broadband, so that when the PN correlation process isolates one path, no significant coherence bandwidth

limitations will exist for PN bandwidths of interest in the 4 - 10 GHz band.

Even though the troposphere does not pose a coherence bandwidth limitation for wideband PN carrier systems, transmission difficulty still occurs when two or more paths are less than a PN correlation function width. In this case the output data signal after the receiver PN correlation processing, will be subjected to amplitude and phase fluctuations. To assess the effect of multipath on error rate a computer program was developed to evaluate PSK error rate performance in the presence of discrete multipath for a representative PN carrier demodulator. The formulation includes local PN timing and phase errors introduced by the code and carrier tracking loops as they track the combined multipath signal. Error rate calculations were carried out for the common two-path case as a function of path delay difference and relative amplitude with the relative phases of the two paths assumed randomly distributed. Clearly, as one might expect, when the two paths are equal or nearly equal in strength, the performance degradation is very large. However, perhaps less obviously, when the delay difference is not a small fraction of a PN pulse width, the paths have to be surprisingly close in amplitude to cause significant degradation. Thus for two paths separated by one half a PN pulse width, the path gains must be closer than 1.4 dB to produce a performance degradation in excess of 3 dB.

An adaptive two-correlator system with corresponding locally generated PN sequences separated by a delay less than a PN correlation function width is analyzed to determine its

effectiveness as an anti-multipath technique for the two-path multipath case. Considerable performance improvement is shown to be possible with this approach because of the effective multipath diversity combining achieved. With this system, in contrast to the single correlation system, equal strength paths do not cause large performance degradation unless the paths are separated by a delay small compared to a chip width.

One potentially serious communication problem was identified as arising from the discrete multipath caused by refractive layers. For this type of propagation phenomena, especially in ground-to-air links, the spurious multipath components are generally larger than the direct path. Since the spread spectrum modem will tend to lock onto the stronger path and since the multipath effect exists in limited spatial regions, it is possible for the spread spectrum modem to lock onto a spurious multipath component and then to lose synchronization when the component disappears.

Some consideration was given to the signal design problem in coherent frequency-hopping PN modems to achieve resistance to multipath. It was found that an appropriate tapering of the probabilities of the various frequency hops can be quite helpful.

A study of channel measurement techniques for RCV channels was carried out. Consideration was given to both time and frequency domain techniques, to the special requirements of RCV channels, to performance, and to relative cost and complexity. As a result of the study it was found that for bandwidths up to 200 MHz a pseudo-random prober and a multiplexed correlation receiver processing technique provide the least complex means of

gathering both the required multipath data needed for channel modeling and for comparative evaluation of modems by "recreating" and "playing back" the channel in the laboratory via stored channel simulation. Some consideration was given to the possible utility for channel measurement of a frequency-hopping PN modem due to be shipped to RADC in the near future. It was found that some useful channel parameter information could be achieved by interfacing with this modem at an appropriate point with some relatively simple signal processing hardware.

1.2 Contents of Report

The limitation on the use of wide-band PN carriers imposed by the propagation medium (including the relevance of coherence bandwidth) is developed in Section 2 by combining appropriate signal processing models of the terminal equipment with the system function models of the propagation channel. In this way the relationship between the output data signal characteristics and the input data signal, PN carrier parameters, and channel parameters is revealed.

Section 3 documents the results and details of the channel modeling investigation. Consideration is given to both propagation modeling and system function (i.e., "black-box") modeling of various canonic propagation effects. In particular the refractive layer, volume scattering, surface reflection and scattering, and complex refractive index of the atmosphere are studied.

The effects of discrete multipath on a PN carrier modem data transmission error rate are taken up in Section 4. Section 5 discusses the channel measurement problem for RCV channels. The final section presents conclusions and recommendations for future work.

SECTION 2

SYSTEM FUNCTION MODELING OF RCV CHANNELS

In order to determine the interrelationship between the RCV system requirements, the propagation channel, and modulation techniques, it is necessary to develop an RCV system model in which all important signal processing operations in the RCV system, both man-made and natural, are adequately characterized and related to the important RCV system parameters. Figure 2.1 presents a basic system model block diagram of a ground-RCV command-control configuration, depicting major signal processing operations. As pointed out in the work statement for this study, the major modeling deficiencies in the RCV system (ground-air or air-air) are connected with the up-link and down-link propagation channels. This section, with the aid of results from Section 3, discusses the nature of the system function models of the propagation channels. The character of the limitation on the use of wide-band PN carriers imposed by the propagation medium (including the relevance of coherence bandwidth) is developed by combining appropriate signal processing models of the terminal equipment with the system function models of the propagation channel in order to relate the output signal to the input data signal and PN carrier waveform parameters.

2.1 System Functions for Time-Variant Channels

The propagation channels are linear systems and may be characterized by time-variant transfer functions (e.g., $T_U(f,t)$ and $T_D(f,t)$) as indicated in Fig. 2.1). This section reviews

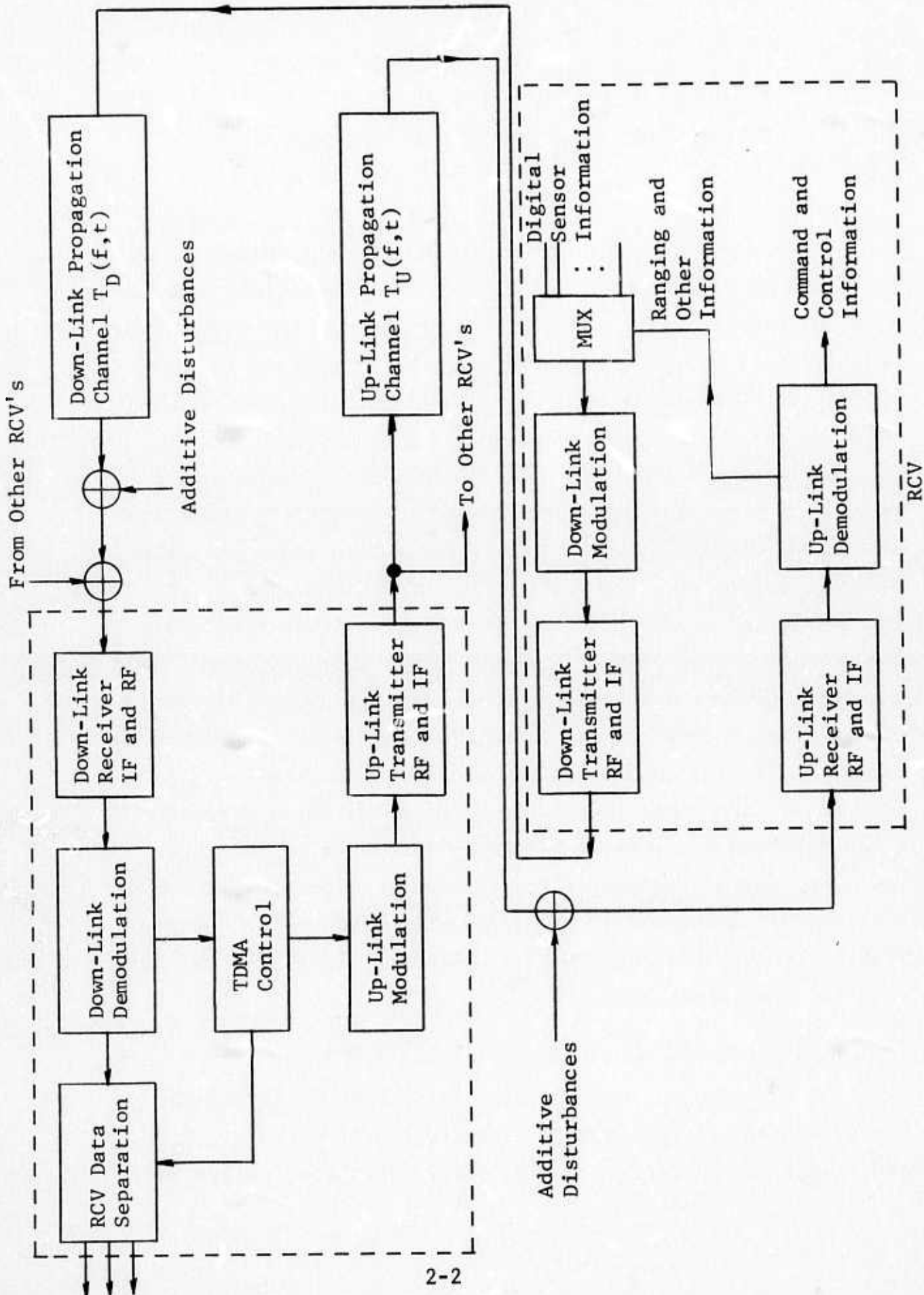


Figure 2.1 System Model Block Diagram for Ground-RCV Configuration

briefly the characterization of randomly time-variant systems with the aid of system functions. In particular, the relationship between multipath spread and frequency selectivity is brought out initially without making any statistical assumptions. It is desirable to characterize the propagation channels as far as possible without introducing statistical assumptions, because these channels will be nonstationary.

There exist a variety of system functions for characterizing the input-output behavior of linear time-varying systems [2.1] [2.2]. For the purposes of the present discussion it is sufficient to confine attention to the time-variant transfer function $T(f,t)$ and the time-variant impulse response $g(t,\xi)$. For simplicity of presentation we shall use complex envelope representation throughout. Thus the input signal would be represented by the complex signal $z(t)$. The real signal would be a narrow-band process with envelope $|z(t)|$ and with phase $\angle z(t)$ measured with respect to carrier phase $2\pi f_0 t$, where f_0 is the carrier frequency.

In complex notation the input-output relationships corresponding to use of $T(f,t)$, $g(t,\xi)$ are

$$w(t) = \int Z(f)T(f,t)e^{j2\pi ft} df \quad (2.1)$$

$$w(t) = \int z(t-\xi)g(t,\xi) d\xi \quad (2.2)$$

where $w(t)$ is the output signal (complex) and $Z(f)$ is the spectrum of $z(t)$.

The transfer function $T(f,t)$ and impulse response $g(t,\xi)$ are Fourier transform pairs,

$$T(f,t) = \int g(t,\xi) e^{-j2\pi f\xi} d\xi \quad (2.3)$$

$$g(t,\xi) = \int T(f,t) e^{j2\pi f\xi} df \quad (2.4)$$

It is readily seen that the time-variant transfer function at the frequency f (actually f Hz away from carrier frequency f_0) is just equal to the complex modulation observed on a received RF carrier transmitted at $f_0 + f$ Hz. Thus the time-varying envelope of this received carrier is $|T(f,t)|$ and the time-varying phase of this received carrier measured with respect to the input phase is $\angle T(f,t)$. The width of the spectrum of a received carrier, i.e., the spectral width of $T(f,t)$ with f fixed, is called the Doppler spread of the channel at $f_0 + f$. This Doppler spread clearly determines the rate of fading of the channel.

If another carrier is transmitted at a different frequency $f_0 + f + \Omega$ sufficiently close to $f_0 + f$, it will be found that the envelopes and phases of the two received carriers essentially fade in step. As the separation frequency is increased, however, $T(f,t)$ and $T(f+\Omega,t)$ will begin to depart. The term coherence bandwidth W_{coh} , is used to define the frequency interval, i.e., maximum value of Ω , for which $T(f,t)$ and $T(f+\Omega,t)$ may be regarded as the fluctuating in step,

$$T(f,t) \approx T(f+\Omega,t) \quad ; \quad \Omega \leq W_{coh} \quad (2.5)$$

From Eq. (2.1) we note that if the spectrum $Z(f)$ of a transmitted signal occupies a bandwidth $W < W_{coh}$, then the output is given by

$$w(t) \approx z(t)T(0,t) \quad (2.6)$$

i.e., the channel acts as a complex multiplier $T(0,t)$ causing all frequency components of $z(t)$ to fluctuate in step. Such a channel is called "flat" fading. (Note that $T(0,t)$ is just the complex modulation observed on a received carrier at the carrier frequency f_0 .) For input signals with bandwidths exceeding W_{coh} , frequency selective distortion will result, i.e., all frequency components will not fluctuate in unison.

The coherence bandwidth does not sharply divide signals into those which are seriously degraded by frequency selective distortion and those which are not. Rather as W decreases, the frequency selective distortion will get less and less until it approaches a level which causes a small enough distortion to be ignored relative to other system nonidealities. It is a basic objective of the study to determine how much bandwidth can be employed for signaling elements in candidate RCV waveforms on the basis of system performance degradation caused by frequency selective fading.

The time variant transfer function of a microwave radio channel differs from the transfer function of a conventional filter in that the latter has a well-defined bandwidth outside of which attenuation is large. While the former has a coherence bandwidth, it is clear from the above discussion that it is not at all like a passband bandwidth. In fact the radio channel will transmit power over bandwidths very very much larger than the coherence bandwidth.

We note from Eq. (2.4) that the time-variant impulse response $g(t, \xi)$ is the Fourier transform of $T(f, t)$ along the frequency variable. Due to this transform relation we know that the maximum rate of variation of $T(f, t)$ with f is determined by the maximum path delay, i.e., the value of ξ beyond which $g(t, \xi)$ is negligible. It is convenient to define the delay occupancy region as the set of delay values over which $g(t, \xi)$ is significantly different from zero. Thus if

$$g(t, \xi) \approx 0 \quad \text{for} \quad \xi < \xi_{\min}, \quad \xi > \xi_{\max} \quad (2.7)$$

then the delay occupancy region is the interval $\xi_{\min} < \xi < \xi_{\max}$. The total multipath spread of the channel, L_{tot} is the difference between the longest and earliest multipath delay. In the case of (2.7),

$$L_{\text{tot}} = \xi_{\max} - \xi_{\min} \quad (2.8)$$

If the delay occupancy region is centered* so that

$$\begin{aligned} \xi_{\min} &= -\frac{1}{2} L_{\text{tot}} \\ \xi_{\max} &= \frac{1}{2} L_{\text{tot}} \end{aligned} \quad (2.9)$$

then the "period" of the most rapid variation of $T(f, t)$ with f is just

* This centering is equivalent to a convenient choice of time origin and represents no sacrifice in generality for characterizing frequency selective distortion.

$$W_{\max} = \frac{1}{L_{\text{tot}}} \quad (2.10)$$

where we use the subscript "max" to indicate that W_{\max} is the maximum separation between samples of $T(f,t)$ vs. f for reconstruction of $T(f,t)$ via the sampling theorem. We shall call W_{\max} the sampling bandwidth. Clearly the coherence bandwidth must be much less than the sampling bandwidth,

$$W_{\text{coh}} \ll W_{\max} = \frac{1}{L_{\text{tot}}} \quad (2.11)$$

If, as a rule-of-thumb, one arbitrarily selects W_{coh} as 1/10 of W_{\max} then from (2.11) we see that a total multipath spread of 10 nanoseconds (not unlikely for multipath due to refractive layers) implies a coherence bandwidth of 10 MHz.

One may define a total Doppler spread parameter B_{tot} , a sampling interval T_{\max} and a coherence duration parameter T_{coh} for time-selective effects analogous to L_{tot} , W_{\max} , and W_{coh} for frequency selective effects. B_{tot} defines the maximum bandwidth over which the spectrum of a received carrier ($T(f,t)$ for fixed f) has significant values and T_{\max} is maximum separation between samples of $T(f,t)$ as a function of t for reconstruction of $T(f,t)$ via the sampling theorem. T_{coh} may be regarded as the interval of time over which the time variant channel changes negligibly, i.e., for such intervals of time the channel may be regarded as "frozen" although possibly dispersive. For multipath due to tropospheric effects T_{coh} will be very much larger than the duration of any typical signaling element in RCV data transmission. Thus computation of intersymbol interference effects can proceed on a "frozen channel" basis.

2.2 The Structure of System Function Models Corresponding to Frequency-Selective Propagation Effects

The general character of the system functions corresponding to frequency selective tropospheric propagation effects may be deduced from Fig. 2.2 which diagrams the way specific frequency selective mechanisms are combined as signal processing operations on the transmitted signal. As indicated in Fig. 2.2, the propagation channel may be represented as the parallel combination of several "paths" each having the same general structure. This structure consists of the cascade of three operations:

- a) A time invariant "atmospheric" filter characterizing the frequency-selective properties of the complex dielectric constant of the atmosphere
- b) An ideal (generally time-varying) delay operator
- c) The parallel combination of a time variant filter modeling the volume scattering and a complex (slowly time varying) gain modeling the strength and phase of the path in the absence of frequency selectivity of the dielectric constant and in the absence of volume scattering.

Strictly speaking, each path should have a separate atmospheric filter, but the paths traverse atmospheric regions sufficiently close to make these filters essentially identical. Section 3.5 shows that in the 4 - 10 GHz band the atmospheric filter, even under worst case conditions, has negligible frequency selectivity. Since it may be assumed that the PN carriers of interest in the 4 - 10 GHz band have bandwidths less than a few GHz, the atmospheric filter may be regarded as essentially non-frequency selective.

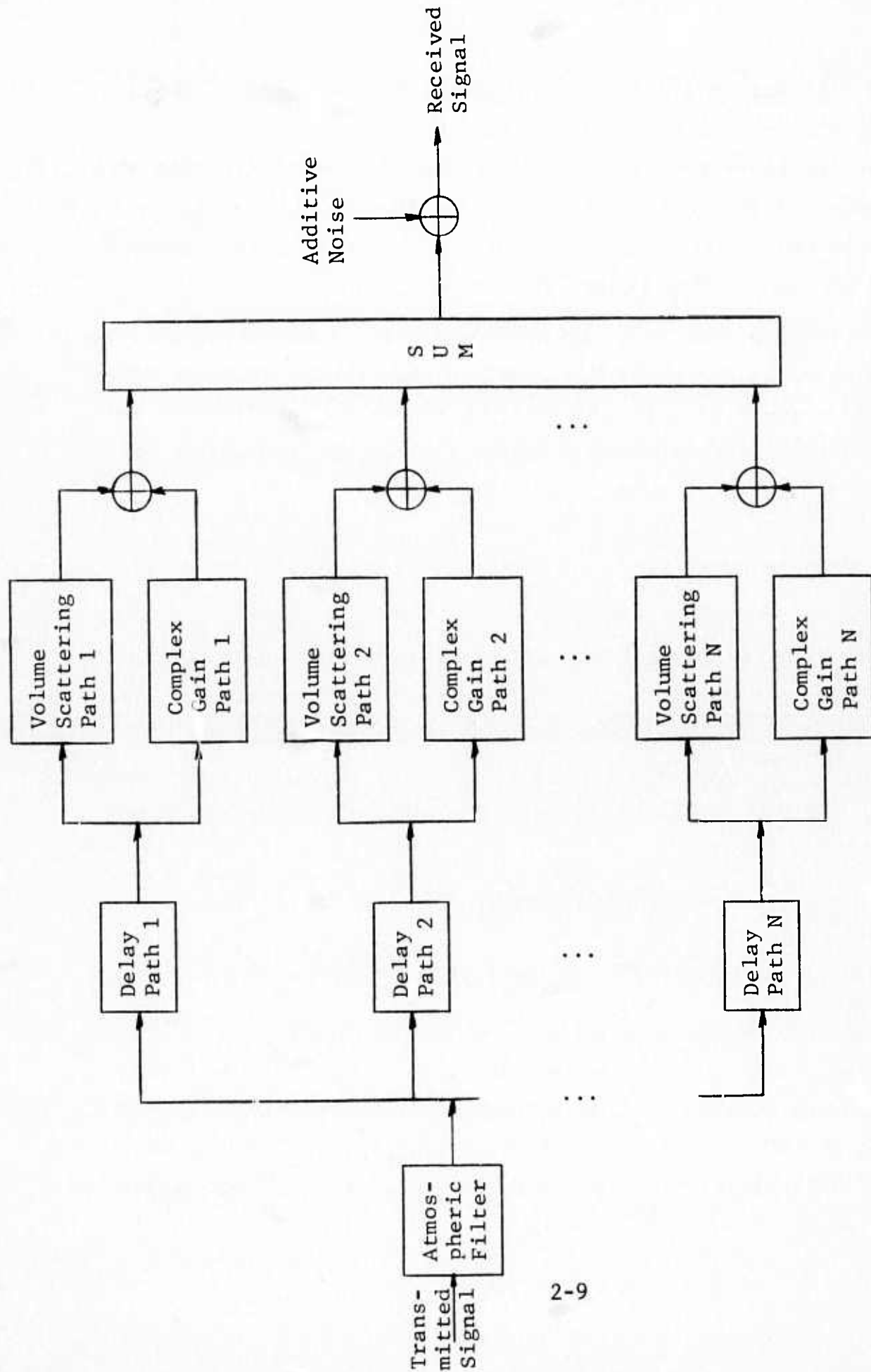


Figure 2.2 General Structure of System Functions for Frequency Selective Tropospheric Propagation Effects

In Section 3.3 it is also shown that even under extreme atmospheric conditions the multipath spread of the volume scattering portion of the troposphere is a small fraction of a nanosecond in the 4 - 10 GHz range. Thus in this frequency range the volume scattering filter in Fig. 2.2 will cause essentially only a flat fading on RCV PN carriers.

The net result of the mild degree of frequency selectivity exhibited by the atmospheric and volume scatter channels relative to the bandwidth of the input signal is to allow the following simple input-output representation for the system of Fig. 2.2 in the absence of additive noise

$$w(t) = \sum_{n=1}^N [G_n + H_n(t)] e^{j2\pi F_n t} z(t - \tau_n) \quad (2.12)$$

where $z(t)$, $w(t)$ are the complex envelopes of the input and output signals, G_n , τ_n , and F_n are the slowly varying complex amplitude, delay and Doppler shift of the n 'th path due to aircraft or layer motion in the absence of volume scattering, and $H_n(t)$ is the more rapidly varying complex gain due to the volume scattering.

The impulse response corresponding to (2.12) is

$$g(t, \xi) = \sum_{n=1}^N [G_n + H_n(t)] e^{j2\pi F_n t} \delta(\xi - \tau_n) \quad (2.13)$$

where $\delta(\cdot)$ is a unit impulse function. Fourier transforming (2.13) we obtain the time-variant transfer function

$$T(f, t) = \sum_{n=1}^N [G_n + H_n(t)] e^{j2\pi F_n t} e^{j2\pi f \tau_n} \quad (2.14)$$

The frequency selectivity in this transfer function is due to the reinforcement and cancellation of the phasor terms $\exp(j2\pi f\tau_n)$. While this type of frequency selectivity can be quite severe and can produce coherence bandwidths much smaller than the bandwidth of typical pulses used in the PN carrier, it will be shown that this selectivity causes no "coherence bandwidth" limitation as far as the use of high PN symbol transmission rates is concerned, because in the limit of high PN symbol rates, the individual path components can be resolved by the correlation process and the PN system can operate with the aid of a single path.

Of course if the symbol rate increases to the point where the bandwidth becomes much bigger than 1 GHz, one must consider the possibility of extreme atmospheric conditions under which the simple model (2.12) will be inadequate and the frequency selectivity of the atmospheric dielectric constant will have to be considered. Section 3.5 indicates that such a condition may occur in the 4 - 8 GHz band only in the case of heavy rainfall. However in this case the attenuation produced by the rainfall is more harmful than the frequency selective degradation of the PN carrier system.

The volume scatter will also become frequency selective under turbulent atmospheric conditions for bandwidths sufficiently larger than 1 GHz. As discussed in Section 3.3, the strength of the volume scatter channel output for a given path is small enough to cause at most only a few dB and a few degrees fluctuation on the paths received signal. Moreover, increasing the PN carrier bandwidth can only improve performance by allowing some of the volume scatter multipath to be discriminated against by the correlation process, as discussed below. Thus volume scattering cannot provide a coherence bandwidth limitation to the use of wideband PN carriers.

Other possible frequency selective propagation effects have been mentioned: scattering and reflection from the surface of the earth and other discrete reflections. The general structure of the system functions corresponding to these propagation effects take the same form as Fig. 2.2 with the box labeled "volume scattering" replaced by an appropriate linear, possibly time-variant operation. For these propagation effects also, in the limit of large PN carrier bandwidths, a particular path can be singled out to the exclusion of the other propagation paths and no coherence bandwidth limitation appears.

2.3 Characterization of RCV PN Carrier Channels

Here we wish to characterize the RCV channel between the baseband data input and output signals so that the relationship between propagation channel characteristics, PN carrier parameters, and data signal degradation may be made explicit. Figure 2.3 shows the signal processing operations of an RCV link including PN carrier modulation and demodulation. The baseband data signal is modulated on a PN carrier. For the purposes of the present discussion this PN carrier may be assumed to have a very general structure, consisting of sequences of M'ary PSK pulses which are frequency-hopped, time-hopped, and time gated for multiple access operation.

At the receiver, a locally generated PN carrier, essentially identical except for a time delay τ , phase shift ψ , and a possible frequency shift, is mixed with the incoming signal and the difference frequency component is selected either at zero frequency or some assigned offset frequency. In Appendix A it is shown that the relationship between the complex

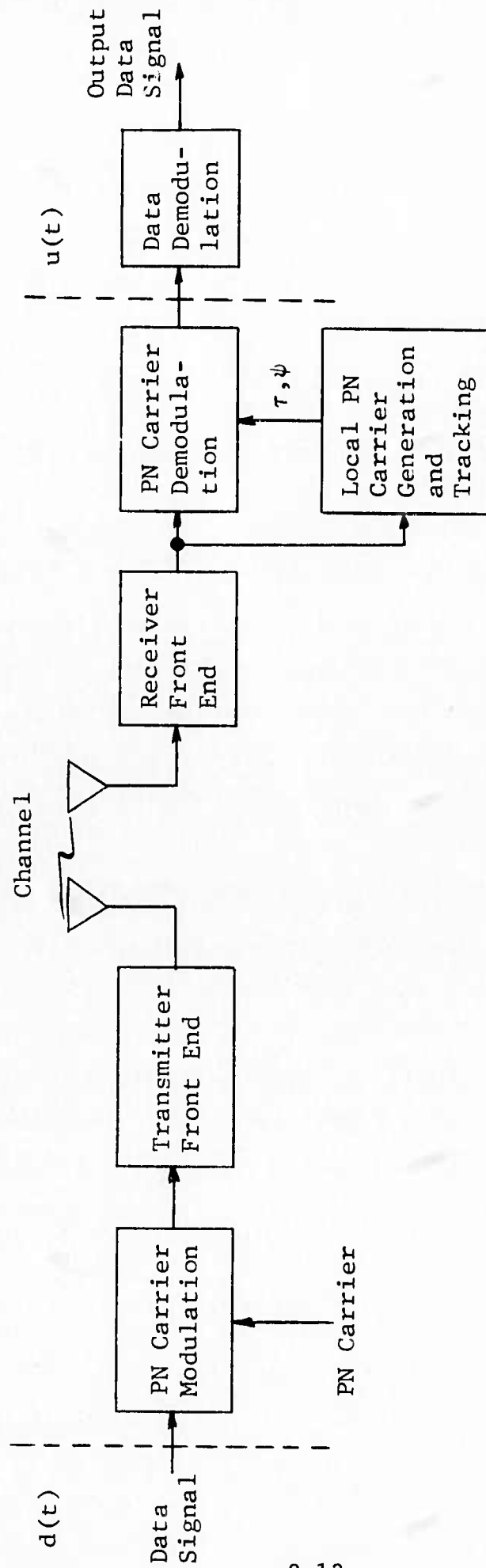


Figure 2.3 Signal Processing Operations of an RCV Link Including Pseudo-Noise Carrier Modulation and Demodulation

envelope of the input data signal $d(t)$ and the output signal after the PN carrier demodulation, $v(t)$, is given very closely by a simple complex multiplication plus an additive noise, i.e.,

$$v(t) = d(t-\tau_0)e^{j\psi}G(t,\tau) + n(t) \quad (2.15)$$

where $n(t)$ is an additive noise, and the complex gain

$$G(t,\tau) = \int R(\tau-\xi)g(t,\xi) d\xi \quad (2.16)$$

where $R(\tau)$ is the autocorrelation function of the PN carrier.

The simple relationship (2.15) applies when the data signal symbol duration is much greater than the ξ -duration of the product $R(\tau-\xi)g(t,\xi)$. This duration can be no bigger than the multipath spread of the channel, which in the present case is surely very much smaller than the duration of a data symbol.

We see from (2.15) that as far as the data signal is concerned the PN carrier waveform and channel enter into a determination of the output signal only through the integral of the product $R(\tau-\xi)g(t,\xi)$. The unimportance of coherence bandwidth for high baud rate PN carrier systems transmitted over channels with the discrete multipath structure of the troposphere (2.13) can be made evident by examination of (2.16) and Fig. 2.4.

In Fig. 2.4(a) the three-path structure

$$g(t,\xi) = e^{j2\pi F_1 t} [G_1 + H_1(t)]\delta(\xi-\tau_1) + e^{j2\pi f_2 t} [G_2 + H_2(t)]\delta(\xi-\tau_2) + e^{j2\pi f_3 t} [G_3 + H_3(t)]\delta(\xi-\tau_3) \quad (2.17)$$

has been sketched. The shaded regions are used to depict the volume scattering multipath. A triangular autocorrelation function of base $2\Delta/m$ has been assumed such as would apply to a binary PSK PN carrier with "chip" width Δ/m for $m = 1, 2, 6$. The delay parameter τ has been set equal to τ_1 so that $R(\tau_1 - \xi)$ is a triangle (unit peak) centered on the first path delay at $\xi = \tau_1$. Note that increasing the integer m increases the PSK chip rate of the PN carrier.

For $m=1$ we note that $G(t, \tau_1)$ contains three terms

$$G(t, \tau_1) = e^{j2\pi F_1 t} [G_1 + H_1(t)] + \frac{2}{3} e^{j2\pi F_2 t} [G_2 + H_2(t)] + \frac{1}{3} e^{j2\pi F_3 t} [G_3 + H_3(t)] \quad (2.18)$$

It follows that for $m=1$, $G(t, \tau)$ will fluctuate considerably in amplitude and phase causing the received data signal SNR to drop to low values, occasionally producing error bursts. (The phase fluctuation problem can be countered somewhat by using differential PSK for the data.) Figure 2.4(b) presents plots of the transfer function* of the channel and of the PN carrier for $m = 1, 2, 6$. Note that for $m=1$ (chip width = Δ) the PN carrier spectrum is mostly within the coherence bandwidth and yet the PN carrier system is suffering considerable degradation.

* We cannot plot complex functions in Fig. 2.4(a) and (b) so we plot real parts of these functions instead.

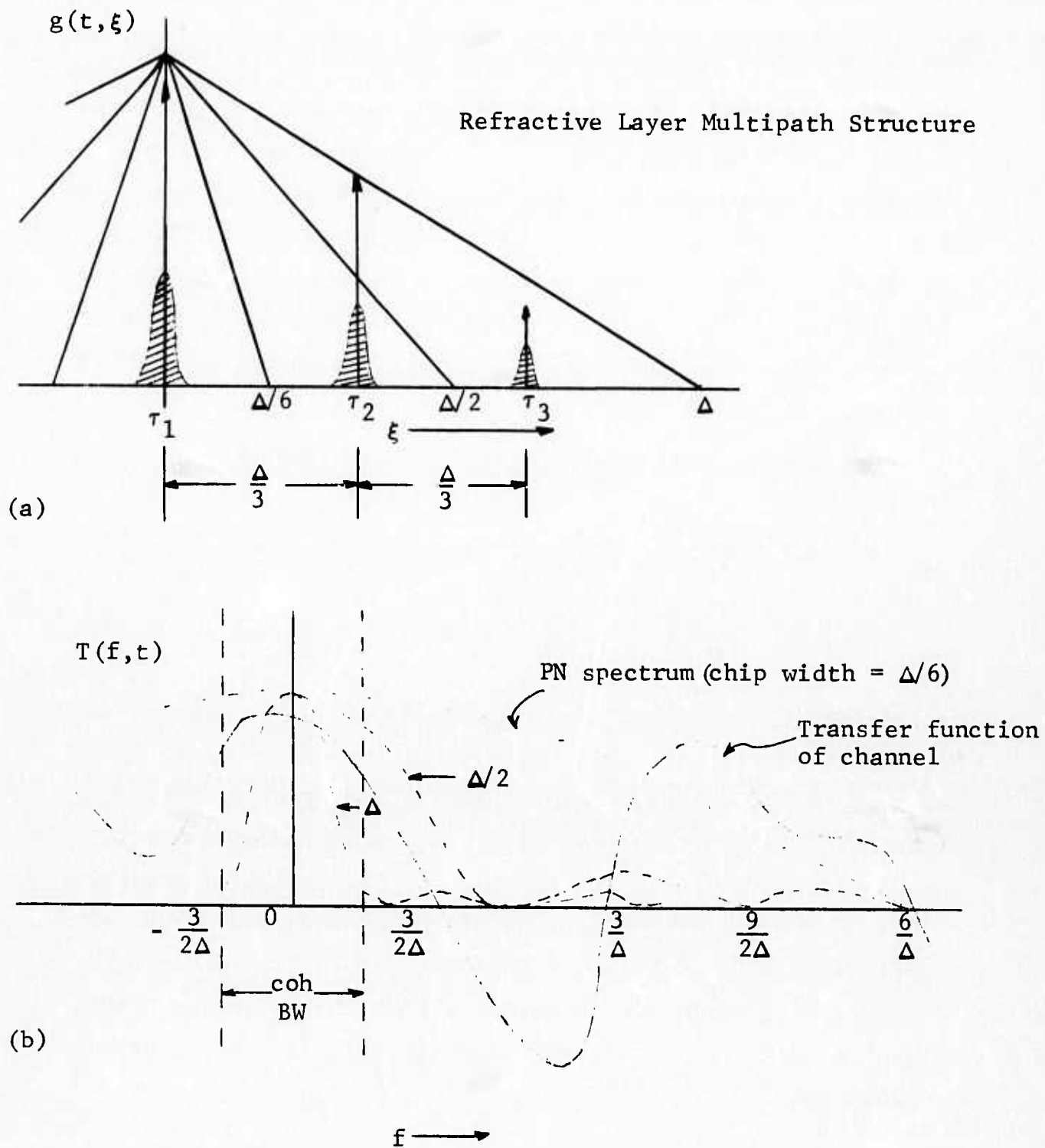


Figure 2.4 Illustration of Effect of Tropospheric Channel Multipath on PN Carrier System

If m is increased to 2 (chip width = $\Delta/2$) we note that one path has been "gated-out" of $G(t, \tau_1)$,

$$G(t, \tau_1) = e^{j2\pi F_1 t} [G_1 + H_1(t)] + \frac{1}{3} e^{j2\pi F_2 t} [G_2 + H_2(t)] \quad (2.19)$$

The fluctuations in $G(t, \tau_1)$ have been considerably improved by increasing the PN carrier bandwidth beyond the coherence bandwidth! Furthermore, increasing m to 6 (chip width = $\Delta/6$) eliminates two of the paths,

$$G(t, \tau_1) = e^{j2\pi F_1 t} [G_1 + H_1(t)] \quad (2.20)$$

and reduces the fluctuations on $G(t, \tau_1)$ to those caused by volume scattering effects alone. Examination of Fig. 2.4(b) shows that for $m=6$ the PN carrier spectrum is violently "chopped" up by the channel's frequency selectivity. The above exercise has proven that the coherence bandwidth of the tropospheric discrete multipath structure does not produce a limitation on the use of ever larger PN carrier bandwidths. In order for the tropospheric multipath structure not to appear discrete, extremely large PN carrier bandwidths virtually encompassing the entire 4 - 10 GHz band would have to be used.

It is evident that to achieve the desired "gating out" of the multipath in the integral (2.16) the autocorrelation function of the PN carrier should be as narrow as possible for a given bandwidth of the PN carrier. To practically achieve very large PN carrier bandwidths, say approaching or exceeding a

Gigahertz, requires some form of frequency hopping. In Appendix B it is shown that very good autocorrelation functions can be achieved for the frequency hopped PN carrier if the probability distribution of the frequency hop is appropriately tapered. Thus in Fig. 2.5 we show the PN carrier (complex envelope) autocorrelation functions for uniform and raised-cosine tapered frequency hop probabilities. It is assumed that the PSK pulse width is Δ and that there are 11 frequency hops n/Δ ; $n=0, \pm 1, \dots, \pm 5$ about the carrier center frequency. The importance of good sidelobes on the PN signal will become even more evident in Section 3.2 where it will be shown that spurious discrete multipath components may exist which are much stronger than the desired path.

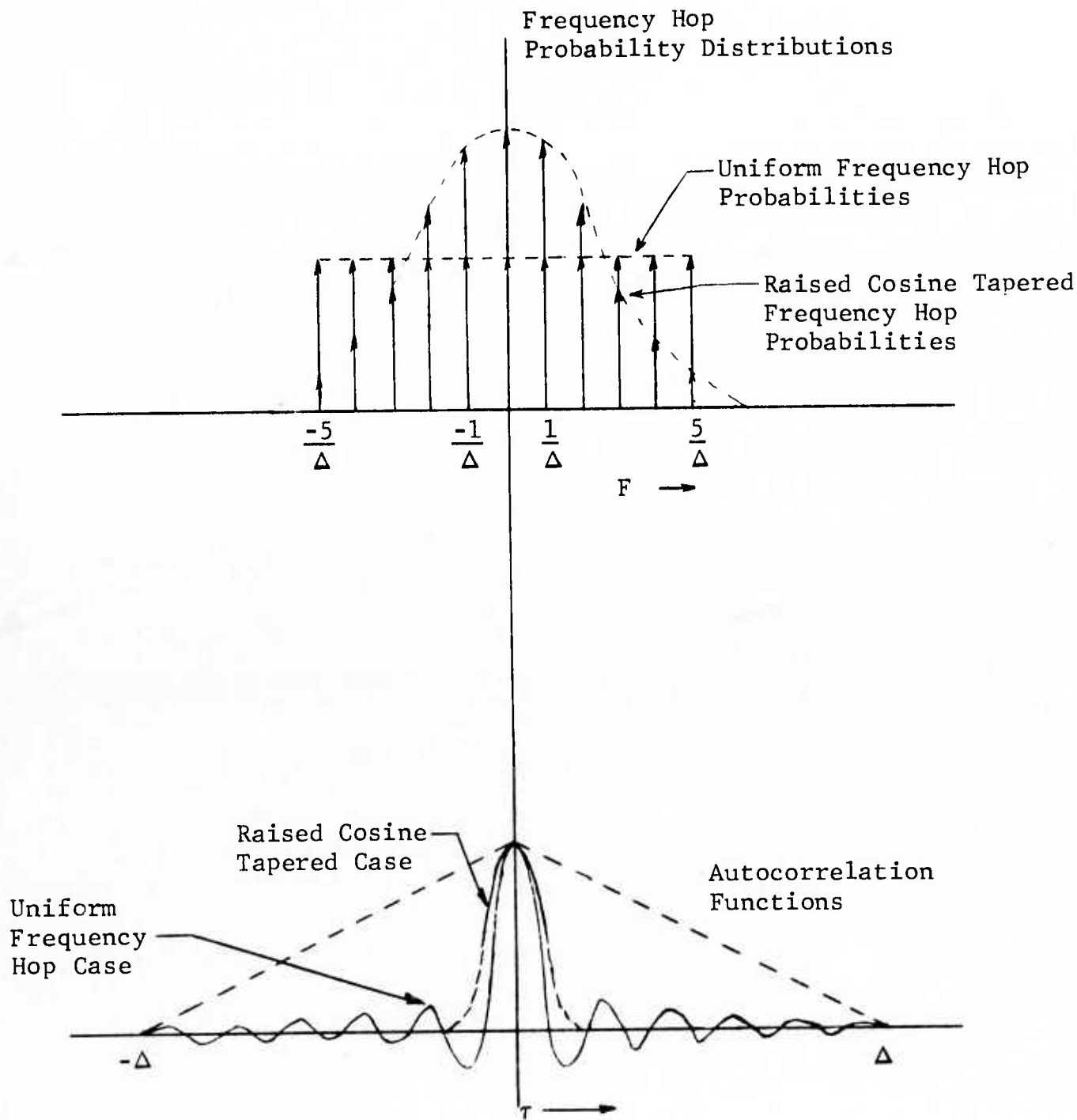


Figure 2.5 PN Autocorrelation Functions for Uniform and Raised Cosine Tapered Frequency Hop Probabilities

SECTION 2
REFERENCES

- [2.1] T. Kailath, "Sampling Models for Linear Time-Variant Filters," MIT Research Lab. of Electronics, Cambridge, Mass., Report No. 352, May 25, 1959.
- [2.2] P. A. Bello, "Characterization of Randomly Time-Variant Linear Channels," IEEE Trans. on Communication Systems, Vol. CS-11, December 1963, pp. 360-393.

SECTION 3 CHANNEL MODELING

This section documents the results and details of the channel modeling investigation. Section 3.1 discusses the rationale for the approach taken in propagation modeling and summarizes some of the results of the multipath and frequency selectivity calculations. Section 3.2 discusses the most serious multipath phenomenon--that caused by refractive layers having a steep negative gradient of refractive index with increasing height. Following this section, Sections 3.3, 3.4, and 3.5 consider in succession the volume scattering channel, the atmospheric channel, and the surface scattering and reflection channel.

3.1 Methods of Approach

In Fig. 3.1 we have presented a classification of propagation effects according to their potential harmful effects on wide-band PN systems. Propagation effects may be broadly classified into those that cause frequency-selective distortion on communication signals and those that do not. It is only the former that may cause special difficulty to high baud rate PN systems. Consequently it is only the former which we have studied in detail.

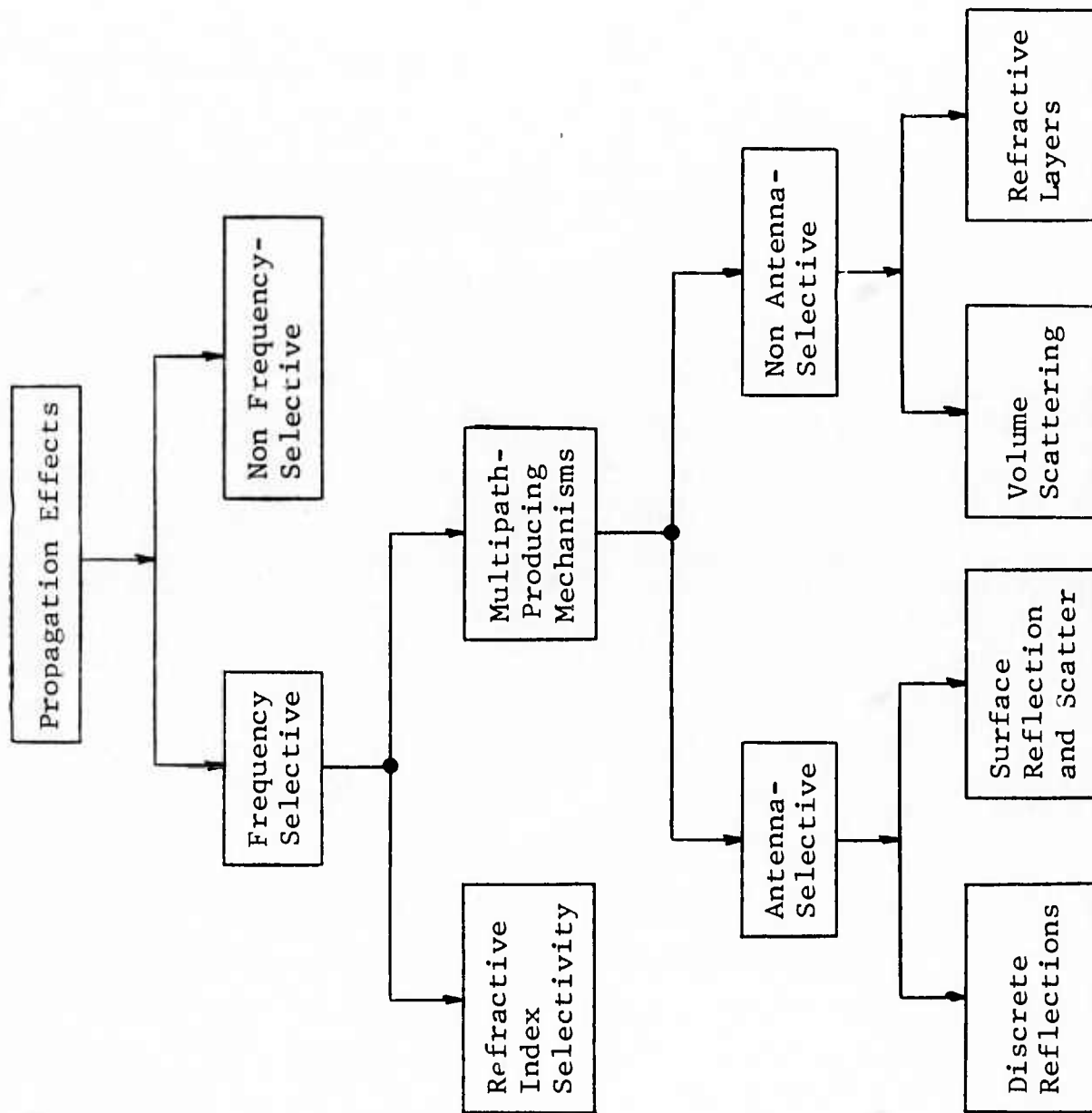


Figure 3.1 Classification of Propagation Effects According to Their Potential Effect on High Baud Rate PN Systems

The frequency selective effects may be further subdivided into those that are caused by multipath and those that are not. The latter type of frequency selectivity is due to the frequency dependence of the complex refractive index of rain, water vapor, and oxygen. As discussed in Section 3.4, in the frequency range of interest, 4 - 10 GHz, these frequency selective effects do not impose significant performance limitations for high baud rate PN systems.

We further subdivide the multipath-producing propagation mechanisms into those that are markedly influenced by the size of the antenna beam width and those that are not. This subdivision is clearly of practical significance in RCV system design. If one assumes well-designed aircraft antennas and large adaptive phased arrays for the ground station with flight patterns prohibited from very low elevation angles it may be possible to greatly reduce multipath caused by reflection and scattering from the surface of the earth and discrete reflections from mountains, buildings, etc.

If care is taken to reduce these multipath effects by system design, there will still remain the multipath effects due to the troposphere itself. These tropospheric effects are of two types: those which produce an essentially spatially random fluctuation in refractive index (labeled volume scattering in

Fig. 3.1) and those which produce layers having sharp vertical negative gradients in refractive index.

Volume scattering effects are essentially ever-present but their intensity varies with weather conditions. From a system-function point of view, the spatially random fluctuations produce a continuously distributed multipath. It is shown in Section 3.3 that even under extreme postulated conditions the continuously distributed multipath spread caused by volume scattering is sufficiently small to cause negligible frequency selective effects even for very high baud rates (say 1 Gigabaud).

The refractive layers can produce discrete multiple paths between transmitter and receiver when the path geometry and layer characteristics assume certain values. The most typical situation is a single dominant layer and two or three paths. Multipath spreads may vary from less than a nanosecond to tens of nanoseconds. It appears that path strengths are of equal strength only in limited regions of space (several miles). In contrast to volume scattering, refractive layers may only occur a small percentage of time for certain geographic areas and a high percentage for other geographic areas. Also, when layers are present, small elevation angles (less than $2 - 3^\circ$) between terminals are required to produce the multiple paths. Nonetheless they appear to be the most serious multipath effects because they cannot be discriminated against by antennas.

3.2 Tropospheric Refraction Channel

Propagation in the troposphere is affected by variations in the refractive index structure which have a scale much larger than a wavelength. These variations act as a complicated lens system which focuses (and defocuses) the transmitted signal into various regions of space. When the same signal is refracted into a region via more than one path, a receiver in that region experiences multipath fading. When the refractive index structure acts to defocus the signal, i.e., focus the energy away from the receiver, a deep signal fade is observed on the link.

With the aid of the equations of geometric optics, the relative amplitudes and delays of multiple paths caused by the commonly occurring layered refractive index structures may be calculated. The propagation modeling is presented in 3.2.1 and the resulting multipath characteristics are given in 3.2.2. Figure 3.19 presents an example of a computation of multipath structure. A number of important features of the multipath structure in LOS links is brought out in the analyses and summarized in Tables 3-1 and 3-2. Some of the more significant results are restated below:

1. In the presence of a stratified refractive index layer, there is a maximum elevation angle for which multipath can occur on ground-air (g-a) links. This results from the fact that in order for multipath to exist, both the terminals must be in close proximity to the layer, (see Section 3.2.2.2). Since under steady-state conditions these layers are measured to have maximum tilt angles of a few degrees ([3.2] reports about 2.3° , [3.10] reports about 1.1°), multipath interference on g-a links is limited to flights with elevation angles less than a few degrees.

Table 3-1
TYPICAL MULTIPATH ON GROUND-AIR LINKS

Elevation Angle of Receiver With Respect to Transmitter	Height of Layer Above Terminals Feet	Extent of Multipath Regions Miles	Range of Delay Differences Nanoseconds	Ratio of Multipath Power P to Direct Path P _d
Greater than about 2-3°	—	No multipath	—	—
Less than about 2-3°	660	No multipath	—	—
	600	92 — 100	15 — 16	$\frac{P}{P_d} > 1$
	300	65 — 100 155 — 200	3 — 10 36 — 72	$\frac{P}{P_d} > 1$
	200	52 — 100 123 — 200	0 — 10 20 — 67	$\frac{P}{P_d} > 1$
	0	0 — 200	0 — 65	$\frac{P}{P_d} = 1$

Table 3-2
TYPICAL MULTIPATH ON AIR-AIR LINKS

Height of Terminals Above* Layer Feet	Minimum Range For Multipath Miles	Delay Difference at 100 Miles Nanoseconds	Relative Power dB
1,000	112	No multipath	—
700	100	0	0
675	98	0.1	-3.9
630	96	0.2	-6
210	70	2.8	-14.3

* When terminals are below layer, Table 3-1 applies.

2. On g-a links, the minimum range at which multipath occurs is dependent on the height of the layer above the terminals. As the layer height increases, the range increases.

3. On g-a links, the number of multipath signals is dependent on the height of the layer above the terminals. As the layer height decreases more multipath signals appear.

4. The strength of these multipath signals is greater than or equal to the direct path signal strength. This phenomenon has been observed by DeLange [3.40] on a 22 mile ground-ground (g-g) microwave link. It should be noted that the spread spectrum modem will tend to lock onto the stronger path. Since the multipath signals will appear and disappear with variable delay, this could capture the modem receiver and then leave it in an out-of-synch condition.

5. The above results also apply to air-air (a-a) links for which the layer is above the terminals.

6. On a-a links for which the layer is below the terminals, the onset of multipath is dependent on the distance of the layer below the terminals. As the layer height decreases, the minimum range at which multipath occurs increases.

7. In both g-a and a-a links, the multipath structure has the same character: at the onset of multipath there are two strong paths at the same delay. As the range increases, these paths separate in delay. The amount of delay separation and relative strengths of the paths is dependent on the refractive index structure and the system geometry (see Sections 3.2.2.2 and 3.2.2.3). Multipath spreads of less than 10 ns will be common on ground-air links.

Fading can also occur in a LOS link when the receiver is in an attenuation region. Unlike multipath fading, this is due to a loss in signal strength within a radio hole or an earth shadow region. The shadowing caused by the intercession of the earth's surface in the propagation path is summarized in Table 3-3. It is seen that the location of the shadow region is affected by the location of a layer when that layer is between the terminals. Thus for a fixed terminal link, a wave-like movement of the layer could cause alternate fading of the received signal. More detailed analyses on each type of fading phenomenon is presented in the main body of this section.

Table 3-3
 TYPICAL EARTH SHADOW REGIONS ON GROUND-AIRCRAFT LINKS

Height of Layer Above Transmitter Feet	Range to Shadow Zone in Miles		
	$h_R = 5K$ Feet	$h_R = 10K$ Feet	$h_R = 15K$ Feet
No layer	100	140	172
2,500	104	148	180
900	114	158	190
500	128	173	204

h_R = height of receiver above transmitter

3.2.1 Propagation Modeling

3.2.1.1 Physical Basis for Layers

The refractive index of the lower atmosphere can be determined directly from microwave refractometer measurements or indirectly from meteorological data. The refractometer utilizes a microwave cavity which has a resonant frequency dependent on the test atmosphere it contains. By tracking the difference in resonant frequency between the test cavity and a sealed cavity, one may monitor refractive index changes with a great deal of accuracy and very little time lag. Since the measurements of temperature, pressure, and humidity are readily available around the world, it is also a common practice to obtain the refractive index indirectly from these constitutive parameters. The refractive index n can then be expressed empirically in N units as (see Ref. [3.1])

$$N = \frac{77.6}{T} \left(P + \frac{4810e}{T} \right) \quad (3.1)$$

where N is the refractivity, given by

$$N = (n-1) 10^6 \quad (3.2)$$

and P , T , and e are the atmospheric pressure, absolute temperature and vapor pressure respectively. Processes such as heating and cooling from the land or sea, wind eddy diffusion, large air mass movement, etc., influence the refractivity profile and in turn cause anomalous propagation in the troposphere.

Measurements of the mean refractive index structures of the troposphere indicate that N decreases with increasing height in an approximately linear fashion with occasional marked departures from this mean. These marked departures manifest themselves as steep gradients of refractive index existing over thin horizontal regions, as shown in Fig. 3.2. Typical refractivity measurements showing this type of profile are given by Kerr [3.2], Beckmann and Spizzichino (Ref. [3.3], Figs. 19.1 - 19.8), Ikegami [3.4], Wong [3.5], and Guinard et al., [3.6]. An extensive world-wide treatment of refractivity profiles is given by Bean and Dutton [3.7] and Bean et al., [3.8].

3.2.1.2 Refractive Index Structures

Measurements taken by the World Radio Refractive Index Data Center at Boulder, Colorado (see Ref. [3.9], Fig. 3) indicate that the mean value of the initial refractive index gradient (measured at Cape Kennedy, Florida) is about

$$\left(\frac{\partial N}{\partial h}\right) = -60 \text{ N units/km.} \quad (3.3)$$

whereas the standard value given by Kerr (Ref. [3.2], p. 53) is

$$\left(\frac{\partial N}{\partial h}\right)_{\text{std.}} = -40 \text{ N units/km.} \quad (3.4)$$

The statistical distributions of layer thickness were measured over a three year period in an arctic, temperate, and tropical maritime climate (see Ref. [3.7], pp. 140-145). The data indicate the existence of layers with thickness varying from about 40 to 400 meters, with mean values given by

$$\omega = \begin{cases} 66 \text{ meters in arctic climate} \\ 97 \text{ meters in temperate climate} \\ 106 \text{ meters in tropical maritime climate.} \end{cases} \quad (3.5)$$

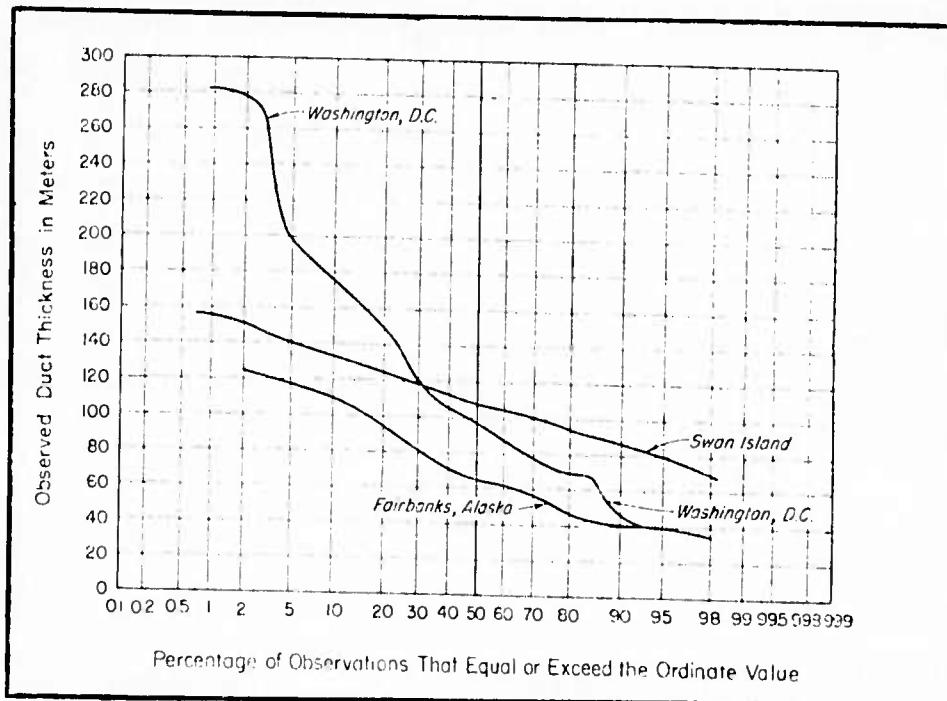
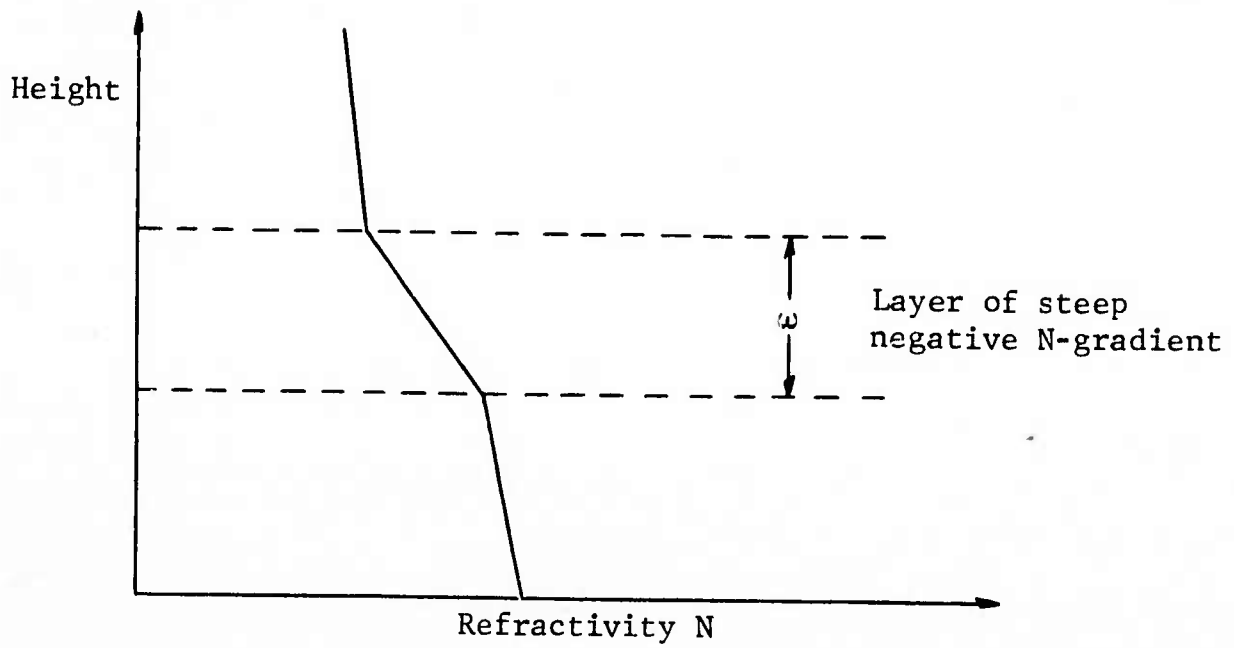


Figure 3.2 Typical Refractivity Profile
 a. Total profile
 b. Distribution of layer thickness (taken from Ref. 3.7).

The distribution of ω obtained from this data as shown by Bean and Dutton is reprinted in Fig. 3.2 for reference. Beckmann and Spizzichino (Ref. [3.3], p. 442) have deduced the thickness of these elevated layers to be less than 100 meters 90% of the time.

The steepest gradient of N observed in the data presented by Bean and Dutton was given by

$$\text{steepest } \left(\frac{\partial N}{\partial h} \right)_{\text{layer}} = -420 \text{ N units/km.} \quad (3.6)$$

The steepness of this negative refractivity gradient exhibits climatic as well as seasonal variations.

These layers are usually assumed to be horizontally stratified, although in the presence of wind shear and frontal inversions, they have been observed (Ref. [3.2], p. 363) to have tilt angles of up to 2.3° . In the presence of multiple convective processes, there may be perturbations in the layered structure which manifest themselves as random wave-like disturbances [3.10]. These would act to change the tilt angles of the layers as a function of both space and time. Due to the complexity, variability, and lack of definitive statistical data, such refractive index structures, along with other possible but infrequent structures, are only listed here under the category of "other structures" (see Fig. 3.3).

3.2.1.3 Radio Propagation in the Presence of Layers

3.2.1.3.1 Geometric Optics for RCV Applications

Geometric optics is the limiting form of physical optics as the wavelength approaches zero. Physical optics results from solutions to the wave equation, while geometric optics utilizes frequency independent ray tracing techniques. For tropospheric communication links at microwave frequencies, ray tracing yields approximate results on delay differences, angle of arrival,

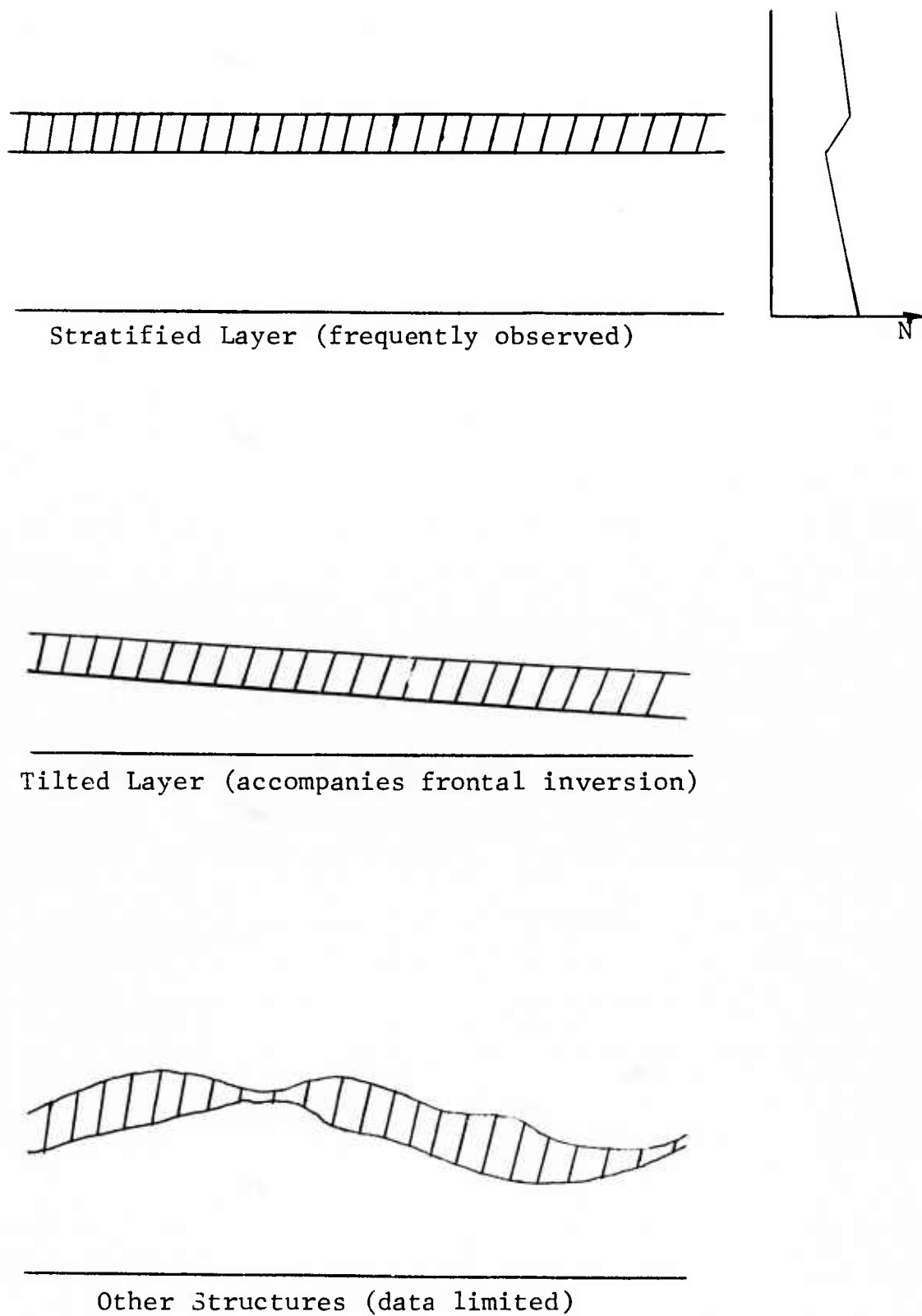


Figure 3.3 Horizontal Variation of N-Profile

and signal power levels. A brief description of the method of geometric optics is presented in Appendix D. The time delay ξ associated with a given ray path is derived in terms of the refractive index profile. It is shown that

$$\xi = \frac{1}{c_0} \int_{\text{path}} n \, d\sigma \quad (3.7)$$

where c_0 is the velocity of propagation in free space, and the integration is performed over the path trajectory. The path trajectory has a local radius of curvature R in a vertical n -gradient of

$$R = -1/(\partial n/\partial z) \quad (3.8)$$

In addition, Snell's law is satisfied along any ray. It is shown below that rays can be traced with respect to the spherical earth by using an earth-flattening coordinate transformation which only has the effect of modifying the refractive index ($n \rightarrow m$) in the flat earth geometry.

3.2.1.3.2 Flat Earth

Assuming that a ray is launched from a height h_T at an angle α over a flat earth (see Fig. 3.4), then Snell's law at any point along that ray can be written as

$$n(z) \cos \beta = n(h_T) \cos \alpha = K \quad (3.9)$$

where β is the inclination of the ray, $n(z)$ is the refractive index, and K is constant. From Eq. (3.9), the tangent of β can be derived as

and signal power levels. A brief description of the method of geometric optics is presented in Appendix D. The time delay ξ associated with a given ray path is derived in terms of the refractive index profile. It is shown that

$$\xi = \frac{1}{c_0} \int_{\text{path}} n \, d\sigma \quad (3.7)$$

where c_0 is the velocity of propagation in free space, and the integration is performed over the path trajectory. The path trajectory has a local radius of curvature R in a vertical n -gradient of

$$R = -1/(\partial n/\partial z) \quad (3.8)$$

In addition, Snell's law is satisfied along any ray. It is shown below that rays can be traced with respect to the spherical earth by using an earth-flattening coordinate transformation which only has the effect of modifying the refractive index ($n \rightarrow m$) in the flat earth geometry.

3.2.1.3.2 Flat Earth

Assuming that a ray is launched from a height h_T at an angle α over a flat earth (see Fig. 3.4), then Snell's law at any point along that ray can be written as

$$n(z) \cos \beta = n(h_T) \cos \alpha = K \quad (3.9)$$

where β is the inclination of the ray, $n(z)$ is the refractive index, and K is constant. From Eq. (3.9), the tangent of β can be derived as

Summary of Geometric Optics (Flat Earth)

Refractive Index: n

Transmitter Height: h_T

Receiver Height: h_R

Snell's Law: $n \cos \beta = \text{constant}$

Ray Curvature: $R = -1/|\nabla n|$

Delay: $\xi = \frac{1}{c_0} \int n d\sigma$

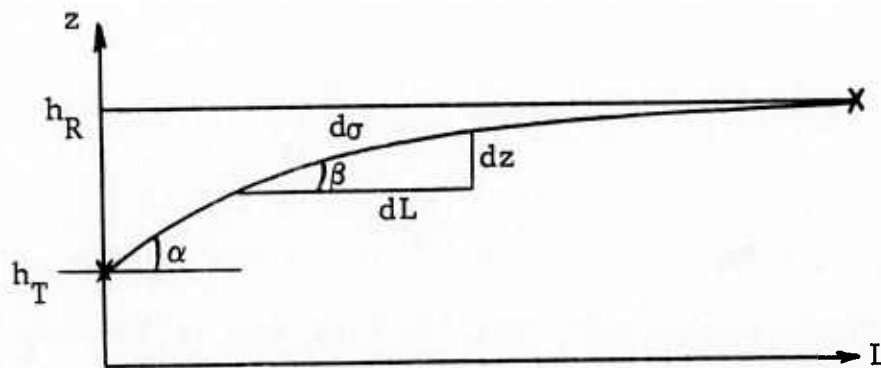


Figure 3.4 Flat Earth Geometry

$$\tan \beta = \frac{\sqrt{n^2(z) - K^2}}{K} \quad (3.10)$$

The differential arc length $d\sigma$ can be written as

$$d\sigma = \cos \beta \, dL + \sin \beta \, dz \quad (3.11)$$

Substituting (3.9) - (3.11) into Eq. (3.7) for the path delay, and evaluating ξ from the transmitting point to the receiving point (L, h_R) gives

$$\xi = \frac{1}{c_0} \int_0^{L_R} K dL + \frac{1}{c_0} \int_{h_T}^{h_R} \sqrt{n^2(z) - K^2} \, dz \quad (3.12)$$

The evaluation of this integral requires the knowledge of the specific n -profile. However, more importantly, it will now be shown that an identical expression can be derived for a spherical geometry with the exception that the actual n -profile is replaced by a modified profile. The calculations for a stratified atmosphere over a spherical earth can then be carried out assuming a flattened earth with an appropriately modified refractive index profile.

3.2.1.3.3 Spherical Earth and the Modified Index

Assuming that a ray is launched from height h_T above a spherical earth at an angle α with respect to a concentric sphere (see Fig. 3.5), then Snell's law at any point along that ray can be written as

$$(a+z)n(z) \cos \beta = (a+h_T)n(h_T) \cos \alpha \quad (3.13)$$

Summary of Geometric Optics (Spherical Earth)

Modified Refractive Index: $m = n + z/a$

Transmitter Height: h_T

Receiver Height: h_R

Snell's Law: $m \cos \beta = \text{constant}$

Ray Curvature: $R = -1/|\nabla m|$

Delay: $\xi = \frac{1}{c_0} \int m d\sigma$

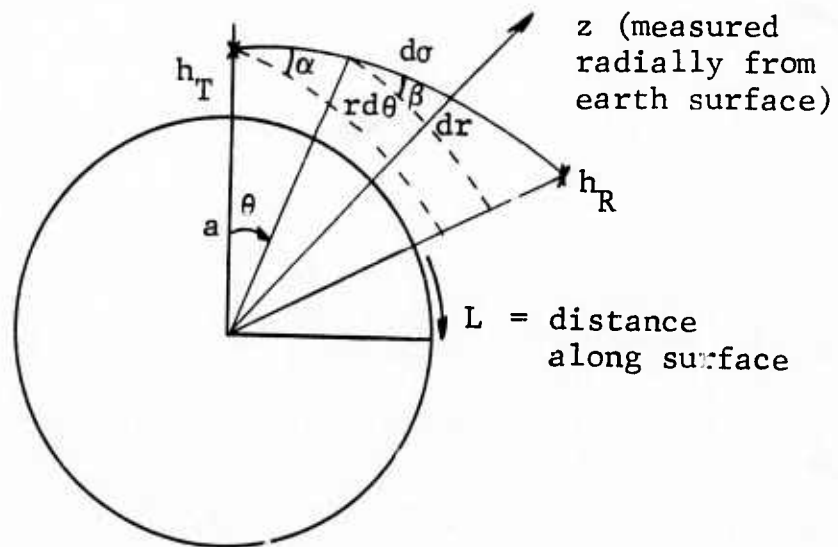


Figure 3.5 Spherical Earth Geometry

where a is the radius of the earth, and z and h_T are measured radially above the surface. Letting

$$m(z) = \left(1 + \frac{z}{a}\right)n(z) \approx n(z) + \frac{z}{a} \quad (3.14)$$

The approximation is close since $n \approx 1$ and $z \ll a$. Equation (3.13) can be written as

$$m(z) \cos \beta = m(h_T) \cos \alpha = K \quad (3.15)$$

The elemental arc length $d\sigma$ is now given by

$$d\sigma = rd\theta \cos \beta + dr \sin \beta \quad (3.16)$$

where

$$d\theta = \frac{dL}{a} \quad (3.17)$$

and L is measured along the surface. Using (3.13) - (3.17) in the evaluation of (3.7), gives the path delay as

$$\xi = \frac{1}{c_0} \int_0^L K dL + \frac{1}{c_0} \int_{h_T}^{h_R} \sqrt{m^2(z) - K^2} dz \quad (3.18)$$

which is identical to the expression (3.12) for the flat earth except that n has been replaced by the modified parameter $m = n(1 + z/a)$.

It is important to note the effect on the ray trajectories of treating the spherical earth as a flat earth with a modified n-profile. Assuming that n varies only in the vertical z-direction, the radius of curvature of a ray is given by Eq. (3.8) as

$$R = -1/(\partial n/\partial z) \quad (3.19)$$

Under the earth flattening coordinate transformation, the modified radius becomes

$$R_{\text{mod}} = -1/(\partial m/\partial z) \quad (3.20)$$

but from Eq. (3.14)

$$\frac{\partial m}{\partial z} \doteq \frac{\partial n}{\partial z} + \frac{1}{a} \quad (3.21)$$

Therefore

$$R_{\text{mod}} = \frac{1}{\frac{1}{R} - \frac{1}{a}} \quad (3.22)$$

Equation (3.22) indicates that if the actual radius of curvature of a ray is equal to the radius of the earth, i.e.,

$$R = a, \quad (3.23)$$

then under the earth flattening coordinate transformation

$$R_{\text{mod}} = \infty \quad (3.24)$$

Likewise if the actual radius of curvature of a ray is infinite, then the modified radius is $-a$, i.e.,

$$R = \infty \quad (3.25)$$

for

$$R_{\text{mod}} = -a. \quad (3.26)$$

Thus it is seen that the coordinate transformation preserves the relative curvature between the ray and the earth. This is shown diagrammatically in Fig. 3.6, and a graph of the modified radius as a function of the N gradient is shown in Fig. 3.7. It should be noted that a similar coordinate transformation can be performed which straightens the rays and changes the radius of the earth to an effective earth's radius. Since this report utilizes the earth flattening transformation, the effective earth's radius (nominally $4/3$ earth's radius) model will not be discussed herein.

3.2.1.3.4 Signal Strength

Consider a bundle of rays traveling from the transmitter to the range L as shown in Fig. 3.8. Although the intensity of the source is infinite (because a point source is assumed), we can express the source strength as the energy per unit time that leaves a unit sphere surrounding the transmitter. Calling this I_{Ω} , the conservation of energy can be expressed as [3.14]

R = actual radius of curvature
 R_{mod} = modified radius of curvature
 a = radius of earth

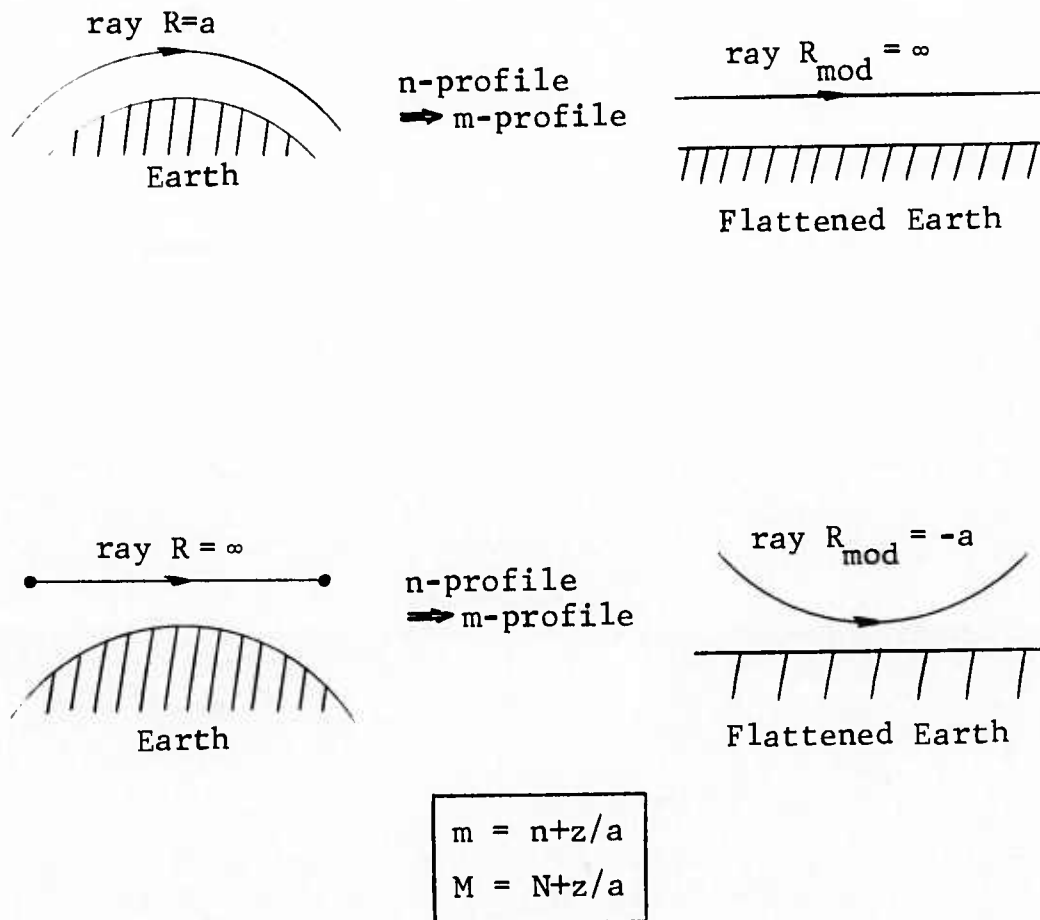


Figure 3.6 Effect of Earth-Flattening Coordinate Transformation on Ray Trajectories

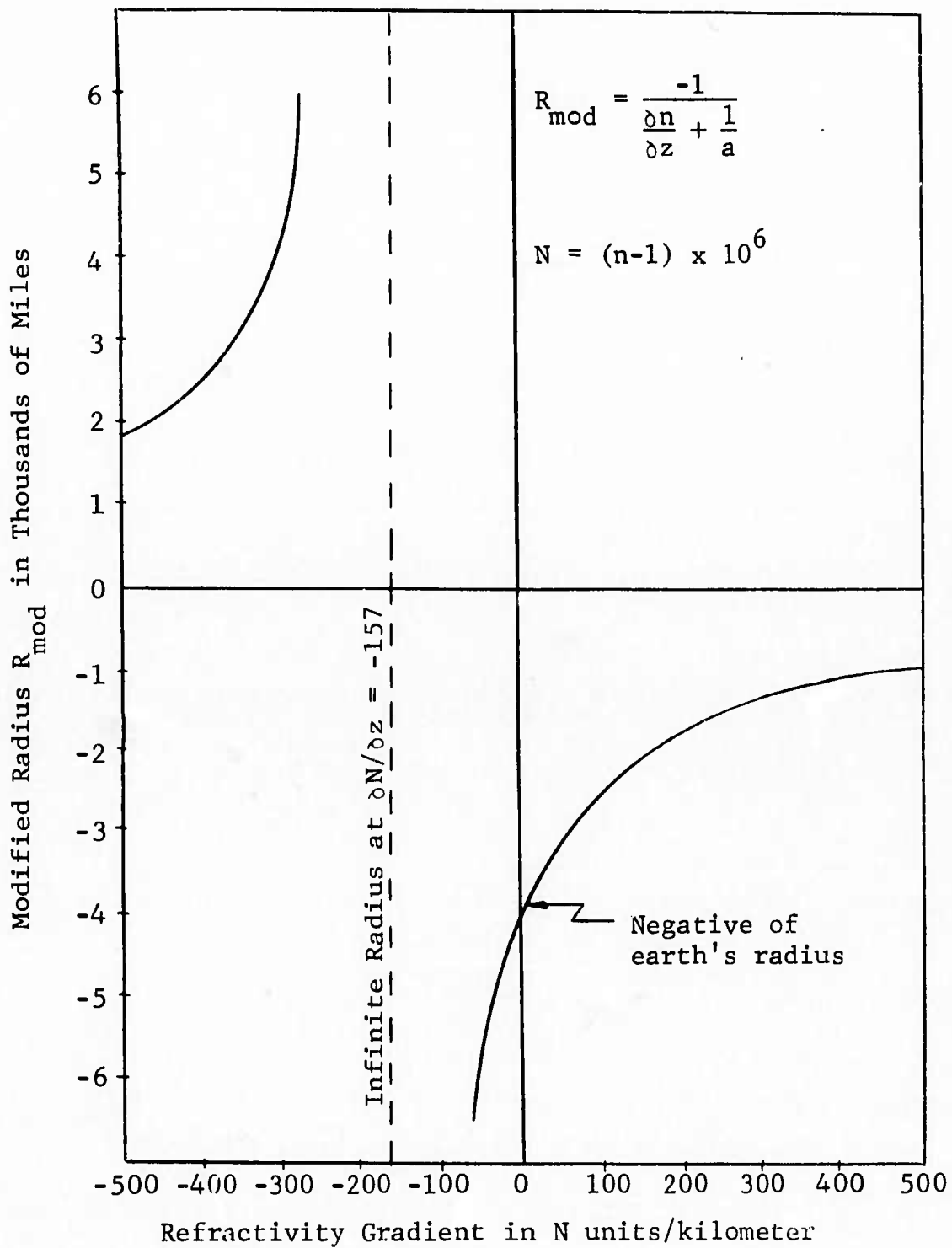


Figure 3.7 Modified Radius of Curvature Versus Refractivity Gradient

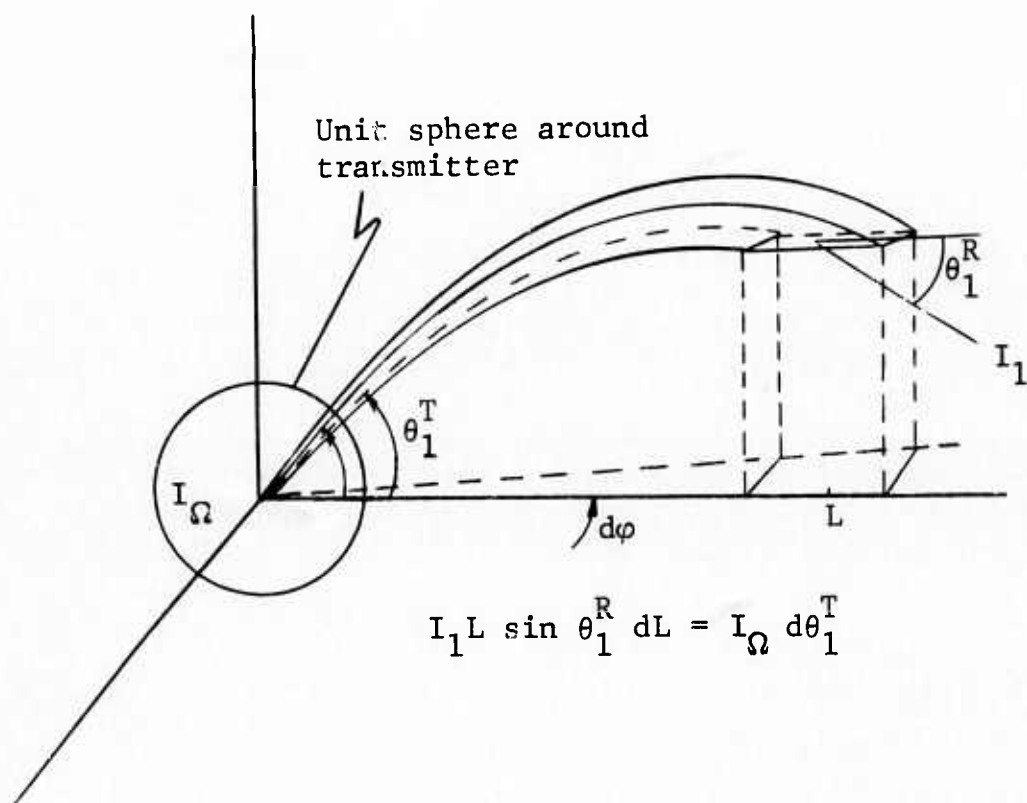


Figure 3.8 Intensity Law

$$I_1 dA_L = I_\Omega \delta\Omega \quad (3.27)$$

where I_1 is the intensity of the signal at L, dA_L is the incremental area normal to the ray trajectory, and $\delta\Omega$ is the area that the ray bundle intercepts on the unit sphere around the source. The area of the ray bundle at L is

$$\delta A = L \delta\varphi \delta L \quad (3.28)$$

where $\delta\varphi$ is in the azimuthal direction. Therefore, the projection of δA normal to the ray trajectory is

$$\delta A_L = \delta A \sin \theta_1^R = L \sin \theta_1^R \delta\varphi \delta L \quad (3.29)$$

where θ_1^R is the angle of the ray at the reception point. $\delta\Omega$ is similarly given in terms of θ_1^T , the ray angle at T, by

$$\delta\Omega = \cos \theta_1^T \delta\theta_1^T \delta\varphi \approx \delta\theta_1^T \delta\varphi \quad (3.30)$$

where the last approximation stems from the fact that for tropospheric LOS links the inclination angles are small. Substituting (3.29) and (3.30) into (3.27) and shrinking the elemental areas to zero gives

$$\frac{I_1}{I_\Omega} = \frac{1}{L \sin \theta_1^R} \frac{d\theta^T}{dL} \quad (3.31)$$

Likewise, if a second bundle of rays with intensity I_2 reaches the element dL by a different path, then

$$\frac{I_2}{I_\Omega} = \frac{1}{L \sin \theta_2^R} \frac{d\theta_2^R}{dL} \quad (3.32)$$

Dividing Eq. (3.31) by (3.32), gives the ratio of the intensities of the two signals which reach this region of space by different paths as

$$\frac{I_1}{I_2} = \frac{\sin \theta_2^R}{\sin \theta_1^R} \frac{d\theta_1^T/dL}{d\theta_2^T/dL} \quad (3.33)$$

Note that if the effective area of the receiving antenna is the same for both multipath signals, (i.e., the antenna does not discriminate against either path), then the power ratio is the same as the intensity ratio and Eq. (3.33) can be used to evaluate the relative power levels of multipath signals. It is interesting to note that the relative power is proportional to the relative slopes of an initial angle versus range (θ^T vs. L) diagram. If for a small change in θ^T , there is a large change in L , the transmitted energy is spread over a large region of space. Likewise, $d\theta^T/dL$ is small, and there is an accompanying reduction of power at a given range L .

It will be convenient in the analysis to express the relative intensities in terms of the normalized parameter k_T and k_R

$$k_T = \frac{2R_0}{L} \sin \theta^T \quad (3.34)$$

$$k_R = \frac{2R_0}{L} \sin \theta^R \quad (3.35)$$

where R_0 is the radius of curvature of the ray.

Then it is simple to show that

$$\frac{\partial k_T}{\partial L} = \frac{-k_T}{L} + \frac{k_R}{\sin \theta^R} \frac{\partial \theta^T}{\partial L} \quad (3.36)$$

Substituting (3.36) into (3.31) gives the intensity law as

$$\frac{I_1}{I_\Omega} = \frac{\partial k_T / \partial L + k_T / L}{L k_R} \quad (3.37)$$

3.2.2 System Function Characteristics

From an input-output point of view, the tropospheric refraction channel can be characterized in terms of the time-variant impulse response, $h(t, \xi)$, [3.28], which is the response at time t to an impulse applied ξ seconds previously. Since tropospheric refraction has the effect of delaying and attenuating the signal as it propagates from transmitter to receiver (over possibly many paths), the impulse response can be written as

$$h(t, \xi) = \sum_{\substack{\text{all} \\ \text{paths}}} \alpha_i \delta(t - \xi_i) \exp [j(\omega_0 + 2\pi f_0 \xi_i)] \quad (3.38)$$

where α_i and ξ_i represent the attenuation and delay of the i 'th path, ω_0 the initial carrier phase, and $2\pi f_0 \xi_i$ the phase change on the carrier (at $f=f_0$) due to the path delay ξ_i . $\delta(\cdot)$ is the unit impulse function. Note that random phase fluctuations due to volume scattering have not been included (see Section 3.3 for a consideration of these). It should be noted that very small changes in delay (0.1 nanosecond for $f_0 = 10$ GHz) cause the phase to change by 2π radians. Therefore, from a modeling point of view it may be more reasonable to assume that the phase can be regarded as uniformly distributed. Then the amplitude and delay profiles of

the multipath signals can be used to characterize the channel from an input-output point of view.

Utilizing the propagation theoretic results of 3.2.1 and the system function calculations of this section it is possible to compute impulse responses. A typical calculation of a "snapshot" of the time-variant impulse response is described in Section 3.2.2.2 and the results are shown in Fig. 3.19 (reproduced here for convenience). It shows the magnitude of $h(t_0, \xi)$, with t_0 chosen to be that instant at which the range to the receiver is 90 miles. The amplitudes and delay are shown relative to the direct path.

3.2.2.1 Earth Shadowing in the Standard Atmosphere

In the standard atmosphere ($\frac{\partial N}{\partial h} = -40 \text{ Nu/km}$) the rays curve away from the earth with a modified radius of curvature R_0 equal to -5280 miles. The ray which just grazes the surface of the earth defines the transition between the region of normal propagation and the shadow region caused by the intercession of the earth in the propagation path. It should be noted that due to diffraction effects near the earth's surface, this transition is not abrupt, but rather, extends over a small interval to either side of the grazing trajectory.

As shown in Fig. 3.9, with the transmitter at a height h_T above the earth, the range to the shadow zone, L_S , is given as a function of the height of the shadow zone, h_S , by

$$L_S = \sqrt{(-R_0)^2 - (-R_0 - h_T)^2} + \sqrt{(-R_0)^2 - (-R_0 - h_S)^2} \quad (3.39)$$

Assuming that the transmitter and receiver heights are much less than R_0 (as is the case for all RCV applications), Eq. (3.39) can be solved for h_S in terms of L_S

$$h_S = h_T + L_S \left(\frac{L_S}{-2R_0} - \sqrt{\frac{2h_T}{-R_0}} \right) \quad (3.40)$$

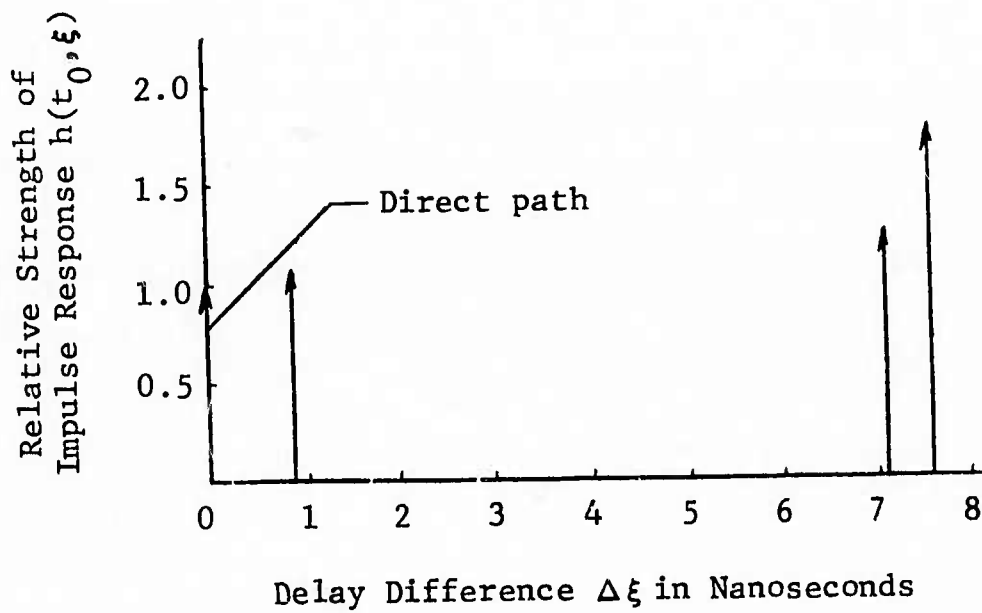
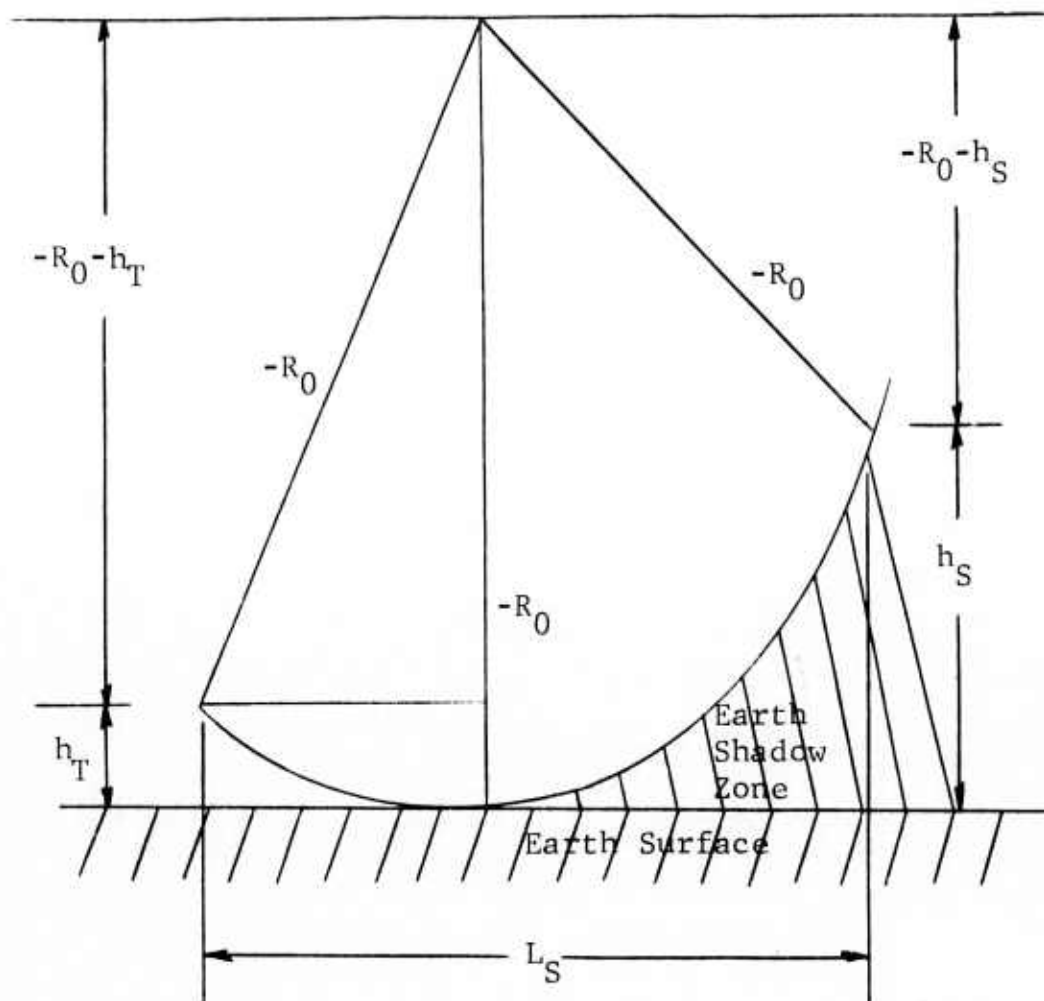


Figure 3.19 Magnitude of Time-Variant Impulse Response $h(t_0, \xi)$
 (t_0 = time at which range $L = 90$ miles, from
 Fig. 3.15; layer thickness $w = 300$ feet, $\partial N / \partial z =$
 -325 N units/km)



h_T = height of transmitter
 $-R_0$ = radius of curvature of ray trajectory
 h_S = height of shadow zone transition
 L_S = range to receiver at height h_S

Figure 3.9 Geometry of Earth Shadow Zone

For ranges much larger than the transmitter height, this is well approximated by

$$h_S = h_T + \frac{L_S^2}{-2R_0} \quad (3.41)$$

A graph of the height above the transmitter at which earth shadowing begins versus the range at which it begins is shown in Fig. 3.10. For example, it is seen that an aircraft at 5000 feet experiences earth shadowing at ranges greater than 100 miles, while an aircraft at 20,000 feet experiences shadowing only at ranges greater than 200 miles.

When an aircraft passes into this shadow zone caused by the intercession of the earth's surface in the direct propagation path, the received signal experiences a slow, deep fade. It is important to note that this type of fading is different in both character and cause than that which results from multipath. The multipath fading is caused by the interference of two or more signals at the receiver. Generally multipath fading is much more rapid than earth bulge fading, and in addition is more amenable to correction by modulation and coding techniques. The remainder of this section is used to calculate the height that a transmitter must have in order to avoid earth-bulge fading to receivers at various ranges and elevation angles.

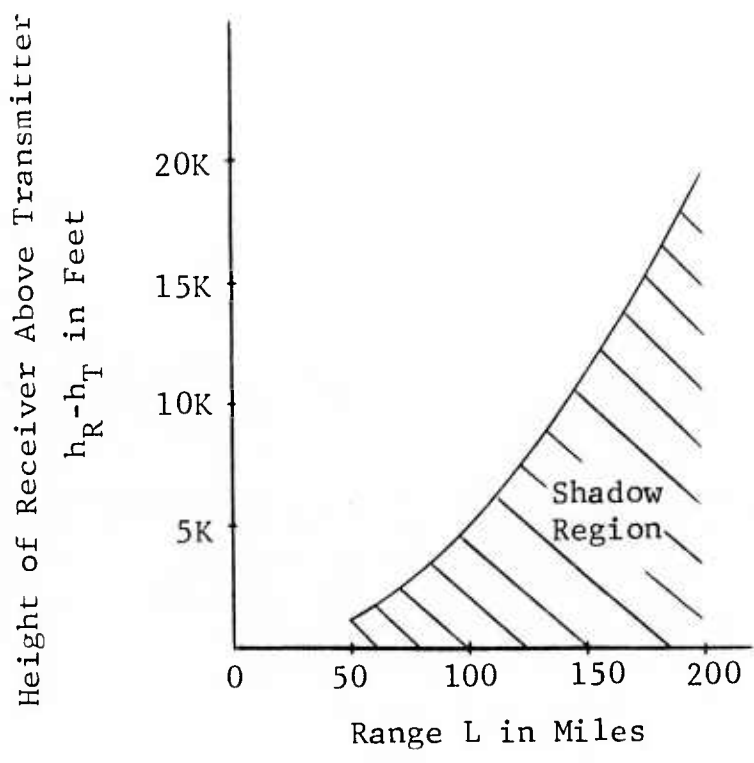


Figure 3.10 Shadow Region in Standard Atmosphere

$$h_R - h_T \approx L^2 / -2R_0$$

The distance a ray descends below the transmitter is given by

$$d = -R_0(1 - \cos \alpha_T) \quad (3.42)$$

which for small α_T , can be well approximated by

$$d = \frac{-R_0 \sin^2 \alpha_T}{2} \quad (3.43)$$

To determine the transmitter height necessary to insure that the direct path is not cut off by the earth, we can set $d = h_T$. Eq. (3.43) can then be written

$$\sin \alpha_T = \sqrt{\frac{2h_T}{-R_0}} \quad (3.44)$$

Substituting (3.44) into (E.7) (see Appendix E) and solving for h_T gives

$$h_T = \frac{L^2}{-8R_0} - R_0 \tan \beta \quad (3.45)$$

where β is the elevation angle of R with respect to T

$$\tan \beta = (h_R - h_T)/L \quad (3.46)$$

Note in the derivation of (3.45), it has been assumed that $\tan \beta \approx \sin \beta \ll 1$ and $L \ll -2R_0$, which are both satisfied in LOS links. A graph of the necessary transmitter clearance height as a function of both range to the receiver and the elevation angle of the receiver is given in Fig. 3.11.

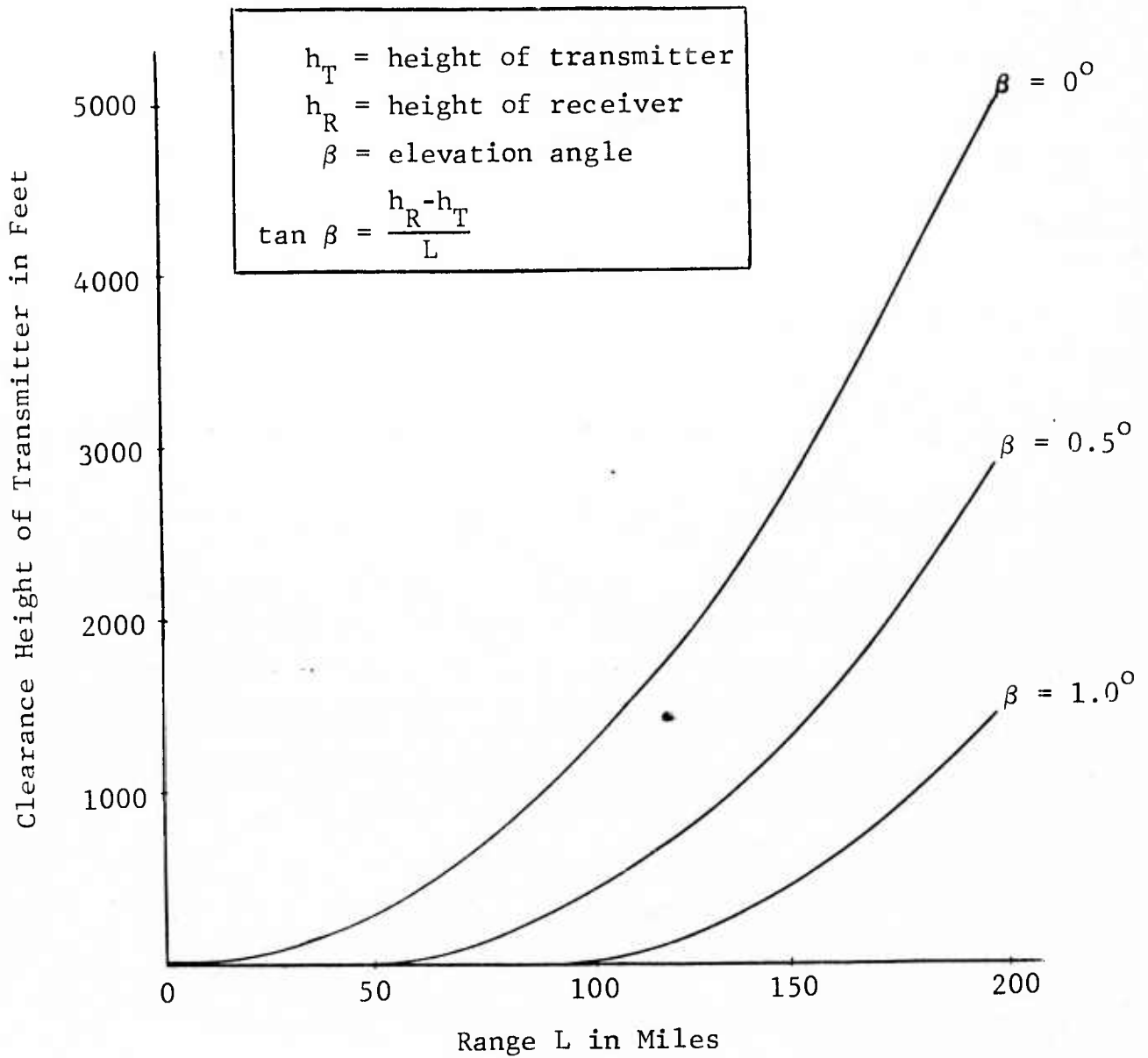


Figure 3.11 Transmitter Height Necessary to Clear Earth Surface as a Function of Range and Elevation Angle

3.2.2.2 Single Stratified Layer Above Terminals

This section considers the case of a single stratified layer of steep negative m-gradient existing above the terminals and embedded in a standard atmosphere. As shown in Fig.F.1, the heights of T, R, and the layer are h_T , h_R and h , respectively. The layer has a thickness w and a negative m-gradient equal to g_1 , whereas outside the layer the m-gradient is positive and equal to g_0 .

The Maximum Height for Refractive Multipath

Refractive multipath occurs when ascending rays are bent back toward the earth. At the turning point the ray angle θ goes to zero and Snell's law can be written as

$$m_0 \cos \theta_0 = m \quad (3.47)$$

where θ_0 and m_0 are the initial ray angle and m-value, and m is the modified refractive index at the turning point. The maximum height at which a turning point can exist is at the top of the layer, and the value of m at that altitude is given by

$$m = m_0 + g_0(h-h_T) + g_1 w \quad (3.48)$$

Substituting (3.48) into (3.47) and solving for h , we get

$$h = h_T - \frac{g_1}{g_0} w - \frac{(1 - \cos \theta_0)m_0}{g_0} \quad (3.49)$$

The maximum height is reached when g_1 is a maximum (negative) value and $\theta_1=0$. Then

$$(h-h_T)_{\max} = \frac{g_{1\max}}{g_0} w \quad (3.50)$$

The maximum negative gradient observed by Bean and Dutton [3.7] is -7.8×10^{-8} mu/ft (-420 N units/km) and the standard gradient is 3.6×10^{-8} mu/ft (-40 N units/km), so that

$$(h-h_T)_{\max} = 2.2 w \quad (3.51)$$

A graph of this maximum separation over the range of observed layer thickness is shown in Fig. 3.12.

This simple result is an important consideration in understanding multipath interference in both air-air and ground-air links. It states that in order to have refractive multipath when the layer is above the terminals, the transmitter can be separated from the layer by no more than about twice the layer thickness. An identical analysis indicates the same is true for the separation between the layer and the receiver. Since the mean thickness of layers is found to be about 300 feet, this means that in order to get refractive multipath, the layer can be no more than about 660 feet above the terminals.

Thus refractive multipath can occur on an air-air or ground-ground link in which the terminals are situated just below a horizontal layer, or in a ground-air link in which the terminals are situated just below a tilted layer. In the latter case, the elevation angle of R with respect to T is then approximately the same as the tilt angle of the layer. In the

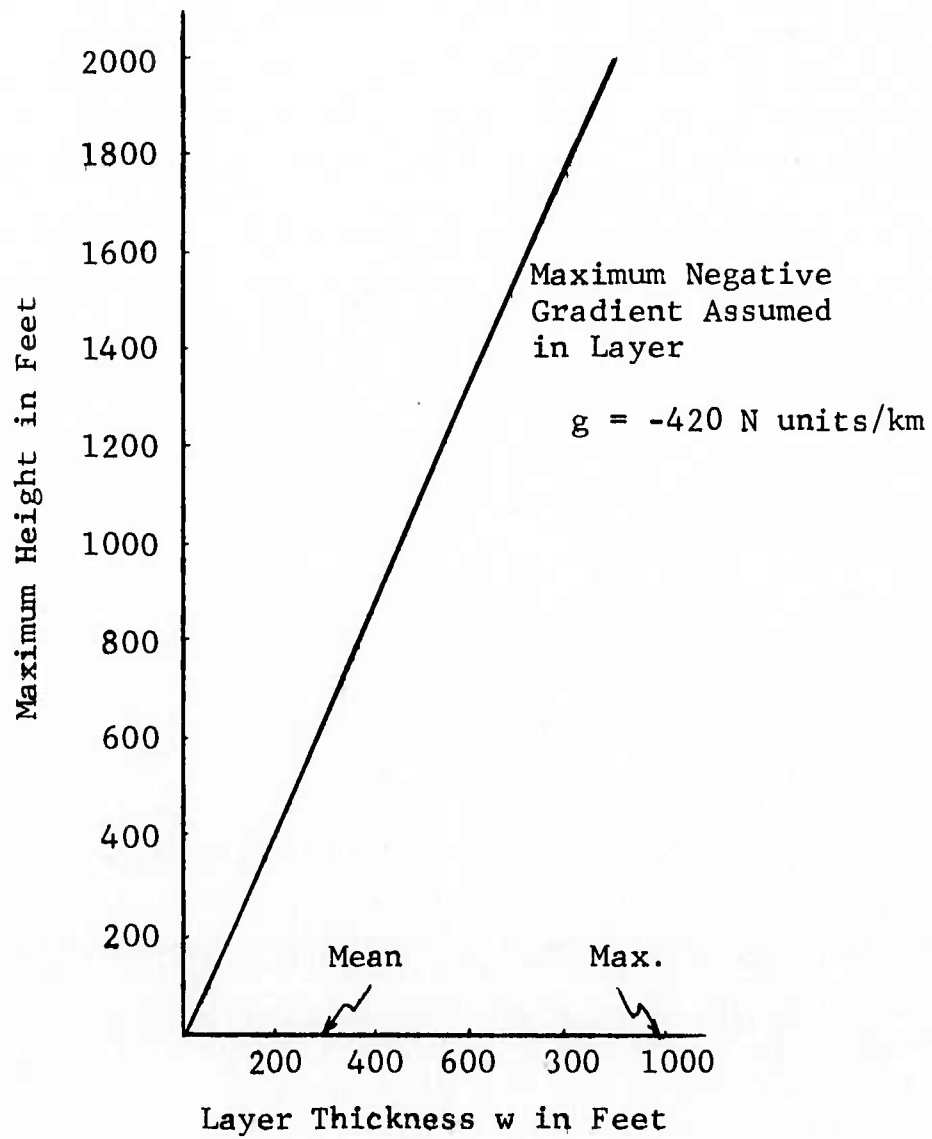


Figure 3.12 Maximum Height of Layer Above Terminals to Allow Refractive Multipath

presence of a frontal inversion, this tilt angle has been measured [3.2] to be as much as about 2.3° . Thus when the terminals are below the layer, refractive multipath is limited to links in which the elevation angle of R with respect to T is less than the tilt of the layer ($\sim 2.3^{\circ}$). This has been substantiated by measurements made at Cheyenne Mountain, Colorado [3.11] in which it was found that over a 14 month period "...no significant multipath propagation occurs for path angles greater than 2° ."

Total Path Delay From T to R

In Appendix F it is shown that the total path delay of a signal which is refracted by the layer in the process of propagating from T to R is given by

$$\xi = \frac{L}{c_0} + \frac{L^3}{24R_0^2 c_0} \left[\frac{3k(k_T^2 + k_R^2) - (k_T^3 + k_R^3)}{2} - \frac{2(k-1)^3}{(n+1)^2 (1-R/R_0)^2} - \frac{3(k_T^2 + k_R^2)}{2} \right] \quad (3.52)$$

where R_0 is the modified radius of curvature of the ray in the region below the layer (see Fig. F.1) and n is the number of extra times the ray trajectory passes in and out of the layer. The parameters k_T , k_R and k are given by

$$n = 0, 1, 2, \dots \quad (3.53)$$

$$k_T = \frac{2R_0}{L} \sin \theta_0^T \quad (3.54)$$

$$k_R = \frac{2R_0}{L} \sin \theta_0^R \quad (3.55)$$

where

$$k = \frac{1}{2} (k_T + k_R) \quad (3.56)$$

The angles θ_0^T and θ_0^R are the take-off and arrival angles of the ray trajectory. The parameters k_T and k_R must simultaneously satisfy the following equations

$$k_R^2 - k_T^2 = - \frac{8R_0(h_R - h_T)}{L^2} \quad (3.57)$$

$$k_R^2 - \frac{(k_T + k_R - 2)^2}{1(n+1)^2(1-R/R_0)^2} + k_T^2 = \frac{8R_0}{L^2} (2h - h_T - h_R) \quad (3.58)$$

It is also shown in Appendix F that the range of values over which k_T and k_R may vary is constrained by the thickness of the layer and the system geometry, s.t.

$$k_{R_{\min}} \leq |k_R| \leq k_{R_{\max}} \quad (3.59)$$

where

$$k_{R_{\min}} = \frac{\sqrt{-8R_0(h_R - h_T)}}{L} \quad (3.60)$$

$$k_{R_{\max}} = \frac{-2R_0}{L} \sqrt{2\left(\frac{w}{R} + \frac{h - h_R}{R_0}\right)} \quad (3.61)$$

R is the known radius of curvature of the ray in the layer (see Fig. 3.7). Note that R is positive because the ray curves toward the earth inside of the layer, while R_0 is negative because the ray curves away from the earth outside of the layer.

The delay of a ray which travels directly from T to R without passing into the layer is shown in Appendix E to be

$$\xi_{\text{direct}} = \frac{L}{c_0} - \frac{L^3}{24R_0^2 c_0} \left\{ 1 + 3 \left(\frac{h_R - h_T}{L} \right)^2 \left[\left(\frac{2R_0}{S} \right)^2 - 1 \right] \right\} \quad (3.62)$$

where S is the slant range

$$S = \sqrt{L^2 + (h_R - h_T)^2} \quad (3.63)$$

The delay difference $\Delta\xi$ between the refracted and the direct paths is then obtained simply by subtracting (3.62) from (3.52) as indicated below

$$\Delta\xi = \xi - \xi_{\text{direct}} \quad (3.64)$$

The complexity of the simultaneous equations (3.57) and (3.58) necessitates a numerical solution for k_T and k_R from which $\Delta\xi$ can be evaluated. The nature of this numerical solution is discussed in Appendix F.

An analytic solution is possible when the receiver and transmitter are at the same height relative to the layer. Since the layer may be tilted as well as horizontal, this becomes a representative situation for ground-air as well as air-air geometries. Thus if we measure h_R and h_T relative to

a plane parallel to the layer, then by specializing the general expression for $\Delta\xi$ such that $h_R = h_T$, the resulting multipath profiles can be applied to ground-air links with a tilted layer as well as air-air links with a horizontal layer.

Letting the difference in height of the layer and the terminals be Δh , i.e.,

$$\Delta h = h - h_T = h - h_R \quad (3.65)$$

the delay difference $\Delta\xi$ becomes

$$\Delta\xi = \frac{L^3}{24R_0^2 c_0} \left[\frac{3k(k_T^2 + k_R^2) - (k_T^3 + k_R^3)}{2} - \frac{2(k-1)^3}{(n+1)^2(1-R/R_0)^2} - \frac{3(k_T^2 + k_R^2)}{2} + 1 \right] \quad (3.66)$$

and from Eq. (3.57), it becomes evident that

$$k_T = \pm k_R \quad (3.67)$$

These two possibilities are studied separately below.

Case I: $k_R = -k_T$ ($k=0$)

Inserting $k_R = -k_T$ into Eq. (3.58) gives a solution for k_T directly

$$k_T = -k_R = \frac{\pm 1}{(n+1)(1-R/R_0)} \sqrt{1 - \frac{L_{\min I}^2}{L^2}} \quad (3.68)$$

where

$$L_{\min I}^2 = -8R_0(n+1)^2(1-R/R_0)^2\Delta h \quad (3.69)$$

Note that in order for k_T and k_R to be real, it is required that

$$L^2 \geq L_{\min I}^2 \quad (3.70)$$

This could also have been derived from the general expressions for k_R and $k_{R_{\min}}$, (3.68) and (3.60), with $h_R = h_T$. An upper bound on L is obtained by requiring $|k_R| < k_{R_{\max}}$ in Eqs. (3.68) and (3.61). This leads to

$$L^2 \leq L_{\max}^2 \quad (3.71)$$

where

$$L_{\max}^2 = -8R_0 \left(\frac{-R_0}{R}\right) (n+1)^2 (1-R/R_0)^2 w \quad (3.72)$$

Thus the range over which multipath interference occurs is defined by

$$L_{\min I}^2 \leq L^2 \leq L_{\max}^2 \quad (3.73)$$

Inspection of (3.69) and (3.72) indicates that the onset of multipath at $L_{\min I}$ is affected by the height of the layer above the terminals, Δh , while the extent of the multipath region is determined by the layer thickness w . Inserting (3.68) into (3.66) gives the delay difference as

$$\Delta \xi = \frac{L^3}{24R_0^2 c_0} \left[1 + \frac{8R_0 \Delta h}{L_{\min I}^2} \left(1 - \frac{L_{\min I}^2}{L^2} \right) \right] \quad (3.74)$$

for both values of k_T . Thus there are two separate paths with the above delay difference. It should be noted that this multipath delay difference has been referenced to the direct path delay, whether or not this direct path actually exists. The regions in which the direct path is cut off by the intercession of the earth's surface in the propagation path can be seen from Figs. 3.10 and 3.11.

The power in the direct path signal is shown in Appendix E to be proportional to inverse range squared, i.e.,

$$P_{\text{direct}} \sim \frac{1}{L^2} \quad (3.75)$$

Similarly, the power in the multipath signal is shown [see Eqs. (3.31) and (3.37)] to be proportional to

$$P \sim \frac{1}{L \sin \theta^R} \frac{\partial \theta^T}{\partial L} \quad (3.76)$$

where

$$\frac{1}{\sin \theta^R} \frac{d\theta^T}{dL} = \left(\frac{\partial k_T}{\partial L} + \frac{k_T}{L} \right) / k_R \quad (3.77)$$

A direct calculation of these quantities for case I where k_T and k_R are defined by Eq. (3.68) gives

$$\frac{P_{\text{direct}}}{P} = 1 - (L_{\text{min}_I} / L)^2 \quad (3.78)$$

Case II: $k_R = k_T = k$

Since solutions for which $k_R = k_T$ are also possible this case must also be examined to provide the total multipath profile. Going through the same steps outlined in case I, it can be shown that the multipath regions lie within the limits of range defined by

$$L_{\min_{II}}^2 \leq L^2 \leq L_{\max}^2 \quad (3.79)$$

where

$$L_{\min_{II}}^2 = -8R_0 [(n+1)^2 (1-R/R_0)^2 - 1] \Delta h \quad (3.80)$$

and L_{\max} is the same as in case I. The corresponding delay difference is given by

$$\Delta \xi = \frac{L^3}{24R_0^2 c_0} (1-k) \left[(1+k) - \frac{16R_0 \Delta h}{L^2} \right] \quad (3.81)$$

where

$$k = \frac{-8R_0 \Delta h}{L_{\min_{II}}^2} \left[-1 \pm (n+1)(1-R/R_0) \sqrt{1 - \frac{L_{\min_{II}}^2}{L^2}} \right] \quad (3.82)$$

The corresponding ratio of direct path power to multipath power is given by

$$\frac{P_{\text{direct}}}{P} = 1 - \frac{(L_{\min_{II}}/L)^2}{1 \mp \sqrt{1 - (L_{\min_{II}}/L)^2 / (n+1)(1-R/R_0)}} \quad (3.83)$$

As in case I, there are two separate paths; in case II, however, they have different delays and signal strengths relative to the direct path. It is interesting to note that when $L = L_{\min_{II}}$, both values of k_T in case I are equal to zero, and one value of k_T is zero in case II. Then, at the range $L_{\min_{II}}$, both paths in case I

and one path in case II coincide in delay. The corresponding ratio of direct path to multipath power for all three of these paths is zero at $L_{\min I}$.

The multipath delay profiles as a function of range are outlined in Figs. 3.13 through 3.16 with the distance between the terminals and layer as a parameter. Typical conditions were chosen with a 300 ft. thick layer ($\partial N/\partial h = -325 \text{ Nu/km}$) embedded in a standard atmosphere. When the distance Δh is 800 feet, there is no multipath over the 200 mile range. At $\Delta h = 600$ feet (Fig. 3.13), there is a small multipath region generated between 92 and 100 miles with delays in excess of 10 nanoseconds. Since these are outside a chip width, the receiver will discriminate against them.

At $\Delta h = 300$ feet (Fig. 3.14), a typical multipath situation is shown. Two multipath regions [corresponding to $n=0$ and $n=1$ in (3.68) and (3.82)] are generated within 200 miles. The first extends from 65 to 100 miles, while the second extends from 155 to 200 miles. In each region, two paths (in addition to the direct path) first appear at $L_{\min II}$ with the same delay; as range increases, these paths separate in delay up to L_{\max} at which point they disappear. Between $L_{\min II}$ and L_{\max} , two other paths appear (at $L_{\min I}$, where $k=0$) and follow closely the delay of one of the earlier occurring paths. The earlier occurring paths are designated (II.1) and (II.2) to correspond to the two values of k_T in case II, and the later paths are designated (I) to correspond to the two paths (of equal delay) in case I.

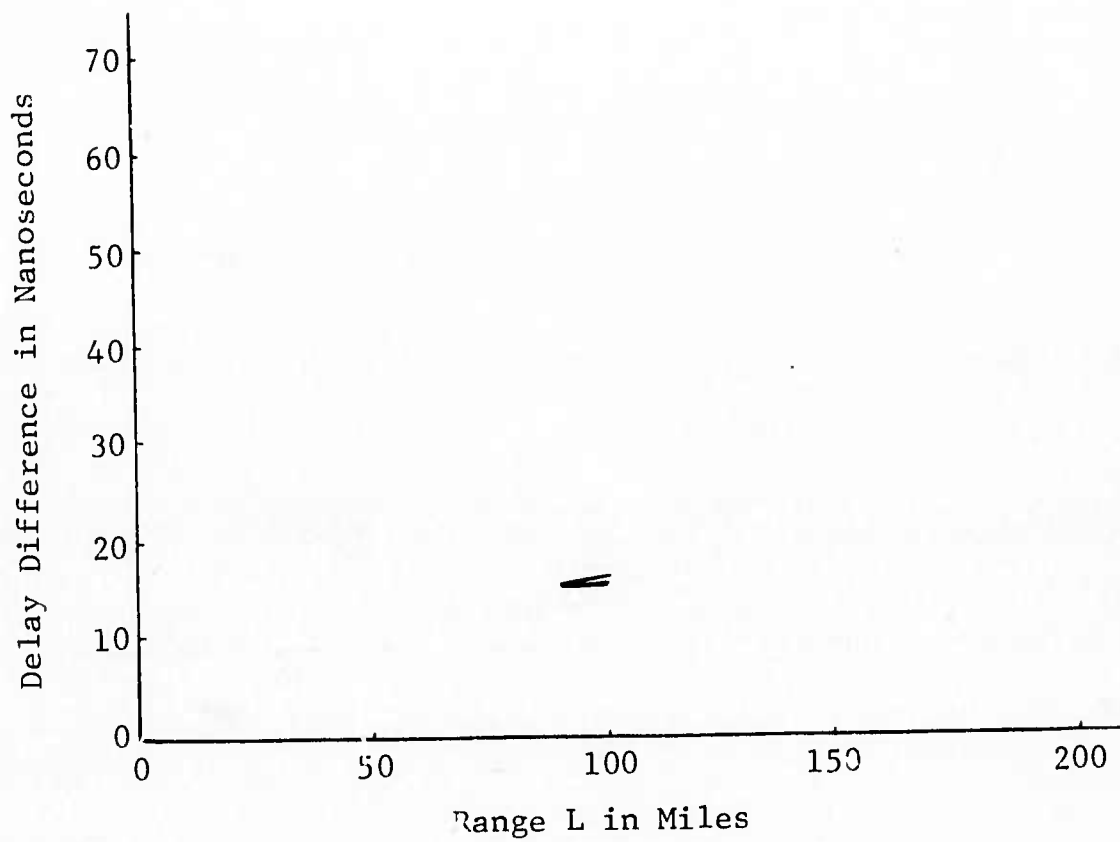


Figure 3.13 Multipath Delay Profile for Single Layer 600 Feet Above Terminals (Layer Thickness $w = 300$ feet, $\partial N/\partial z = -325$ N units/km)

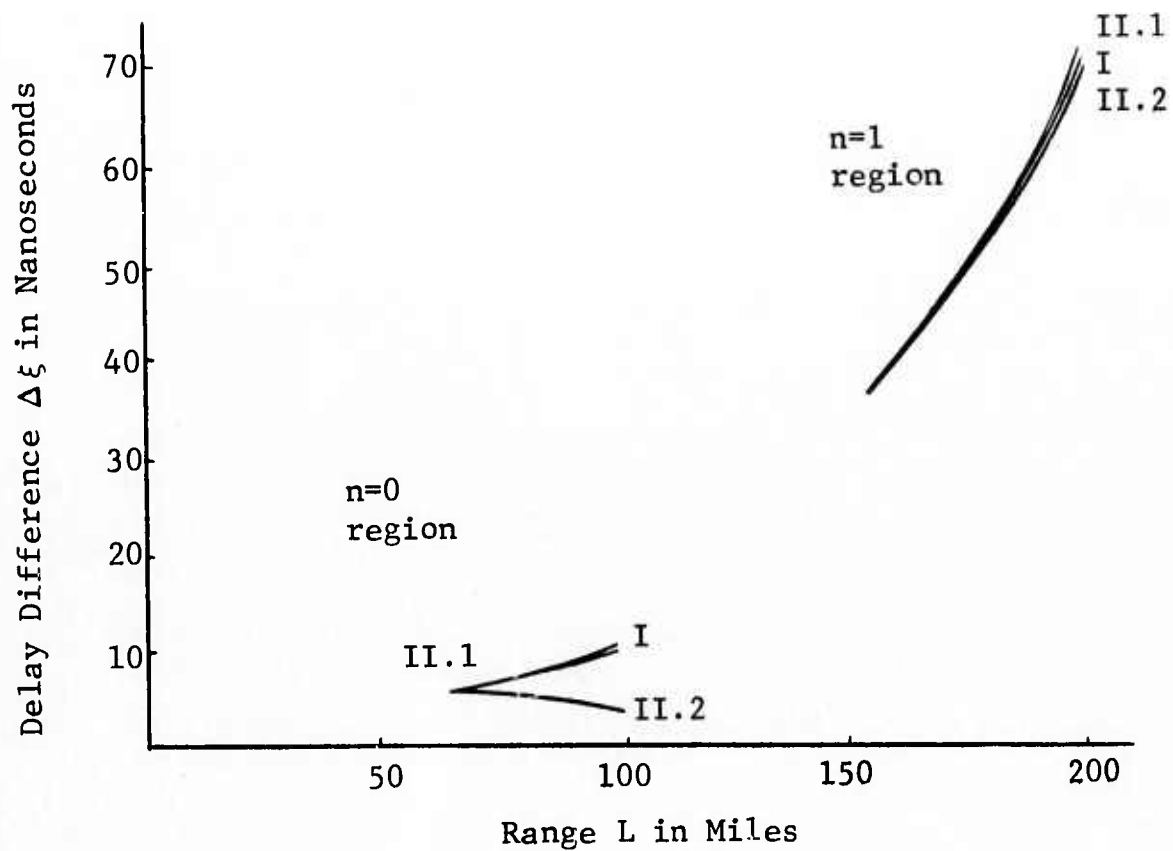


Figure 3.14 Multipath Delay Profile for Single Layer 300 Feet Above Terminals (Layer Thickness $w = 300$ feet, $\partial N/\partial z = -325$ N units/km)

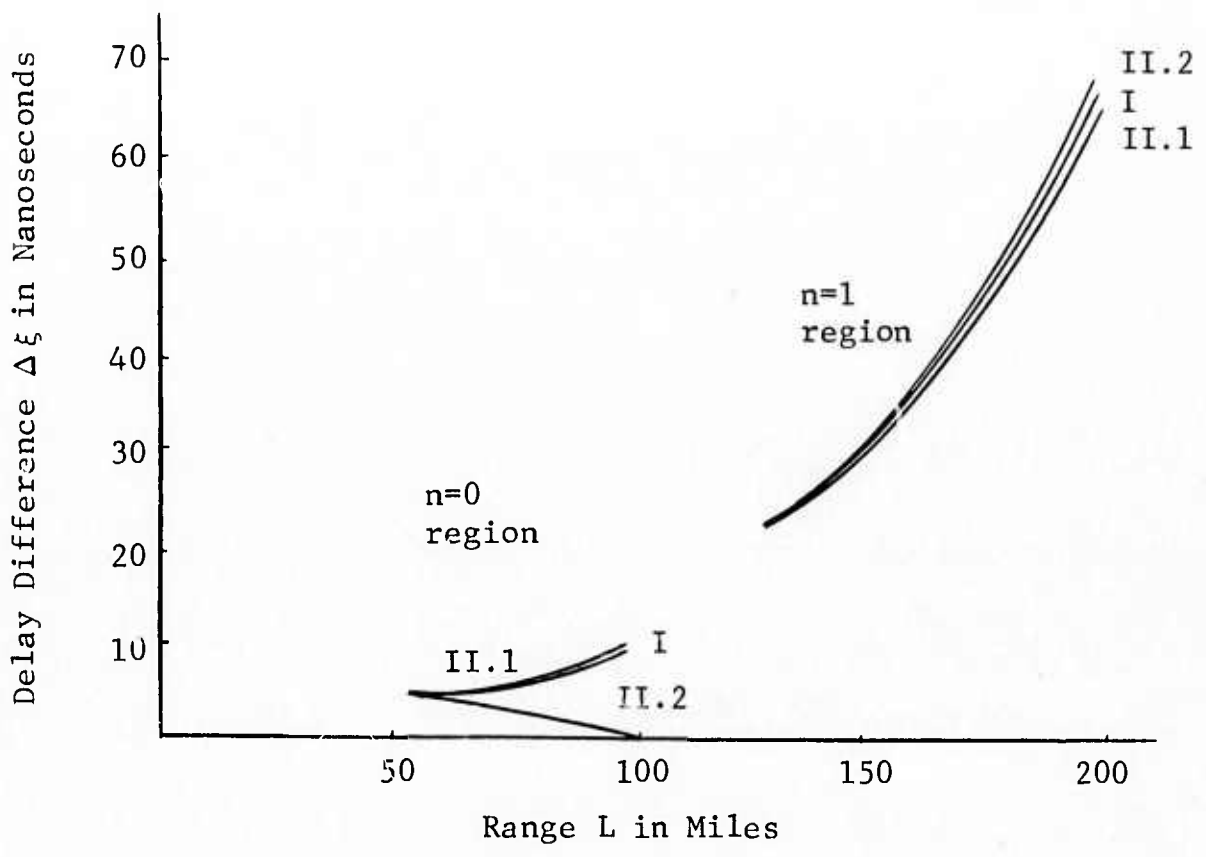


Figure 3.15 Multipath Delay Profile for Single Layer 200 Feet Above Terminals (Layer Thickness $w = 300$ feet, $\partial N/\partial z = -325$ N units/km)

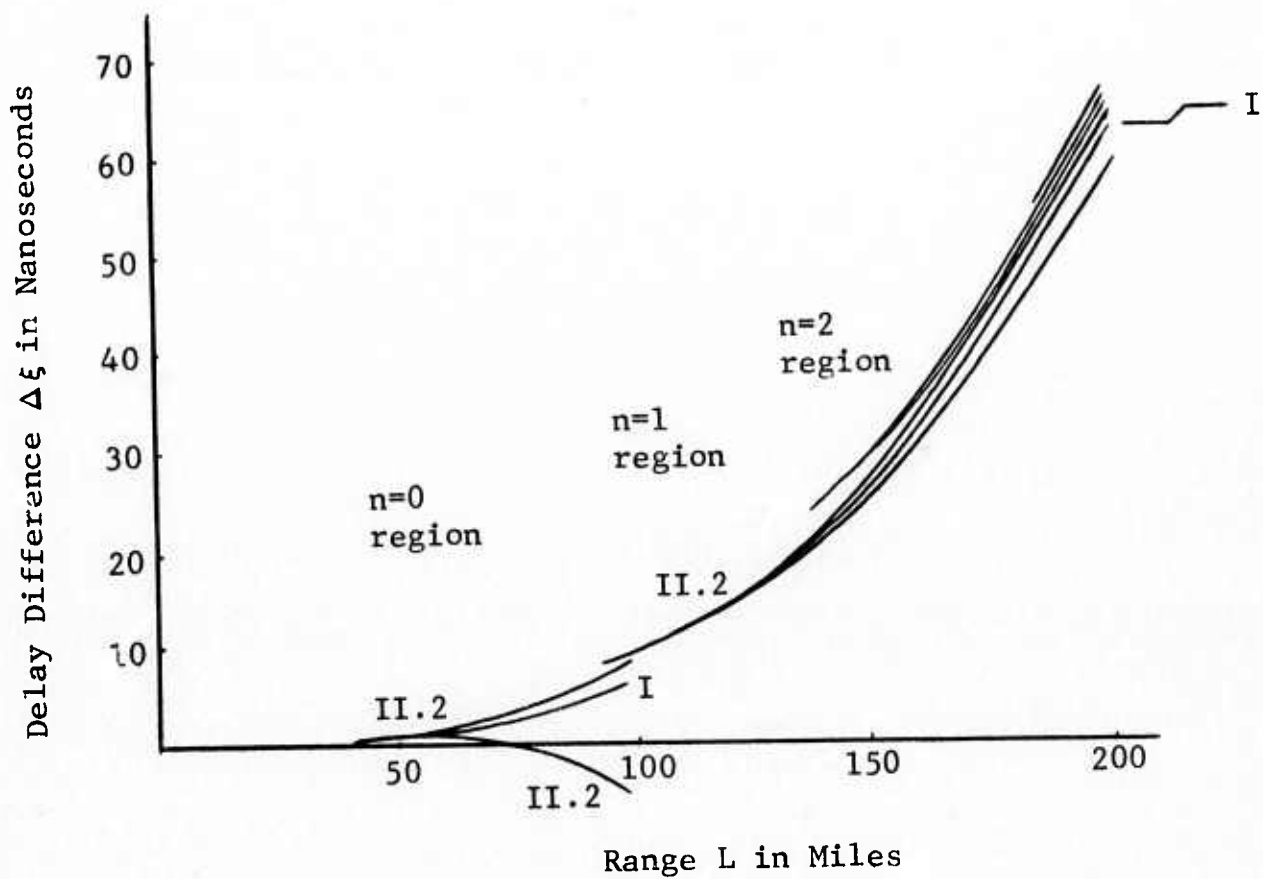


Figure 3.16 Multipath Delay Profile for Single Layer 100 Feet Above Terminals (Layer Thickness $w = 300$ feet, $\partial N/\partial z = -325$ N units/km)

At $\Delta h = 200$ feet (Fig. 3.15), the same type of delay profiles exist, except that the multipath regions now extend from 52 to 100 miles and from 75 to 200 miles. At $\Delta h = 100$ feet (Fig. 3.16), several overlapping multipath regions exist from 38 to 200 miles. In each region (corresponding to each value of n), the multipath exhibits this same character, i.e., two paths separating in delay as range is increased, with two closely aligned paths joining in at a larger range.

The amplitude of the direct path with respect to each of these multipaths is shown in Fig. 3.17. The curves are normalized so as to be universally applicable to all the delay profiles shown. For each path, it is seen that at the onset of interference ($L = L_{\min}$), the multipath is focused to give a high intensity with respect to the direct path. Although the curves indicate that at that point the multipath is infinitely greater than the direct path, (i.e., $P_d/P = 0$), this is not the case, since at such a focal point, the assumptions of geometric optics break down. It suffices to say that the multipath is the stronger signal, and as one moves away from $P_d/p = 0$, the curves become an accurate representation.

As the range increases from L_{\min} , both multipath signals in case I and path 2 in case II attenuate toward the direct path signal strength. Path 1 in case II likewise begins to attenuate, but then intensifies once again at $L = L_{\min_I}$ (where $k_T = k_R = 0$), before attenuating once more toward the direct path signal strength. This same behavior is repeated in each multipath region that exists in links with the layer a distance Δh above the terminals.

Ratio of Direct Path Signal Amplitude to Multipath Signal Amplitude

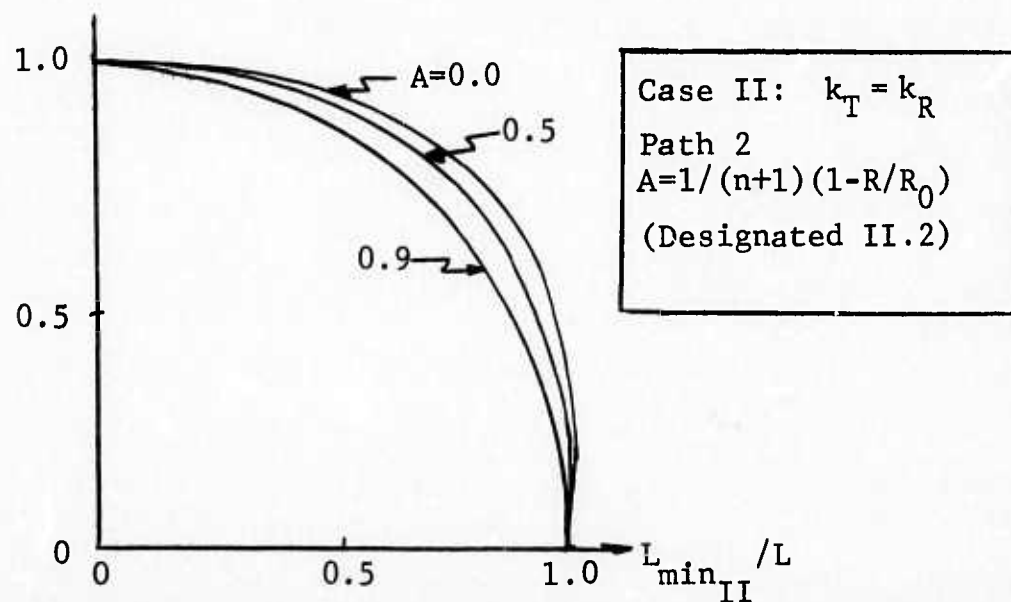
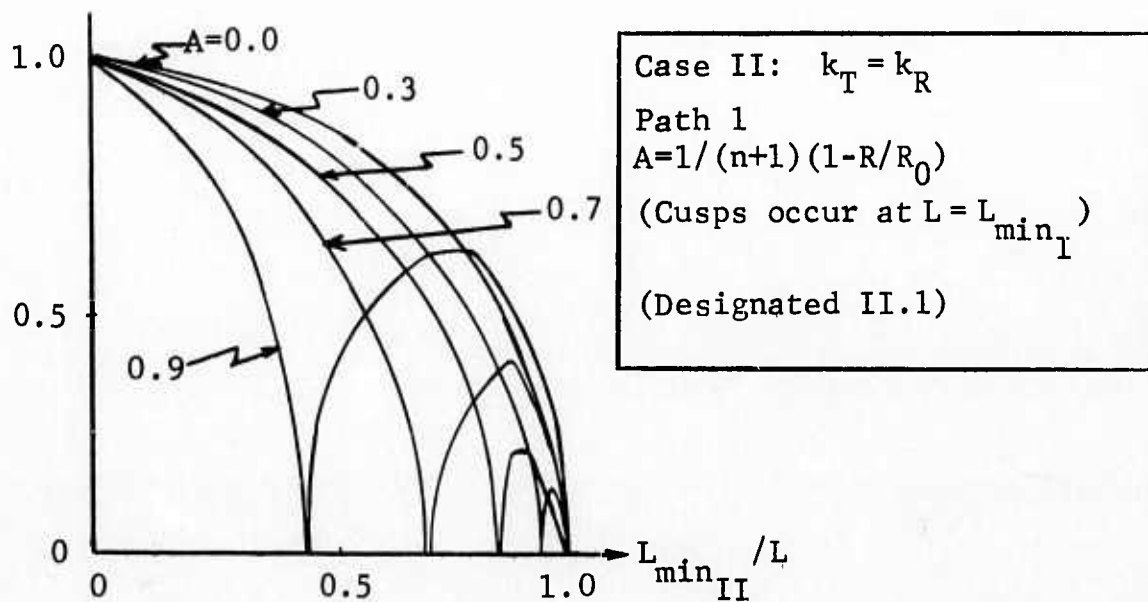
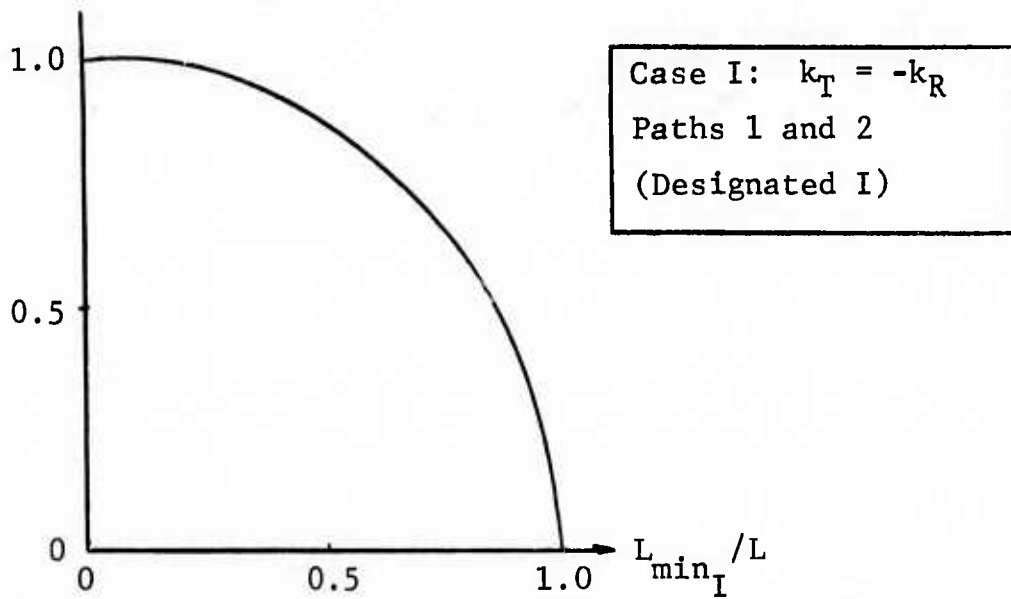


Figure 3.17 Normalized Curves of Amplitude Versus Range

It is interesting to note the behavior of the multipath as the terminals approach the layer, i.e., as $\Delta h \rightarrow 0$. The minimum range at which multipath occurs becomes zero for both case I and case II, i.e.,

$$\lim_{\Delta h \rightarrow 0} L_{\min I} = \lim_{\Delta h \rightarrow 0} L_{\min II} = 0 \quad (3.84)$$

Since the maximum range at which multipath occurs for each value of n is not dependent on Δh , L_{\max} remains unchanged. Taking the limit of $\Delta \xi$ as Δh approaches zero gives

$$\Delta \xi = C_n L^3 \quad (3.85)$$

where

$$C_n = \frac{1}{24R_0^2 C_0} \left[1 - \frac{1}{(n+1)^2 (1-R/R_0)^2} \right] \quad (3.86)$$

for case I and

$$\Delta \xi = D_n L^3 \quad (3.87)$$

where

$$D_n = \frac{1-k_0^2}{24R_0^2 C_0} \quad (3.88)$$

and

$$k_0 = 1/[1 \pm (n+1)(1-R/R_0)] \quad (3.89)$$

for case II.

In both cases the multipath power becomes the same as the direct path power, i.e.,

$$\frac{P_{\text{direct}}}{P} = 1 \quad (3.90)$$

In both cases, the maximum value of $\Delta\xi$ is approached as n goes to infinity, and is given by

$$\Delta\xi_{\text{max}} = \frac{L^3}{24R_0^2C_0} \quad (3.91)$$

The minimum value of $\Delta\xi$ is obtained from case II when n is as small as possible in the multipath region under consideration. For the regions corresponding to $n = 0, 1$, the minimum delays are given by

$$\Delta\xi_{\text{min}} = \frac{1-(R_0/R)^2}{24R_0^2C_0} L^3, \quad n=0 \quad (3.92)$$

$$\Delta\xi_{\text{min}} = \frac{\frac{-4R}{R_0} (1 - \frac{R}{R_0})}{24R_0^2C_0(1-2R/R_0)^2} L^3, \quad n=1 \quad (3.93)$$

A graph of $\Delta\xi_{\text{max}}$ and $\Delta\xi_{\text{min}}$ as a function of range is given in Fig. 3.18.

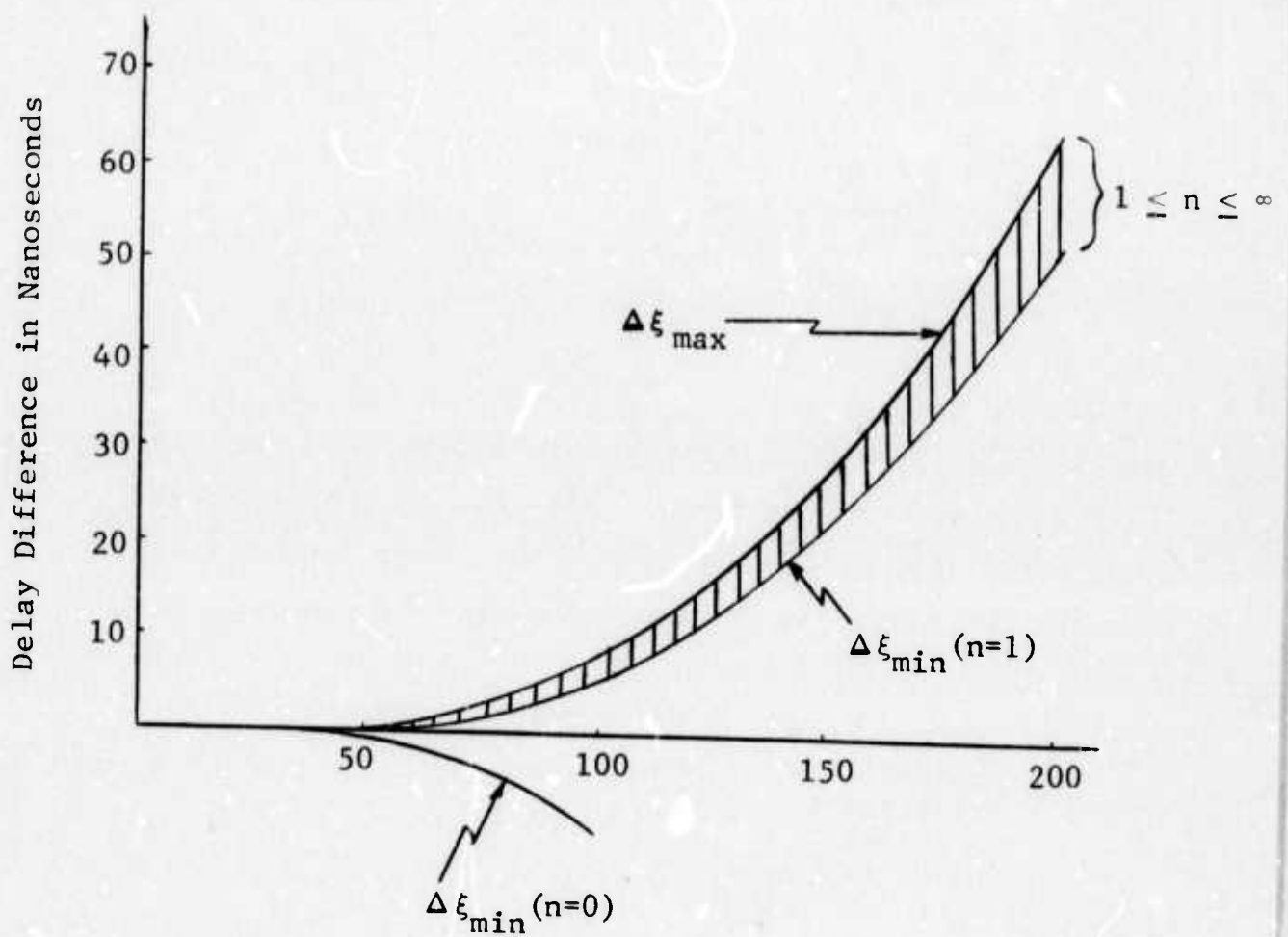


Figure 3.18 Multipath Delay Profiles for Single Layer Just Above Terminals (Layer Thickness $w = 300$ feet, $\partial N / \partial z = -325$ N units/km)

To generate the time-varying impulse response $h(t, \xi)$ at any value of range, one would simply take a cut parallel to the delay axis at that range and read the delay values. These represent the relative delays at which impulses would reach the receiver due to a single transmitted impulse. The relative strengths of the impulses can be read off the universal amplitude curves of Fig. 3.17. For example, in Fig. 3.15 at $L = 90$ miles, there are 4 paths with delays of

$$\begin{array}{l} \text{Path delays} \\ \text{at 90 miles} \\ \text{relative to} \\ \text{direct path} \end{array} \left\{ \begin{array}{l} 7.6 \text{ nanosec. (case II.1)} \\ 7.2 \text{ nanosec. (case I)} \\ 7.2 \text{ nanosec. (case I)} \\ 0.8 \text{ nanosec. (case II.2)} \end{array} \right.$$

Since in that region $L_{\min I} = 66.5$ miles and $L_{\min II} = 53.1$ miles $L_{\min I}/L = 0.74$ and $L_{\min II}/L = 0.59$. Since $n=0$ and $-R/R_0 = 0.66$ the parameter A has the value 0.6. Therefore, the relative strength of the direct path with respect to each multipath signal is obtained from Fig. 3.17 as

$$\begin{array}{l} \text{Direct path} \\ \text{strength} \\ \text{relative to} \\ \text{multipath} \\ \text{strengths} \end{array} \left\{ \begin{array}{l} 0.57 \text{ (case II.1)} \\ 0.67 \text{ (case I)} \\ 0.67 \text{ (case I)} \\ 0.88 \text{ (case II.2)} \end{array} \right.$$

Assuming that the direct path has unit strength, then the strength of each multipath with respect to the direct path is

$$\text{Multipath strengths relative to direct path strength} \begin{cases} 1.75 \text{ (case II.1)} \\ 1.49 \text{ (case I)} \\ 1.49 \text{ (case I)} \\ 1.14 \text{ (case II.2)} \end{cases}$$

The impulse response can then be written as

$$\begin{aligned} h(t_0, \xi) = & \delta(t_0 - \xi_d) \exp(j\omega_d) + 1.14 \delta(t_0 - \xi_d - 0.8 \times 10^{-9}) \exp(j\omega_1) \\ & + 1.49 \delta(t_0 - \xi_d - 7.2 \times 10^{-9}) \exp(j\omega_2) \\ & + 1.49 \delta(t_0 - \xi_d - 7.2 \times 10^{-9}) \exp(j\omega_3) \\ & + 1.75 \delta(t_0 - \xi_d - 7.6 \times 10^{-9}) \exp(j\omega_4) \end{aligned}$$

where t_0 is the time at which the range to the receiver is 90 miles, and ξ_d is the direct path delay. One may relate the phases $\phi_d, \phi_1, \dots, \phi_4$ to phase shifts at the carrier frequency corresponding to the different path delays, if desired. However it may be more meaningful to regard these phase angles as uniformly distributed random variables when, (as appears to be typical) the delay differences are much larger than a period at the carrier frequency. The magnitude of $h(t_0, \xi)$ is shown in Fig. 3.19 as a function of the delay difference. $\Delta\xi = \xi - \xi_d$.

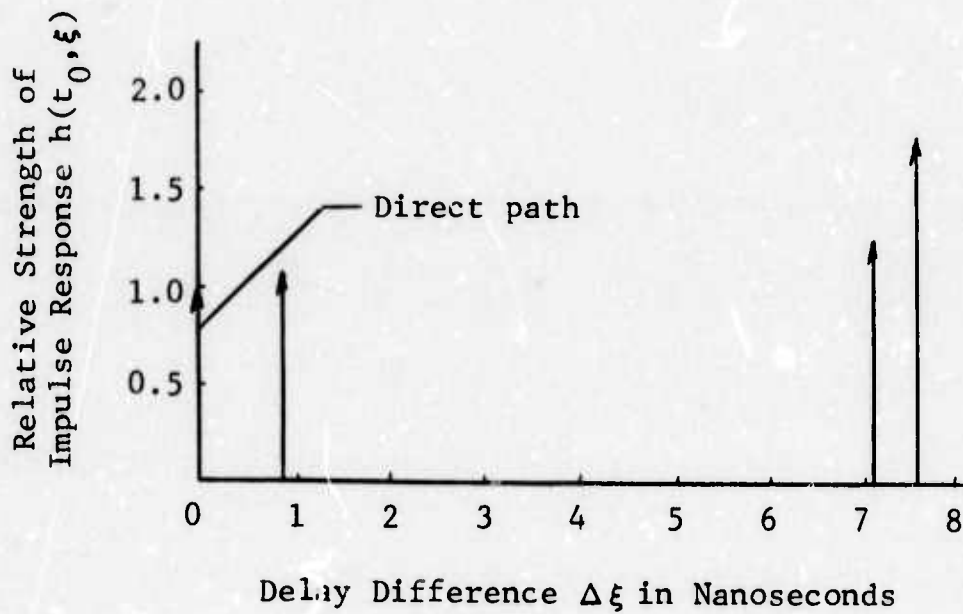


Figure 3.19 Magnitude of Time-Variant Impulse Response $h(t_0, \xi)$
 (t_0 = time at which range $L = 90$ miles, from
 Fig. 3.15; layer thickness $w = 300$ feet, $\partial N / \partial z =$
 -325 N units/km)

3.2.2.3 Single Stratified Layer Below Terminals

This section considers the case of a single stratified layer of steep negative m-gradient existing below the terminals and embedded in a standard atmosphere. This corresponds to typical conditions for air-air communication links. As shown in Fig. H.1 if the positive z direction is defined downward, the resulting ray trajectory can be viewed as that of a layer of positive m-gradient existing above the terminals and embedded in a negative m-gradient. The multipath profile remains unchanged, but the geometry then becomes analogous to that studied in 3.2.2.2. In the inverted geometry the heights of T, R and the layer are h_T , h_R and h , respectively. The layer has thickness w and a positive m-gradient equal to g_1 , whereas outside the layer the m-gradient is negative and equal to g_0 .

The total path delay from T to R is shown in Appendix H to be given by

$$\begin{aligned}\xi = & \frac{R_0}{c_0} [(m_0 + \cos \theta_0^T)(\theta_0^T - \theta_1) - \sin \theta_0^T + \sin \theta_1] \\ & + \frac{R}{c_0} [(m_0 + \cos \theta_0^T)(\theta_1 - \theta_2) - \sin \theta_1 + \sin \theta_2] \\ & + \frac{R_0}{c_0} [(m_0 + \cos \theta_0^T)\theta_2 - \sin \theta_2] \\ & + \frac{R_0}{c_0} [(m_0 + \cos \theta_0^R)(\theta_0^R - \theta_1) - \sin \theta_0^R + \sin \theta_1]\end{aligned}$$

(continued on next page)

(3.94)

$$\begin{aligned}
& + \frac{R}{c_0} [(m_0 + \cos \theta_0^R)(\theta_1 - \theta_2) - \sin \theta_1 + \sin \theta_2] \\
& + \frac{R_0}{c_0} [(m_0 + \cos \theta_0^R)\theta_2 - \sin \theta_2]
\end{aligned} \tag{3.94}$$

Continued)

where R and R_0 are the radii of curvature of the trajectory inside and outside the layer, θ_1 and θ_2 are the angles of the ray trajectory at the bottom and top of the layer, and θ_0^T and θ_0^R are the take-off and arrival angles of the ray. These angles are shown in Appendix H to be constrained by

$$R_0 \sin \theta_0^T - 2(R_0 - R)(\sin \theta_1 - \sin \theta_2) + R_0 \sin \theta_0^R = L \tag{3.95}$$

$$h - h_T = R_0(\cos \theta_1 - \cos \theta_0^T) \tag{3.96}$$

$$h - h_R = R_0(\cos \theta_1 - \cos \theta_0^R) \tag{3.97}$$

$$w = R(\cos \theta_2 - \cos \theta_1) \tag{3.98}$$

where L is the range to the receiver measured along the earth. The delay relative to the direct path is then given by

$$\Delta \xi = \xi - \xi_{\text{direct}} \tag{3.99}$$

where ξ_{direct} is given by Eq. (3.62).

The exact analytic solution to the simultaneous transcendental equations (3.95) - (3.98) is not possible. However, the angles have been determined using a standard Newton-Raphson technique for various values of the parameters. The results are presented below for both fixed and moving terminals. The fixed terminals correspond to a higher altitude experimental link (Mt. Haleakala-Mauna Loa, Hawaii) while the moving terminals represent typical air-air links

Fixed Terminals

The high altitude experimental link which exists between Mt. Haleakala and Mauna Loa, Hawaii, is representative of a typical air-air communication link, and for that reason, it is given particular emphasis in this section. The terminals are 100 miles apart at a height of about 2 miles, [3.12]: In this region there is a warm, moist air layer known as the trade-winds inversion formed by the meeting of low altitude surface winds with high altitude tropical air [3.13]. This process builds up a stratocumulus cloud layer along with a temperature inversion and results in a steep negative gradient of refractive index. As this layer rises, it builds up a cumulus structure which finally breaks up and becomes unstable at high altitudes. Guinard et al. [3.6] have observed the presence of this layer in Oahu, Hawaii at heights of about 8 thousand feet.

Since the terminals are fixed, multipath characteristics will change when the layer is in motion. This section examines the ramifications of a rising layer of steep negative gradient of refractive index below the terminals. Although the layer is likely to become unstable at higher altitudes, that eventuality

has not been treated in this analysis. The sequence of events which generate multipath is shown in Fig. 3.20.

- (a) A direct path exists between the transmitter T and the receiver R when the layer is far below the terminals. Although this ray actually curves downward over the (spherical) earth, an earth-flattening coordinate transformation has been performed which causes the ray tracing to curve upward (see Section 3.2.1.3).
- (b) As the layer rises, it cuts off the direct path and refracts rays toward R, although not enough to cause interference at R.
- (c) Here the layer continues to interrupt the direct path and refracts two paths into R causing multipath interference.
- (d) When the layer rises above the terminals, the direct path again appears and in addition some refracted paths are present.
- (e) At a higher altitude, these refracted paths are again diverted away from R, leaving only the direct path.

Conditions (d) and (e) were examined in detail in Section 3.2.2.2.

Case I Nominal Layer Below Terminals

The nominal conditions chosen for the Hawaii experimental link correspond approximately to the meteorological conditions discussed in Section 3.2.1.2. The gradient of refractive index outside the layer is chosen as the standard value given in (3.4)

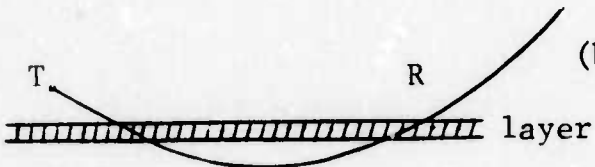
$$\frac{\partial N}{\partial z} = -40 \text{ N units/km outside layer} \quad (3.100)$$

Transmitter

Receiver



(a) direct path in standard atmosphere



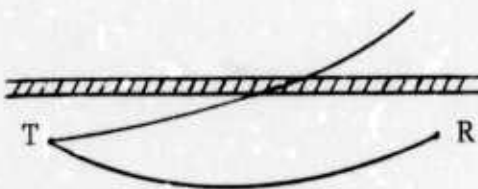
(b) direct path is cut off by layer



(c) two rays are refracted into R



(d) direct path plus refracted paths



(e) multipath ray does not reach R

Figure 3.20 Ray Trajectories as a Function of Layer Height

while inside the layer the index has a steeper gradient given by

$$\frac{\partial N}{\partial z} = -160 N \text{ units/km inside layer} \quad (3.101)$$

From Eq. (3.22) and Fig. 3.7, the radii of curvature of the rays can be found to be

$$R_0 = -5280 \text{ miles outside layer} \quad (3.102)$$

$$R = 200,000 \text{ miles inside layer} \quad (3.103)$$

The negative sign indicates that the rays outside the layer curve away from the earth. The refractivity N is related to the refractive index n by

$$N = (n-1) \times 10^6 \quad (3.104)$$

The thickness of the layer is given by

$$\omega = 140 \text{ meters} \quad (3.105)$$

This corresponds to a relatively thick layer for a tropical climate, (see Fig. 3.2). Multipath calculations for a relatively thin layer are made in Case II. The layer is considered to be a distance Δh below the terminals. Figure 3.21 gives a graph of initial angle at which a ray is launched versus the range L at which the ray reaches a point at the same height as

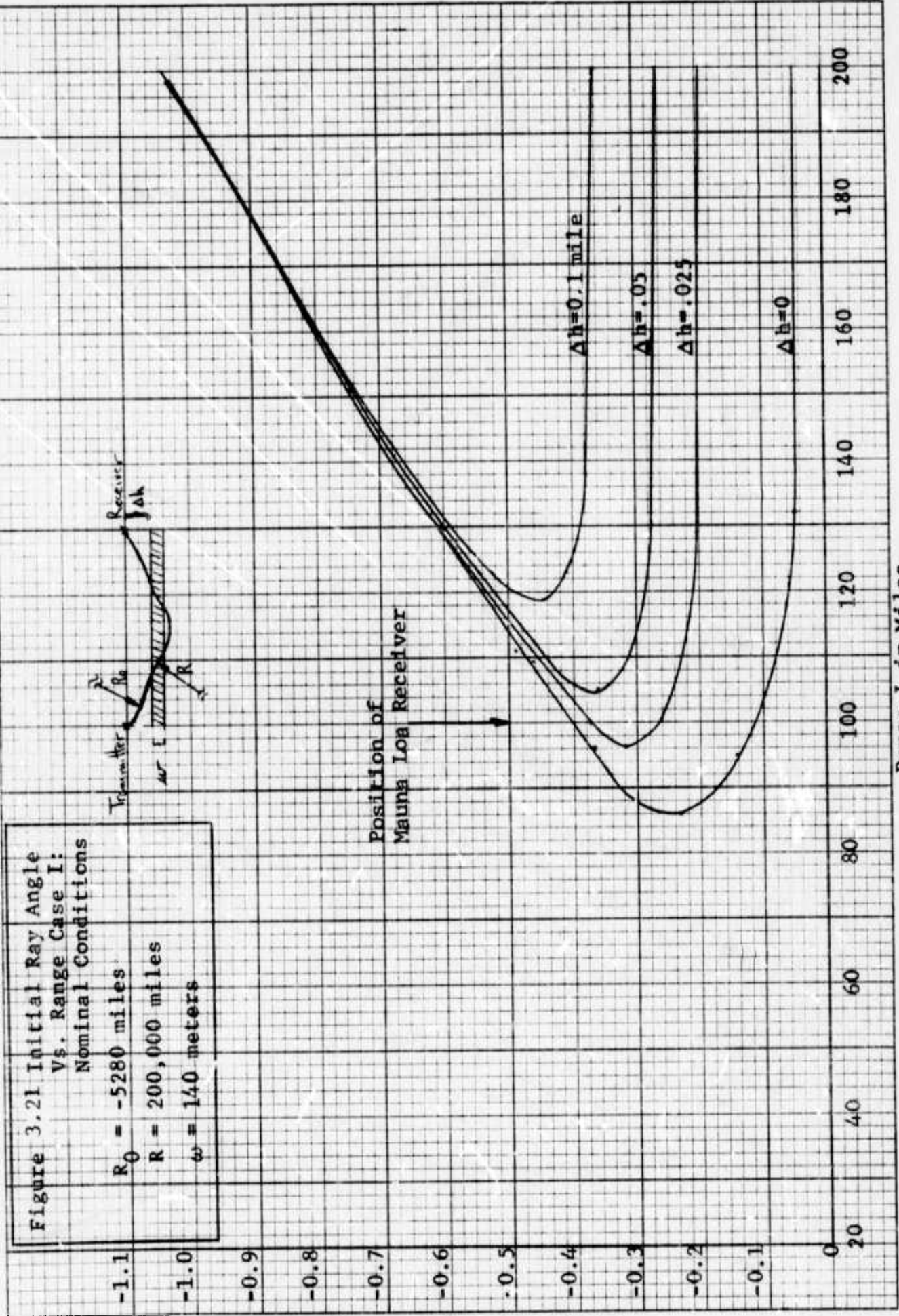


Figure 3.21 Initial Ray Angle Vs. Range Case I: Nominal Conditions

the transmitter. A family of curves is generated by changing the height of the layer such that Δh varies from $\Delta h = 0.1$ mile (528 ft.) to $\Delta h = 0$ mile.

It is seen from Fig. 3.21 that when the layer is 0.1 mile below the terminals there are no rays which intercept the receiver (at $L = 100$ miles). When the layer rises to about 0.035 mile below the terminals, the first refracted ray reaches R. As the layer continues to rise, two refracted rays reach the receiver. At $\Delta h = .025$, one of these rays is launched at an initial angle of -0.37 degree while the other is launched at -0.26 degree. These two rays arrive at the receiver at different delays and with different amplitudes. The power delivered to the receiver over each of these two paths is proportional to the slope of the angle vs. range diagram (see Section 3.2.1.3), and the delay difference can be calculated from the initial angles. As the layer rises toward $\Delta h = 0$, the two paths separate in angle and one path is attenuated with respect to the other.

Letting the signal received over one path be $S_1(t)$, then the signal received over the other path is given by

$$S_2(t) = \alpha S_1(t - \Delta\xi) \quad (3.106)$$

where the relative power level P is proportional to α^2 , and $\Delta\xi$ is the relative delay. A graph of P versus $\Delta\xi$ is given in Fig. 3.22. It is seen that the multipath delay difference is less than a nanosecond, and further, that the second path is quickly attenuated with respect to the first.

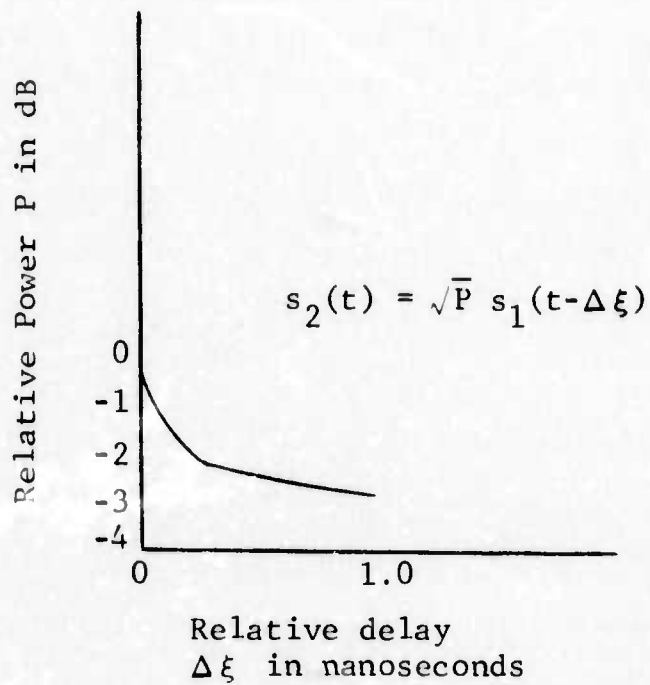


Figure 3.22 Relative Power Vs. Relative Delay

Case I: Nominal Conditions, Layer Below Terminals

Ray Curvature

Outside Layer: $R_0 = -5280$ miles

Ray Curvature

Inside Layer : $R = 200,000$ miles

Layer Thickness: $\omega = 140$ meters

In the length of time it takes for the layer to rise from $\Delta h = .035$ mile, a 10 GHz signal would therefore experience about 10 fades, i.e., one fading cycle each time the delay difference changed by 0.1 nanosecond. Ikegami [3.4] has observed layers near Mt. Tsukuba, Japan, rising this distance in about 30 minutes. This would produce a fading period of about 3 minutes. Measurements taken on the Hawaii experimental link at 10 GHz by Thompson [3.12] indicate the occurrence of deep fades at intervals of from 1 to 3 minutes (see Fig. 3.23). The faster fading observed in Fig. 3.23 is most likely due to the breaking up of the layer by high altitude turbulence. This phenomenon has not been treated in the analysis presented here.

Case II Thin Layer Below Terminals

The effects of a layer thinner than that reported in Case I is given here. The layer thickness ω is

$$\omega = 42.7 \text{ meters,} \quad (3.107)$$

while the other parameters remain the same, i.e.,

$$\frac{\partial N}{\partial z} = -40 \text{ N units/km outside layer} \quad (3.108)$$

$$\frac{\partial M}{\partial z} = -160 \text{ N units/km inside layer} \quad (3.109)$$

$$R_0 = -5280 \text{ miles outside layer} \quad (3.110)$$

$$R = 200,000 \text{ miles inside layer} \quad (3.111)$$

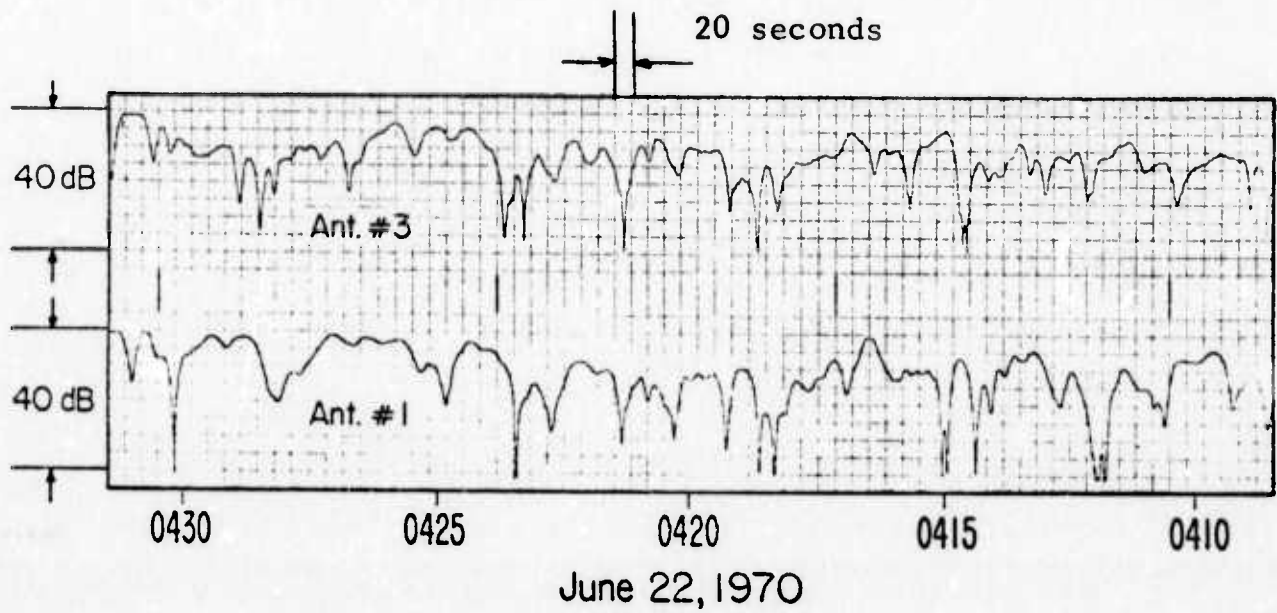


Figure 3.23 Fading Record on Hawaii Experimental Link at 10 GHz
(Taken from Ref. 3.12)

The diagram of initial ray angle versus range, L , is shown in Fig. 3.24. Here it is seen that the refracted rays first reach the receiver (at $L = 100$ miles) when $\Delta h = 0.135$ mile (723 ft.) compared to $\Delta h = 0.035$ mile for the thicker layer. Thus as the layer becomes thinner, it has the ability to produce interference at R from a lower altitude. Again it is observed that as the layer rises ($\Delta h \rightarrow 0$), the difference between the initial take-off angles of the rays increases, and one of the paths attenuates rapidly with respect to the other. The relative power and delay of the two paths is plotted in Fig. 3.25. Here the total range of delay difference is larger. However, since the second path is attenuated by more than 10 dB at 1 nanosecond, it will not appreciably interfere with the first path at larger delay differences.

Case III Layer of Steep n-Gradient Below Terminals

In this case the nominal conditions were varied to produce a much steeper negative gradient of refractive index in the layer, i.e.,

$$\frac{\partial N}{\partial z} = -300 \text{ N units/km in layer} \quad (3.112)$$

From Fig. 3.7 this produces a radius of curvature within the layer given by

$$R = 4300 \text{ miles in layer} \quad (3.113)$$

The n-gradient outside the layer was varied slightly to give

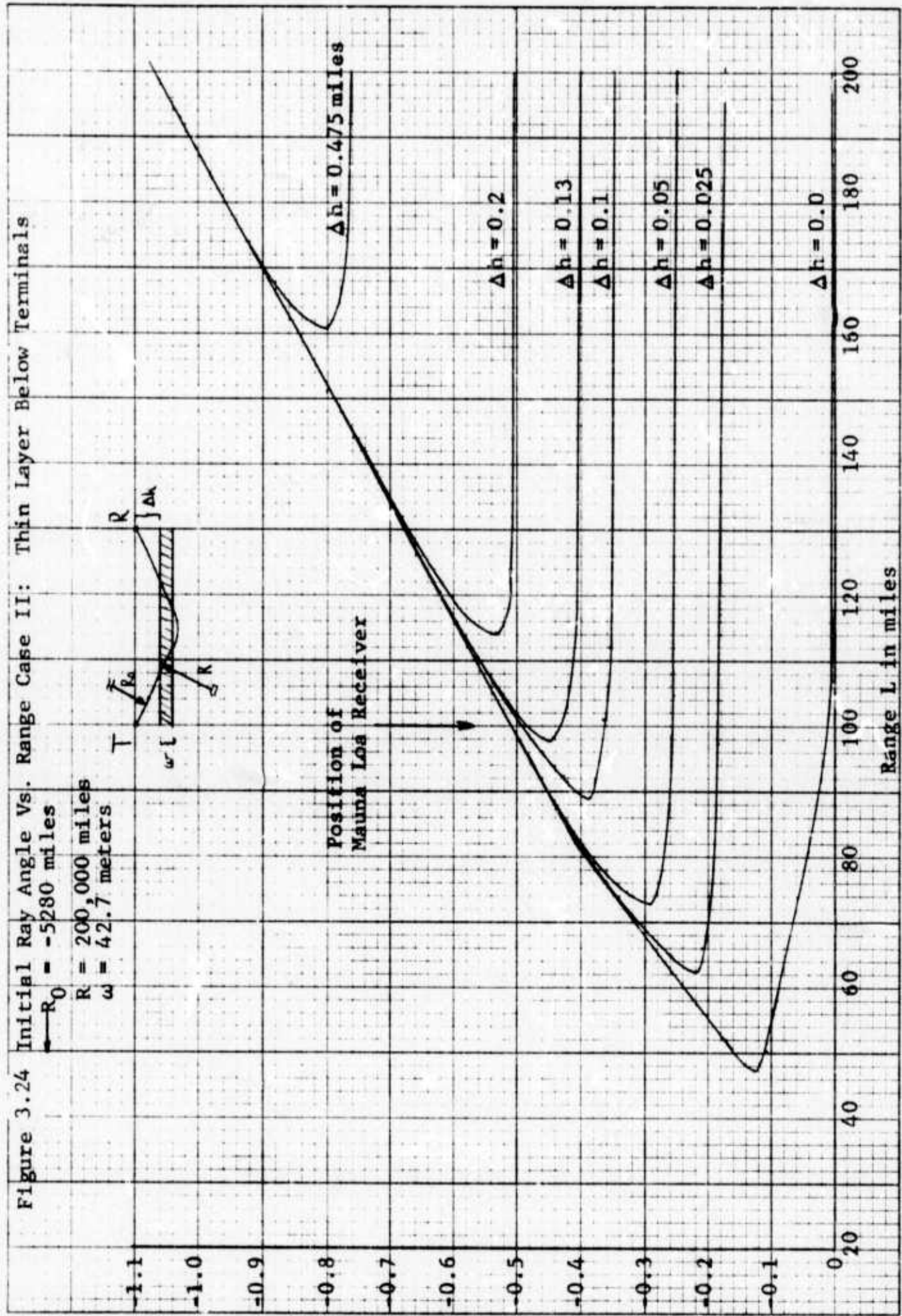
$$\frac{\partial N}{\partial z} = -60 \text{ N units/km outside layer} \quad (3.114)$$

Figure 3.24 Initial Ray Angle Vs. Range Case II: Thin Layer Below Terminals

$R_0 = -5280$ miles
 $R = 200,000$ miles
 $\omega = 42.7$ meters



Position of Mauna Loa Receiver



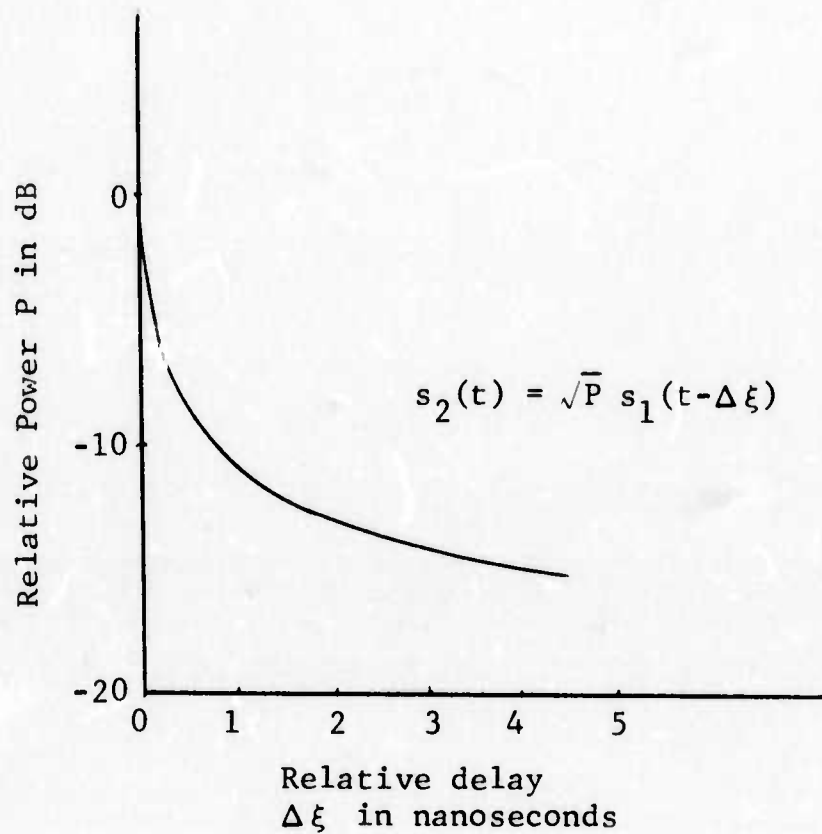


Figure 3.25 Relative Power Vs. Relative Delay

Case II: Thin Layer Below Terminals

Ray Curvature

Outside Layer: $R_0 = -5280$ miles

Ray Curvature

Inside Layer : $R = 200,000$ miles

Layer Thickness: $\omega = 42.7$ meters

$$R_0 = -6400 \text{ miles outside layer} \quad (3.115)$$

and the nominal layer thickness was used

$$\omega = 140 \text{ meters} \quad (3.116)$$

From the initial angle versus range diagram (Fig. 3.26), it is seen that there are no refracted rays reaching the Mauna Loa receiver ($L = 100$ miles) and there is in turn no interference under these conditions.

Case IV Thin Layer of Steep n-Gradient Below Terminals

In this case the nominal conditions were varied to produce a much steeper negative n-gradient in addition to a much thinner layer, i.e.,

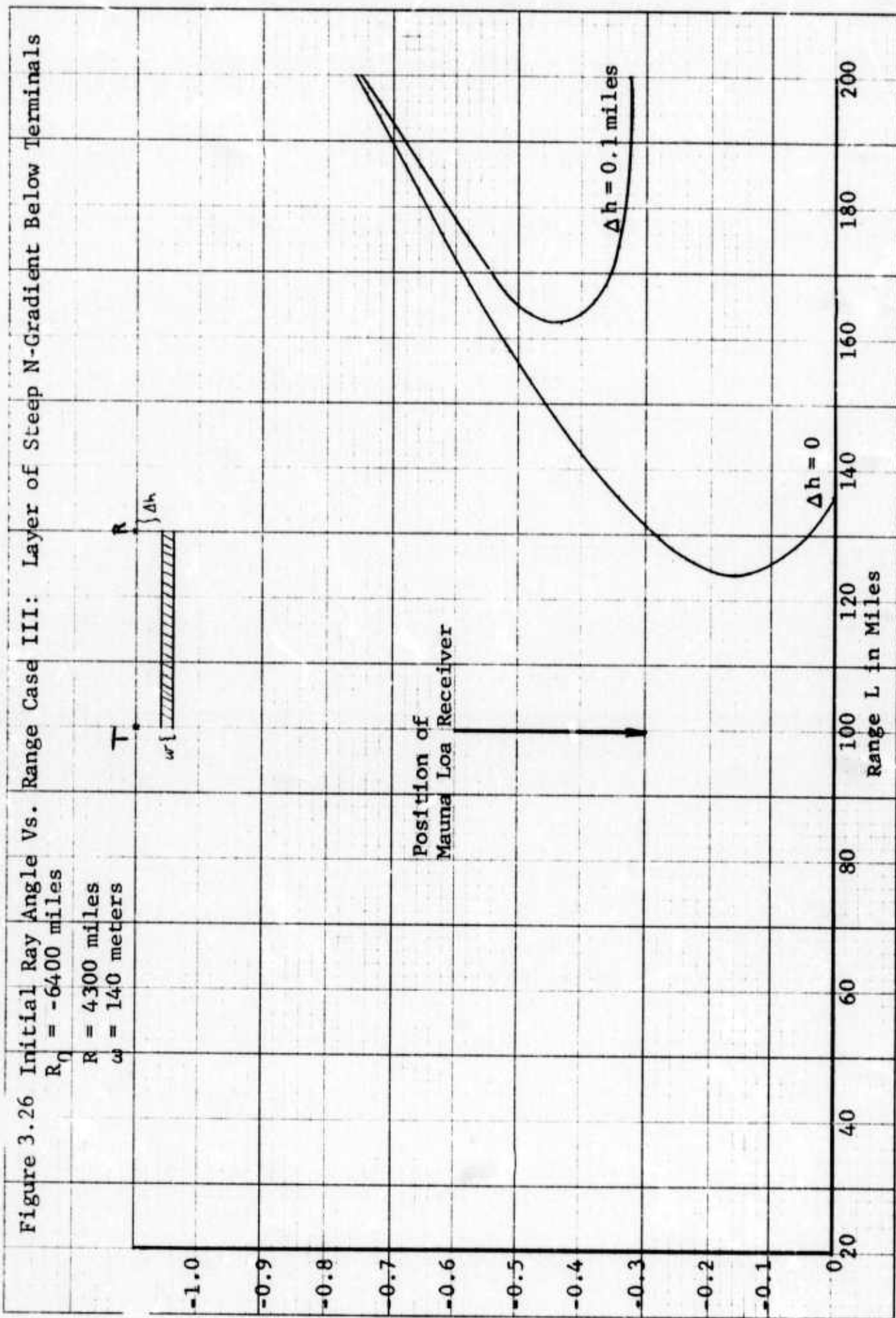
$$\frac{\partial N}{\partial z} = -300 \text{ N units/km in layer} \quad (3.117)$$

$$\omega = 42.7 \text{ meters} \quad (3.118)$$

From Fig. 3.7, it is seen that

$$R = 4300 \text{ miles in layer} \quad (3.119)$$

The n-gradient and radius of curvature outside the layer remained at their nominal values



Initial Ray Angle in Degrees

$$\frac{\partial N}{\partial z} = -40 \text{ N units/km outside layer} \quad (3.120)$$

$$R_0 = -5280 \text{ miles outside layer.} \quad (3.121)$$

The initial ray angle versus range diagram is shown in Fig. 3.27. Here it is seen that the refractive rays first enter the receiver when $\Delta h = 0.1$ mile and again separate in delay as one path becomes attenuated. The relative power of the two paths as a function of their relative delay is shown in Fig. 3.28. Again the second path is attenuated by about 10 dB at a delay difference of 1 nanosecond.

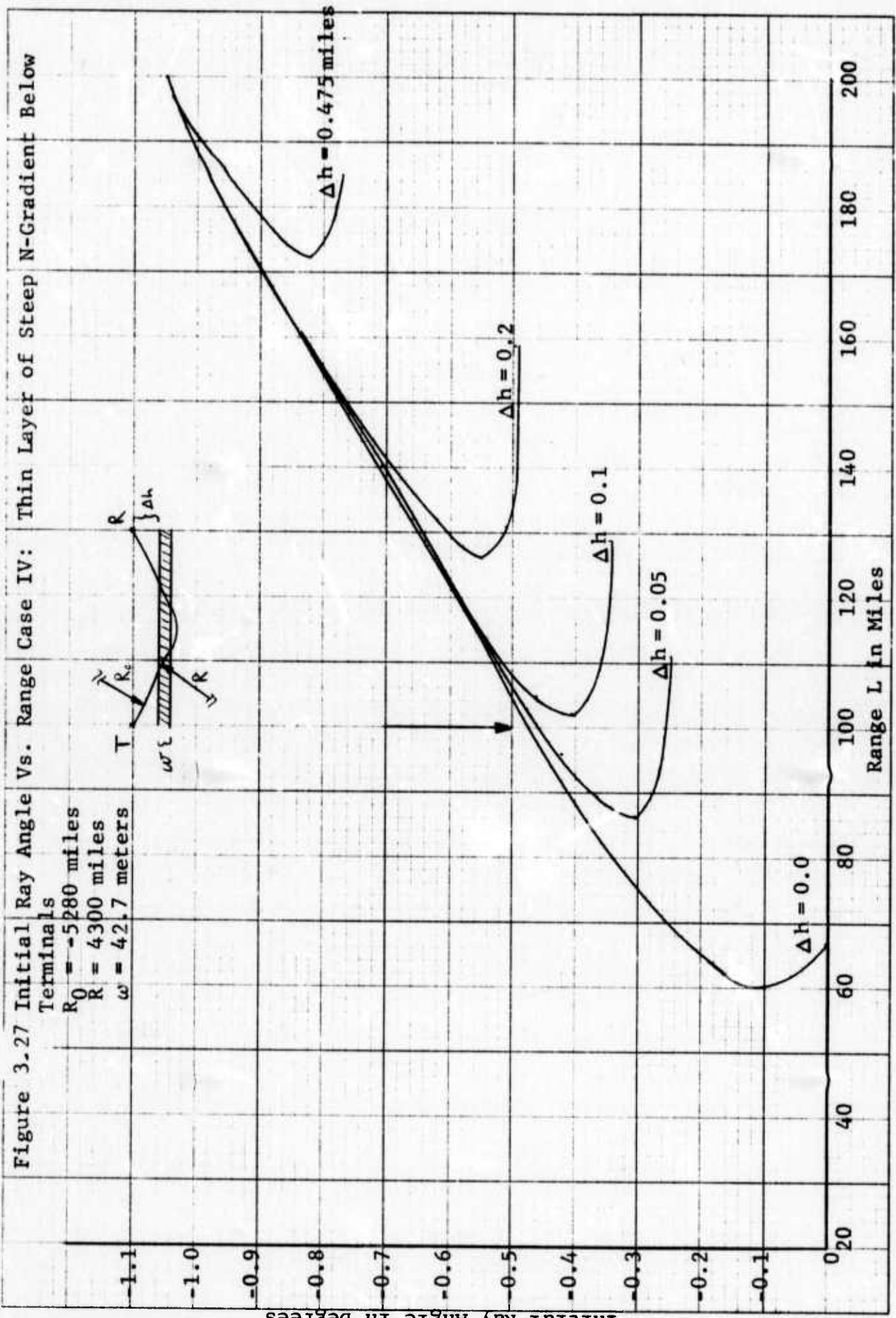
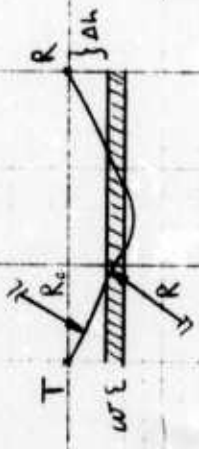
Moving Terminals

The above calculations for the Hawaii experimental link were carried out at a range of $L = 100$ miles. However, the analysis was done with enough generality to gain insight into the case where the relative distance between terminals is changing as in the case of air-air communications. In this case, the movement of the aircraft through an interference region causes the signal to experience fading. In addition to the delay difference between signals arriving at the receiver over different paths, there is an induced Doppler frequency shift due to the different angles of arrival of the rays.

Analysis of the air-air link can be provided by inspection of the initial angle versus range curves given in Figure 3.24, where the case of a thin layer a distance Δh below the terminals is considered. When Δh is a constant 0.1 mile below the aircraft, there is no reception of

Figure 3.27 Initial Ray Angle Vs. Range Case IV: Thin Layer of Steep N-Gradient Below

Initial Ray Angle
Terminals
 $R_0 = 5280$ miles
 $R = 4300$ miles
 $\omega = 42.7$ meters



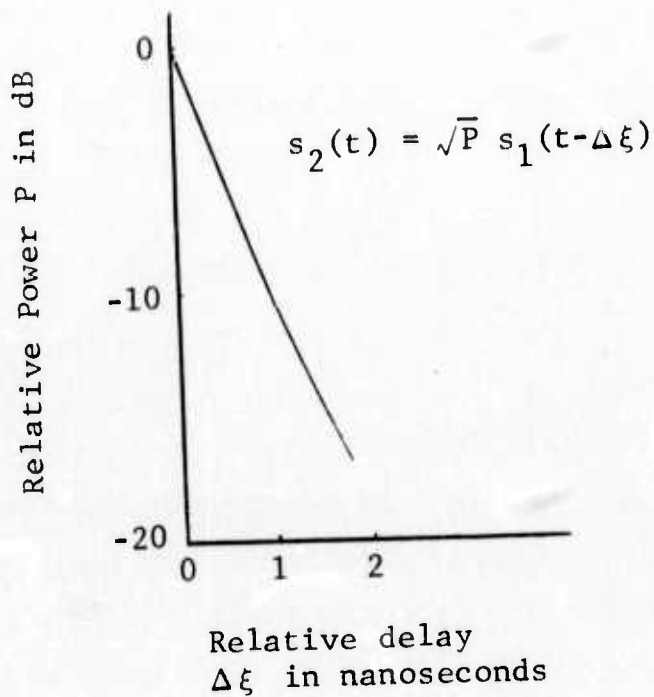


Figure 3.28 Relative Power Vs. Relative Delay

Case IV: Thin Layer of Steep
N-Gradient Below Terminals

Ray Curvature

Outside Layer: $R_0 = -5280$ miles

Ray Curvature

Inside Layer : $R = 4300$ miles

Layer Thickness: $\omega = 42.7$ meters

refracted rays until the range between terminals is greater than 89 miles. At this point, two paths reach the receiver and begin to interfere. As the range to the RCV (receiver) increases, the two paths separate in delay, and one becomes attenuated with respect to the other. Calculations show that at 100 miles the second path is about 9 dB down from the first, and the delay difference between the paths is about 0.6 nanoseconds. As the range to the RCV increases, the second path becomes negligibly small compared to the first. This is evidenced on the initial angle versus range diagram (Fig. 3.27) by the fact that the slope of the diagram reaches a steady value for the upper ray while it approaches zero for the lower ray.

Thus, the effect of a layer on an air-air link in which the range to the RCV continually increases, is to create a small region of non-negligible interference, (in the above case, about 8 miles long), through which the RCV passes. A quantitative measure of the fading rate can be derived by considering a 10 GHz signal arriving at the RCV over two paths. As the two paths went from 0 to 0.6 nanoseconds delay difference, their sum would go through 6 fading cycles. A jet aircraft traveling at 600 miles per hour would take 48 seconds to pass through this 8 mile interference region, so that the time for a fading cycle would be

$$T = \frac{48 \text{ seconds}}{6 \text{ cycles}} = 8 \text{ seconds/cycle} \quad (3.122)$$

Now from Figs. 3.27 and 3.28, it is seen that the two rays are separated by at most about 0.001 radians (≈ 0.06 degrees) before one path becomes negligible (down 10 dB). The maximum Doppler shift $\Delta\nu_{\max}$, between the two signals is obtained when the two aircraft are moving in opposite directions along one of the ray trajectories, and is given by

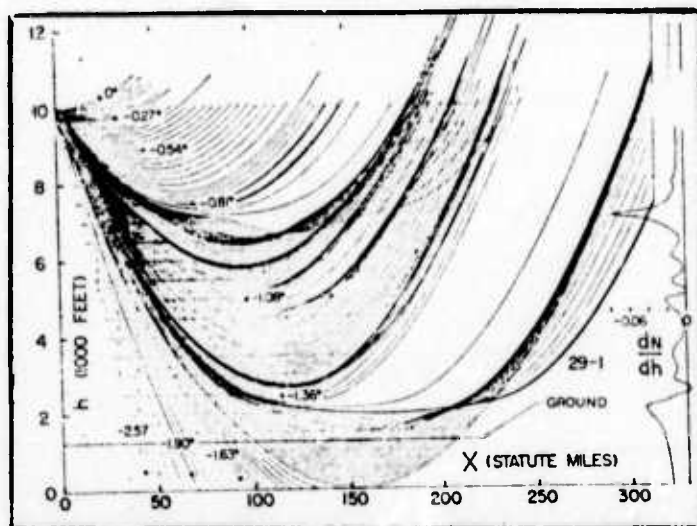
$$\Delta\nu_{\max} = \frac{2f_0 v}{c} [1 - \cos (.001)] \quad (3.123)$$

Again considering a jet aircraft moving at 600 miles per hour with a 10 GHz carrier frequency, the minimum time between fades is given by

$$T_{\min} = \frac{1}{\Delta\nu_{\max}} = 112 \text{ seconds/cycle} \quad (3.124)$$

It is evident then that the fading caused by the relative Dopplers between the two path signals is much slower than that caused by the changes in refractive path structure.

An in-flight test which substantiates the existence of this interference region was reported by Wong [3.5]. A thin layer was measured 3,000 feet below the airborne terminals, and the onset of multipath was at a range of about 180 miles. A ray tracing given by Wong and reproduced as Fig. 3.29 in this report, indicates that this interference region spans about 10 miles at 10,000 feet. The analysis provided in Case II of this section also indicates that for $\Delta h = 3,000$ feet (0.57 mile), interference begins at a range of 183 miles.



(This was obtained by a linear extrapolation of the data presented in Fig. 3.24.) Thus the onset and duration of the multipath interference predicted by the analysis presented in this report, are reasonably close to those shown in Wong's ray tracing and measured in the in-flight test.

The actual N-profile presented in Wong's data indicates the presence of several layers. From the ray tracing presented by Wong, it is apparent that the effect of additional layers is to focus the rays into separate regions of space. It is to be expected that as the RCV executes its flight plan, it will pass through these separate interference regions experiencing the type of multipath described by the single layer theory in each region, i.e., two separate paths, separating in delay and Doppler, with one becoming quickly attenuated with respect to the other. A detailed analysis of the multi-layered profile is given in Section 3.2.2.5.

3.2.2.4 Single Stratified Layer Between Terminals

When a layer of steep negative gradient of refractive index intercedes in the propagation path between the receiver and transmitter, it acts to focus the signal to a region of space dependent on the relative positions of the layer and terminals. The essential effect is to change the location of the shadow zone discussed in Section 3.2.2.1. If the terminals are fixed and the layer is moving vertically, it is possible that the receiver may be brought into a shadow zone induced by this motion, thus causing a fade on the link. Unlike multipath fading which is caused by the interference of signals, this type of fading is caused by the absence of signal in a radio-hole.

To quantitatively describe this process, the trajectory of a typical ray is shown in Fig. 3.30. The layer has thickness w , and is at a height h . The ray is launched at an angle θ_0 , enters and leaves the layer at θ_1 and θ_2 , and is received at θ_3 . If it is assumed that θ_0 is the minimum angle at which a ray is launched, then the region below the trajectory lies in an attenuation zone. The trajectory itself defines the transition between the region of normal signal strength and attenuated signal strength.

Using the methods outlined in Appendix F, it is easy to show that the distance from T to R measured along the earth is

$$L = -R_0(\sin \theta_1 - \sin \theta_0) + R(\sin \theta_1 - \sin \theta_2) \\ - R_0(\sin \theta_3 - \sin \theta_2) \quad (3.125)$$

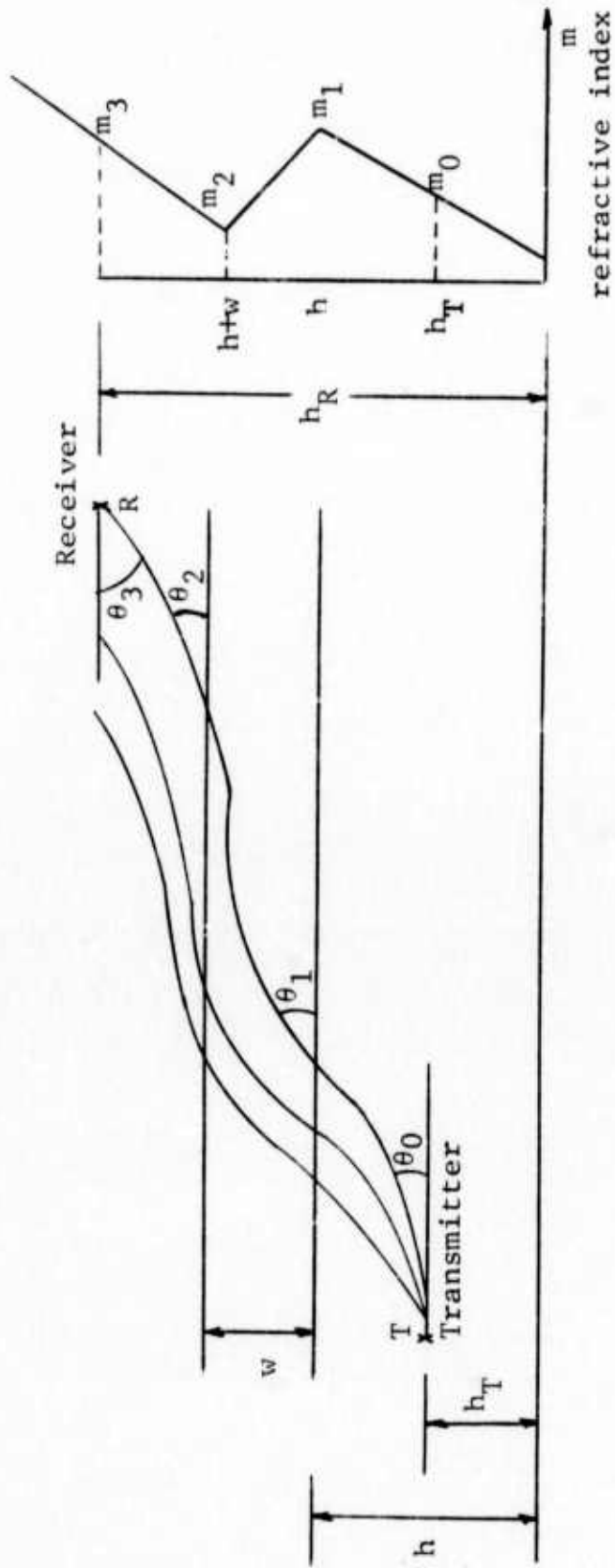


Figure 3.30 Ray Trajectory for Layer Between Terminals

where $-R_0$ and R are the ray curvatures outside and inside the layer, respectively. Each of the angles is known in terms of θ_0 from Snell's law, i.e.,

$$\cos \theta_i = \frac{m_0}{m_i} \cos \theta_0 \quad i = 1, 2, 3 \quad (3.126)$$

where the various values of refractive index m_i are given by

$$m_1 = m_0 - \frac{(h-h_T)}{R_0} \quad (3.127)$$

$$m_2 = m_0 - \frac{(h-h_T)}{R_0} - \frac{w}{R} \quad (3.128)$$

$$m_3 = m_0 - \frac{(h-h_T)}{R_0} - \frac{w}{R} - \frac{h_R - h - w}{R_0} \quad (3.129)$$

If the initial launch angle of the ray is zero, then the small angles θ_i can be determined from (3.126) as

$$\theta_i \approx \sin \theta_i \approx \sqrt{2 \frac{m_i - m_0}{m_i}} \quad (3.130)$$

Substituting (3.127) - (3.130) into (3.125), the range to the shadow zone can be well approximated by

$$L = \left(1 - \frac{R}{R_0}\right) \sqrt{-2R_0(h-h_T)} \left[1 - \sqrt{1 - \left(\frac{-R_0}{R}\right) \left(\frac{w}{h-h_T}\right)}\right] \\ + \sqrt{-2R_0 \left[(h_R - h_T) - w \left(1 - \frac{R_0}{R}\right) \right]} \quad (3.131)$$

A graph of the range to the shadow zone versus the height of the shadow zone is shown in Fig. 3.31. With the height of the intervening layer as a parameter, it is evident that if the terminals are fixed, a moving layer could cause the receiver to be placed in a radio hole. A wave-like movement of the layer could thus cause periodic fading of the received signal.

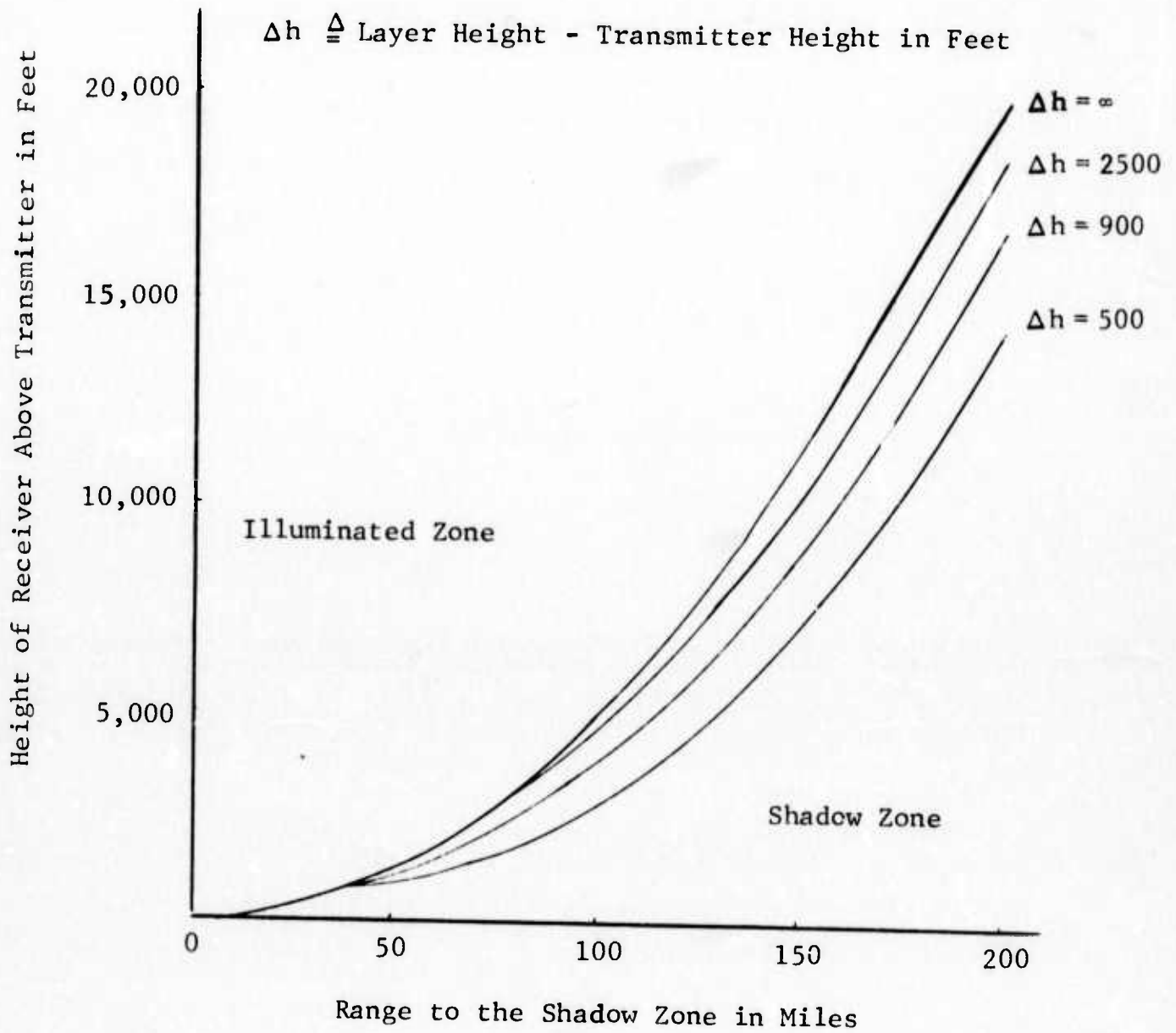


Figure 3.31 The Location of the Earth Shadow Zone With a Layer in the Standard Atmosphere

(Layer Thickness = 300 feet, Ray Curvature in Layer = 3500 miles)

3.2.2.5 Multilayer Profile

In the presence of a multilayered refractive index profile, the multipath characteristics will be similar to those outlined in the previous sections for the single layers. When the layers are above the terminals, for the reasons given in 3.2.2.2, only the one in close proximity to the terminals will cause multipath. Thus the analysis pertaining to a single layer above the terminals applies directly. When several layers are between the terminals, the shadow region will be modified in the same manner as discussed in 3.2.2.4 for a single layer. When the layers are below the terminals, the effect of the several layers is to focus the signal into several multipath regions, each with the same character as those outlined for the single layer.

Since it is prohibitively difficult to obtain analytic expressions for multipath in arbitrary multilayer profiles, a ray tracing technique was developed (see Appendix I) in which the propagation delay (relative to free space) was computed as a function of range for each ray trajectory.

The refractive index profile used to illustrate the effect of multilayers is a piecewise linear approximation to that presented by Wong (Fig. 3.29). Table 3-4 gives the multilayer profile which was used in this analysis.

An air-air flight path was executed with the transmitter and receiver at 10,000 feet. A graph of the initial launch angle θ of a ray versus the range L at which it intercepts the receiver is given in Fig. 3.32. Since the signal strength is

Table 3-4
MULTILAYER REFRACTIVE INDEX PROFILE

Height of Layer K Feet	dN/dh Nu/ft	dm/dh mu/ft
12	-.012	3.6×10^{-8}
7.25	-.012	3.6×10^{-8}
7.0	-.08	-3.2×10^{-8}
6.2	-.005	4.3×10^{-8}
5.8	-.012	3.6×10^{-8}
5.4	0	4.8×10^{-8}
5.1	-.012	3.6×10^{-8}
4.75	0	4.8×10^{-8}
4.40	-.02	2.8×10^{-8}
3.60	0	4.8×10^{-8}
2.60	-.01	3.8×10^{-8}
2.25	0	4.8×10^{-8}
1.50	-.04	0.8×10^{-8}
0	-.02	2.8×10^{-8}

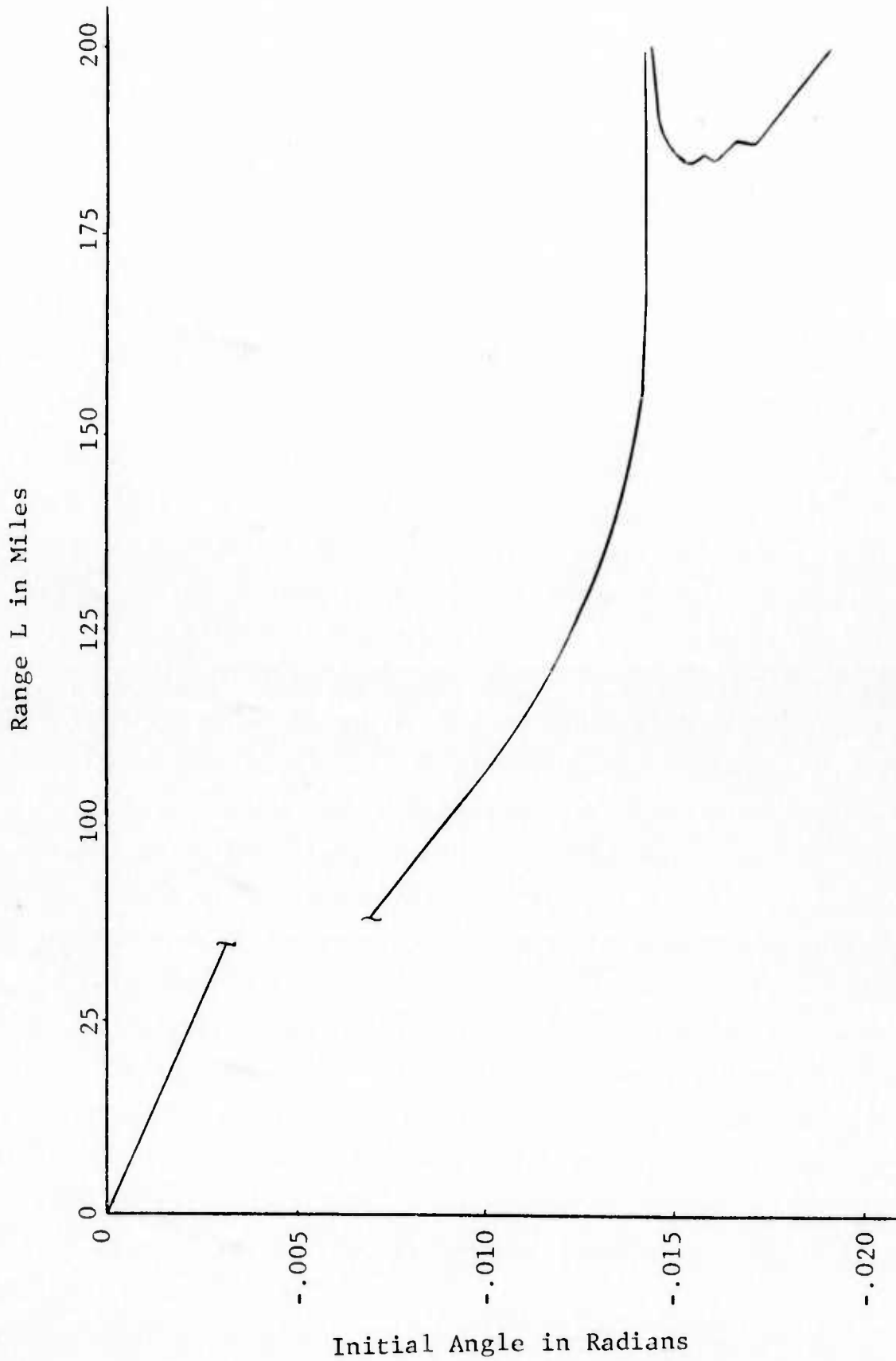


Figure 3.32 Initial Angle Vs. Range Diagram for Multilayer Profile
 (see Table 307 for profile)

proportional to the slope of the θ versus L diagram, it is evident that the receiver enters a radio hole at about 150 miles. It subsequently enters a multipath region which extends from about 185 to 200 miles. Within this region, there are several overlapping, double-valued portions of the θ versus L diagram, similar to those given in Section 3.2.2.3 for a single layer below the terminals. It is to be expected then that the multipath structure for each of these portions will be similar, i.e., two paths which initially have the same delay and subsequently separate in delay as range increases.

Calculation of the multipath profile indicates that in this interference region (185 - 200 miles), the multipath is separated from the direct path by more than 200 nanoseconds. However, since the direct path is small compared to the multipath (as evidenced by the small relative slope of θ versus L), it is assumed that the receiver will lock on to the much stronger multipath signals. The relative delay of these several multipath signals is shown in Fig. 3.33. It is seen that at each range where the θ versus L diagram has a new double-valued portion, a new pair of paths is generated which separate in delay as range increases. The number of separate paths present in each range interval and the maximum delay separation for each is summarized in Table 3-5. These results agree qualitatively with the ray tracing presented by Wong (see Fig. 3.29 of this report) in which the radio hole and multipath region can be viewed as areas of low and high ray densities respectively. The delay profiles presented in Fig. 3.33 and Table 3-5 provide an extension of Wong's analysis necessary to determine (spread spectrum) receiver performance.

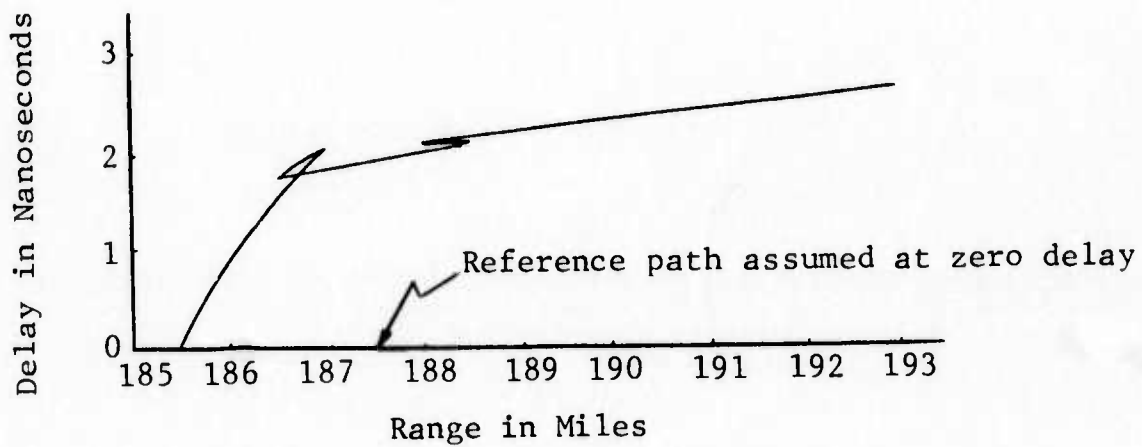


Figure 3.33 Delay Profile for Multilayer Refractive Index Structure

Table 3-5
SUMMARY OF MULTIPATH FOR MULTILAYER PROFILE

Range Interval Miles	Number of Paths	Maximum Delay Separation Nanoseconds	Comments
0 - 185.5	1	—	Direct path only
185.5 - 186.5	2	1.7	Severely attenuated direct path not included in rest of table
186.5 - 187	4	2.0	
187 - 188	2	2.1	
188 - 188.5	4	2.2	
188.5 - 193	2	2.7	
193 - 200	2	—	One path much stronger than other

3.3 Volume Scattering Channel

Volume scattering effects in the troposphere are due to two cases; atmospheric turbulence and hydrometeors (rain, snow, etc.). The multipath distribution associated with these effects is continuous rather than discrete, as in the case of refractive layers. In this section estimates are provided for the strength, delay power spectrum and frequency correlation function of the atmospheric-turbulence-caused volume scattering. These calculations allow a determination of the possible coherence bandwidth limitations of atmospheric turbulence in the transmission of high baud rate PN carriers. With regard to hydrometeors, it is shown that even under the most extreme postulated conditions, the received scattered power is negligible relative to that due to the direct paths. Therefore the multipath spread caused by the hydrometeors is not considered.

In 3.3.1 below, consideration is first given to the propagation physics aspect of volume scattering. Then the relationship between the system function characteristics (e.g., delay power spectrum) and propagation characteristics is developed in 3.3.2.

3.3.1 Propagation Modeling

In addition to stable layering effects which produce the steep gradients in refractive index discussed in Section 3.2, there are continuous spatially random fluctuations in refractive index. These fluctuations are present throughout the atmosphere and sometimes exist in turbulent layers. In order

to characterize these refractive index fluctuations for purposes of propagation analysis, a statistical approach must be used.

An assumption that is often used [3.16] is that the refractive index is a homogeneous isotropic field (or equivalently spatially wide-sense stationary and isotropic field) i.e., that the cross-correlation function between the refractive index at spatially separated points depends only on the separation distance,

$$\overline{n(\vec{R}_1, t)n(\vec{R}_2, t)} = C(|\vec{R}_1 - \vec{R}_2|) \quad (3.132)$$

where \vec{R}_1 , \vec{R}_2 are radius vectors to the two points in question, $n(\vec{R}, t)$ is the refractive index departure from unity at the point \vec{R} and time t , and $C(\cdot)$ is the spatial correlation function. The refractive index in N units of the previous section is related to n by

$$N = 10^6(n-1) \quad (3.133)$$

While the relationship (3.132) is only approximate over limited regions of space because of the spatial nonstationarity of the physical processes (e.g., pressure, temperature, humidity) determining $n(\vec{R}, t)$, the use of (3.132) as the basis for a statistical analysis can provide meaningful results if used with proper understanding of its limitations.

Fourier spectral analysis of the spatial fluctuations of refractive index is of basic importance to analytical and experimental treatments of propagation through random media.

Three, two, and one-dimensional spectral analyses may be defined for the spatial fluctuations. For the purposes of the present discussion it is sufficient to define a spatial power spectrum or "wave-number spectrum" as the Fourier transform of the spatial correlation function

$$P(k) = \int_0^{\infty} C(r) \cos 2\pi kr \, dr \quad (3.134)$$

$$C(r) = \int_0^{\infty} P(k) \cos 2\pi kr \, dk \quad (3.135)$$

The function $P(k)$ describes the "intensity" of the various spatial frequencies of $n(\vec{R}, t)$. The very low frequencies apply to the intensity of fluctuations in $n(\vec{R}, t)$ with characteristic sizes that are very large in space, while the higher frequencies determine the intensity of small scale fluctuations in $n(\vec{R}, t)$. It is the latter type of fluctuations that are of relevance to volume scattering.

To carry out tractable analysis and computations of the effect of refractive index fluctuations on system function characteristics it is necessary to dichotomize refractive index fluctuations into "small-scale" (large k -value) and "large-scale" (small k -value) fluctuations, i.e.,

$$n(\vec{R}, t) = n_s(\vec{R}, t) + n_L(\vec{R}, t) \quad (3.136)$$

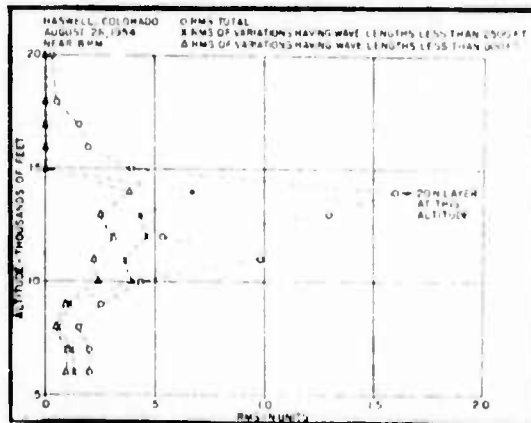
where $n_s(\cdot)$, $n_L(\cdot)$, represent the small and large scale fluctuations, respectively. The separation (3.136) implies an analogous representation of $C(r)$ and $P(k)$ into small-scale and large-scale spatial refractive index fluctuations

$$C(r) = C_s(r) + C_L(r) \quad (3.137)$$

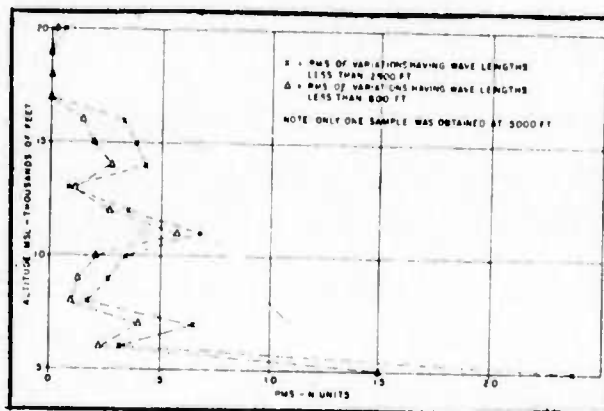
$$P(k) = P_s(k) + P_L(k) \quad (3.138)$$

Generally speaking, the large scale fluctuations in space are also slowly fluctuating in time and conversely, the small scale fluctuations in space are the more rapidly fluctuating components in time. Thus diurnal changes in the refractive index structure would be ascribed to $n_L(\vec{R}, t)$ while the rapid fluctuations in $n(\vec{R}, t)$ with t would be ascribed to $n_s(\vec{R}, t)$. It is recognized that this dichotomy into fast small-scale, and slow large-scale fluctuations is heuristic but it appears to be the only way to analytically handle the time and spatial nonstationarities of the refractive index field.

Estimates of the parameters of refractive index fluctuations can be obtained by examination of airborne refractometer measurements. A summary of airborne refractometer measurements in the United States was given by C. M. Crain [3.17] in 1955. Figure 3.34 reproduces Figs. 8 and 10 of [3.17] which present airborne refractometer-measured values of $\sqrt{n^2}$ in N units as a function of altitude. Figure 8 applies to a particular



RMS Variations in Index of Refraction Over Haswell, Colorado, on August 26, 1954.



Average of RMS Variations in Index of Refraction for Six Flights Over Southeastern Colorado in August, 1954

Figure 3.34 Measurement of RMS Index of Refraction [3.17]

day while Fig. 9 applies to an average over six days. To obtain information on the intensity of different spatial wavelengths, a spectral analysis of refractometer readings was undertaken with time related to distance by the velocity of the aircraft. Thus in Figs. 8 and 10 it will be noted that $\sqrt{n^2}$ is given in three forms: a total RMS value, an RMS value for fluctuations having wavelengths less than 2500 ft., and an RMS value for fluctuations having wavelengths less than 800 ft. For wavelengths less than 800 ft. an average RMS N of a small fraction of an N unit is observed.

Another parameter needed in theoretical calculations is the "scale of turbulence" for the small scale fluctuations. This is an average wavelength for the small scale fluctuations. Sometimes it is defined as the "correlation-distance" of the spatial correlation function. It appears difficult to arrive at definitive numbers here. Gjessing [3.18] suggests 10 meters as the "right order of magnitude." Muchmore and Wheelon [3.19], quoting the work of Crain, et al [3.20], mention the range 20 ft. (6m) at the surface to 100 - 200 ft. (30 - 60m) at high elevations, but they include the large scale fluctuations. In the subsequent section we will study the implications of such sizes of scales of turbulence and $\sqrt{n^2}$ values of system function characteristics.

There exist basically only two tractable, approximate, generally useful approaches for modeling radio propagation at microwave frequencies-geometrical optics [3.22] and single or "Born" scattering approaches [3.23]. Geometrical optics has already been used in Section 3.2 to determine system function characteristics corresponding to steep negative gradients in refractive index occurring in finite layers in an otherwise

homogeneous atmosphere. Here we are concerned with adding the atmospheric inhomogeneities and determining their effect on the system function characteristics of a single path. Both single scattering and geometric optics theories are useful in this regard although single scattering is used exclusively to handle the refractive index fluctuations due to hydrometeors.

There exists a simpler approximate single scattering theory [3.16] that models the medium in terms of a scatter cross-section per unit volume. The received signal power due to the scattering is computed by summing up the scattered power from infinitesimal volumes assuming bistatic radar theory. We shall carry out such a computation for rain utilizing scattering cross-section results from Crane [3.21]. The scattering cross-section approach has been used extensively for atmospheric turbulence characterization also, but it is not as suitable as the more general single scattering approach for the present line-of-sight analysis.

3.3.2 System Function Characteristics

3.3.2.1 Atmospheric Turbulence

We consider first the application of single scattering to computation of system function characteristics. Many studies have been conducted in the past utilizing single scattering to characterize the fluctuations on a single received carrier (e.g., Wheelon [3.24], Booker and Gordon [3.23], Muchmore and Wheelon [3.25] and Tatarski [3.16].) Such calculations, while interesting, are not relevant to the basic problem of interest

in RCV channel modeling, the evaluation of multipath and frequency selectivity characteristics. Only two such relevant studies have been reported in the literature, those of Muchmore and Wheelon [3.26] and Bello [3.27]. The calculations by Muchmore and Wheelon are considerably more restricted than those of Bello. The former dealt with plane wave transmission (not directly applicable to ground-air and air-air communications) and a real rather than complex formulation which makes their results incomplete for application to narrow band transmission. Moreover Muchmore and Wheelon did not actually develop statistical "black-box" models for the channel.

Before utilizing some results from [3.27] it is necessary to define some second-order statistical properties of random time variant linear channels. The discussion in Section 2 on the characterization of fading dispersive channels did not depend upon particular statistical assumptions and is thus valid for statistically stationary and nonstationary channels. For scatter radio channels it is useful to define certain idealized statistical models based upon assumed behavior of the correlation functions of system functions. Here we discuss only the wide sense stationary uncorrelated scatter (WSSUS) model. The reader is referred to [3.28] for a more general discussion.

For the WSSUS model, by hypothesis, the correlation function of the time variant transfer function takes the simple form

$$\overline{T^*(f, t)T(f + \Omega, t + \tau)} = R(\Omega, \tau) \quad (3.139)$$

i.e., the cross-correlation function between the complex envelopes of received carriers transmitted Ω Hz apart is dependent only on the frequency separation Ω and time lag τ . The

function $R(\Omega, \tau)$ is called the time-frequency correlation function. For Ω or τ identically zero we use the notation

$$R(\Omega, 0) = q(\Omega) \quad (3.140)$$

$$R(0, \tau) = p(\tau) \quad (3.141)$$

Note that $q(\Omega)$, called the frequency correlation function, can be interpreted as the autocorrelation function along the frequency axis of the "snapshot" at time t' of a time variant transfer function, $T(f, t')$. It is also the cross-correlation between two received carriers as a function of separation frequency. When the frequency separation $\Omega = \Omega_1$ is such that the cross-correlation function $q(\Omega)$ is very near the maximum value $q(0)$ for all $|\Omega| < \Omega_1$ it is clear that all transmitted frequency components within a band of frequencies of width less than Ω_1 will be received fluctuating in a highly correlated fashion. Thus one may define the coherence bandwidth in terms of Ω_1 , if desired.

The time correlation function $p(\tau)$ is the autocorrelation function of the complex envelope of a received carrier. Clearly one may define the coherence duration parameter T_{coh} in terms of $p(\tau)$ in the same way W_{coh} can be defined in terms of $q(\Omega)$.

For the WSSUS channel one may show that (3.139) implies

$$\overline{g^*(t, \xi)g(t+\tau, \eta)} = Q(\tau, \xi)\delta(\eta - \xi) \quad (3.142)$$

where $\delta(\cdot)$ is the unit impulse function, and $Q(\tau, \xi)$ has been called the tap gain correlation function because it is proportional to the autocorrelation function of the fluctuations in the complex tap gain at delay ξ in the differential tapped delay line model interpretation of Eq. (3.142). The value of $Q(\tau, \xi)$ at $\tau=0$, $Q(\xi)$, is a profile of scattering intensity as a function of delay ξ called the delay power spectrum,

$$Q(\xi) = Q(0, \xi) \quad (3.143)$$

The tap-gain and time-frequency correlation functions are Fourier transform pairs. In particular the delay power spectrum and frequency correlation functions are Fourier transform pairs, i.e.,

$$q(\Omega) = \int Q(\xi) e^{-j2\pi\xi} d\xi \quad (3.144)$$

As has been pointed out previously, the RCV channels, like all radio channels, are not statistically stationary. However, as for most radio channels, the time and frequency selective behavior is approximately stationary or quasi-stationary for time intervals and bandwidths much greater than the durations and bandwidths of signaling elements of interest. A quasi-stationary scatter channel may then be postulated for modeling such channels in which $R(\Omega, \tau)$ and $Q(\tau, \xi)$ are possibly slowly varying with time and at a given time instant change little for small percentage changes in carrier frequency.

In [3.27] calculations utilizing the single scattering theory have been carried out for the delay power spectrum $Q(\xi)$ and frequency correlation function $q(\Omega)$ associated with homogeneous isotropic refractive index fluctuations [3.16] on a line-of-sight link. Two important parameters that arise in these calculations are the scattering and power parameters,

$$N_S = \frac{\lambda_0 D}{8\Lambda^2} \quad (3.145)$$

$$P_0 = \frac{8\pi^2 \Lambda D \overline{|n^2|}}{\lambda_0^2} \quad (3.146)$$

where

D = path length

λ_0 = wavelength at carrier frequency

$\overline{|n^2|}$ = $C(0)$ is the mean squared value of refractive index fluctuations

and Λ is a scale of turbulence parameter defined in the two equivalent forms

$$\Lambda = \frac{\int_0^{\infty} C(r) dr}{C(0)} \quad (3.147)$$

$$\Lambda = \frac{P(0)}{\int_0^{\infty} P(k) dk} \quad (3.148)$$

In the form (3.148) it may be recognized as the reciprocal of the "noise-bandwidth" of the spectrum $P(k)$. For the case of an exponential shaped correlation function $C(r)$, Λ is equal to the spatial separation at which the correlation function drops to $1/e$.

Depending upon the size of these parameters compared with unity, different modeling approaches are useful for characterizing input-output relationships and distinctly different system function properties exist. Table 3-6 presents a summary of these considerations organized into four different cases corresponding to the four possible inequalities. It will be shown that cases II and III are of most relevance for RCV links in the 4 - 10 GHz band (assuming small-scale fluctuation effects).

The calculations carried out in [3.27] utilizing single scattering theory assume that $P_0 \ll 1$. When this inequality is true, P_0 corresponds to the power at the output of the volume scattering channel normalized to the direct path power. The scattering parameter N_S has a strong effect on the statistical character of the input-output relationships. When $N_S < 1$ the channel causes negligible frequency selective distortion on narrow band radio signals (signals whose bandwidths are small compared to the carrier frequency). In addition, the output

Table 3-6

SUMMARY COMMENTS ON COMPUTATIONALLY USEFUL PROPAGATION MODELS AND GROSS SYSTEM FUNCTION CHARACTERISTICS FOR HOMOGENEOUS ISOTROPIC REFRACTIVE INDEX FLUCTUATIONS (MEDIUM-LIMITED RATHER THAN ANTENNA-LIMITED PROPAGATION ASSUMED)

Case	Scatter Parameter	Power Parameter	Propagation Model Useful	System Function Characteristics
I	$N_S < 1$	$P_0 > 1$	Geometrical Optics	Negligible multipath distortion. Channel randomly phase modulates transmitted carrier with large phase deviation.
II	$N_S < 1$	$P_0 < 1$	Geometrical Optics Single Scattering	Negligible multipath distortion. Channel phase modulates transmitted carrier with small deviation and approximate Gaussian statistics.
III	$N_S > 1$	$P_0 < 1$	Single Scattering	Multipath distortion for narrow-band signal transmission with amount depending on size of N_S . $N_S \gg 1$ required for significant distortion. For $N_S \gg 1$ channel has non-zero-mean complex Gaussian statistics.
IV	$N_S > 1$	$P_0 > 1$	No simple models available	Multipath distortion. For $N_S \gg 1$ zero-mean complex Gaussian statistics seem likely.

Table 3-6

SUMMARY COMMENTS ON COMPUTATIONALLY USEFUL PROPAGATION MODELS AND
GROSS SYSTEM FUNCTION CHARACTERISTICS FOR HOMOGENEOUS ISOTROPIC REFRACTIVE INDEX
FLUCTUATIONS (MEDIUM-LIMITED RATHER THAN ANTENNA-LIMITED PROPAGATION ASSUMED)

Case	Scatter Parameter	Power Parameter	Propagation Model Useful	System Function Characteristics
I	$N_S < 1$	$P_0 > 1$	Geometrical Optics	Negligible multipath distortion. Channel randomly phase modulates transmitted carrier with large phase deviation.
II	$N_S < 1$	$P_0 < 1$	Geometrical Optics Single Scattering	Negligible multipath distortion. Channel phase modulates transmitted carrier with small deviation and approximate Gaussian statistics.
III	$N_S > 1$	$P_0 < 1$	Single Scattering	Multipath distortion for narrow-band signal transmission with amount depending on size of N_S . $N_S \gg 1$ required for significant distortion. For $N_S \gg 1$ channel has non-zero-mean complex Gaussian statistics.
IV	$N_S > 1$	$P_0 > 1$	No simple models available	Multipath distortion. For $N_S \gg 1$ zero-mean complex Gaussian statistics seem likely.

of the volume scatter channel appears essentially in quadrature to the direct channel causing only phase modulation ($P_0 \ll 1$). This same result is obtained from geometrical optics. Both analyses for $N_S < 1$ lead to an rms value of phase fluctuations in radians of

$$\overline{\alpha^2} = P_0 \quad (3.149)$$

As N_S becomes sufficiently larger than unity (assuming still $P_0 \ll 1$) the volume scatter channel output develops fluctuating components both in-phase and quadrature to the direct path carrier, the statistics of the fluctuations begin to approach complex Gaussian, and frequency selective distortion becomes perceptible for narrow band signals.

While cases II and III discussed above are on relatively firm ground from an analytical modeling point of view, cases I and IV are much less firm. In the case of case I, it is customary to utilize geometrical optic treatment which leads to (3.148) as an expression for the rms phase fluctuations even when these are many radians. It appears that (3.148) can be used for large and small scale spatial fluctuations provided basic restrictions on the use of geometrical optics are fulfilled (see Section 3.2). In the case of case IV with $P_S \gg 1$ virtually no quantitative analysis are available. A full wave theory treatment is necessary—neither single scattering nor geometric optics can be accurate here. Cases I and IV have the common condition that $P_0 > 1$. In case I, as P_0 gets ever

larger than unity, the resultant large phase modulation will remove any steady carrier component. It appears that an analogous phenomenon must take place in case IV, i.e., the non-fluctuating (or direct path) component must get weaker as more and more power gets scattered. Using central limit theorem arguments one would deduce that for $N_S \gg 1$ as P_0 becomes much bigger than unity the received signal must exhibit complex Gaussian statistics. In addition the multipath and frequency selective characteristics deduced from single scattering analyses are likely to provide underestimates of the channel distortion.

We consider now ranges of values of the parameters N_S , P_0 due to atmospheric turbulence for RCV links in the 4 - 10 GHz frequency band. N_S may be expressed in the form

$$N_S = \left(\frac{\Lambda_0}{\Lambda} \right)^2 \quad (3.150)$$

where

$$\Lambda_0 = \frac{1}{2} \sqrt{\frac{\lambda_0^D}{2}} \quad (3.151)$$

is a convenient reference value of scale of turbulence. For $\Lambda > \Lambda_0$ there will be negligible selectivity for narrow band signal transmission. For Λ to any extent smaller than Λ_0 there will be perceptible frequency selectivity for narrow band signals.

Table 3-7 presents plots of Λ_0 in meters as a function of path distance in Km for $f_0=4$ and $f_0=10$ GHz. It will be recalled that Muchmore and Wheelon [3.19] quote that measurements by Crain [3.17] have resulted in values of Λ varying from 6 at

Table 3-7
 VALUE OF λ_0 IN METERS AS A FUNCTION OF PATH DISTANCE AND CARRIER FREQUENCY

		Path Distance in Kilometers				
		20	40	80	160	320
Carrier	4 GHz	13.7	19.4	27.4	38.8	54.8
Frequency	10 GHz	8.4	11.8	16.7	23.6	33.4

the surface rising quickly to 60 meters, with increasing altitude. Examination of Table 3-7 reveals that at $\Lambda = 60$ meters $N_S < 1$ throughout the 4 - 10 GHz band but that for $\Lambda = 6$ meters the situation reverses and $N_S > 1$ throughout the 4 - 10 GHz band. Consequently there will be occasions, particularly at the longer paths and lower altitudes, when the volume scattering channel can cause frequency selective distortion on narrow band signals. To provide quantitative estimates of this degree of distortion as a function of N_S Fig. 3.35 presents reproductions of Figs. 4 and 5 of [3.27]. These are theoretical calculations of delay power spectrum and frequency correlation function for a Gaussian shaped spatial refractive index correlation function

$$\frac{C(r)}{C(0)} = \exp [-\pi r^2 / 4\Lambda^2] \quad (3.152)$$

These curves are plotted* as a function of normalized delay and frequency separation variables y and x , respectively

$$y = \frac{\xi/T_0}{N_S/2} \quad (3.153)$$

$$x = \frac{\Omega}{f_0} (N_S/2) \quad (3.154)$$

* In this figure from [3.27] N is used instead of N_S . This should not be confused with N as used in this report for refractive index.

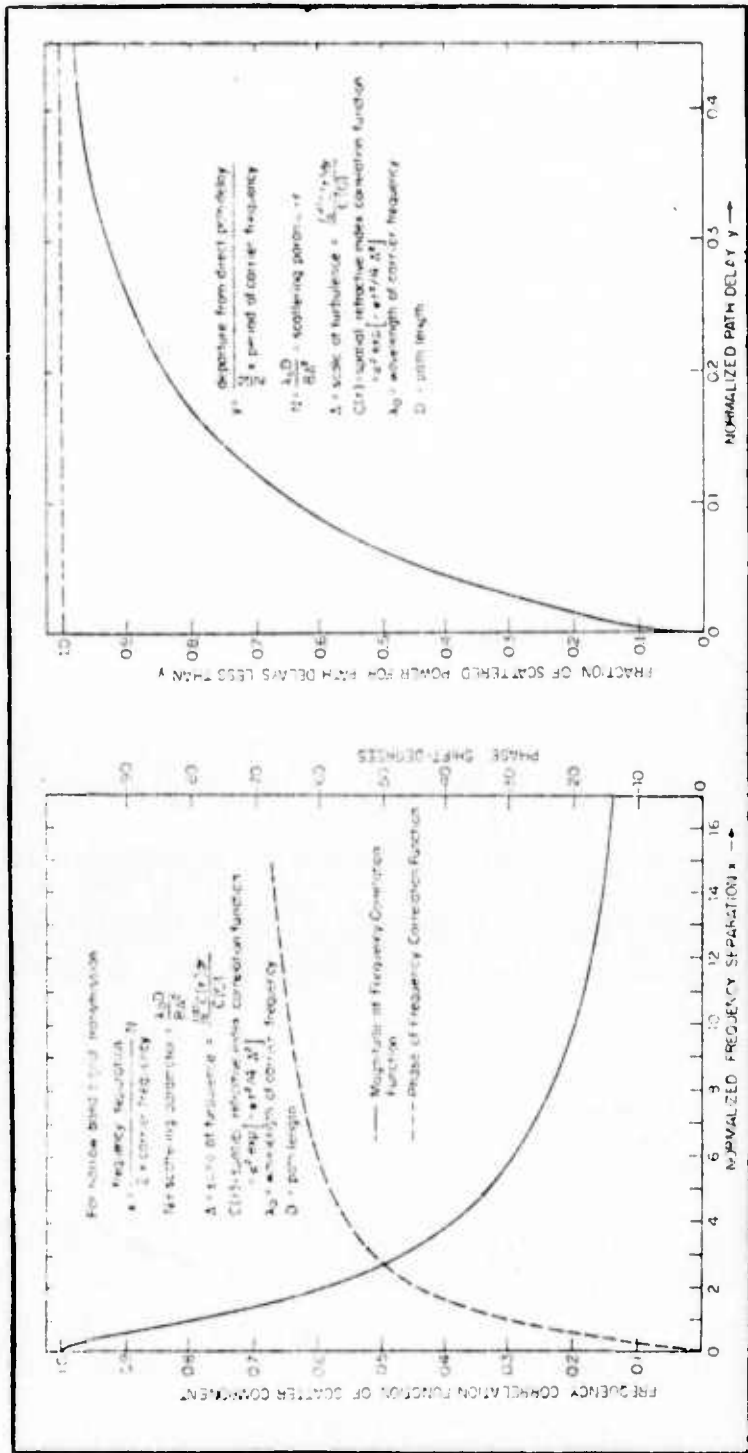
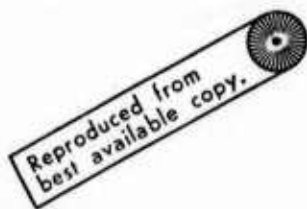


Figure 3.35 Frequency Correlation Function and Delay Power Spectrum for Volume Scattering Channel



where ξ is the delay variable (relative to the direct path delay) used in the delay power spectrum $Q(\xi)$ and Ω is the frequency shift variable in the frequency correlation function $q(\Omega)$. The quantity

$$T_0 = 1/f_0 \quad (3.155)$$

is the period of the carrier.

In the derivation of these functions the effect of antenna gain patterns in reducing the effective scattering volume has been neglected. Reference [3.27] presents analytical expressions that include the effect of antenna patterns (see Eq. (291)). It may be shown from these results that if

$$\frac{\lambda^2}{4\pi^2 \Lambda^2 \psi_m^2} \ll 1 \quad (3.156)$$

the antenna beamwidth ψ_m may be neglected for Gaussian beam patterns

$$G(\psi) = \exp(-2\psi^2/\psi_m^2) \quad (3.157)$$

at transmitter and receiver. One may set

$$\psi_m \approx \frac{\lambda_0}{d} \quad (3.158)$$

where d is the diameter of a parabolic antenna. Using (3.158) in (3.156) the requirement for neglect of antenna patterns is

$$\Lambda^2 \gg \left(\frac{d}{2\pi}\right)^2 \quad (3.159)$$

This inequality appears valid for the range of Λ expected and the likely sizes of antennas. The theoretical expressions for the curves given in Fig. 3.35 are

$$R(x) = \frac{1}{\sqrt{(1+j2x)^2-1}} \ln [1+j2x + \sqrt{(1+j2x)^2-1}] \quad (3.160)$$

$$Q(y) = \pi \exp(-\pi y) K_0(\pi y) \quad ; \quad y > 0 \quad (3.161)$$

in which $K_0(\cdot)$ is the modified Bessel function of the second kind and order zero.

Approximately 99 percent of the area under $Q(y)$ lies between $y=0$ and $y=.61$. Thus 99% of the scattered power occurs for path delays relative to the direct path delay of $\approx .3 N_S T_0$. Thus the scattering parameter N_S must exceed $3 \frac{1}{3}$ if the multipath spread of the scatter component is to exceed the duration of a single RF cycle!

While we have gone to the trouble to determine whether the scatter component will be frequency selective, this question is not nearly as important as the size of the scatter component relative to the direct path component. If the direct path component is large compared to the scatter component the frequency selectivity of the scatter component will actually be beneficial for high baud rate PN carriers because the "gating"

operation of the PN carrier demodulation process will then reduce the scatter component as discussed in Section 2. We consider now the range of values to be expected for P_0 .

Consider the worst case: $f_0 = 10$ GHz, $\Lambda = 60$ m, $D = 320$ km. For this case

$$P_0 = (1.7)N^2 \quad (3.162)$$

where N stands for the RMS value of the refractive index fluctuations expressed in N units. In Section 3.3.1 it was pointed out that values of N equal to a fraction of a unit are to be expected even including spatial fluctuations with wavelengths up to 240m (800 ft). A value of $N = 1/4$ for the small scale fluctuations seems like a reasonably large value. This still leads to a value of $P_0 \ll 1$. Since P_0 increases as N^2 however, as N increases much beyond $1/4$ P_0 will become large enough to violate the conditions of validity of single scattering theory. It should be noted that measurements do show some layered regions in space with N values of 1 or 2 units. Thus it is possible that in limited regions P_0 could exceed unity. However it should be noted that (3.162) was for the case of $\Lambda = 60$ for which $N_S < 1$. With the even larger values of Λ associated with the large values of N , $N_S \ll 1$ and case I of Table 3-7 would apply, indicating large phase fluctuations but negligible frequency selectivity for narrow-band signals. These large phase fluctuations are produced by the large scale fluctuations in refractive index and are likely to be slowly fluctuating in time.

In summary, for RCV links up to 200 miles in length and operating frequencies from 4 - 10 GHz, the observed degree of small-scale atmospheric fluctuations in refractive index applied to a homogeneous isotropic model lead to a received signal small compared to the direct path signal. The large scale fluctuations will cause slow phase modulation which can be several radians on the longest links. It should be noted, however, that even if the scattered signal produces a small P_0 , at the longest ranges this P_0 could be large enough to cause several dB peak-to-peak amplitude fluctuations in the received signal. In any case, the frequency selectivity associated with the volume scattering channel does not constitute a limiting factor in wide-band PN carrier transmission.

3.3.2.2 Hydrometeors

Rain, hail, and snow both absorb and scatter propagating electromagnetic waves. Our concern in this section is with the scattering properties of these hydrometeors which produce a volume scattering multipath affect. The majority of attention in the literature has been devoted to modeling the scattering and attenuation properties of rain. Fortunately, for the purposes of the present analysis, we need only consider rain because it is not only more frequent but it is more severe in its affect on electromagnetic waves.

If σ denotes the scattering cross-section per unit volume for rain, then utilizing bistatic radar theory, the scattered power received normalized to the direct path power received may be expressed as the volume integral*

* This expression does not account for depolarization, which is negligible here.

$$P_0 = \frac{D^2}{4\pi^2} \iiint \frac{G_T(\vec{R})G_R(\vec{R})}{d_T^2 d_R^2} \sigma(\vec{R}) dV \quad (3.163)$$

where dV is the volume element, G_T , G_R are the transmitter and receiver antenna gain patterns normalized to the direct path gains, D is the path length, d_T and d_R are the distances from the transmitter and receiver, respectively to the scattering point, and $\sigma(\vec{R})$ is the scattering cross-section per unit volume.

We assume conically symmetric beams and a geometry as shown in Fig. 3.35. Using a cylindrical coordinate system

$$dV = r dr d\eta dz \quad (3.164)$$

and assuming conically symmetric beam patterns

$$G_T(\vec{R}) = f\left(\frac{R}{z+D/2}\right) \quad (3.165)$$

$$G_R(\vec{R}) = q\left(\frac{R}{z-D/2}\right) \quad (3.166)$$

$$d_T = \sqrt{R^2 + (D/2+z)^2}$$

$$d_R = \sqrt{R^2 + (D/2-z)^2} \quad (3.167)$$

it is found that

$$P_0 = \frac{D^2}{2\pi} \int_0^{\infty} \int_{-D/2}^{D/2} R f\left(\frac{R}{z+D/2}\right) g\left(\frac{R}{D/2-z}\right) \frac{\sigma(R,z)}{[R^2 + (\frac{D}{2} + z)^2][R^2 + (\frac{D}{2} - z)^2]} dz dR \quad (3.168)$$

Assuming narrow beam Gaussian shaped antennas and constant scattering cross-section the integral (3.168) simplifies to

$$P_0 = \sigma \frac{D^2}{4\pi} \int_{-D/2}^{D/2} \frac{\alpha^2 \beta^2}{\beta^2 (D/2-z)^2 + \alpha^2 (D/2+z)^2} dz \quad (3.169)$$

where

$$f(\theta) = \exp \left[-\frac{\theta^2}{\alpha^2} \right] \quad (3.170)$$

$$g(\theta) = \exp \left[-\frac{\theta^2}{\beta^2} \right] \quad (3.171)$$

and 2α , 2β are the e^{-1} beam widths of the Gaussian antenna patterns.

Carrying out the integrations

$$P_0 = \frac{\sigma D \alpha \beta}{4\pi} \left[\tan^{-1} \left(\frac{\alpha}{\beta} \right) + \tan^{-1} \left(\frac{\beta}{\alpha} \right) \right] \quad (3.172)$$

It remains to select values for the scattering cross-section σ , beam widths α , β , and distance D . From Crane [3.21] we find that the scattering cross-section/unit volume is given by

$$\sigma = \frac{\pi^5}{\lambda^4} |K|^2 Z \quad (3.173)$$

where $|K|^2$ is a function of the dielectric constant of liquid water and is typically near 1 [3.29], and Z is a parameter dependent on the distribution of rain drops of different sizes

usually expressed in units of mm^6/m^3 . The following experimental values of Z were kindly provided by Crane from a report to be published [3.30]: for % of occurrences of .001, .01, .1, and .5 the values of Z measured at 3 km altitudes were 50, 47, 39, and 33 dB (relative to one mm^6/m^3), respectively. From these values and (3.173) we obtain Table 3-8 for scattering cross-sections/meter³ at 4 and 10 GHz.

For antenna beam widths we have selected a 3 ft. dish for the aircraft and a 30 ft. dish for the ground station. This leads to $\alpha = .118$, $\beta = .0118$ radians at 4 GHz and $\alpha = .0473$, $\beta = .00473$ radians at 10 GHz. Using the above values for α , β , Z , λ and a path length of 100 miles, we obtain the scatter to direct path power ratios indicated in Table 3-9. Note the very low values of scattered power even assuming that rain occurs along the entire 100 mile length of the path! One may conclude that rain scattering may be neglected in the 4 - 10 GHz band for RCV links.

Table 3-8

RAIN SCATTERING CROSS SECTIONS/m³ AT 4 AND 10 GHz

% Occurrence	$Z_{\text{mm}^6/\text{m}^3}$ in dB	Scattering Cross Section/m ³ (unit m ⁻¹)	
		4 GHz (7.5 cm)	10 GHz (3 cm)
.001	50	1.14×10^{-7}	1.26×10^{-5}
.01	47	5.70×10^{-8}	6.29×10^{-6}
.1	39	9.12×10^{-9}	1.0×10^{-6}
.5	33	2.28×10^{-9}	2.5×10^{-7}

Table 3-9
 RECEIVED SCATTER/DIRECT PATH POWER RATIOS P_0 DUE TO RAIN FOR
 100 MILE PATH, 3' AND 30' ANTENNA DISHES, AT 4 AND 10 GHz

% Occurrence	Scatter/Direct Path Power Ratio P_0 (in dB)	
	4 GHz	10 GHz
.001	-65.2	-42.7
.01	-68.2	-45.7
.1	-76.2	-53.7
.5	-82.2	-59.7

3.4 Atmospheric Filter Characteristics

Due to the frequency dependence of the complex dielectric constant of water vapor and oxygen some frequency selective effects will occur on a transmitted signal even in a strictly uniform atmosphere. This frequency selective behavior has been made evident in our system function model of the RCV link in Section 2 by the inclusion of a filter labeled "atmospheric filter." In this section we assess the importance of this filter in limiting the use of high baud rate PN carriers over long line-of-sight distances in the 4 to 10 GHz band.

We consider first the effect of the atmospheric gases, water vapor and oxygen. Following this we shall discuss the affect of rain.

Two basic frequency dependencies of complex dielectric constants may be identified for atmospheric gases: the resonant and non-resonant [3.31]. In the non-resonant case the dielectric constant ϵ is given by

$$\epsilon(f) = \frac{\epsilon_0 - \epsilon_\infty}{1 + j \frac{f}{\Delta f}} + \epsilon_\infty \quad (3.174)$$

where Δf is called the line-breadth constant and the real quantity $\epsilon_0 - \epsilon_\infty$ is the change in ϵ from zero to infinite frequency, while ϵ_0 is the zero frequency value of dielectric constant. The real and imaginary parts of this non-resonant dielectric constant are given by

$$\epsilon_r = \frac{\epsilon_0 - \epsilon_\infty}{1 + \left(\frac{f}{\Delta f}\right)^2} + \epsilon_\infty = \left(\frac{\Delta f}{c}\right)^2 \frac{\epsilon_0 - \epsilon_\infty}{\left(\frac{\Delta f}{c}\right)^2 + \frac{1}{\lambda^2}} + \epsilon_\infty \quad (3.175)$$

$$\epsilon_i = - \frac{\epsilon_0 - \epsilon_\infty}{1 + \left(\frac{f}{\Delta f}\right)^2} \cdot \frac{f}{\Delta f} = - \left(\frac{\Delta f}{c}\right) \frac{1}{\lambda} \frac{\epsilon_0 - \epsilon_\infty}{\left(\frac{\Delta f}{c}\right)^2 + \frac{1}{\lambda^2}} \quad (3.176)$$

where c is the velocity of light and λ is the wavelength corresponding to the frequency f

$$c = f\lambda \quad (3.177)$$

The non-resonant case is typical of the dielectric constant of oxygen for frequencies much lower than 60 GHz. In particular it is applicable in the 4 - 10 GHz range.

The resonant type dielectric constant has the form

$$\epsilon = 1 + \frac{Af_0^2}{f_0^2 - f^2} \left\{ 1 - \frac{\Delta f}{2} \frac{\left(\frac{f}{f_0} + 1\right)\left(\frac{f}{f_0}\right)}{[\Delta f - j(f_0 - f)]} - \frac{\Delta f}{2} \frac{\left(\frac{f}{f_0} - 1\right)\left(\frac{f}{f_0}\right)}{[\Delta f + j(f_0 + f)]} \right\} \quad (3.178)$$

where A is a dimensionless constant and f_0 is the resonant frequency. For water vapor such a resonance exists with $f_0 = 22.2$ GHz ($\lambda_0 = 1.35$ cm) and for oxygen with $f_0 = 60$ GHz ($\lambda_0 = .5$ cm). The real and imaginary parts of (3.178) are

$$\begin{aligned}
\epsilon_i &= -\frac{A}{2} f \left\{ \frac{\Delta f}{(\Delta f)^2 + (f_0 - f)^2} + \frac{\Delta f}{(\Delta f)^2 + (f_0 + f)^2} \right\} \\
&= -\frac{A}{2} \frac{1}{\lambda} \left\{ \frac{\Delta f/c}{(\Delta f/c)^2 + \left(\frac{1}{\lambda_0} - \frac{1}{\lambda}\right)^2} + \frac{\Delta f/c}{(\Delta f/c)^2 + \left(\frac{1}{\lambda_0} + \frac{1}{\lambda}\right)^2} \right\}
\end{aligned} \tag{3.179}$$

and

$$\begin{aligned}
\epsilon_r &= 1 + \frac{A f_0^2}{f_0^2 - f^2} \left\{ 1 - \frac{(\Delta f)^2}{2} \frac{\left(\frac{f}{f_0} + 1\right)\left(\frac{f}{f_0}\right)}{(\Delta f)^2 + (f_0 - f)^2} \right. \\
&\quad \left. - \frac{(\Delta f)^2}{2} \frac{\left(\frac{f}{f_0} - 1\right)\left(\frac{f}{f_0}\right)}{(\Delta f)^2 + (f_0 + f)^2} \right\} \\
&= 1 + \frac{A}{1 - \left(\frac{\lambda_0}{\lambda}\right)^2} \left\{ 1 - \frac{1}{2} \left(\frac{\Delta f}{c}\right)^2 \frac{\left(\frac{\lambda_0}{\lambda} + 1\right)\left(\frac{\lambda_0}{\lambda}\right)}{(\Delta f/c)^2 + \left(\frac{1}{\lambda_0} - \frac{1}{\lambda}\right)^2} \right. \\
&\quad \left. - \frac{1}{2} \left(\frac{\Delta f}{c}\right)^2 \frac{\left(\frac{\lambda_0}{\lambda} - 1\right)\left(\frac{\lambda_0}{\lambda}\right)}{(\Delta f/c)^2 + \left(\frac{1}{\lambda_0} + \frac{1}{\lambda}\right)^2} \right\}
\end{aligned} \tag{3.180}$$

A plane wave of frequency f propagating a distance D through a homogeneous medium with dielectric constant ϵ and free space permittivity would be subject to the complex gain change, i.e., transfer function,

$$H(f) = \exp [-j2\pi fD/c n(f)] \quad (3.181)$$

where $n(f)$ is the refractive index

$$n(f) = \sqrt{\epsilon(f)} = \sqrt{1+\epsilon(f)-1}$$

$$\approx 1 + \frac{\epsilon(f) - 1}{2} \quad \text{for} \quad |\epsilon-1| \ll 1 \quad (3.182)$$

In all cases of interest in radio propagation through the troposphere $|\epsilon-1|$ will be very much smaller than 1. Thus we use

$$H(f) = \exp [-j2\pi D/c f] \exp [-j\pi D/c f(\epsilon_r(f)-1)]$$

$$\times \exp [\pi D/c f\epsilon_i(f)] \quad (3.183)$$

In the resonant and non-resonant cases discussed above ϵ_i is negative. Thus the last factor including $\epsilon_i(f)$ causes an attenuation with increasing distance. The real part of the refractive index causes a generally non-linear phase shift with frequency. It may be seen that the attenuation in dB per kilometer and phase shift in radians/kilometer can be expressed as

$$\nu(f) = \frac{2\pi}{\lambda} 10^6 \log_{10} e \cdot \epsilon_i(f) \quad (3.184)$$

$$\theta(f) = -2\pi fD/c - 2\pi fD/c(\epsilon_r(f)-1) \quad (3.185)$$

where λ is in centimeter units.

Bean and Dutton [3.32] present expressions for γ in the case of oxygen at atmospheric pressure and temperature = 293°K:

$$\gamma_1 = \frac{.34}{\lambda^2} \left[\frac{\Delta\nu_1}{\frac{1}{\lambda^2} + \Delta\nu_1^2} + \frac{\Delta\nu_2}{(2 + \frac{1}{\lambda})^2 + \Delta\nu_2^2} + \frac{\Delta\nu_2}{(2 - \frac{1}{\lambda})^2 + \Delta\nu_2^2} \right] \quad (3.186)$$

where λ is the wavelength in centimeters and $\Delta\nu_1 = .018 \text{ cm}^{-1}$ at m^{-1} , $\Delta\nu_2 = .049 \text{ cm}^{-1}$ at m^{-1} .

The attenuation due to water vapor with a humidity of ρ gms/ m^3 at 273°K is given as

$$\gamma_2 = \rho \frac{3.5 \times 10^{-3}}{\lambda^2} \left[\frac{\Delta\nu_3}{(\frac{1}{\lambda} - \frac{1}{1.35})^2 + \Delta\nu_3^2} + \frac{\Delta\nu_3}{(\frac{1}{\lambda} + \frac{1}{1.35})^2 + \Delta\nu_3^2} \right] \quad (3.187)$$

where $\Delta\nu_3 = .087 \text{ cm}^{-1} \text{ atm}^{-1}$.

Figure 3.36 reproduces Fig. 7.1 of [3.32] which shows γ_1 and γ_2 as a function of frequency. Note that in the 4 - 10 GHz range the attenuation due to water vapor is small compared to that due to oxygen, at least for the representative value of humidity quoted. Moreover one may readily find by examination of (3.185) that the first term in (3.185), the non-resonant term, is dominant in the 4 - 8 GHz range. Thus as far as the attenuation due to atmospheric gases are concerned we need concern ourselves only with the non-resonant term in the complex dielectric

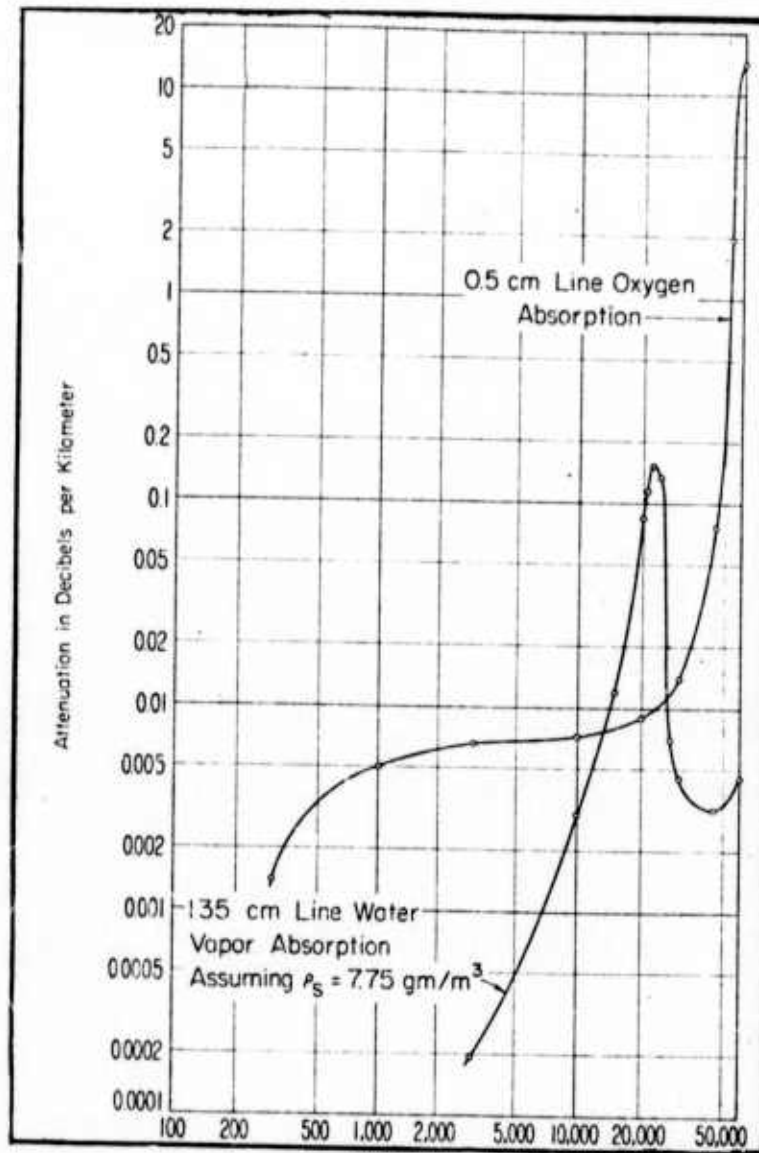


Figure 3.36 Atmospheric Absorption by the 1.35 cm Line of Water Vapor and the 0.5 cm Line of Oxygen

constant of oxygen. A similar study of phase variation reveals that the non-resonant term is dominant also. Thus we use this non-resonant term only, to characterize the atmospheric filter.

The constants in (3.174) can be found by comparing the attenuation computed from (3.176) and (3.184) with the first term in (3.186). The result is

$$\epsilon(f) = \frac{.125 \times 10^{-6}}{1 + \frac{j}{(.018)(\lambda)}} \quad (3.188)$$

Computation of attenuation and nonlinear phase change over the entire 4 - 10 GHz band for a 320 km path utilizing (3.188) reveals only a fraction of a dB and a fraction of a degree change. One may conclude that atmospheric gases can produce no frequency selective limitation on the utilization of high baud rate PN carriers in the 4 - 10 GHz band.

We turn our attention now to the case of heavy rainfall. This case has been studied in detail by Crane [3.33], [3.34] and we need only quote his results. He used two models of rain volume, one representative of heavy rain and the other of extremely heavy rain because he anticipated correctly that only at the extreme rain rates would pulse distortion be perceptible. He found that the primary effect of rain scattering was attenuation. His summary statement on distortion is, "At very large bandwidths, greater than 2 GHz, pulse lengthening gets to be larger than 2 percent for frequencies in the 4.0 to 15.5 GHz range for rain rates in excess of 196 mm/hr and propagation distances of the order of the largest distance possible in heavy rain storms."

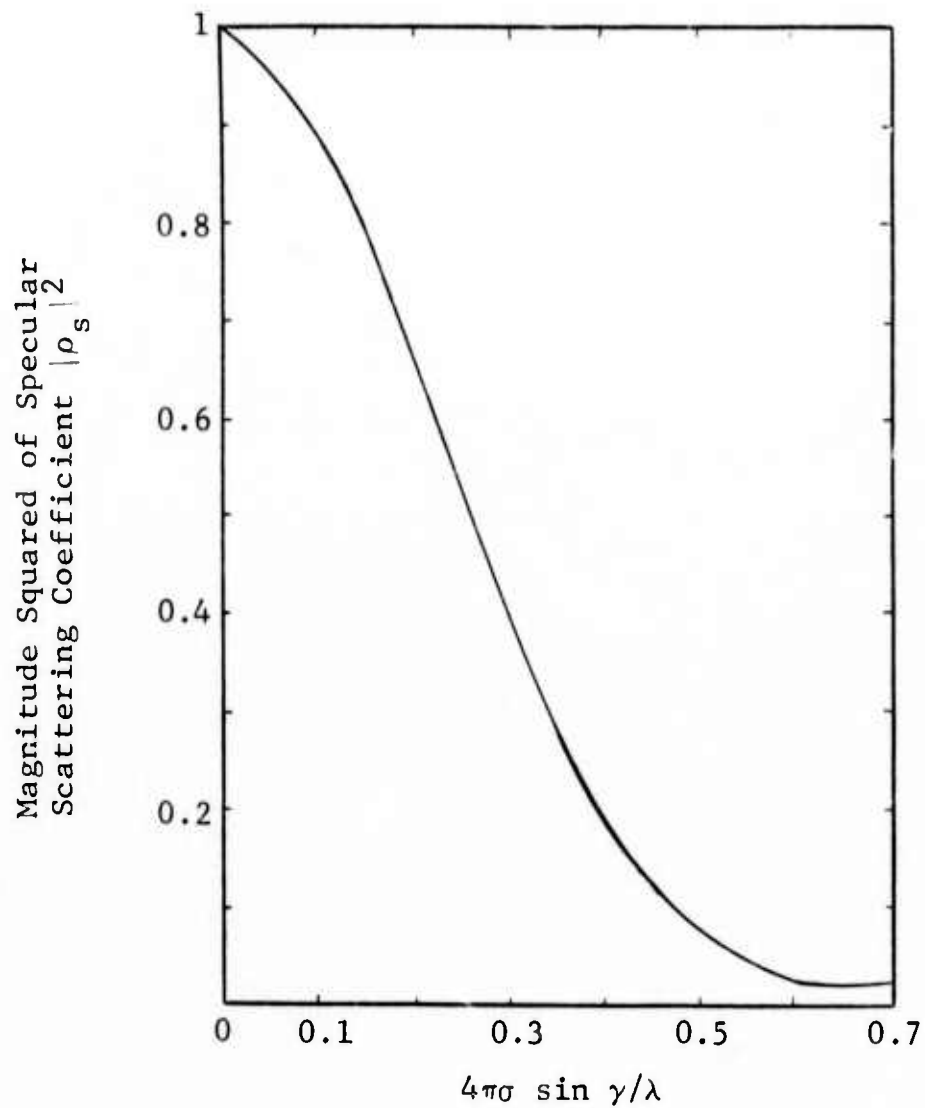
We conclude from this section that frequency selectivity of the atmospheric filtering channel (including atmospheric gases and rain) does not pose a limitation to high baud rate PN carrier transmission.

3.5 Surface Scatter and Reflection Channel

In this section the multipath characteristics of ground reflected signals is presented. The worst-case multipath is expressed in terms of the specular scattering coefficient, ρ_s , which is shown in Fig. 3.37. From the normalized delay curves shown in Fig. 3.38, it is evident that for some RCV flight paths, the specular-to-direct path delay difference may be well within a chip width. It is further shown that the ground terminal may successfully discriminate against this specular component with antenna beamwidths less than about 4° (see Fig. 3.39 and Table 3-10). A normalized Doppler curve is given in Fig. 3-40.

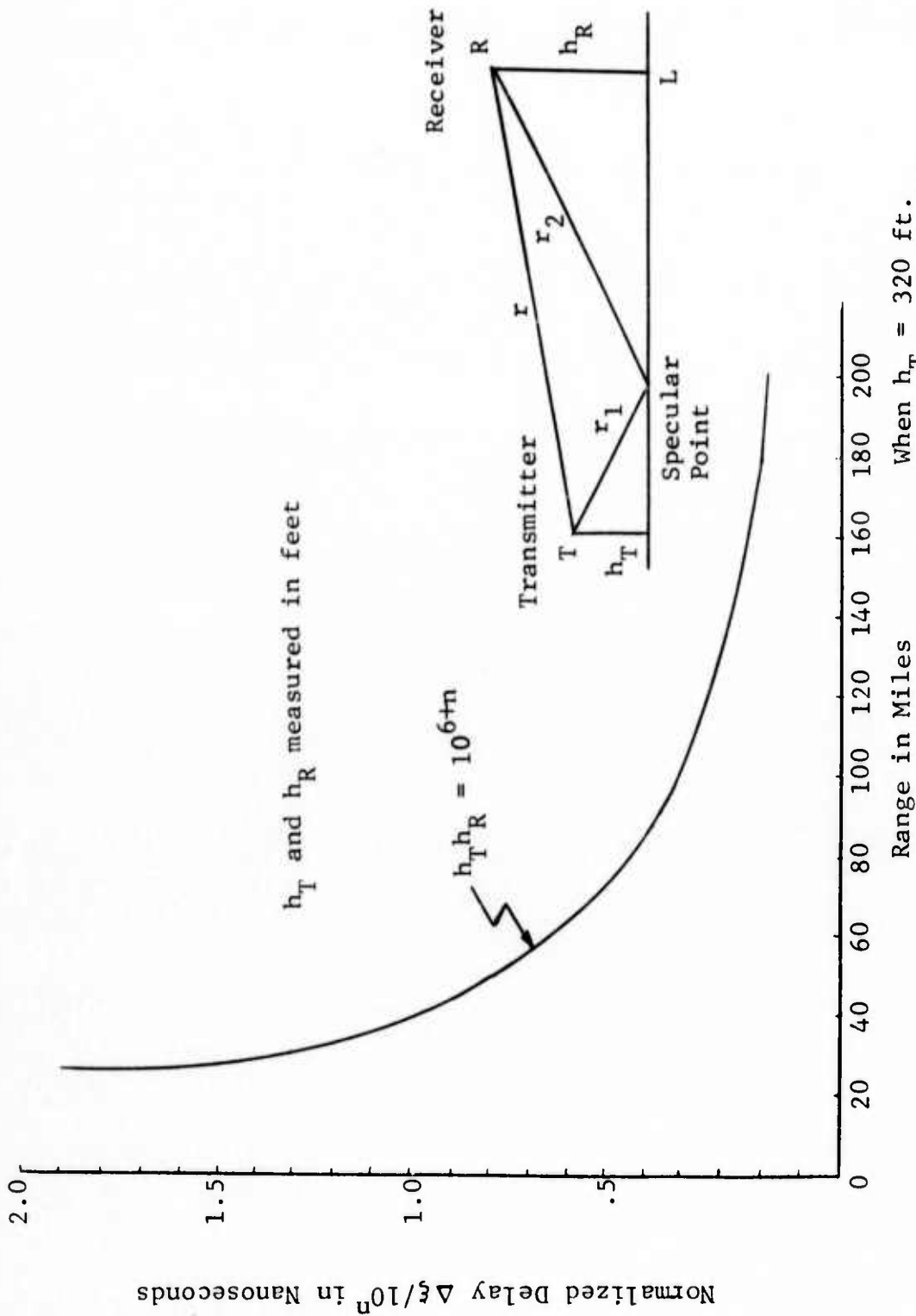
3.5.1 Propagation Modeling

Insofar as the characterization of ground reflected multipath is concerned, the surface of the earth can be modeled as a two-dimensional random process. The signal scattered from this random dielectric interface has a specular and diffuse component. The specular component describes the mean signal strength, while the diffuse component characterizes the fluctuations about this mean. (See Appendix J for precise definitions of these two components.) The specular power is concentrated at a single delay, while the diffuse power is



σ = standard deviation of surface height fluctuations
 γ = grazing angle
 λ = wavelength of carrier

Figure 3.37 Specular Scattering Coefficient Vs. Apparent Surface Roughness (taken from [3.38])



When $h_T = 320$ ft.
 and $h_R = 32,000$ ft.
 $\Delta\xi = 10$ nanosec @ 38 miles

$$\Delta\xi = \frac{1}{c} (r_1 + r_2 - r) \approx \frac{2h_T h_R}{cL}$$

When $h_T = 10^2$ ft.
 and $h_R = 10^4$ ft.
 $\Delta\xi = 1$ nanosec @ 38 miles

Figure 3.38 Specular Delay as a Function of Height and Range

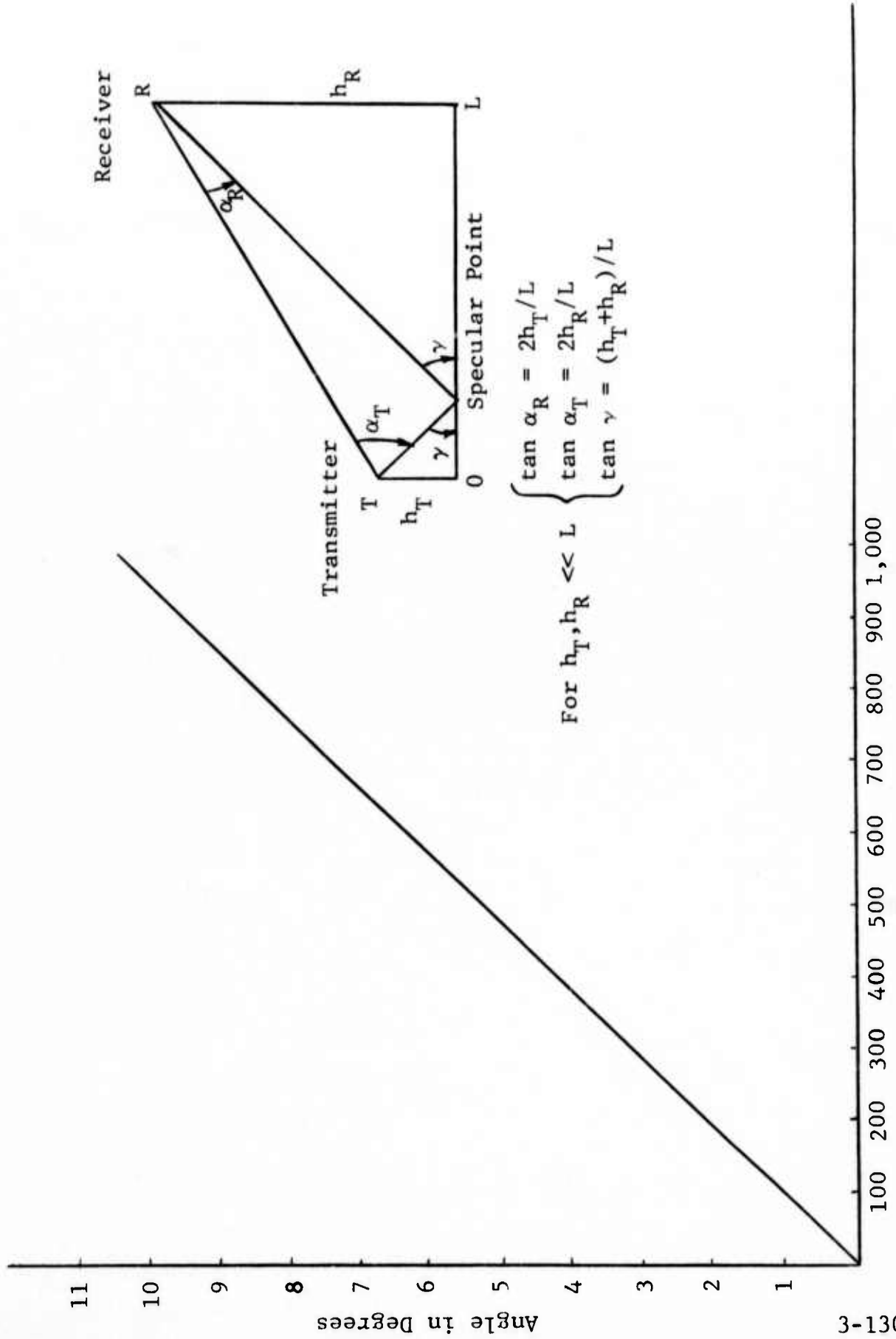


Figure 3.39 Elevation and Grazing Angles as a Function of Height and Range

Table 3-10
 ANTENNA BEAMWIDTH NECESSARY TO DISCRIMINATE
 AGAINST SPECULAR GROUND MULTIPATH

Aircraft Height Feet	Ground Antenna Beamwidth in Degrees		
	Range = 200 Miles	Range = 100 Miles	Range = 50 Miles
1,000	*	*	*
5,000	*	*	4
10,000	*	4	8
30,000	6.4	13	27
60,000	13	27	55

* Aircraft in earth shadow zone (standard atmosphere).

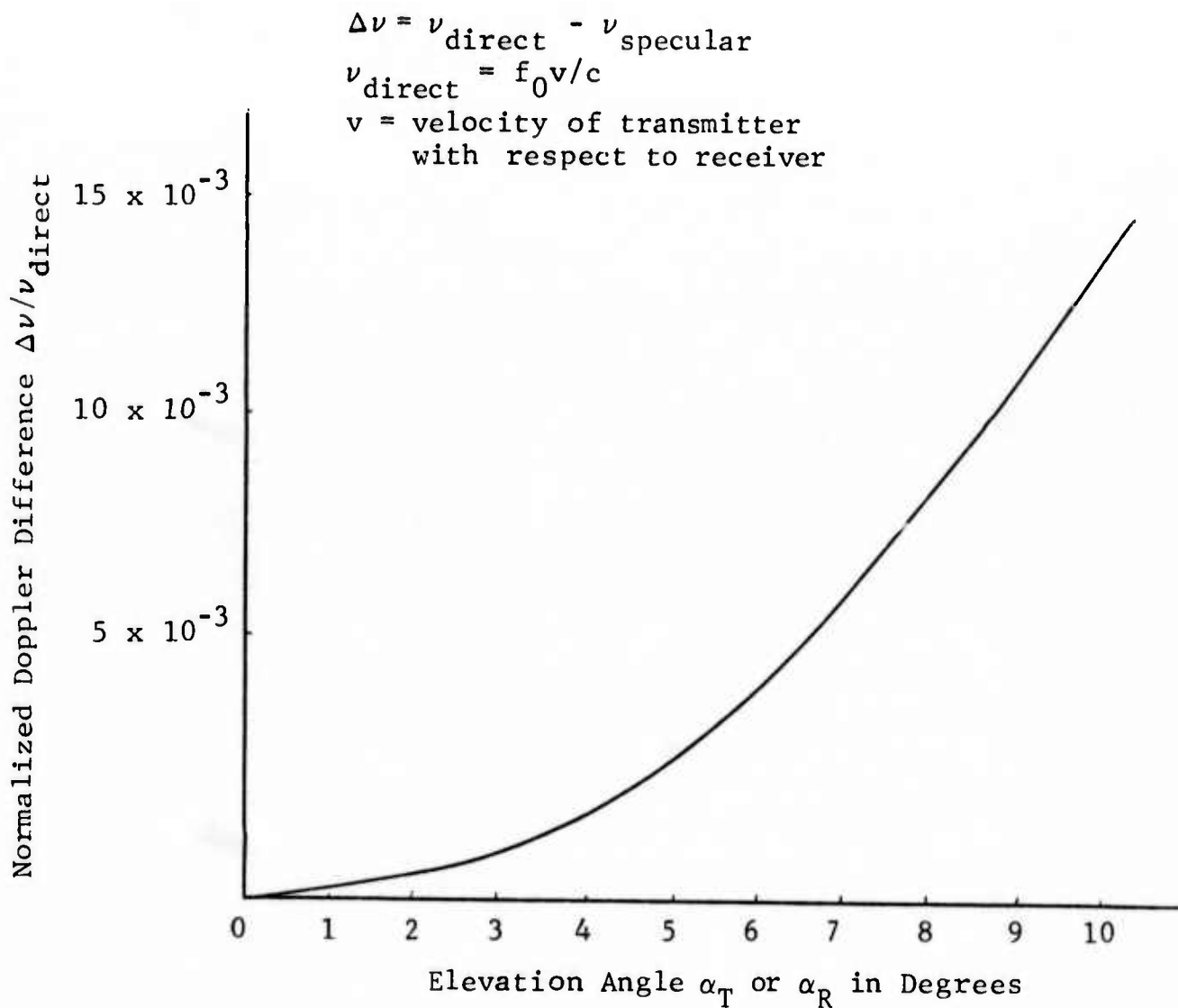


Figure 3.40 Doppler Shift as a Function of Elevation Angle

distributed over a range of delays greater than the specular delay. Since the spread spectrum receiver discriminates against larger delays, the diffuse power tends to be rejected by the properties of the PN signaling scheme. Moreover, as the grazing angles of the incident and scattered radiation decreases, the earth appears to be smoother. At the low grazing angles such as those encountered in LOS links, the specular component predominates. Therefore, due to both the receiver characteristics and the low grazing angles of the LOS links under study, the specular component of the scattered signal is the predominant effect in determining system performance.

The specular reflection coefficient R_s is given by the ratio of the specular reflected field strength to the incident field strength; for a smooth surface R_s is defined by

$$(R_s)_{\text{smooth}} = \frac{(E_{\text{sp}}^r)_{\text{smooth}}}{E^i} \quad (3.189)$$

When the scattering surface is a perfectly conducting, smooth plane, R_s equals unity, and when it is finitely conducting, R_s

is the appropriate Fresnel reflection coefficient R_H or R_V (for horizontal or vertical polarization). When the surface is a smooth sphere with radius much greater than a wavelength, a geometric optics approximation to the scattered fields can be obtained by modifying the Fresnel reflection coefficients by a divergence factor D ,

$$R_s = DR_{H,V} \quad (3.190)$$

where

$$D = \left[\left(1 + \frac{2r_1 r_2}{a(r_1 + r_2) \sin \gamma} \right) \left(1 + \frac{2r_1 r_2}{a(r_1 + r_2)} \right) \right]^{-1/2} \quad (3.191)$$

The extension of these relationships has been provided by Beckmann and Spizzichino [3.3] for a perfectly conducting rough surface

$$(R_s)_{\text{rough}} = \frac{(E_{sp}^r)_{\text{rough}}}{E^i} = \rho_s (R_s)_{\text{smooth}} \quad (3.192)$$

where

$$\rho_s = \frac{(E_{sp}^r)_{\text{rough}}}{(E_{sp}^r)_{\text{smooth}}} \quad (3.193)$$

A heuristic argument which extends the use of Eq. (3.192) to finitely conducting surfaces is presented in [3.3]. This extension is not theoretically well founded (see the discussion

in Appendix K of this report), and the degree to which it becomes a reasonable approximation is not presently known. However, since the maximum value of the reflection coefficient occurs when the surface is perfectly conducting, this represents worst case (maximum power) multipath. The reflection coefficients for the various surfaces are summarized in Table 3-11.

For a normally distributed, perfectly conducting surface with a Gaussian shaped correlation function ρ_s is given by [3.3]

$$\rho_s = \exp (-g/2) \quad (3.194)$$

where g is a roughness factor equal to

$$g = (4\pi\sigma \sin \gamma/\lambda) \quad (3.195)$$

and σ , γ and λ are the standard deviation of the surface, the grazing angle, and the wavelength, respectively. If the transmitted field has an amplitude E_0 , then the field incident on the surface is E_0/r_1 . Now the scattered field above the surface is $E_0\rho_s D/r_1$, and the received field is $E_0\rho_s D/r_1 r_2$. The amplitude of the direct path signal is E_0/r_{TR} . Therefore, the ratio of the specular power to the direct path power is given by

$$\frac{P_{\text{specular}}}{P_{\text{direct}}} = \left(\frac{r_{TR}}{r_1 r_2}\right)^2 \rho_s^2 D^2 \quad (3.196)$$

Substituting Eqs. (3.191), (3.194) and (3.195) into (3.196) and assuming $\frac{2r_1}{a} \ll 1$ gives

Table 3-11

SUMMARY OF REFLECTION COEFFICIENTS

Surface Characteristic	Mean Surface	Surface Conductivity	Specular Reflection Coefficient R_s	Comments
Smooth surface	Plane	∞	1	Exact theory
		Finite	$R_{H,V}$	Exact theory
	Sphere	∞	D	Geometric optics approximation
		Finite	$DR_{H,V}$	Geometric optics approximation
Rough surface	Plane	∞	ρ_s	Exact theory
		Finite	$\rho_s R_{H,V}$	Heuristic derivation
	Sphere	∞	$\rho_s D$	Geometric optics approximation
		Finite	$\rho_s DR_{H,V}$	Heuristic derivation and geometric optics approximation

R_H reflection coefficient for horizontal polarization

R_V reflection coefficient for vertical polarization

D divergence coefficient

ρ_s specular scattering coefficient

$$\frac{P_{\text{specular}}}{P_{\text{direct}}} = \left(\frac{r_{\text{TR}}}{r_1 r_2}\right)^2 \frac{\exp [-(4\pi\sigma \sin \gamma / \lambda)^2]}{\left(1 + \frac{2r_1 r_2}{a(r_1 + r_2) \sin \gamma}\right)} \quad (3.197)$$

It should be noted that this specular to direct power ratio is calculated for a non-fading direct path. However, if the direct path fades (independently of the specular path) then this ratio will be increased accordingly. A graph of the specular reflection coefficient ρ_s as a function of the roughness parameter g is given in Fig. 3.36.

3.5.2 System Function Characteristics

This section examines the relationship between the specular component of a ground reflected signal and the direct path signal for a variety of LOS communication geometries. The specular component is defined in Appendix J, and an integral formulation for this component is presented in Appendix K. It is shown that the mean value of the received signal is not in general proportional to the signal scattered from the mean surface unless the surface conductivity is infinite. It is also shown that small scale surface irregularities do not contribute to the specular component of the received signal. Worst case multipath power calculations are made in section 3.4.1 in terms of the specular scattering coefficient which is shown in Fig. 3.37. The delay difference $\Delta\xi$ between the direct path signal and the specular component is computed in Appendix L. A graph of $\Delta\xi$ as a function of range for various receiver and transmitter heights is shown in Fig. 3.38. Assuming the delay differences of interest are those less than 20 nanoseconds, it is seen that

when the product $h_T h_R$ is less than 10^7 ft^2 , the values of $\Delta\xi$ are less than 20 nanoseconds for ranges between 20 and 200 miles.

The discrimination provided by the antennas against multipath can be determined by comparing the antenna beamwidth to the angle formed by the direct and specular ray. This angle is shown in Fig. 3.39 as a function of range and terminal heights. If half the antenna beamwidth is smaller than the angle between the direct and specular rays, then multipath discrimination will be provided. For example if the beamwidth is 4° ($\frac{B}{2} = 2^\circ$), then when $2h_R/L$ (measured in feet per mile) is greater than 200, the angle between the rays will be greater than 2° , and will therefore attenuate the scattered path. Otherwise, both signals will enter the receiver with little antenna discrimination. The narrowest beamwidths are needed at a range of 200 miles (maximum range). A table of antenna beamwidths necessary to provide discrimination against the specular ground reflected path up to range of 200 miles is shown in Table 3-13 for various aircraft heights and ranges.

The normalized (maximum) Doppler shift between the direct and specular paths is derived in Appendix L and plotted in Fig. 3.40. When the angle between the two rays is 3° , (this is the maximum angle that need be considered for a 6° beamwidth antenna), the Doppler difference is seen to be $1.5 \times 10^{-3} \nu_{\text{direct}}$. For a jet aircraft traveling at 600 miles per hour using a carrier frequency of 10 GHz, $\nu_{\text{direct}} = 8.96 \text{ KHz}$, and the direct to specular Doppler difference is

$$\Delta\nu = 13.4 \text{ Hz} \quad (3.198)$$

SECTION 3
REFERENCES

- [3.1] E. K. Smith and S. Weintraub, "The Constants in the Equation for Atmospheric Refractive Index at Radio Frequencies," Proc. of IRE, Vol. 41, August 1953, pp. 1035-1037.
- [3.2] D. E. Kerr, Propagation of Short Radio Waves, Dover Publications, Inc., New York, 1965.
- [3.3] Beckmann, P., and Spizzichino, A., The Scattering of Electromagnetic Waves From Rough Surfaces, Pergamon Press, Ltd., 1963.
- [3.4] F. Ikegami, "Influence of an Atmospheric Duct on Microwave Fading," IRE Trans. on Antennas and Propagation, July 1959, pp. 252-257.
- [3.5] M. S. Wong, "Refraction Anomalies in Airborne Propagation," Proc. of IEEE, Vol. 46, pp. 1628-1638, September 1958.
- [3.6] N. W. Guinard, et al., "Propagation Through an Elevated Duct: Tradewinds III," IEEE PGAP, July 1964, pp. 479-490.
- [3.7] Bean, B. R., and Dutton, E. J., Radio Meteorology, National Bureau of Standards Monograph 92, March 1, 1966.
- [3.8] Bean, et al., "A World Atlas of Atmospheric Radio Refractivity," Essa Monograph No. 1, U.S. Government Printing Office, Washington, D.C., 1966.
- [3.9] H.T. Dougherty, "A Survey of Microwave Fading Mechanisms Remedies, and Applications," Essa Technical Report ERL 69-WPL4, U.S. Government Printing Office, Washington, D.C., March 1968.
- [3.10] E. E. Gossard, "The Reflection of Microwaves by a Refractive Layer Perturbed by Waves," IEEE Trans. on Antennas and Propagation, May 1962, pp. 317-325.

- [3.11] C. C. Watterson, J. R. Juroshek, and J. L. Demmer, "SHF Bandwidth Study, Phase III," NBS Report 8842, U.S. Department of Commerce, NBS, Boulder, Colorado.
- [3.12] M. C. Thompson, Jr., H. B. Janes, L. E. Wood, and D. Smith, "Phase and Amplitude Scintillations of Microwave Signals Over an Elevated Atmospheric Path," Report of NASA Contract Order No. 1-31028, ITS, Boulder, Colorado, May 10, 1971.
- [3.13] H. Riehl, Tropical Meteorology, McGraw-Hill Book Co., Inc., New York, New York, 1954.
- [3.14] G. A. Deschamps, "Ray Techniques in Electromagnetics," Proc. of IEEE, Vol. 60, No. 9, September 1972, pp. 1022-1035.
- [3.15] C. L. Ruthroff, "Multiple-Path Fading on Line-of-Sight Microwave Radio Systems as a Function of Path Length and Frequency," BSTJ, Vol. 50, No. 7, September 1971, pp. 2375-2398.
- [3.16] V. I. Tatarski, Wave Propagation in a Turbulent Medium, New York, McGraw-Hill, 1961.
- [3.17] C. M. Crain, "Survey of Airborne Microwave Refractometer Measurements," Proc. of the IRE, October 1955, pp. 1405-1411.
- [3.18] D. T. Gjessing, "Atmospheric Structure Decoded From Forward Scatter Wave Propagation," Report E-148, Norwegian Defense Research Establishment, April 1968, p. 6.
- [3.19] Muchmore and Wheelon, "Line-of-Sight Propagation Phenomena-I Ray Treatment," Proc. IRE, October 1955, p. 1448.
- [3.20] C. M. Crain, A. W. Straiton, and C. E. vonRosenberg, "A Statistical Survey of Atmospheric Index-of-Refraction Variation," Trans. IRE, Vol. AP-1, pp. 43-46, October 1953.

- [3.21] R. K. Crane, "Microwave Scattering Parameters for New England Rain," Lincoln Lab. Technical Report No. 426, October 3, 1966.
- [3.22] D. E. Kerr, Propagation of Short Radio Waves, Dover, 1965, Chapter 2.
- [3.23] H. C. Booker and W. E. Gordon, "A Theory of Radio Scattering in the Troposphere," Proc. IRE, Vol. 38, pp. 401-412, April 1950.
- [3.24] A. D. Wheelon, "Radio-Wave Scattering by Tropospheric Irregularities," J. Res. Nat. Bur. Stand., Section D, Radio Prop., Vol. 63D, pp. 205-232, September-October, 1959.
- [3.25] R. B. Muchmore and A. D. Wheelon, "Line-of-Sight Propagation Phenomena, Ph. II Scattered Components," Proc. IRE, Vol. 43, pp. 1450-1458, October 1955.
- [3.26] R. B. Muchmore and A. D. Wheelon, "Frequency Correlation of Line-of-Sight Signal Scintillations," IEEE Trans. on Antennas and Propagation, Vol. AP-11, pp. 46-51, January 1963.
- [3.27] P. A. Bello, "A Study of the Relationship Between Multipath Distortion and Wavenumber Spectrum of Refractive Index in Radio Links," Proc. IEEE, Vol. 59, No. 1, January 1971, pp. 47-75.
- [3.28] P. A. Bello, "Characterization of Random Time-Variant Linear Channels," IRE Trans. on Comm. Systems, Vol. CS-11, pp. 360-393, December 1963.
- [3.29] R. K. Crane, "Propagation Phenomena Affecting Satellite Communication Systems Operating in the Centimeter and Millimeter Wave Bands," Proc. IEEE, Vol. 59, No. 2, February 1971, pp. 173-188.
- [3.30] R. K. Crane, "Virginia Precipitation Scatter Experiment-Data Analysis," to be published by NASA Goddard Space Flight Center.

- [3.31] D. E. Kerr, Propagation of Short Radio Waves, Section 8, Dover, 1965.
- [3.32] B. R. Bean and E. J. Dutton, Radio Meteorology, National Bureau of Standards Monograph 92, March 1, 1966, p. 272.
- [3.33] C. R. Crane, "Coherent Pulse Transmission by Rain," IEEE Trans. on Antennas and Propagation, Vol. AP-15, No. 2, March 1967, pp. 252-256.
- [3.34] C. R. Crane, "Coherent Pulse Transmission by Rain," Lincoln Lab. Technical Report 1966-63, 27 December 1966.
- [3.35] C. M. Beamer, et al., An Investigation of Airborne Microwave MARCOM Relay, Final Report No. SEG-TR-66-31, Vol. II, Contract No. AF 33(615)-1900, Prepared for Wright-Patterson Air Force Base, Ohio by Collins Radio Co., Dallas, Texas.
- [3.36] J. K. DeRosa, The Characterization of Multipath and Doppler Fading in Earth Scatter Communication, Navigation, and Radar Links, Ph.D. Thesis, Northeastern University, Department of Electrical Engineering, Boston, Mass., 1972.
- [3.37] A. A. Kovalev and S. I. Pozdnyak, "The Scattering of Electromagnetic Waves by Statistically Rough Surfaces With Finite Conductivity," Radiotekhnika, Vol. 16, pp. 31-36, 1961.
- [3.38] H. Berger and J. E. Evans, "Diversity Techniques for Air-Borne Communications in the Presence of Ground Reflection Multipath," Technical Note No. 1972-27, Lincoln Labs., MIT, September 1972.
- [3.39] ITT Reference Data for Engineers, H. W. Sames & Co., New York, 1972, pp. 25-26.
- [3.40] O. E. DeLange, "Propagation Studies at Microwave Frequencies by Means of Very Short Pulses," BSTJ, January 1952, pp. 91-103.

- [3.41] L. H. Doherty, "Geometric Optics and the Field at a Caustic," Ph.D. Dissertation, Dept. of E.E., Cornell University, Ithaca, New York, 1952.
- [3.42] G. A. Deschamps, "Ray Techniques in Electromagnetics," Proc. of IEEE, Vol. 60, No. 9, September 1972, pp. 1022-1035.

SECTION 4

PERFORMANCE EVALUATION

This section discusses the work carried out on the evaluation of the effects of multipath on RCV spread spectrum modems. The rationale for the method of approach adopted is presented in Section 4.1. Section 4.2 presents error probability results as families of curves of error probability as a function of SNR, with the indexing parameters being the multipath spread relative to a chip width and the relative strengths of paths. The spread spectrum modem analyzed is presented in Section 4.3. The details of the analysis leading to the computer programs for predicting error rate performance are presented in Sections 4.4 and 4.5. Section 4.6 presents and analyzes a two-channel receiver which gives substantially improved performance under multipath conditions.

4.1 Method of Approach

In order to evaluate the performance of an RCV spread spectrum modem in the presence of refractive multipath we clearly need mathematical models of both the input-output behavior of the propagation medium and the modem operation. In the analysis we have assumed a coherent RCV modem utilizing a binary PSK spread spectrum carrier upon which is superimposed a binary PSK data signal. While this is the simplest possible such modem, it appears to be of considerable practical interest because of the appearance of high speed logic which can produce spread spectrum signals of hundreds of megahertz bandwidth.

Section 3 has examined the various propagation phenomena in the 4 - 10 GHz band relevant to limitations on high chip rate PN carrier transmission. As a result of this examination it

may be concluded that discrete multipath presents the most serious form of system degradation when two or more paths have delays less than the width of the PN carrier autocorrelation function. The relative phase shift of the multipath components varies much more rapidly than their relative amplitude as a function of aircraft position. In the 4 - 10 GHz range the wavelengths are sufficiently small that many multiples of 2π radians relative phase shift will frequently occur with aircraft flight in regions where multipath exist. Thus a simple, but useful multipath model for evaluating error rates on a short-term basis involves the assumption of random uniformly distributed phases for a fixed set of path amplitudes. A canonic case of interest is the two-path model with random phased paths. While the succeeding sections formulate error rate expressions for N-paths, actual numerical evaluations are carried out for two paths.

It should be recognized from the results of Section 3.2 that the troublesome refractive multipath presents a highly nonstationary statistical phenomena. From the results of Section 3.2 one may actually estimate the time variant multipath structure associated with a given layer and link geometry as a function of aircraft position. Characteristic patterns for this multipath structure were noted in Section 3.2. The computer programs developed here may be used in conjunction with these patterns to predict error burst behavior as a function of aircraft position. It has already been noted that a refractive multipath component can build up sufficient strength to "steal" the tracking loops. Moreover the delay separation between the multipath component and direct path can build up to more than a PN correlation width. As a result, if the multipath component vanishes, as can happen for some geometries, a loss of lock of the locally generated PN carrier system can occur. Such

behavior can be understood by examining the performance of the PN carrier system for the two-path model evaluated here.

4.2 Effect of Multipath on RCV Spread Spectrum Receiver

The following sections analyze the effect of multipath on a spread-spectrum receiver. The most significant outcome of this detailed analysis is the ability to draw a curve of error probability versus signal-to-noise ratio applicable to any desired multipath condition. A representative collection of error probability curves for the case of two-path propagation is given in Figs. 4.1 through 4.5. Before discussing these results we will briefly review the assumptions under which they were derived. For the details of the derivation the reader is referred to subsequent sections.

The discrete-path channel has been discussed in detail earlier in this report. For the present analysis we have assumed binary PSK modulation and a received signal of the form

$$s(t) = \sum_{n=1}^N \alpha_n m(t-t_n) \cos(\omega_c t + \theta_n) + n(t) \quad (4.1)$$

With each of the N propagation paths there is associated an amplitude α_n , delay t_n , and phase θ_n . The composite modulation (data and pseudo-random sequence) is $m(t)$ and the additive Gaussian noise is $n(t)$. In analyzing the behavior of the receiver we have assumed that the path strengths α_n are fixed while the phases θ_n are slowly varying. As a result, the receiver is able to track the received signal of Eq. (4.1) at all times; for any set of parameters $\{\alpha_n, \theta_n\}_{n=1}^N$ there corresponds an instantaneous error probability. However, the only meaningful measure of performance is the average error probability which is obtained by averaging over all values of the phases $\{\theta_n\}_{n=1}^N$.

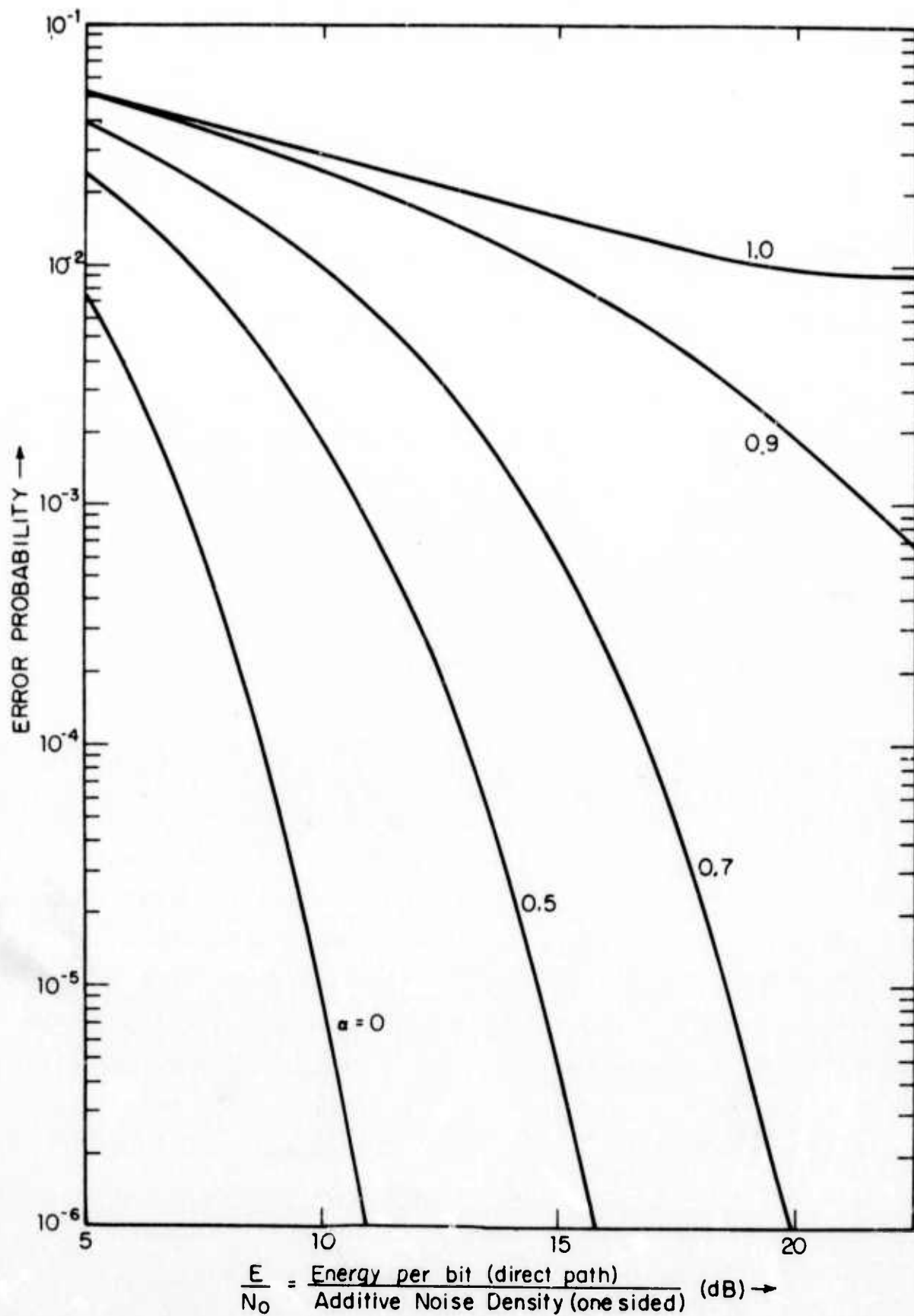


Figure 4.1 Error Probability for Coherent Detection of Spread-Spectrum Binary PSK Data; Two-Path Channel Model, Delay Difference $t_d = 0.0$ Chip, Various Relative Amplitudes α

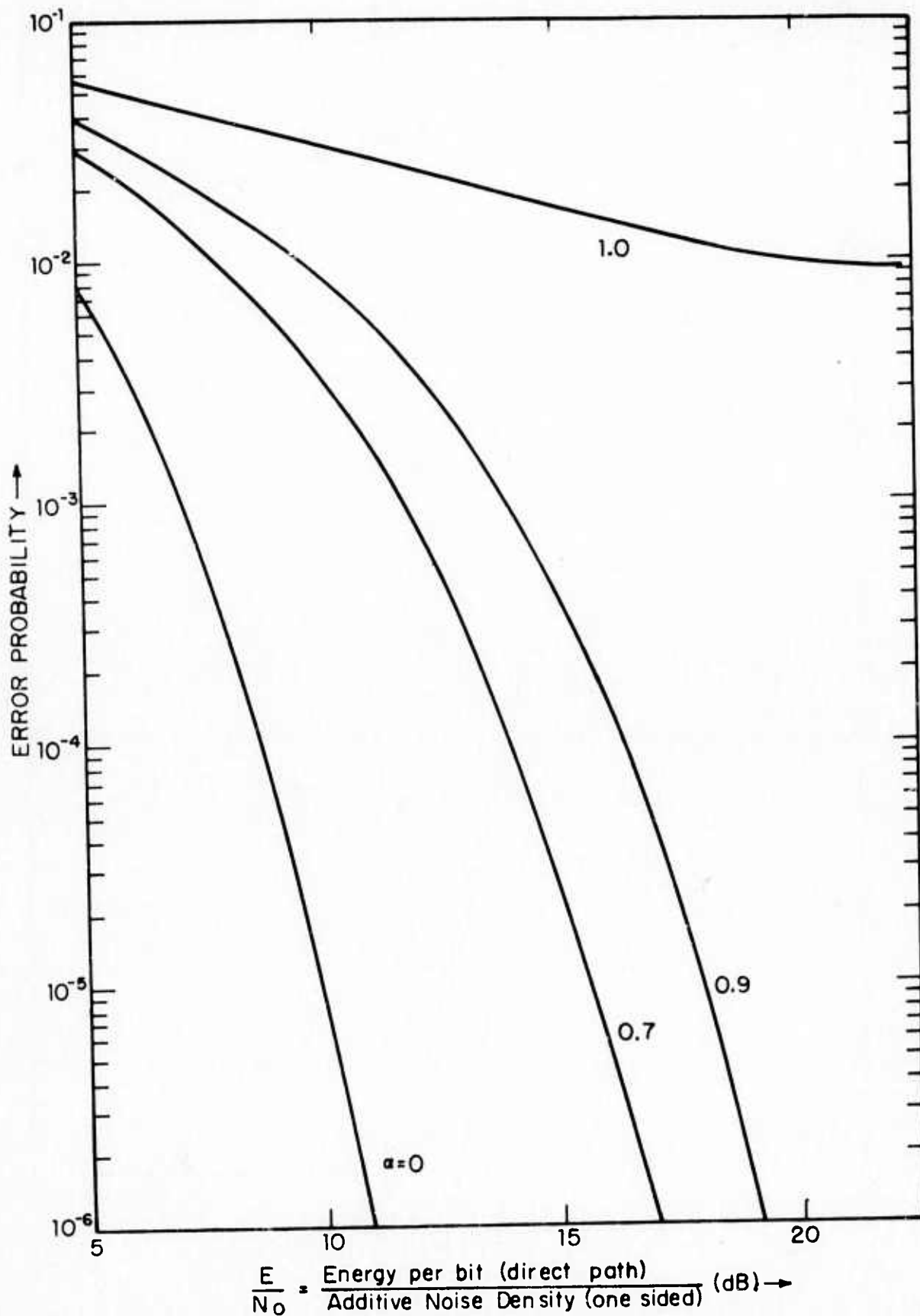


Figure 4.2 Error Probability for Coherent Detection of Spread-Spectrum Binary PSK Data; Two-Path Channel Model, Delay Difference $t_d = 0.25$ Chip, Various Relative Amplitudes α

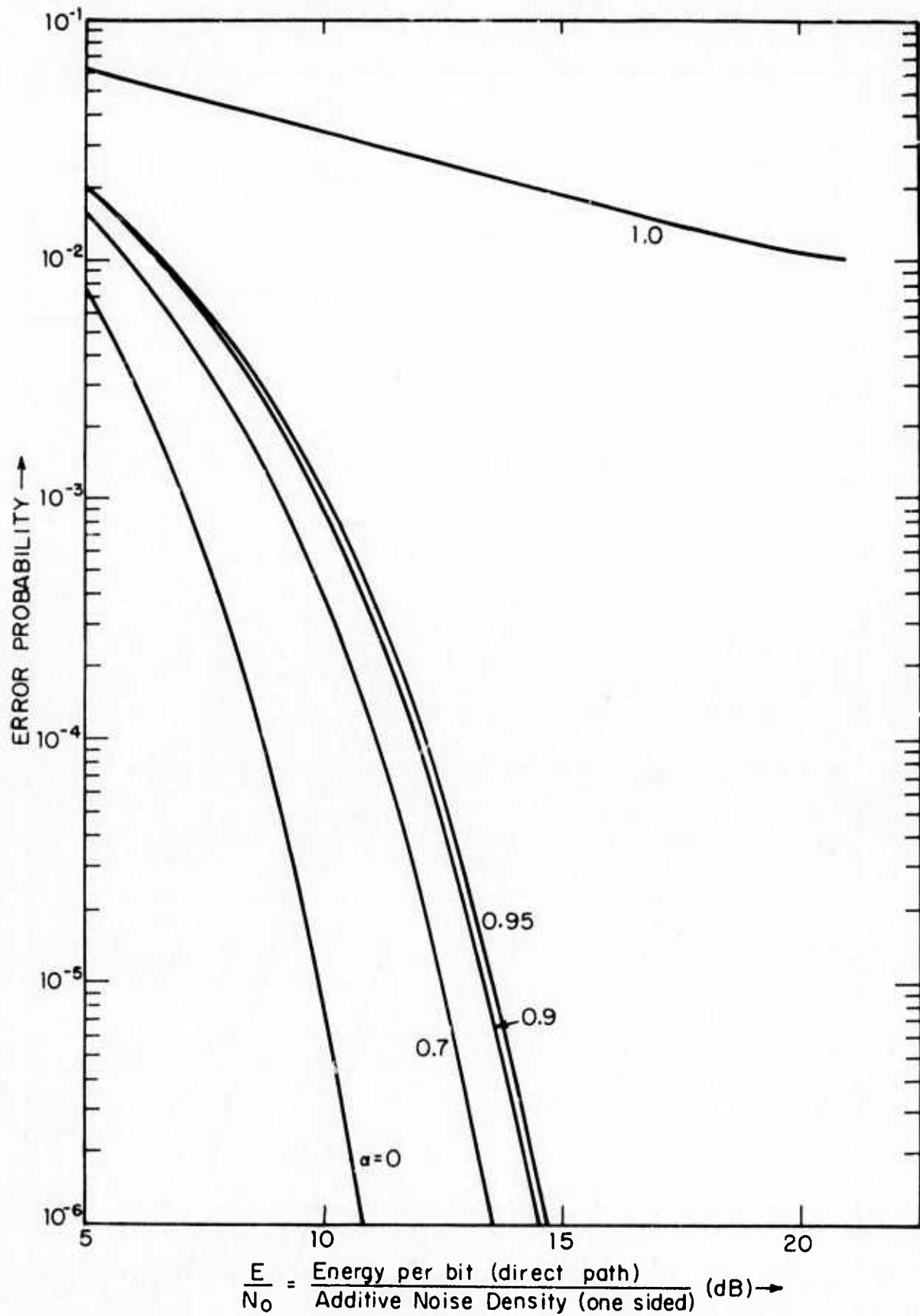


Figure 4.3 Error Probability for Coherent Detection of Spread-Spectrum Binary PSK Data; Two-Path Channel Model, Delay Difference $t_d = 0.50$ Chip, Various Relative Amplitudes α

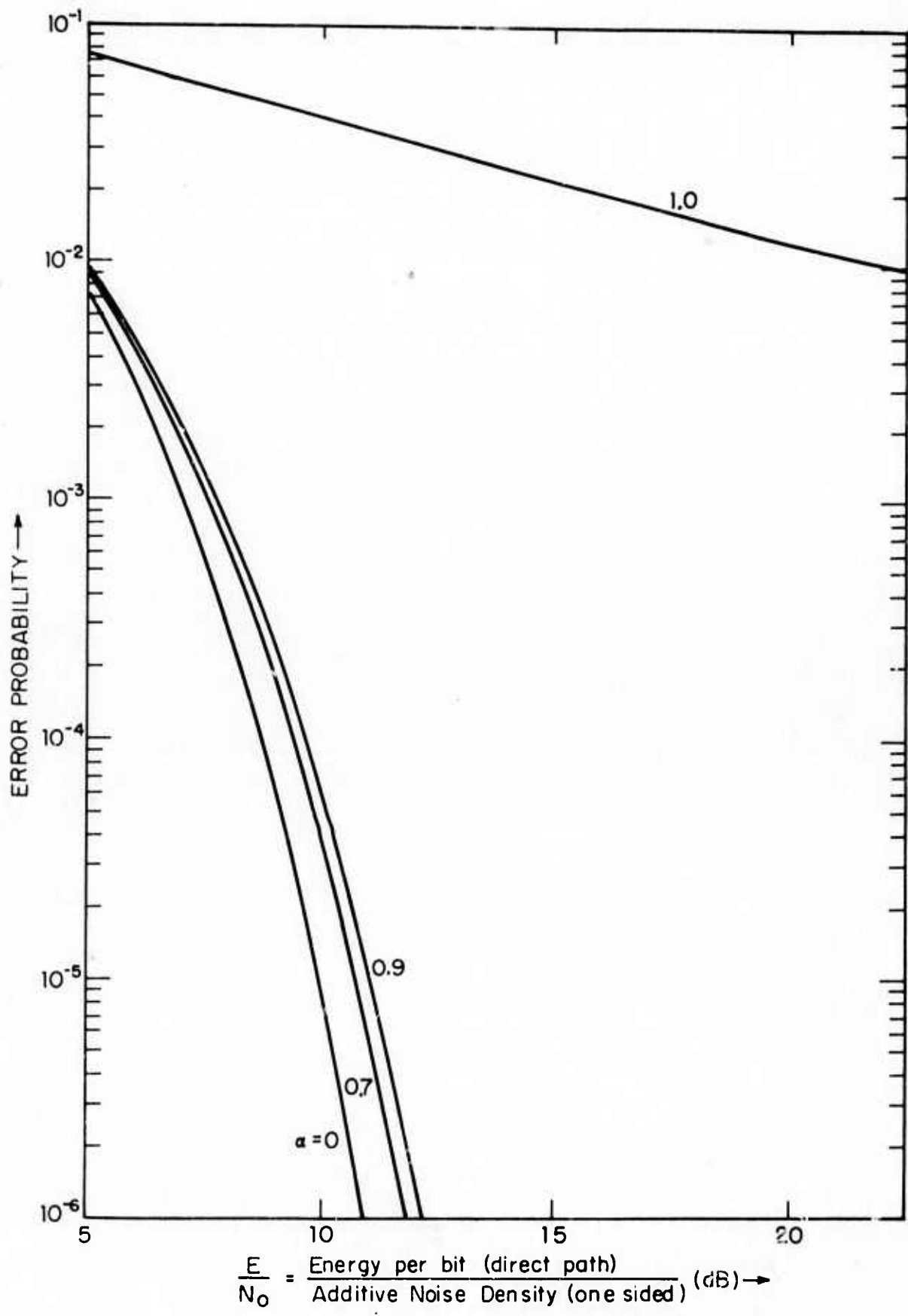


Figure 4.4 Error Probability for Coherent Detection of Spread-Spectrum Binary PSK Data; Two-Path Channel Model, Delay Difference $t_d = 0.75$ Chip, Various Relative Amplitudes α

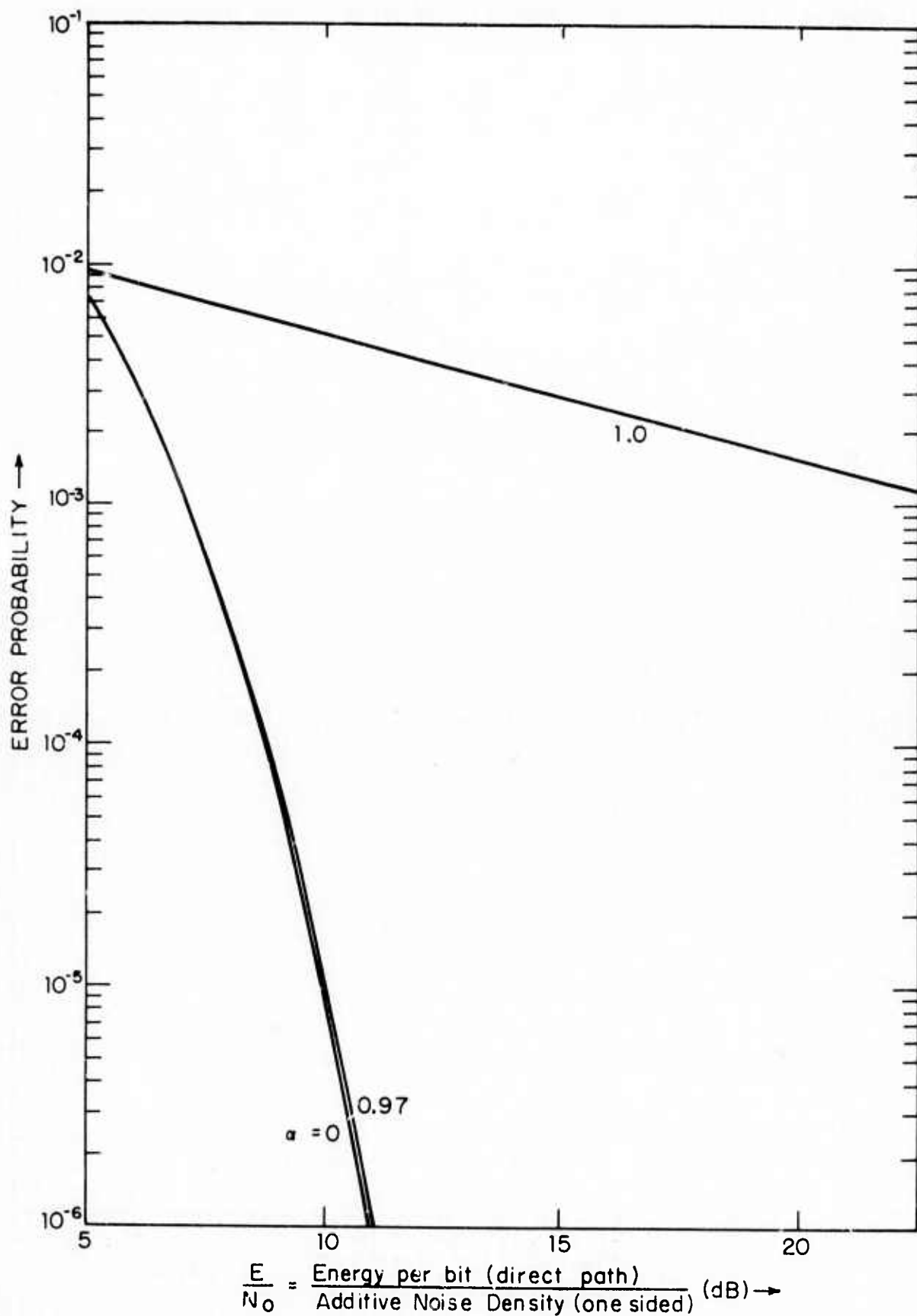


Figure 4.5 Error Probability for Coherent Detection of Spread-Spectrum Binary PSK Data; Two-Path Channel Model, Delay Difference $t_d = 1.0$ Chip, Various Relative Amplitudes α

Although the techniques employed in the analysis are valid regardless of the number of paths N , numerical calculations would be cumbersome for large N because of the necessity for averaging over the N dimensional region defined by

$$0 \leq \theta_n \leq 2\pi \quad n = 1, 2, \dots, N \quad (4.2)$$

Therefore, practical application of this technique is limited to small values of N . However, it is the cases $N=2$ and $N=3$ which were identified in Section 3 as those most likely to occur in an RCV link.

The results to be presented in this section are for the $N=2$ case. In this case we will write the received signal in the more explicit form

$$s(t) = \sqrt{\frac{2E}{T}} [m(t) \cos \omega_c t + \alpha m(t-t_d) \cos (\omega_c t + \theta_m)] + n(t) \quad (4.3)$$

Here, the principal path has energy E over a data bit period T . The second path is delayed t_d seconds and its relative amplitude is α . The slowly varying phases of the two paths are represented by a single relative phase θ_m . The noise is assumed to be white with density $N_0/2$.

The results presented in this section apply only to the specific receiver model analyzed. Details of the receiver model may be found in Section 4.3; briefly, operation is coherent with derived references for both carrier and code.

Any practical receiver will include some bandpass filtering; this will significantly affect performance by changing the shape of the cross-correlation function of the received and local PN sequences. Therefore, the analysis has included the

effect of such filtering. For the examples a Gaussian band-pass filter with 3 dB bandwidth equal to 1.5 times the chip rate was assumed.

Considering the results shown in Figs. 4.1 - 4.5* it is clear that there are many combinations of delay (t_d) and relative amplitude (α) which produce substantial degradation of performance. For zero delay a relative path strength of 0.7 produces a loss of 8 to 9 dB compared to the performance in the absence of the second path ($\alpha=0$). As the delay of the second path is increased, significant degradation is experienced only for greater values of α . However, performance when $\alpha=1$ (equal amplitude signals) is completely degraded for delays up to and including 1.0 chip. When the delay is increased to 1.25 chips, the receiver can distinguish between the two signals and track either without substantial interference from the other. Thus even for $\alpha=1$ the degradation is a small fraction of a dB for $t_d = 1.25$.

The inter-related behavior of α and t_d is illustrated more compactly in Fig. 4.6 which shows the direct-path E/N_0 necessary for an error probability of 10^{-4} . This is plotted against α with t_d as a parameter. One may also interpret Fig. 4.6 as a plot of reduction in spread spectrum processing gain as a function of t_d , α for 10^{-4} error probability by interpreting dB increases in E/N_0 as effective reductions in processing gain.

* See Section 4.5 for analytical formulation of error rate calculation.

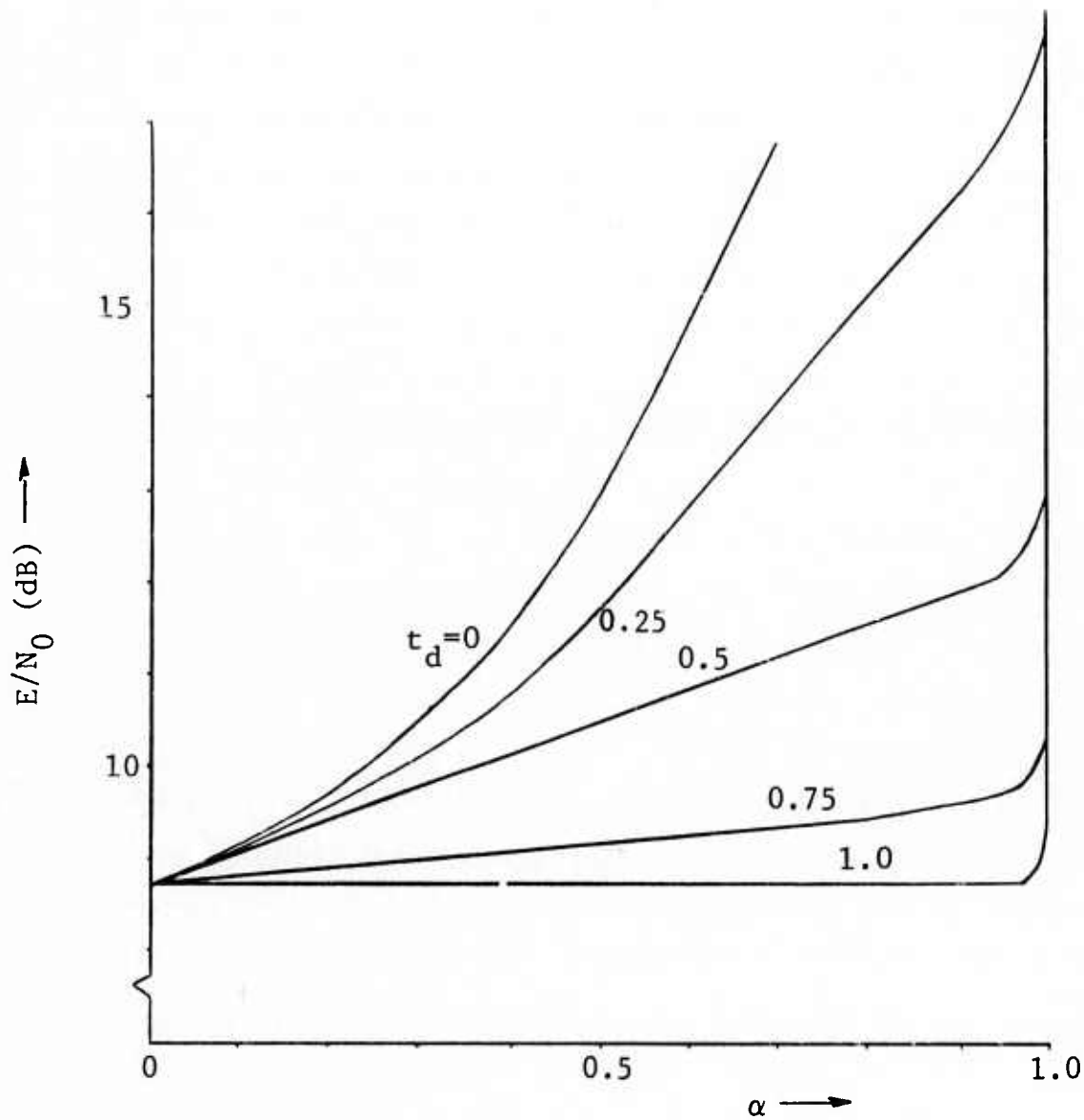


Figure 4.6 E/N_0 Required to Give Error Probability of 10^{-4}

4.3 System Analyzed

An RCV spread-spectrum receiver must contain three fundamental elements: carrier tracking loop, code tracking loop, and data detection circuitry. Additional elements are required for acquisition, but these are not relevant to the present analysis of post-acquisition tracking. The relationship of the three basic elements is shown in Fig. 4.7. The two tracking loops are highly inter-dependent, since the carrier loop supplies a local carrier to the code loop which in turn supplies a local code to the carrier loop. A principal objective of the analysis will be to calculate the behavior of these loops in the presence of multipath. Another important aspect of the system shown in Fig. 4.7 is that a continuous estimate of the data polarity is fed back from the detection unit to both of the loops in order to "wipe-off" the data modulation. If this were not done, the desirable correlation properties of the pseudo-random sequence used to spread the spectrum would be destroyed. In the analysis to follow, we will assume that the estimate fed back to the tracking loop is perfect, so that the correlation properties of the pseudo-random sequence are preserved. In an actual system, the effect of a noisy estimate can be modeled as a reduction in the effective signal strength.

A more detailed block diagram of the coupled tracking loop is shown in Fig. 4.8. For clarity, the "wiping-off" of the data modulation is not shown. This operation could be performed either by phase-reverse-keying the input signal prior to the loop or by phase-reverse keying the VCO output inside the loop.

An understanding of the behavior of the tracking loops may be obtained by considering the simple case of a single-path input signal of the form

$$r(t) \cos \omega_c t$$

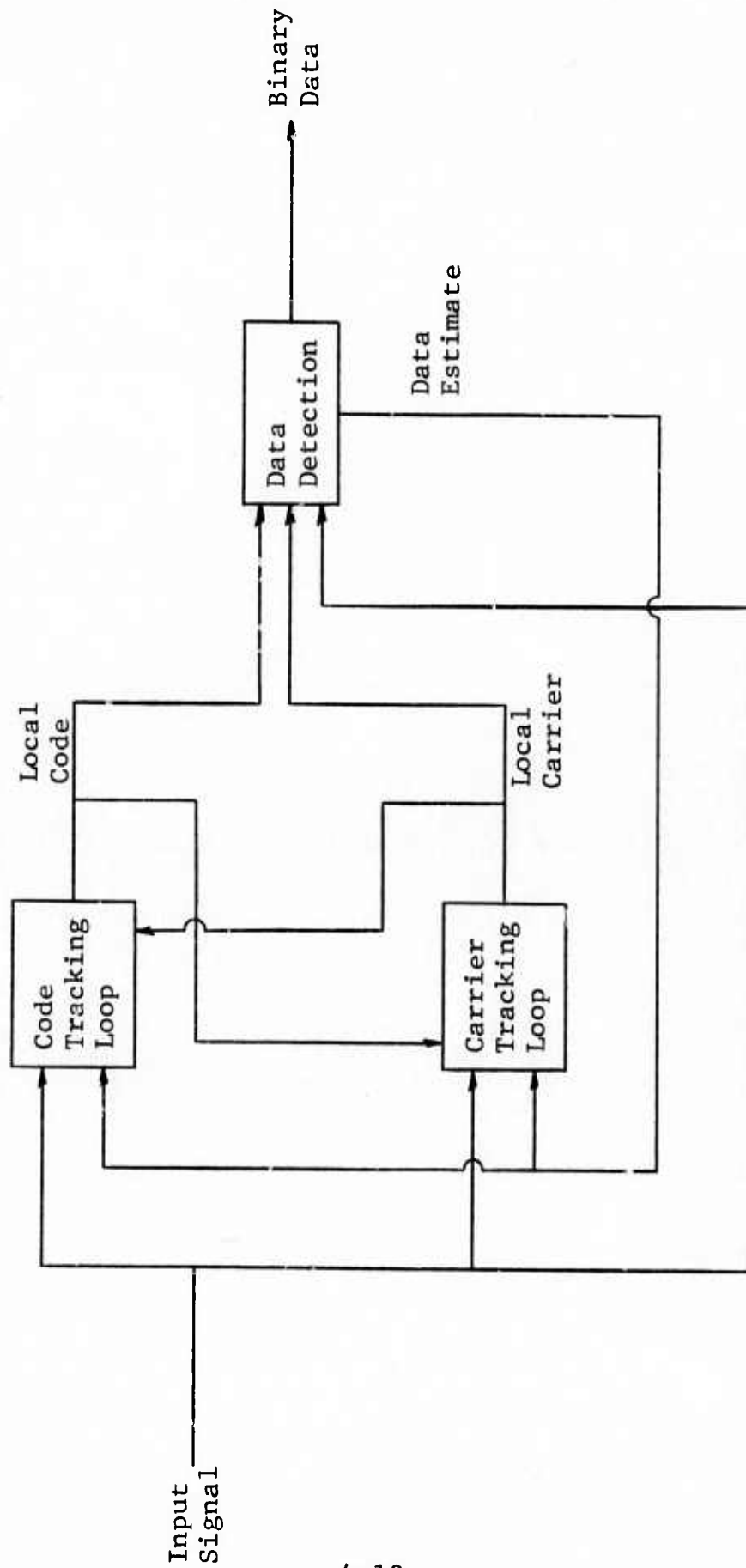


Figure 4.7 Simplified Block Diagram of RCV Spread Spectrum Receiver

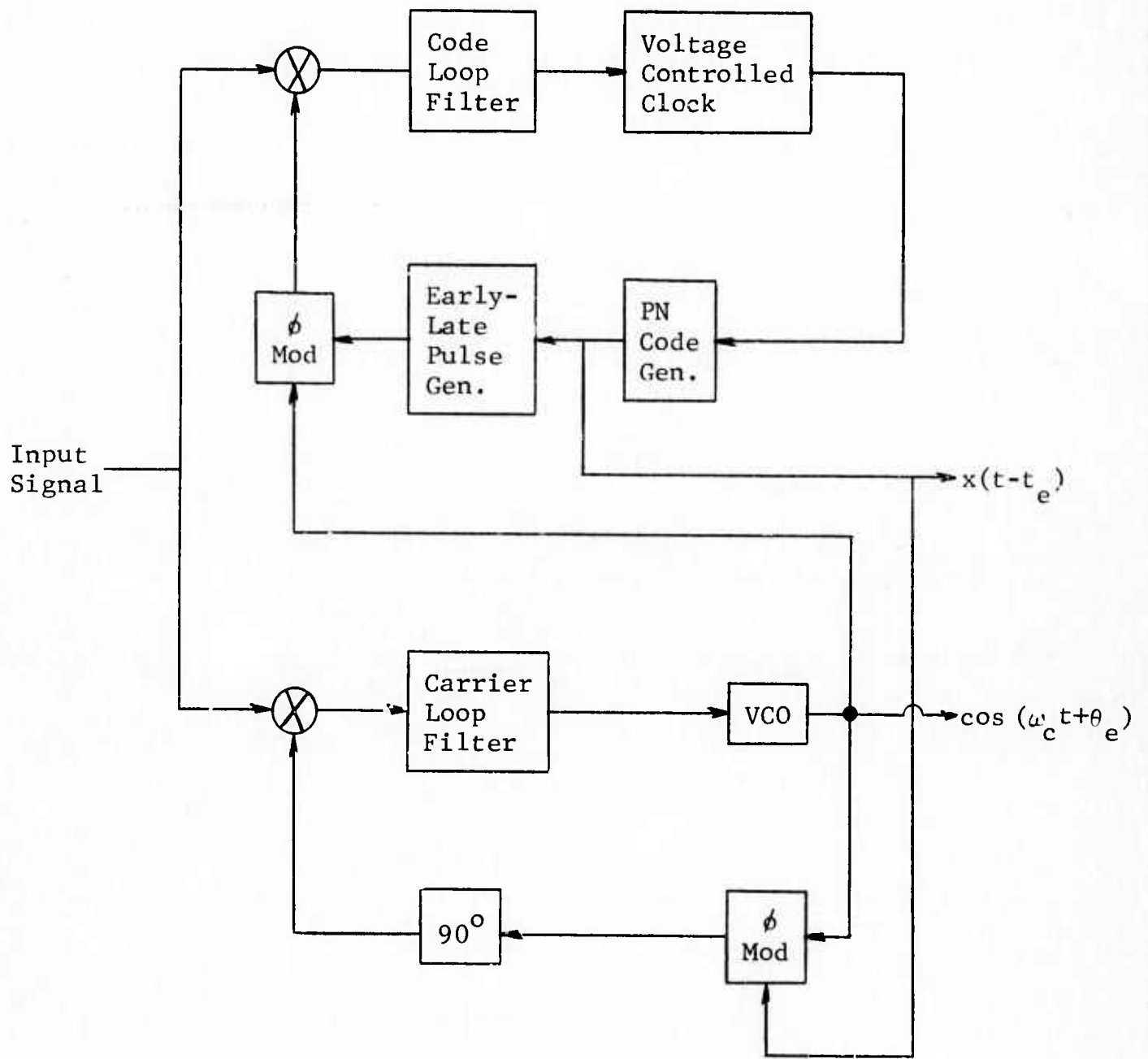


Figure 4.8 Code and Carrier Tracking Loops of a Spread-Spectrum Receiver

where $r(t)$ is the pseudo-random code modulation. In this case the open-loop error voltages appearing in the carrier and code loops are

$$F(t_e, \theta_e) = R(t_e) \sin \theta_e \quad (4.5)$$

and

$$G(t_e, \theta_e) = S(t_e) \cos \theta_e \quad (4.6)$$

where $R(t_e)$ is the correlation function of the received code $r(t)$ and the local code $x(t)$ and $S(t_e)$ is the correlation function of $r(t)$ and the output of the split-pulse generator in the code loop. The phase θ_e and timing t_e which will occur in the closed loops are found by setting $F(t_e, \theta_e)$ and $G(t_e, \theta_e)$ equal to zero and solving the resulting pair of simultaneous equations. For this simple case the solution will be

$$t_e = \theta_e = 0 \quad (4.7)$$

in view of the fact that $S(t_e)$ is an odd function. However, when multipath is present the simultaneous equations obtained by setting $F(t_e, \theta_e)$ and $G(t_e, \theta_e)$ equal to zero will no longer be simple, and must be solved on the digital computer to obtain values of θ_e and t_e . This solution will depend on the amplitude and phase of all signal components present at the receiver. For any such solution the strength of the signal available for data detection may be calculated and used to calculate error probability, as a function of the additive noise level. To obtain the average error probability, the loop equations must be solved for all combinations of input signal phases.

4.4 Formulation of Tracking Analysis

4.4.1 General Formulation

The general multipath signal model is given by Eq. (4.1). The corresponding open-loop error voltages for the carrier and code tracking loops are

$$F(t_e, \theta_e) = \sum_{n=1}^N \alpha_n R(t_e - t_d) \sin(\theta_e - \theta_n) \quad (4.8)$$

and

$$G(t_e, \theta_e) = \sum_{n=1}^N \alpha_n S(t_e - t_d) \cos(\theta_e - \theta_n) \quad (4.9)$$

When both loops are locked both of these voltages may be considered zero. Thus, a solution of the simultaneous transcendental equations

$$F(t_e, \theta_e) = 0 \quad (4.10)$$

$$G(t_e, \theta_e) = 0 \quad (4.11)$$

given a set of values (t_e^*, θ_e^*) for which both loops will be in lock. The stability of the loops will depend on the sign of the open-loop error voltage for small changes in the controlled parameter. Thus the stability of the carrier loop will be determined by the sign of

$$\left. \frac{\partial F(t_e, \theta_e)}{\partial \theta_e} \right|_{(t_e^*, \theta_e^*)} \quad (4.12)$$

and the stability of the code loop will be determined by the sign of

$$\left. \frac{\partial G(t_e, \theta_e)}{\partial t_e} \right|_{(t_e^*, \theta_e^*)} \quad (4.13)$$

The designation of which sign corresponds to stability is essentially a matter of convention. Consider the carrier loop in the absence of multipath; to preserve the meaning of θ_e we wish the stable point to be $\theta_e = 0$ rather than $\theta_e = \pi$. This is accomplished by establishing the following condition for stability:

$$\left. \frac{\partial F(t_e, \theta_e)}{\partial \theta_e} \right|_{(t_e^*, \theta_e^*)} > 0 \quad (4.14)$$

The same reasoning may be applied to the code tracking loop; we will assume that the split-gate waveform consists of a positive pulse followed by a negative pulse so that $S'(0) < 0$. As a consequence the condition for stability of this loop is

$$\left. \frac{\partial G(t_e, \theta_e)}{\partial t_e} \right|_{(t_e^*, \theta_e^*)} < 0 \quad (4.15)$$

Numerical solution of Eqs. (4.10) and (4.11) can be readily obtained using, for example, the Newton-Raphson technique. Consideration of more than two paths does not result in any

difficulty. However, because of the multi-dimensional integration required to compute average error probabilities, only the N=2 case will be considered further at present. In the next sections we consider the tracking for the N=2 case in more detail.

4.4.2 Two-Path Formulation

For the two-path case, the received signal is given by the more convenient expression of Eq. (4.3). In this case the open-loop error voltages become

$$F(t_e, \theta_e) = \sqrt{\frac{2E}{T}} [R(t_e) \sin \theta_e + \alpha R(t_e - t_d) \sin (\theta_e - \theta_m)]$$

(4.16)

$$G(t_e, \theta_e) = \sqrt{\frac{2E}{T}} [S(t_e) \cos \theta_e + \alpha S(t_e - t_d) \cos (\theta_e - \theta_m)]$$

(4.17)

In the remainder of this section we will consider solutions to Eqs. (4.10) and (4.11) when $F(t_e, \theta_e)$ and $G(t_e, \theta_e)$ are given by Eqs. (4.16) and (4.17). We will take the point of view that θ_m is slowly varying with time. The rate of this variation will be such that the two receiver loops track the received signal without loss of lock. Thus a continuous sequence of solutions to Eqs. (4.10) and (4.11) for values of θ_m between 0 and 2π is required.

In solving Eqs. (4.10) and (4.11) we will use the correlation functions $R(t)$ and $S(t)$ derived in Appendix M. These assume that the local code and the output of the split-pulse generator are unfiltered, while the received sequence has passed through a Gaussian filter having an rf bandwidth equal to 1.5 times the chip rate.

4.4.3 Solutions in the Fixed Phase Case

In this section we examine tracking behavior when the two received signals have a fixed phase relationship; two cases are considered: $\theta_m = 0$ and $\theta_m = \pi$. A detailed study of these cases will be useful later on, when solutions for other values of θ_m are required, as well as offering insight into loop behavior.

Substituting the value $\theta_m = 0$ into Eqs. (4.8) and (4.9) gives (neglecting the factor $\sqrt{\frac{2E}{T}}$ which is not significant in the tracking analysis)

$$F(t_e, \theta_e) = [R(t_e) + \alpha R(t_e - t_d)] \sin \theta_e \quad (4.18)$$

and

$$G(t_e, \theta_e) = [S(t_e) + \alpha S(t_e - t_d)] \cos \theta_e \quad (4.19)$$

For the assumed Gaussian filter $R(t)$ is positive (see Appendix M for a graph) for all values of t ; therefore the only solutions to the equation $F(t_e, \theta_e) = 0$ are $\theta_e = 0$ or $\theta_e = \pi$. The latter may be eliminated by taking the derivative of Eq. (4.18) with respect to θ_e and comparing with Eq. (4.14). Thus the only value of θ_e at which the carrier will track is

$$\theta_e^* = 0 \quad (4.20)$$

Substituting this result into Eq. (4.19) gives the open-loop error voltage of the code tracking loop:

$$G(t_e, 0) = S(t_e) + \alpha S(t_e - t_d) \quad (4.21)$$

The stable tracking point(s) of the code loop will be given by the zero(s) of this function. From Fig. M.3 it is clear that the initial non-zero values assumed by $S(t)$ are positive and that the final non-zero values are negative. The same must then be true of $G(t_e, 0)$ as given by Eq. (4.21). As a direct consequence of this, the number of zeroes of $G(t_e, 0)$ will be odd. Experience with the particular $S(t)$ assumed indicates that only two cases actually occur.

1. One zero crossing with negative slope (stable)
2. Three zero crossings; two with negative slope (stable), separated by one with positive slope (unstable).

Whether case 1 or case 2 actually occurs is determined by the values of the parameters α and t_d . Graphs of $S(t_e, 0)$ for two parameter choices which result in the two cases are shown in Figs. 4.9 and 4.10. The first case is that of a relatively short delay ($t_d = 0.5$ bits) with the result that the correlation functions of the two paths overlap; the timing of the local sequence falls somewhere between the two received sequences. In Fig. 4.10 the arrival times are separated enough ($t_d = 1.2$ bits) that it is possible for the receiver to track either of the received signals (with a small error due to the presence of

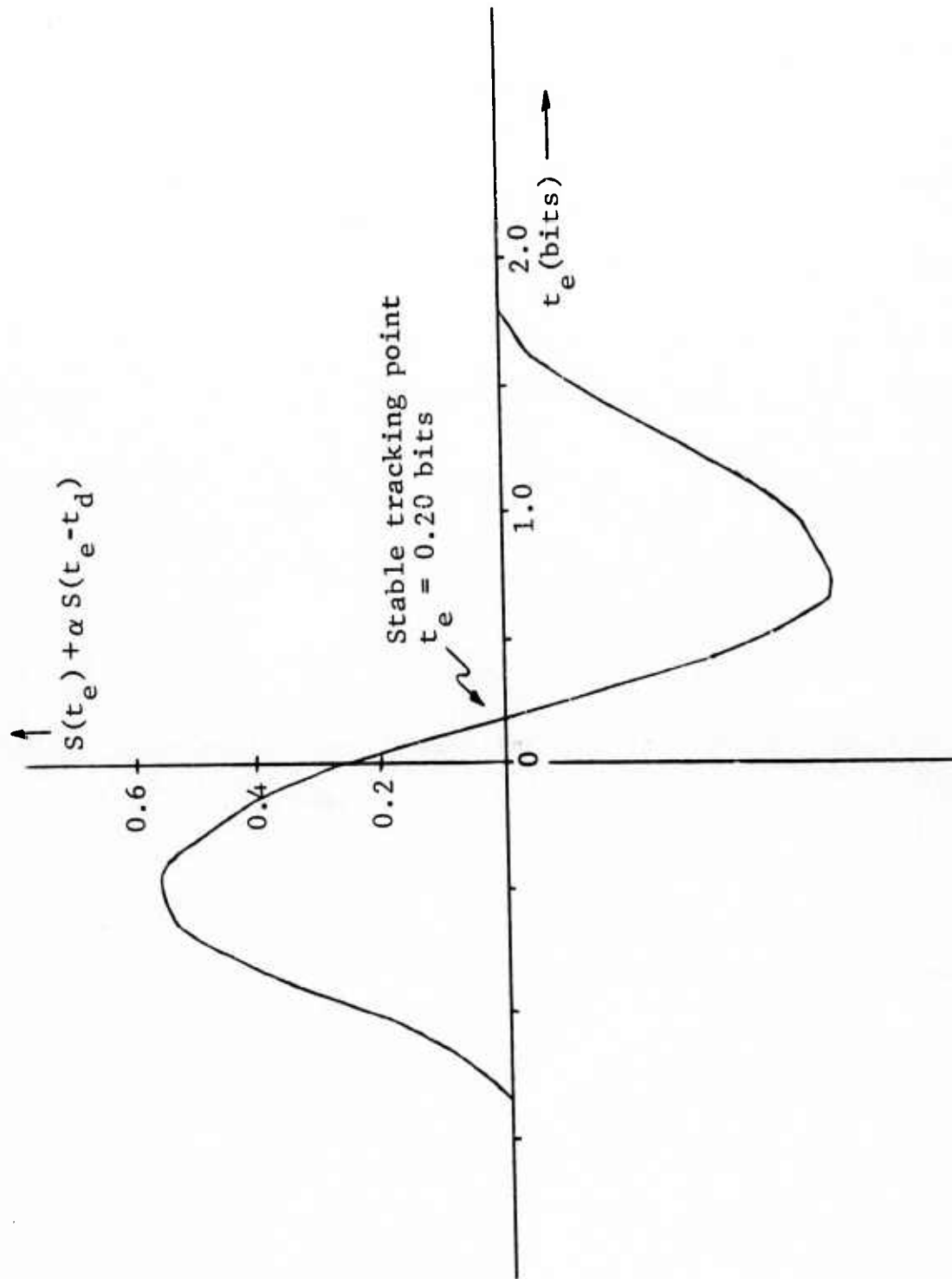


Figure 4.9 Open Loop Error Voltage, $\alpha=0.7$, $t_d=1.2$ bits, $\theta_m=0$

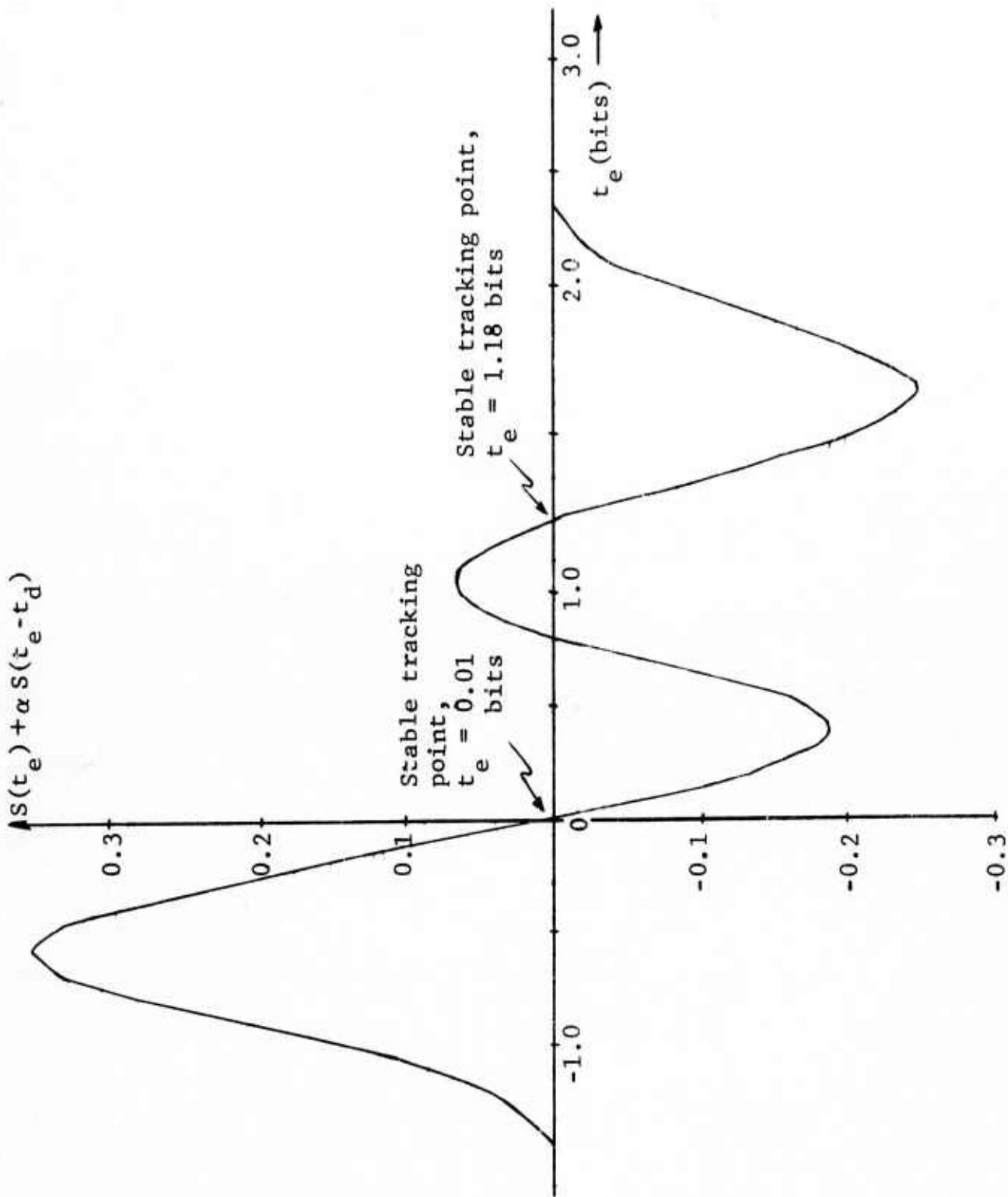


Figure 4.10 Open Loop Error Voltage, $\alpha=0.7$, $t_d \approx 1.2$ bits, $\theta_m=0$

the other). This tracking behavior may be summarized by plotting the code loop error t_e as a function of multipath delay, as in Fig. 4.11. Note that for $t_m < 1.2$ bits only one stable tracking point exists, while for $t_m \geq 1.2$ bits two such points exist.

A similar analysis may be performed for the other fixed-phase case: $\theta_m = \pi$. In this case it can be shown that tracking points are related to the zeroes of the function

$$S(t_e) - \alpha S(t_e - t_d) \quad (4.22)$$

Two values of θ_e are possible, 0 and π . In the first case, the derivatives determining the stability of the tracking point are given by

$$\frac{\partial F}{\partial \theta_e} = R(t_e) - \alpha R(t_e - t_d) \quad (4.23)$$

and

$$\frac{\partial G}{\partial t_e} = S'(t_e) - \alpha S'(t_e - t_d) \quad (4.24)$$

In the second case, these derivatives are given by the same expressions with signs reversed. Experience with examples indicates that for most values of t_e , two stable tracking points exist, one with $\theta_e = 0$ and another with $\theta_e = \pi$, as shown in Fig. 4.12. The first value of θ_e is associated with negative values of t_e and the second with larger positive values of t_e . As t_d is increased and the correlation functions separate, the value of

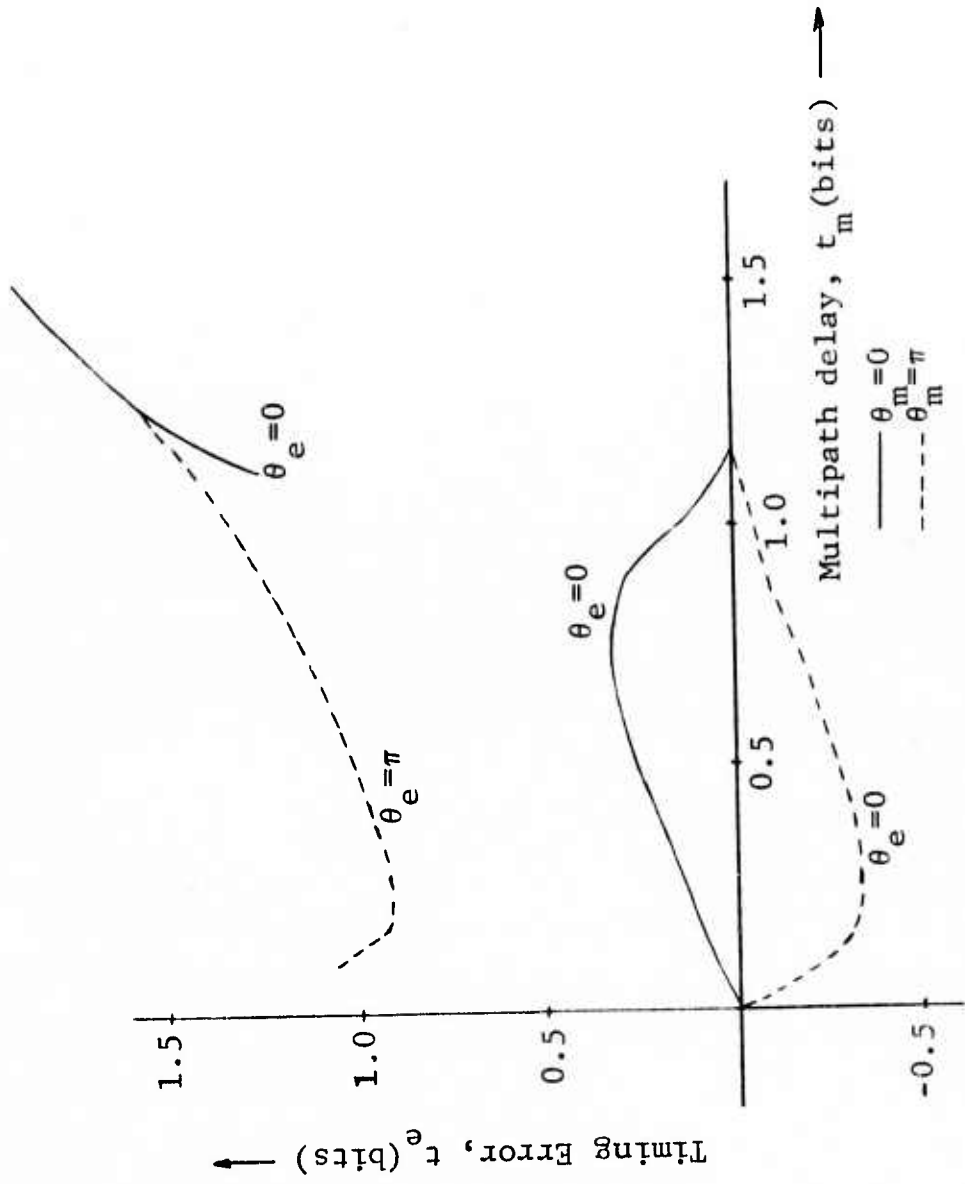


Figure 4.11 Code Loop Tracking Error as a Function of Multipath Delay, for Fixed Multipath Phase ($\alpha=0.7$)

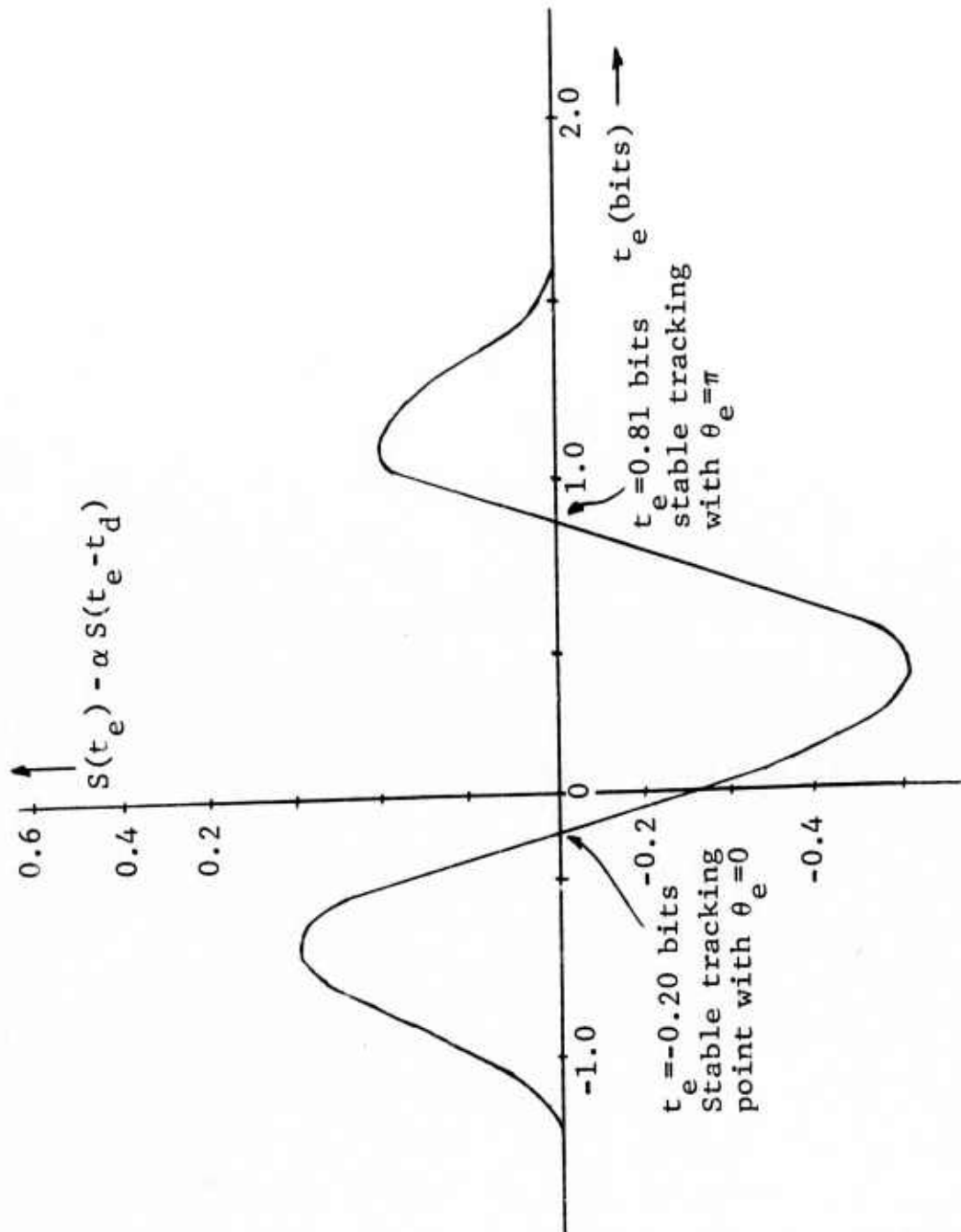


Figure 4.12 Open Loop Error Voltage, $\alpha=0.7$, $t_d=0.5$, $\theta_m=\pi$

t_e corresponding to $\theta_e=0$ becomes zero (perfect tracking of the first signal) and the value of t_e corresponding to $\theta_e=\pi$ becomes equal to t_d (perfect tracking of the second signal). The behavior of these solutions as a function of t_e is also shown in Fig. 4.11.

4.4.4 Solutions for Varying Phase

As discussed earlier, an actual receiver will encounter slowly varying phases, rather than fixed phases, as analyzed in the preceding section. If we assume that this variation is slow compared to the time constants of the loops involved, this implies timing and phase error functions

$$t_e(\theta_m) \quad \text{and} \quad \theta_e(\theta_m) \quad 0 \leq \theta_m \leq 2\pi \quad (4.25)$$

which are periodic in θ_m , and which represent solutions to Eqs. (4.10) and (4.11) for all values of θ_m . In this section we numerically calculate such functions by means of the Newton-Raphson technique for solving simultaneous equations. It should be emphasized that this is not equivalent to simulating the exact loop behavior since it does not consider the loop dynamics. Thus consideration should be given to signal dynamics vis-a-vis loop bandwidths before applying these or subsequent results.

We will begin by referring back to Fig. 4.11 which shows tracking points for fixed multipath phases. It is interesting to observe that for $0.1 \leq t_e < 1.1$ two tracking points exist for $\theta_m=\pi$ while only one exists for $\theta_m=0$. Clearly only one complete solution of the form of (4.23) can exist if there is only one fixed-phase solution at $\theta_m=0$. The presence of a second

fixed-phase solution at $\theta_m = \pi$ indicates the presence of a partial solution to the varying-phase problem in the vicinity of $\theta_m = \pi$; however, this will not be considered further at present.

The technique used to derive solutions of the form (4.25) is to begin with the known (fixed phase) solution at $\theta_m = 0$. These values of t_e and θ_e are used as the starting point for computing a solution at $\theta_m = \Delta$ by means of the Newton-Raphson technique. The process is then repeated, using the solution at $\theta_m = \Delta$ as a starting point for finding a solution at $\theta_m = 2\Delta$, and so forth. In the results to be presented, the step size Δ was chosen to be 10° . A complete solution is shown in Fig. 4.13 for the case $\alpha = 0.7$ and $t_d = 0.5$ bits. Phase and timing errors as well as loop gains are plotted as a function of θ_m . Solutions such as this will subsequently be used to calculate average error probabilities for the data detection process.

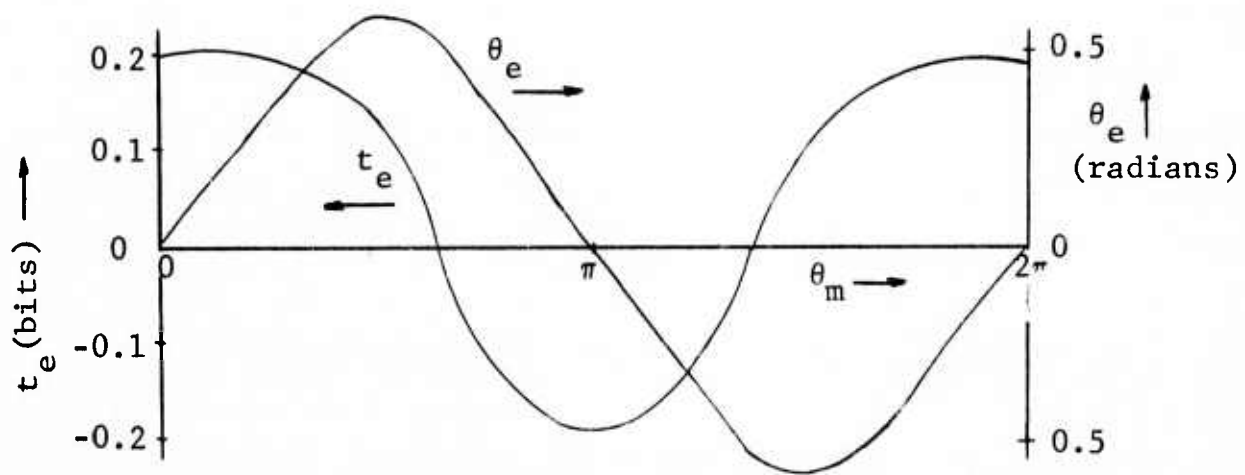
4.5 Error Probability Calculation

4.5.1 General Formulation

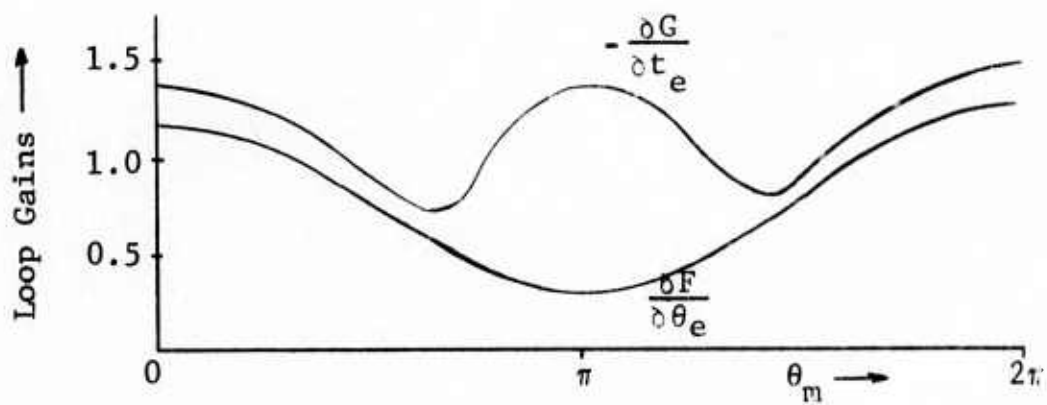
The general multipath signal model is given by Eq. (4.1). The local reference phase and timing are θ_e and t_e ; the output of a coherent detector is then

$$d(t) \sum_{n=1}^N \alpha_n R(t_e - t_d) \cos(\theta_e - \theta_n) + \text{noise} \quad (4.26)$$

where $d(t)$ ($= \pm 1$) is the data modulation. Assuming integrate and dump detection over a bit period T the magnitude of the signal component at the decision point is



a) Timing and Phase Errors



b) Loop Gains

Figure 4.13 Varying-Phase Solution for $\alpha=0.7$, $t_d=0.5$ bits

$$S(\alpha_1, \dots, \alpha_N, \theta_1, \dots, \theta_N) = \sum_{n=1}^N \alpha_n R(t_e - t_d) \cos(\theta_e - \theta_n) \quad (4.27)$$

and the variance of the Gaussian noise is shown in Appendix C to be

$$\sigma^2 = \frac{\sqrt{2}}{T} \int_{-\infty}^{\infty} R_x(u) R_n(u) du \quad (4.28)$$

In this last expression $R_x(t)$ is the autocorrelation of the local PN sequence and $R_n(t)$ is the autocorrelation function of the additive noise after passing through the receiver bandpass filtering. Thus the instantaneous error probability is given by

$$P_e(\alpha_1, \dots, \alpha_N, \theta_1, \dots, \theta_N) = 1 - \Phi\left(\frac{S(\alpha_1, \dots, \alpha_N, \theta_1, \dots, \theta_N)}{\sigma}\right) \quad (4.29)$$

where $\Phi(\cdot)$ is the Gaussian cumulative distribution function.

To obtain the average error probability for a particular multipath situation it is necessary to average over the slowly-varying phases; thus

$$P_e(\alpha_1, \dots, \alpha_N) = \int d\theta_1 \dots \int d\theta_N p(\theta_1, \dots, \theta_N) P_e(\alpha_1, \dots, \alpha_N, \theta_1, \dots, \theta_N) \quad (4.30)$$

In particular, for uniform independent phases, the average error probability is given by

$$P_e(\alpha_1, \dots, \alpha_N) = \frac{1}{(2\pi)^N} \int d\theta_1 \dots \int d\theta_N P_e(\alpha_1, \dots, \alpha_N, \theta_1, \dots, \theta_N) \quad (4.31)$$

Results obtained up to this time are for the $N=2$ case which is discussed briefly below.

4.5.2 Two-Path Formulation

In the two-path case the simpler notation of Eq. (4.3) is used. In this notation the detector signal component corresponding to Eq. (4.27) is

$$S(\alpha, t_d, \theta_m) = R(t_e) \cos \theta_e + \alpha R(t_e - t_d) \cos(\theta_e - \theta_m) \quad (4.32)$$

The resulting instantaneous error probability is

$$P_e(\alpha, t_d, \theta_m) = 1 - \Phi\left(\frac{S(\alpha, t_d, \theta_m)}{\sigma}\right) \quad (4.33)$$

where the noise variance σ^2 is unchanged from Eq. (4.28). The average error probability is then

$$P_e(\alpha, t_d) = \frac{1}{2\pi} \int_0^{2\pi} P_e(\alpha, t_d, \theta_m) d\theta_m \quad (4.34)$$

Extensive results have been computed numerically from these equations; these were presented in Section 4.2. Values of t_e and θ_e needed to compute $S(\alpha, t_d, \theta_m)$ are obtained from the tracking analysis described in Section 4.4. Further expressions for the noise variance σ^2 are to be found in Appendix C.

4.6 A Two-Channel Receiver

This chapter has presented the performance of a conventional spread-spectrum receiver. Essentially, two phase-locked loops are used to track carrier and code phase. These derived references are then used to coherently detect the data which has phase-modulated the carrier at a much lower rate than that of the pseudo-noise code. In the absence of multipath, or when the multipath delay is greater than one or two chip durations, this form of detection is quite satisfactory. However, in the presence of multipath returns delayed by a chip or less, considerable degradation occurs, due to destructive interference (fading) between the signal components. In view of this we have considered a technique of deriving an additional channel from the received signal. The second channel is derived by means of a delayed code sequence, in order to obtain a diversity effect in the presence of multipath. The two channels are combined coherently prior to final detection of the data. This section will present a description and analysis of the system considered, as well as computer-generated performance curves.

Figure 4.14 presents a block diagram of the receiver structure needed to derive references for two-channel detection. The upper and middle PLL's are the code and carrier tracking loops which have been described and analyzed previously, although the data feedback is not shown here for clarity. The third loop is an additional carrier loop required to derive a carrier reference for the second channel. Because a delayed

Extensive results have been computed numerically from these equations; these were presented in Section 4.2. Values of t_e and θ_e needed to compute $S(\alpha, t_d, \theta_m)$ are obtained from the tracking analysis described in Section 4.4. Further expressions for the noise variance σ^2 are to be found in Appendix C.

4.6 A Two-Channel Receiver

This chapter has presented the performance of a conventional spread-spectrum receiver. Essentially, two phase-locked loops are used to track carrier and code phase. These derived references are then used to coherently detect the data which has phase-modulated the carrier at a much lower rate than that of the pseudo-noise code. In the absence of multipath, or when the multipath delay is greater than one or two chip durations, this form of detection is quite satisfactory. However, in the presence of multipath returns delayed by a chip or less, considerable degradation occurs, due to destructive interference (fading) between the signal components. In view of this we have considered a technique of deriving an additional channel from the received signal. The second channel is derived by means of a delayed code sequence, in order to obtain a diversity effect in the presence of multipath. The two channels are combined coherently prior to final detection of the data. This section will present a description and analysis of the system considered, as well as computer-generated performance curves.

Figure 4.14 presents a block diagram of the receiver structure needed to derive references for two-channel detection. The upper and middle PLL's are the code and carrier tracking loops which have been described and analyzed previously, although the data feedback is not shown here for clarity. The third loop is an additional carrier loop required to derive a carrier reference for the second channel. Because a delayed

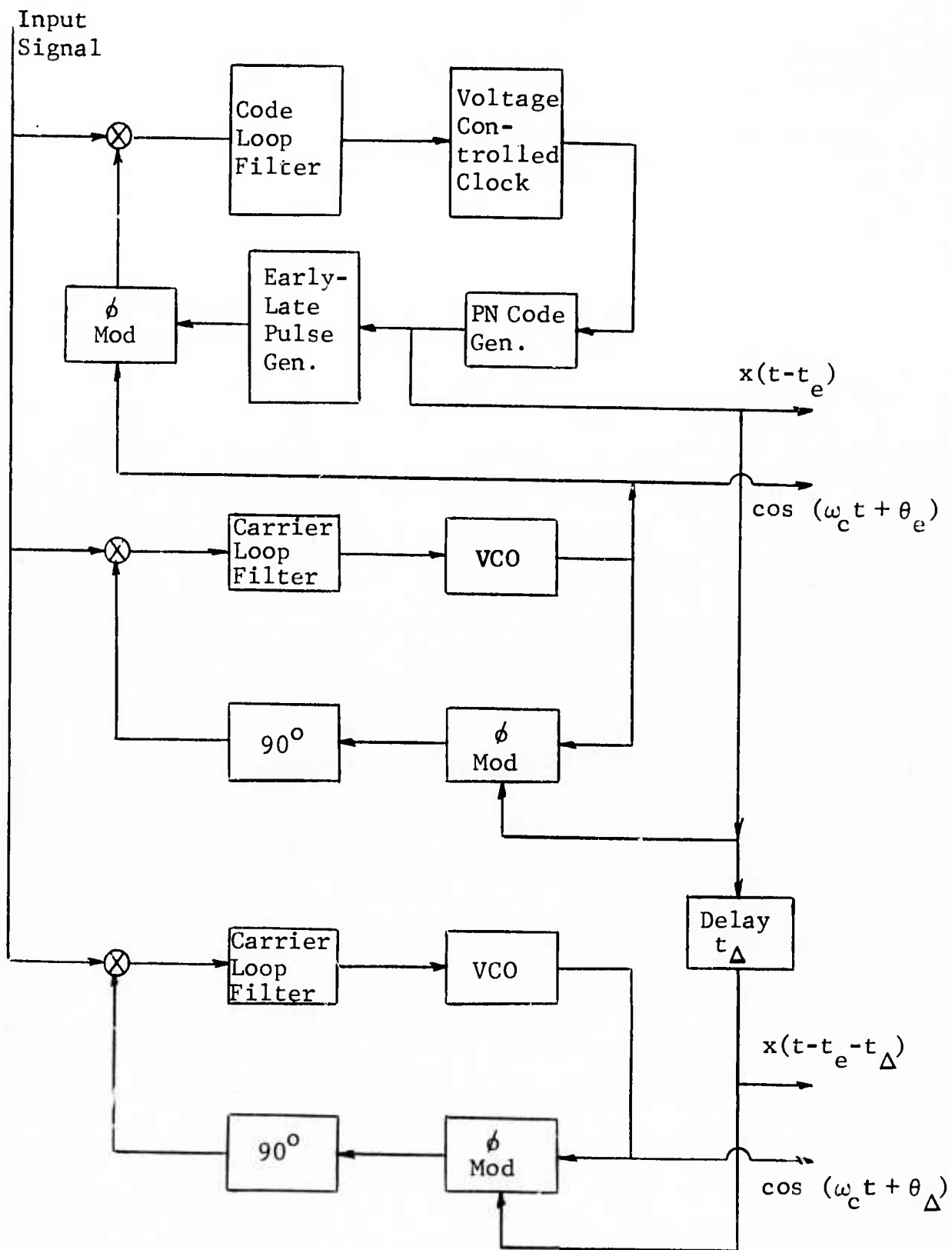


Figure 4.14 Reference Extraction for Two-Channel Detection (Data Feedback not Shown)

version of the local code is used in this loop, its output phase θ_{Δ} will be different than that of the primary carrier loop. The outputs of this circuitry are two code references $x(t-t_e)$ and $x(t-t_e-t_{\Delta})$ and the corresponding carrier reference $\cos(\omega_c t + \theta_e)$ and $\cos(\omega_c t + \theta_{\Delta})$. The parameter t_{Δ} is an independent variable. Selection of this parameter to give optimum performance will depend on the strength and delay of the multipath.

The combining and detection process is shown in Fig. 4.15. We are assuming a signal of the form

$$\begin{aligned} & \sqrt{\frac{2E}{T}} r(t)d(t) \cos \omega_c t \\ & + \alpha \sqrt{\frac{2E}{T}} r(t-t_d)d(t-t_d) \cos(\omega_c t + \theta_m) \\ & + n(t) \end{aligned}$$

where E is the energy per data bit in the direct path signal, T is the data bit duration, $r(t)$ is the filtered PN sequence, and $d(t)$ is data modulation. The output of the channel 1 integrate and dump circuit is

$$\sqrt{\frac{2E}{T}} [R(t_e) \cos \theta_e + \alpha R(t_e - t_d) \cos(\theta_e - \theta_m)] + N_1$$

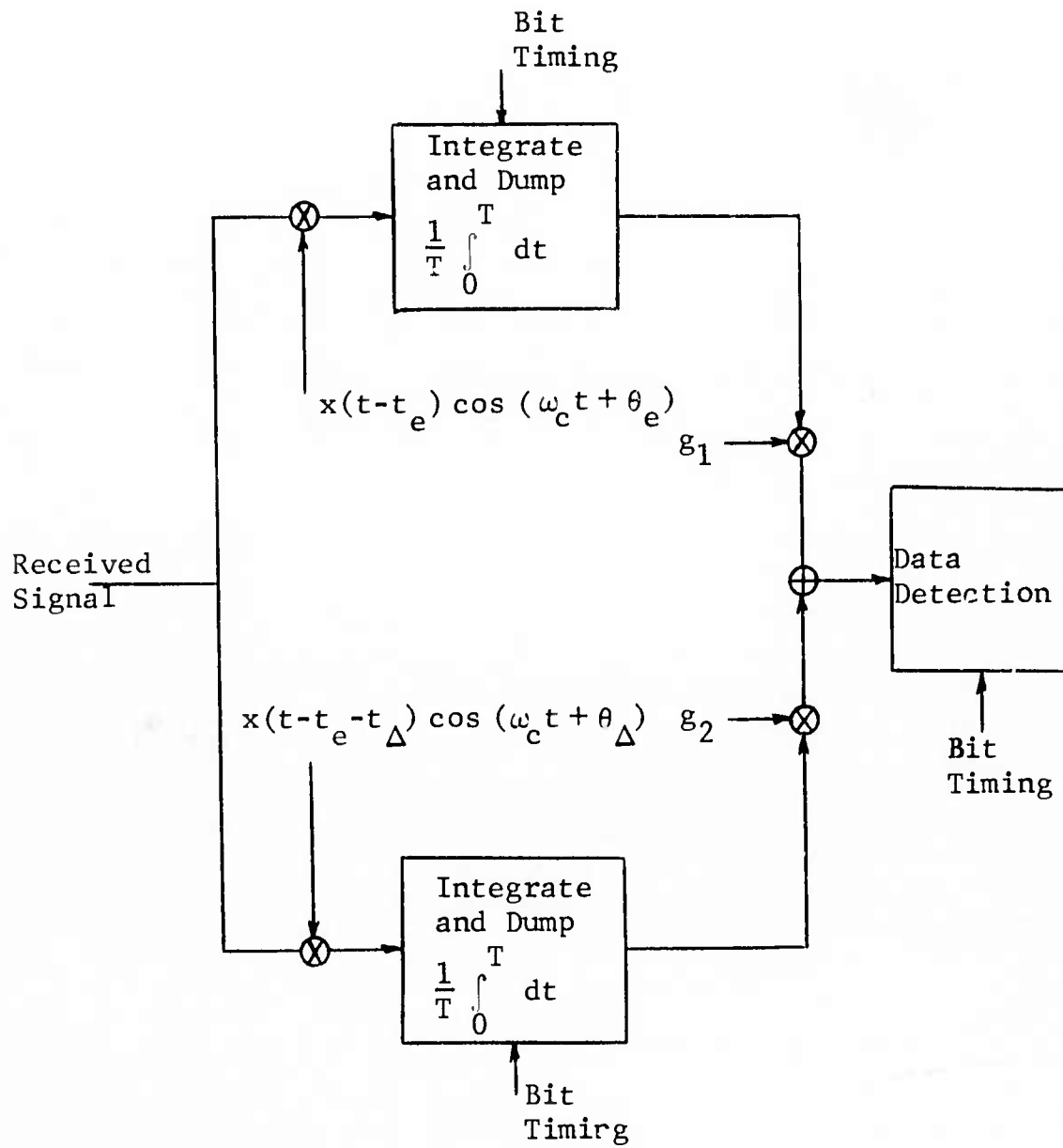


Figure 4.15 Two-Channel Combining and Detection

and the channel 2 output is

$$\sqrt{\frac{2E}{T}} [R(t_e + t_\Delta) \cos \theta_\Delta + \alpha R(t_e + t_\Delta - t_d) \cos (\theta_\Delta - \Delta_m)] + N_2$$

If white Gaussian noise of spectral height $N_0/2$ is assumed at the receiver input, the noise voltages N_1 and N_2 are zero-mean, correlated Gaussian random variables with equal variances:

$$\text{Var } [N_1] = \text{Var } [N_2] = \sigma^2$$

$$\rho \triangleq \frac{E[N_1 N_2]}{\sigma^2}$$

It is shown in Appendix C that

$$\sigma^2 = \frac{\sqrt{2}}{T} \int_{-\infty}^{\infty} R_x(u) R_n(u) du$$

and

$$\rho = \frac{\int_{-\infty}^{\infty} R_x(u-\Delta) R_n(u) du}{\int_{-\infty}^{\infty} R_x(u) R_n(u) du} \cos (\theta_e - \theta_\Delta)$$

where $R_x(t)$ is the correlation function of the unfiltered PN sequence and $R_n(t)$ is the low-pass correlation function of the noise after passing through the receiver band-pass filtering. In the appendix expressions are derived for σ^2 and ρ when the receiver filtering is Gaussian, as assumed previously.

Figure 4.15 shows channel gains g_1 and g_2 preceding the combining. Choice of these gains will determine the performance of the two-channel system. We will assume they are chosen to maximize the post-combining signal-to-noise ratio. In other words, we will analyze a maximal-ratio combiner. We note in passing that to implement such a combiner the receiver must be capable of estimating signal strength in both channels as well as the noise correlation ρ . The solution to the maximal-ratio problem is well known; in this case the result is that

$$g_1 = (S_1 - \rho S_2)g_0$$

$$g_2 = (S_2 - \rho S_1)g_0$$

where S_1 and S_2 have been defined as the signal components of (2) and (3), respectively. The factor g_0 is an arbitrary gain independent of the channel. The resulting signal-to-noise ratio is given by

$$\frac{S_1^2 - 2\rho S_1 S_2 + S_2^2}{\sigma^2(1-\rho^2)}$$

Sections 4.4 and 4.5 described the numerical procedure for determining θ_e and t_e as functions of θ_m and calculating the resulting average error probabilities in the non-diversity case. In the diversity case the tracking of the secondary carrier loop must also be considered in order to calculate θ_Δ as a function of θ_m ; otherwise, the method of calculation is unchanged. Figure 4.16 shows various results calculated for the

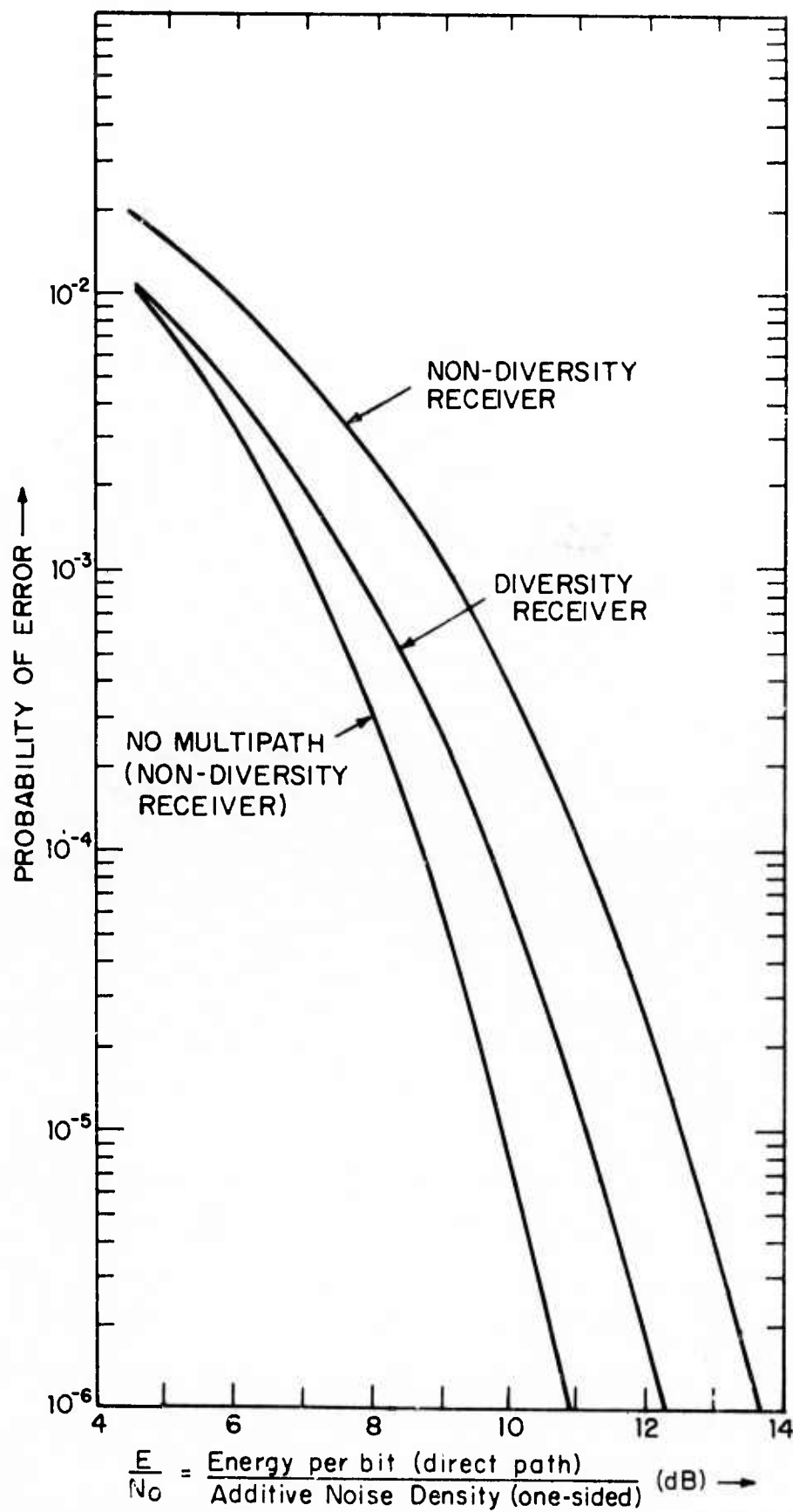


Figure 4.16 Calculated Error Probabilities for Various Receivers; Multipath Delay Difference $t_d = 0.5$ Chip, Relative Amplitude $\alpha = 0.7$ 4-38

particular case where the relative strength α of the multipath signal is 0.7 and the multipath delay is 0.5. The right-hand curve is the performance of a non-diversity receiver under these conditions. The curve immediately to the left gives the performance of a maximal-ratio diversity receiver with delay t_{Δ} chosen to be 0.9. The left-most curve shows the performance of the non-diversity receiver in the absence of a multipath signal. This curve is 0.35 dB to the right of the ideal curve for coherent detection of binary antipodal signals. This 0.35 dB represents the loss due to the assumed band-pass filtering in the receiver.

As mentioned earlier, the delay t_{Δ} chosen to implement the second channel is a design parameter affecting performance. For the situation considered above the value $t_{\Delta} = 0.9$ is approximately optimum. This was determined by calculating the performance for various values of t_{Δ} . This is illustrated in Fig. 4.17 which shows the error probability at an E/N_0 of 10.5 dB as a function of t_{Δ} . (Also shown is the performance of an equal-gain diversity receiver at the same signal-to-noise ratio.)

Two additional cases have been calculated; both with the same multipath delay (0.5 chip). Figures 4.18 and 4.19 present results for a relative path strength of 0.9. In this case performance of the non-diversity receiver is slightly worse than for a relative strength of 0.7, but performance of the diversity receiver has actually improved. This is because of the increase in total energy of the received signal. Note that in this case the optimum spacing (t_{Δ}) for the diversity channel is again 0.9

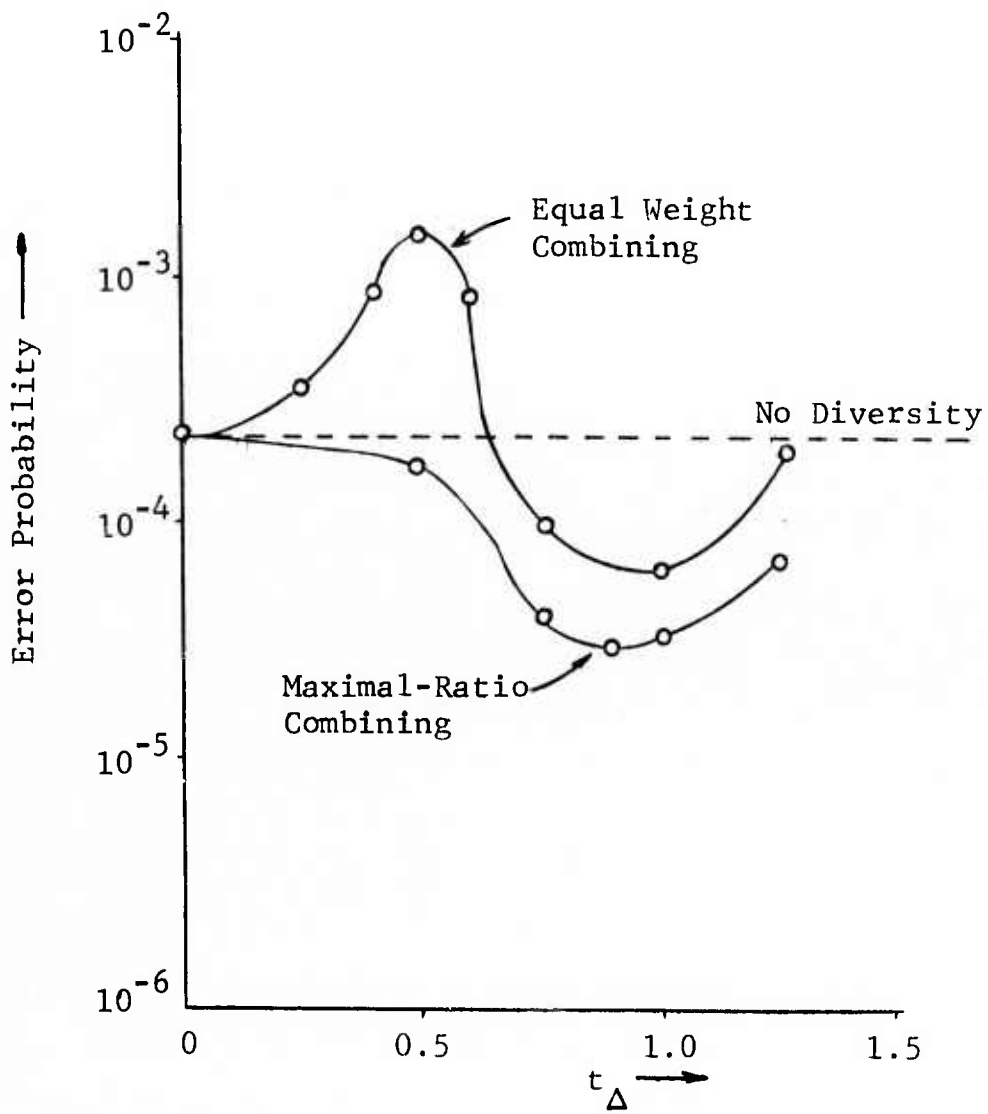


Figure 4.17 Performance as a Function of t_{Δ}
 ($\alpha=0.7$, $t_d=0.5$, $E/N_0=10.5$ dB)

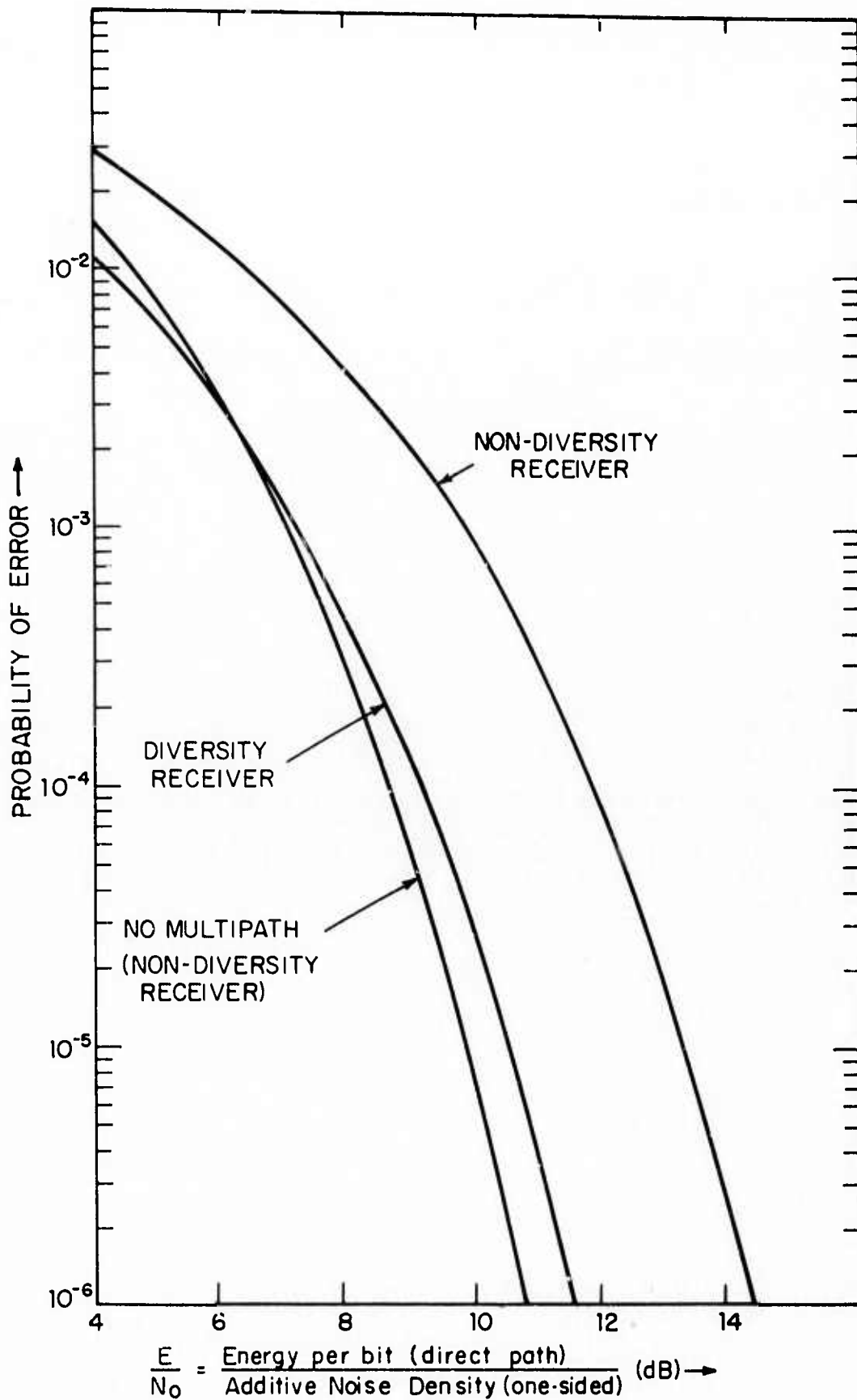


Figure 4.18 Calculated Error Probabilities for Various Receivers; Multipath Delay Difference $t_d = 0.5$ Chip, Relative Amplitude $\alpha = 0.9$ 4-41

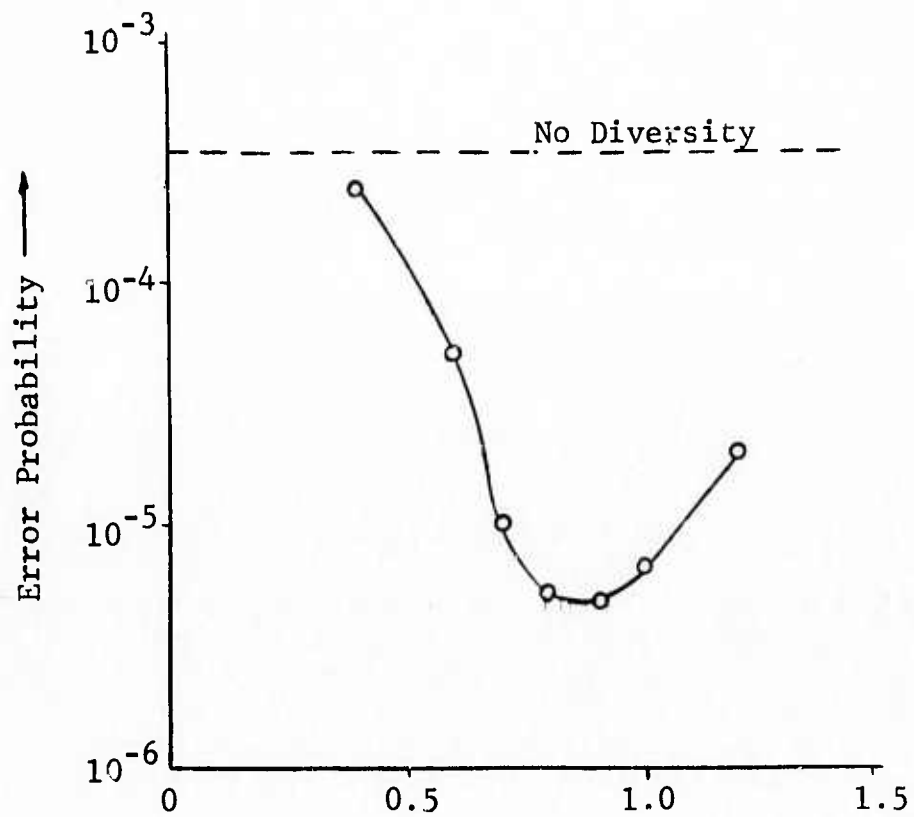


Figure 4.19 Performance as a Function of t_{Δ}

($\alpha=0.9$, $t_d=0.5$, $E/N_0=11$ dB)

chip. The final case considered is that of equal-strength signals ($\alpha = 1.0$); results are shown in Figs. 4.20 and 4.21. For this case performance of the non-diversity receiver is completely degraded. This is because the signal available for detection is zero when the relative phase θ_m is equal to 180° . However, performance of the diversity receiver is only 2 dB less than that of the non-diversity receiver in the absence of multipath. This clearly demonstrates the value of the diversity technique. Note that in this case the optimum value of t_Δ has shifted to 0.5. The effect of varying the relative path delay t_d on the optimum value of t_Δ has not yet been explored.

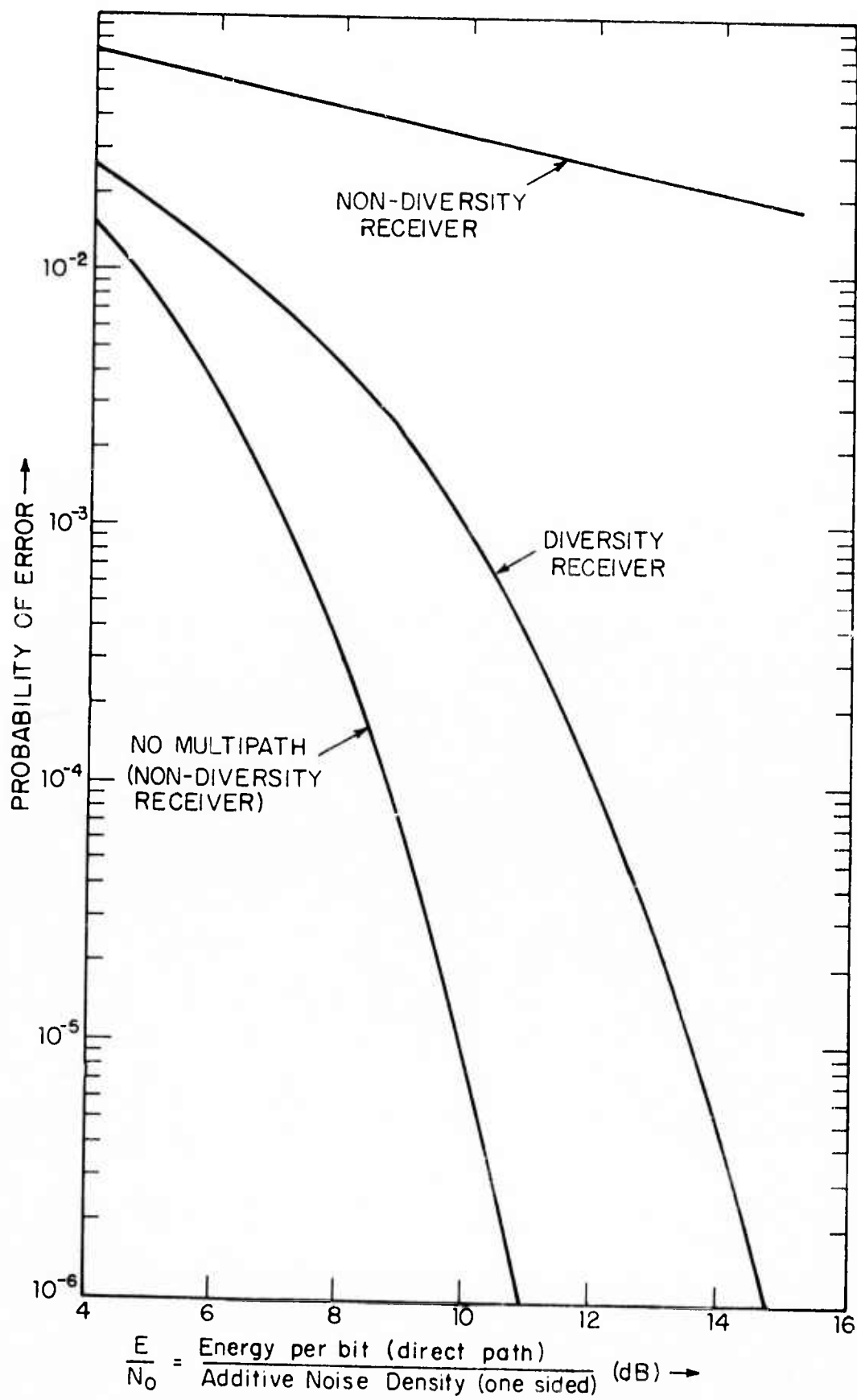


Figure 4.20 Calculated Error Probability for Various Receivers; Multipath Delay Difference $t_d = 0.5$ Chip, Relative Amplitude $\alpha = 1.0$ 4-44

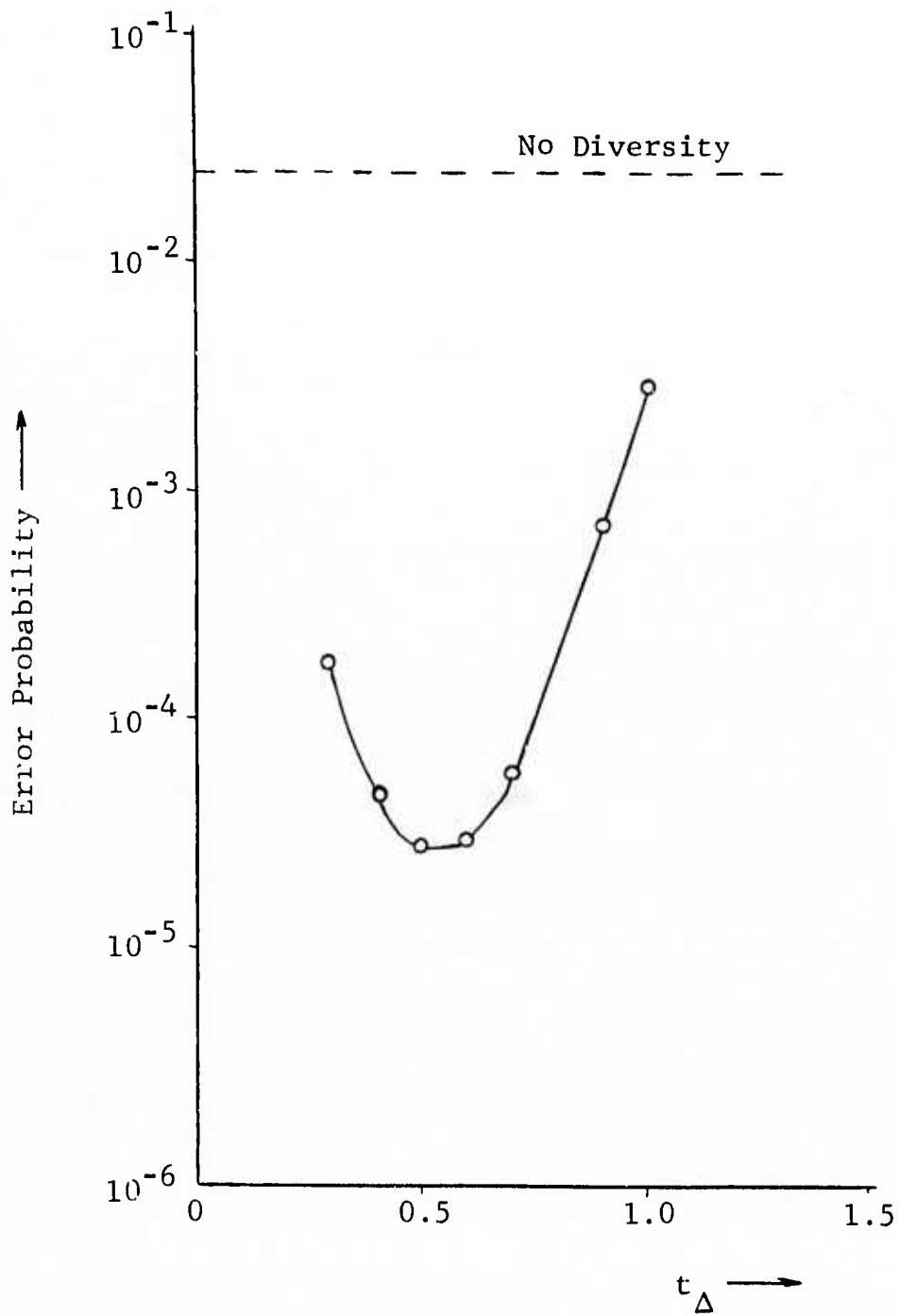


Figure 4.21 Performance as a Function of t_{Δ}

($\alpha=1.0$, $t_d=0.5$, $E/N_0=13$ dB)

SECTION 5

CHANNEL MEASUREMENTS

The line-of-sight (LOS) tropospheric channel utilized in RCV applications, although usually well behaved, is occasionally subject to multipath and deep fading. To maximize the probability of success in procuring spread-spectrum modems that will work effectively over such a channel, the initial modem designs should take account of the channel characteristics and subsequent experimental models should undergo comparative tests over validated simulated channels.

In Section 5.1 below we present the method of approach of utilization of channel measurements that should be used in developing modems, when time and funds permit. Section 5.2 discusses the channel measurement needs for the RCV channel both in respect to what is known or can be estimated presently about the channel characteristics and what channel characteristics particularly affect spread spectrum modem performance. Section 5.3 presents a comparative study of candidate channel measurement techniques for the RCV channel and arrives at a recommendation which meets the channel measurement requirements with minimum cost and maximum flexibility for expansion to flight experiments and stored channel simulation. Section 5.4 considers the use of a specific frequency hopping PN modem for channel probing. Appendix G provides the mathematical backup to these sections, which have been kept non-mathematical.

5.1 A Rational Approach to Modem Development

The most effective approach to the development of optimum modulation and demodulation techniques for a specific class of channels involves a sequence of steps as diagrammed in Fig. 5.1.

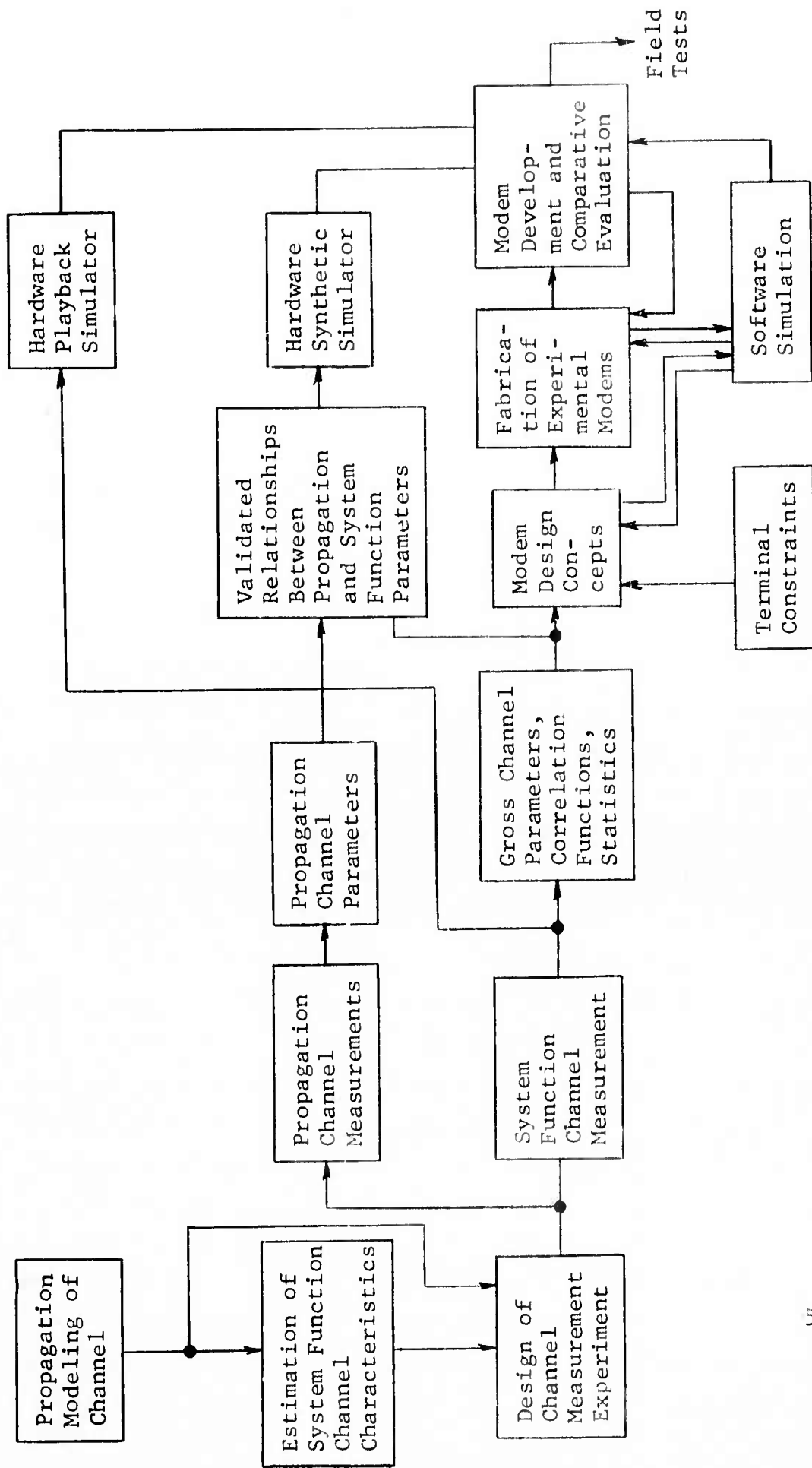


Figure 5.1 Utilization of Channel Measurements in Modem Development

These steps involve the measurement and modeling of channel characteristics to provide the basis for optimum modem design concepts and the utilization of channel simulators for the development, acceptance testing, and comparative evaluation of implemented modems prior to field testing.

As indicated in Fig. 5.1, the design of the channel measurement experiment involves an initial analytic modeling effort to determine the relationship between significant parameters in the propagation and system function models of the channel. From this modeling effort one may estimate multipath spreads, Doppler spreads, frequency correlation functions, delay power spectra, etc. as a function of propagation channel parameters such as refractive index gradients and as a function of system parameters such as range, velocity vectors of terminals, antenna patterns, etc. The proper design of the channel probing signal, measurement equipment, and data reduction requires at least that a gross estimate of maximum multipath spread and Doppler spread be available and that the bandwidth be specified over which the channel is to be characterized.

The channel measurement experiment should involve both propagation and system function type measurements in order to validate the initially estimated relationship between the two channel models. It is important to develop such validated relationships because the time and expense associated with channel measurements prevent the collection of measurements under all physical cases of interest. Thus for example in the Hawaii measurements it is desirable that refractive index spatial structure be measured. If, on the basis of measurements,

validated relationships have been developed between, say, multipath and refractive index gradient, then it will be possible to estimate the effects of other gradients even though such gradients did not occur in the experiments.

System function channel measurements connected with the multiplicative (distorting) and additive disturbances may be taken separately because of their independence. The signal distortion properties of the channel are characterized by measurements at four levels of increasing complexity:

1. Measurement of gross parameters of system function (e.g., coherence bandwidth, Doppler spread, etc.)
2. Measurement of correlation functions of system functions (e.g., frequency correlation function, delay power spectrum, etc.)
3. Measurement of probability distributions of system functions (e.g., probability distributions of amplitude and phase on a received carrier)
4. Measurement of system functions (e.g., time-variant transfer function and impulse response).

Measurements 1-3 in conjunction with terminal constraints, such as bandwidth and power, are useful for bounding the distortions caused by the channel and allow a considerable narrowing of the possible modulation and demodulation techniques to be considered.

In the development of modems both software and hardware simulators are useful. Software simulations are useful during the early stages of modem development where modem concepts are checked out for inclusion in design specifications and where acceptance specifications are developed. They are also useful during the design of the modem by allowing a prediction of performance degradation that would be caused by a proposed design change. The hardware simulator comes into play when modems have been built, both for final checkout and adjustment of the modem prior to acceptance testing, and for the acceptance testing itself.

Two basic types of channel simulators may be identified, each having separate functions in modem development. These two types of simulators are called the synthetic channel simulator and the playback channel simulator. The synthetic channel simulator creates a reproducible channel which has average statistical properties approximating the measurements 1-3. Due to the validated relationships between the system function and propagation channel parameters it is then possible to create synthetic channel conditions which would have been observed if sufficient time could have been expended in the channel measurements. For example, in the case of steep refractive index gradient layers one might deduce that certain gradients and layer structures not actually observed in the propagation measurements are still reasonably likely and would produce certain multipath structure. The synthetic channel can be set to model this situation.

The playback channel is used to recreate the same instantaneous system functions that were measured in 4 above, with appropriate measured additive noise, if ordinary thermal noise

is not sufficient. Whereas only the approximate statistical behavior is reproduced by the synthetic simulation, the exact instantaneous system function (and representative noise) that existed during the measurements is "played back" by the playback simulation. While the synthetic simulator is of great help in checking out bit-sync tracking and acquisition, and further narrowing the modems of interest through comparative modem performance evaluation under identical conditions, these conditions only approximate the statistical behavior of the actual channel. In order to achieve low error rates in digital communication it is necessary to consider the rare events on the "tails" of probability distributions which cannot be reproduced by the synthetic channel. However, all such rare events which have occurred in the system functions during channel measurements will be accurately reproduced by the playback simulator. Note, moreover, that the playback channel allows a comparative evaluation of modem performance over the same time-bandwidth portion of an actual channel, a feat which is impossible in direct field testing of modems!

As a final point, during field testing of the modems, it is desirable, if practical, to obtain channel measurements simultaneously, in the same frequency band as the data transmission uses. To obtain gross channel parameters and channel correlation functions, it is sufficient to carry out measurements in an adjacent band. Sometimes the data signal itself can be used for these types of measurements. For measurements of instantaneous system functions to be useful they should be carried out in the same band as the data signal. In the case of wide-band channels with slow fading, such as the RCV channel, this type of parallel probing is feasible.

5.2 A Look at RCV Channel Measurement Needs

The present stage of the utilization of channel measurements in the development of modems for the RCV channel is at the beginning of the task flow diagram in Fig. 5.1. CNR is engaged in propagation modeling utilizing assumed refractive index structure to estimate system function characteristics. This modeling and available channel measurements will provide essential data for the design of channel measurement experiments. Some experiments will be undertaken by ITS in Hawaii, hopefully to gather both propagation channel characteristics (measured refractive index structure coupled with weather conditions) and system function characteristics. It is the purpose of this section to develop recommendations for techniques to be used in the system function measurements so that the data necessary for system design may be obtained most economically.

Available experiments and analyses indicate that under severe fading multipath conditions the LOS tropospheric channel may be characterized by a few, often two, discrete paths whose phases and amplitudes have random fluctuations with the amplitude showing considerably less fluctuation than the phase. Analysis of the performance of a spread spectrum system over such a channel reveals that a detailed knowledge of the multipath structure and the fluctuation statistics of individual paths is essential to predict performance. It follows that whatever channel probing technique is selected it should allow the determination of these multipath characteristics.

Another point to keep in mind is that the experiment set up for Hawaii is for fixed terminals, whereas at least one RCV channel terminal, if not both, will be moving. Thus the measurement equipment should be designed to be economically upgraded to handle moving terminals.

Finally, the channel measurements taken should be usable to drive a playback channel simulator unit when funds permit its construction. The playback channel capability is particularly important in the present case because the multipath phenomena only occurs a small percentage of the time. This factor becomes particularly relevant when flight tests are used because of their expense. Of course all the other reasons for using a playback channel quoted in Section 5.1 apply here also.

Before leaving this section to consider candidates for channel measurements, we discuss the reasons why a detailed knowledge of the multipath and path fluctuation statistics are essential to prediction of spread spectrum modem performance over the RCV channel.

The multipath discrimination capabilities of a spread spectrum system allows operation over a single path P_1 if the other paths are sufficiently far removed in path delay relative to this path. Let us first consider this case. Then the other delayed (or advanced) versions of the spread spectrum signal appear at the system output as "self-noise" terms which are each R dB below their strengths relative to P_1 at the input, where R is the system processing gain. In order to assess the level of this output self noise, the combined power in all other paths relative to P_1 should be known. Clearly, in order to

determine the performance characteristics when synchronized to P_1 , the amplitude and phase statistics of P_1 should be known. It seems reasonable to assume that the phase varies sufficiently slowly to allow tracking by a carrier tracking loop, no matter what its statistics. However, the amplitude statistics of P_1 are clearly necessary to evaluate performance. To summarize, if there are N paths and they are far enough apart in delay (greater than twice a chip duration to allow for equipment band-limiting) then it should be sufficient in the evaluation of system performance to know the N individual path amplitude statistics and the residual power in the $N-1$ different combinations of N paths taken $N-1$ at a time. However, to obtain the amplitude statistics of the path it is necessary to measure them simultaneously and no special channel measurement is necessary for the residual power measurement.

Analysis indicates that the paths cannot always be assumed sufficiently separated in delay to prevent coherent contributions from two paths appearing simultaneously at the correlator output. When this happens the coherent contribution at the correlator output for a given pseudo-noise sequence timing depends upon the amplitude, relative phases, and relative path delays of the paths involved. Thus, unless one is willing to assume some statistics for the relative amplitudes, phases, and delay differences, a rather complete measurement of the path complex gains and structure must be undertaken to evaluate system performance.

5.3 Comparison of Measurement Techniques

In Section 5.3.1 we present some general considerations to narrow the class of channel measurement techniques worth considering in detail. Section 5.3.2 presents a detailed consideration of the techniques surviving Section 5.3.1 Appendix G provides analytical backup.

5.3.1 General Considerations in the Selection of Probing Techniques

The number of possible channel measurement techniques is large. Any transmitted waveform with sufficient bandwidth and structure to allow measurement and ambiguity resolution of the multipath structure of the channel is a potential candidate for a probing waveform. Any receiver structure which is capable of realizing the corresponding measurement and ambiguity resolution is a potential candidate for a proper demodulator. However, the following considerations limit the number of techniques worth studying in detail:

- a) practicality of waveform generation
- b) desire for power utilization efficiency
- c) desire for large bandwidths to be characterized
- d) importance of generating measurement information usable to drive stored channel simulators at some future date (which implies coherent receiver processing)
- e) cost and complexity
- f) constraint of linear or nonlinear power amplification.

The types of practical, easily generatable wide-band probing waveforms fall into the following categories:

- 1) pulse train; low duty cycle, low TW product
- 2) pulse train; high duty cycle, high TW product
- 3) linear frequency sweeps
- 4) discrete (stepped) frequency sweeps
- 5) pseudo noise sequences (maximal length shift register sequences of ± 1 modulating a carrier)
- 6) multiple carrier transmission
- 7) rapid periodic (e.g., sinusoidal) phase or frequency modulation to generate uniformly spaced essentially equal amplitude side-bands.

In the frequency band that is to be probed, the available power amplifiers operate at saturation for maximum average radiated power. Thus low duty cycle pulse trains and multiple carrier transmissions, which have high peak/average power ratios, are not very desirable from the point of view of maximizing radiated power. Unless the loss in average power is balanced by sufficient compensating advantages, there is no point in considering them further. In fact we have been unable to find sufficient compensating advantages to warrant their further consideration.

As pointed out in Section 5.2, the important basic channel system function information needed for evaluation of RCV channels concerns the multipath structure of the channel, which is a time domain description. Some of the probing waveforms catalogued above (1 - 7) lead most directly to frequency domain measurements, namely, frequency sweeping, frequency stepping, and parallel tone transmission waveforms. Since

multipath structure is the desired end product, use of these latter techniques imply additional processing at the receiver to convert the frequency domain to time domain information, i.e., some form of Fourier transformation. Unless the increased processing requirements are offset by sufficient compensating advantages, there is no strong reason to consider these basically frequency domain approaches.

A search through items a) - f) above reveals that there may be a compensating advantage in item c), the desire for large bandwidths. In the case of RCV spread spectrum multiple access communications, the data rate requirements appear to be of the order of 100 Mbs. For binary PSK transmission with a moderate amount of filtering in the receiver and no frequency hopping, one must expect the channel bandwidth that needs to be characterized to be of the order of 200 MHz. As will be seen in Section 5.3.2, to achieve flat radiated spectra over 200 MHz the time domain techniques can use pulse widths of the order of 5 ns with some equalization at the receiver. This appears within the state of the art even for generation of pseudo-noise maximal-length shift register sequences of durations long enough to provide adequate resolution. It follows that there is no justification at this time for considering the frequency domain processing approaches.

The above considerations have narrowed down the transmitted, probing waveforms to large TW product pulse trains and PN (pseudo-noise) sequences and have narrowed down the receiver processing to those which compute multipath structure in some form. Actually, the PN sequence waveform may be

regarded as a large TW product pulse train, where the "pulse" length is interpreted as the duration of the shift register sequence. It should be noted that not all pulse trains are useful for the coherent processing at the receiver necessary for collection of data useful to stored channel operation. In particular, as shown in Appendix A, repetitive pulsing of a large TW product filter at the transmitter is not suitable unless the carrier frequency is a harmonic of the pulse repetitive rate. In considering the problem of generating large TW product pulse trains with good sidelobe properties for their autocorrelation functions, it becomes evident that the sidelobes of the PN sequence* are not likely to be bettered. Moreover the PN sequence is easily generated. Thus consideration is limited to this type of transmitted signal in the succeeding section.

5.3.2 Comparison of Matched Filter and Correlation Techniques

The previous discussion has narrowed the selection of transmitted probing waveforms to a maximal length shift register sequence of (+1)'s and (-1)'s modulating a carrier. Here we compare the two techniques of utilizing the received waveform for channel measurement: the matched filter and correlation techniques.

*As discussed in Appendix G we are dealing here with the periodic autocorrelation function of the PN sequence, which in the discrete case has sidelobes $\frac{1}{P^2}$ below the main peak for a period P.

In the matched filter technique a filter is used whose impulse response is matched to one period of the shift register sequence (surface wave acoustic bandpass matched filters seem to be reaching state-of-the-art for such an application). The ideal filter output for an input periodic PN sequence is just the periodic correlation function of the sequence. For the large periods that may be employed in practice the side lobes can be made low enough so that this periodic correlation function consists of a single isolated narrow pulse occurring at the sequence period. For rectangular "chips" of duration Δ , this narrow pulse would be a triangle with base 2Δ . As a result, in the case of probing a channel, the matched filter output will equal the periodic pulse response of the channel. In other words, one achieves at the matched filter output essentially the same waveform as would result from transmitting low duty cycle narrow pulses of duration Δ and using a receiver filter with impulse response of duration Δ . What the matched filter PN sequence combination has done is allow maximum utilization of prime power at the transmitter, while still achieving the periodic narrow pulse response.

One of the basic requirements that we have placed upon the measurement technique to be selected, is that the data collected, in addition to providing the basic multipath information for analysis, should also be usable to drive a stored channel simulator when funds permit its construction. The matched filter output alone, without further processing, does not satisfy this requirement because its bandwidth (> 200 MHz) is too large to allow economical recording. Figure 5.2 presents a simplified block diagram of a matched filter receiver in which

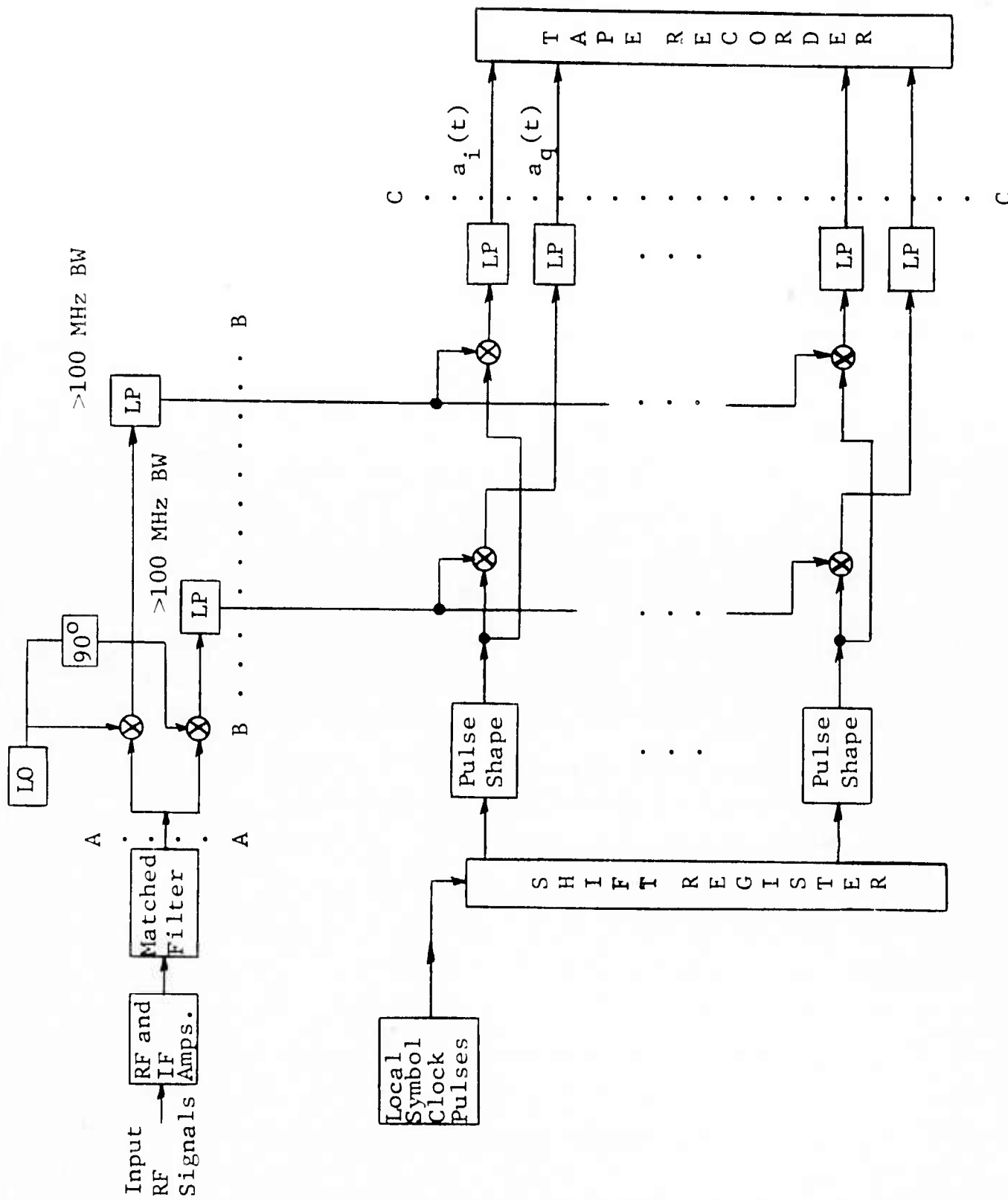


Figure 5.2 Simplified Block Diagram for Matched Filter Techniques: Low Pass Sampling

additional processing has been provided to make the measurement output suitable both for economical tape recording to allow computer analysis of multipath structure and for stored channel simulation. To understand why the matched filter output at interface A-A (or B-B for in-phase and quadrature components) and the actual recorded outputs at C-C contain the same information, while the former cannot be economically recorded and yet the latter requires no more than an audio recorder, it will be necessary to digress briefly to a discussion of the characteristics of time varying impulse responses.

Figure 5.3 depicts the periodic pulse response of a base-band time-variant channel for three successive pulses. Let the bandwidth of this signal be W . Samples marked with x's occur somewhat faster than the Nyquist rate at $2W_1$. An analog recorder of bandwidth W would be required to record this pulse response. A digital recorder would have to A/D convert at a rate $2W_1$ of samples/sec. to avoid aliasing errors. Note, however that the channel is very slowly time varying. The samples marked with the same letter occur in the same relative position in each pulse response. Thus, for example, the samples marked with c are the third samples from the beginning of a pulse response. The successive samples marked with c may be regarded as samples of a very slowly time varying function $c(t)$ which has a bandwidth B very much smaller than W . If these samples are represented by narrow pulses of varying amplitude and fed to a filter of bandwidth B , the function $c(t)$ can actually be obtained. Note from 5.3 that there are only 14 samples per pulse response. Thus if $a(t)$, $b(t)$, ... $n(t)$ are obtained in the same way as $c(t)$ a total analog recording bandwidth of $14B$ Hz is required instead

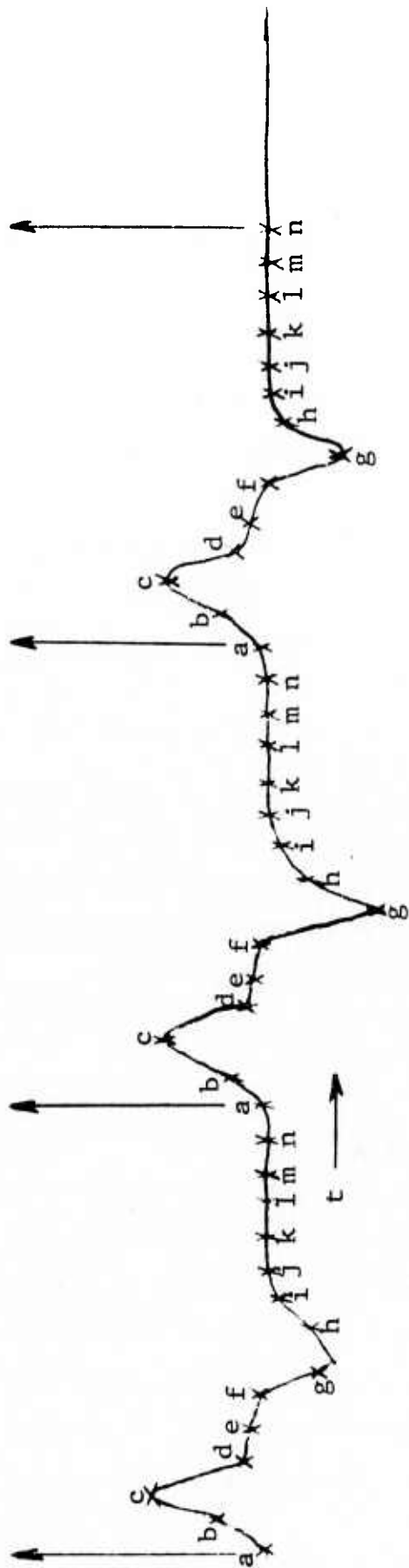


Figure 5.3 Periodic Pulse Response of Baseband Time-Variant Channel. Samples With x's Occur Faster Than Nyquist Rate. Samples Marked With Same Letter Occur in Same Relative Position in Each Pulse Response.

of W Hz. For digital recording A/D conversions would have to occur at a rate of $28B/\text{second}$ instead of $2W_1/\text{second}$. Note that since we can always reconstruct the Nyquist samples in 5.3, no loss of information can occur.

In the case of radio channels one must deal with band-pass pulse responses, which can be decomposed into two baseband pulse responses. This procedure is indicated in Fig. 5.1 in going from the interface A-A to B-B. A local oscillator output and a 90° shifted output are used to mix the matched filter response to DC, producing the "in-phase" and "quadrature" components of the matched filter output (referenced to the local oscillator phase). Examination of the operations in going from B-B to C-C for these two baseband pulse responses may be seen to be exactly analogous to the reconstruction of the functions $a(t)$, $b(t)$, ... described above in reference to Fig. 5.3. We have labeled one pair of outputs $a_i(t)$, $a_q(t)$ to note the analogy with $a(t)$ where i, q denote "in-phase" and "quadrature."

The implication of this recording method for the RCV LOS channel is quite dramatic. The bandwidth of the matched filter output will exceed 200 MHz, making analog or digital recording not even feasible. But the fading rate of the channel is slow. While calculations have not been completed, one may estimate B to be at most of the order of a Hz. The number of complex samples required per pulse equals the pulse response of the channel measured in units of 5 nanoseconds. For a path with 100 nanoseconds multipath 20 in-phase and quadrature low pass channels of bandwidths less than one Hz would be required, for a

total recording bandwidth of 30 Hz!! Finally we point out that the functions $a_i(t)$, $a_q(t)$; $b_i(t)$, $b_q(t)$; ... ; are precisely those needed to drive a stored channel simulation.

Before turning to a discussion of the correlation technique we would like to point out that Fig. 5.2 is only one method of implementing the sampling process and is included for discussion purposes only. Thus we show in Fig. 5.4 an alternate implementation of the sampling process which utilizes band-pass sampling pulses instead of video sampling pulses.

As Fig. 5.5 indicates, the correlation technique involves cross-correlating the received signal with a set of delayed replica's of a locally generated PN sequence. In Appendix G it is shown that this procedure yields the functions $a_i(t)$, $a_q(t)$; $b_i(t)$, $b_q(t)$; ... directly. In addition, as shown in Appendix G, the SNR performances of the matched filter and correlation techniques are identical. Finally, a comparison of the signal processing operations in Figs. 5.2 and 5.5 reveals that the processings are essentially identical if the matched filter plus symbol pulse generator cost and complexity in Fig. 5.2 is equated with that of the PRN generator in Fig. 5.5. It is believed that the PRN generator is less expensive.

A bandpass correlator version is shown in Fig. 5.6. It is believed that this approach will lead to a superior design. The design approach actually recommended for initial implementation is shown in Fig. 5.7. This approach is called the Multiplexed Band-Pass Correlation technique. It involves the use of a single bandpass correlator whose local PN reference is

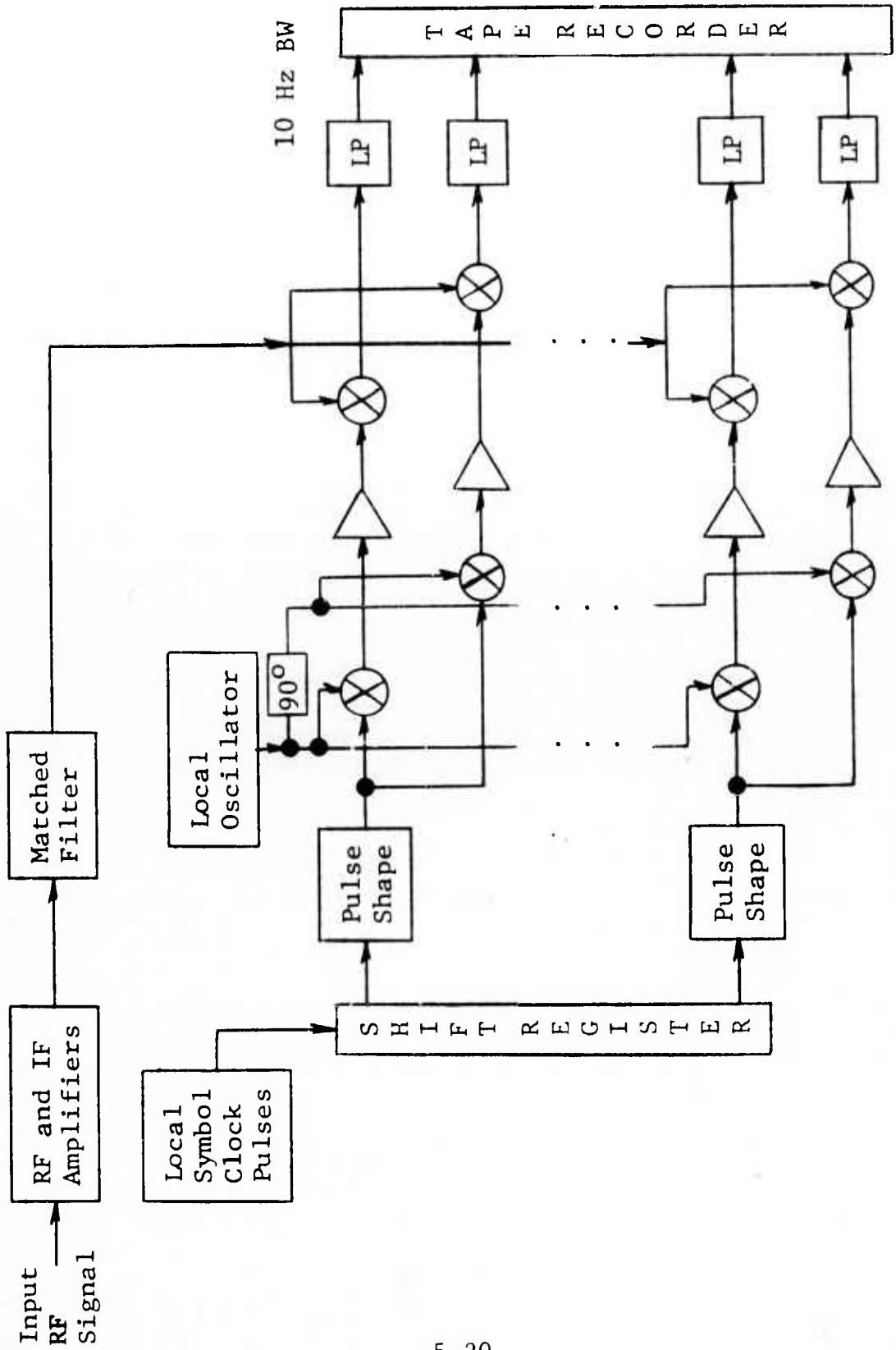


Figure 5.4 Simplified Block Diagram for Matched Filter Technique: Band-Pass Sampling

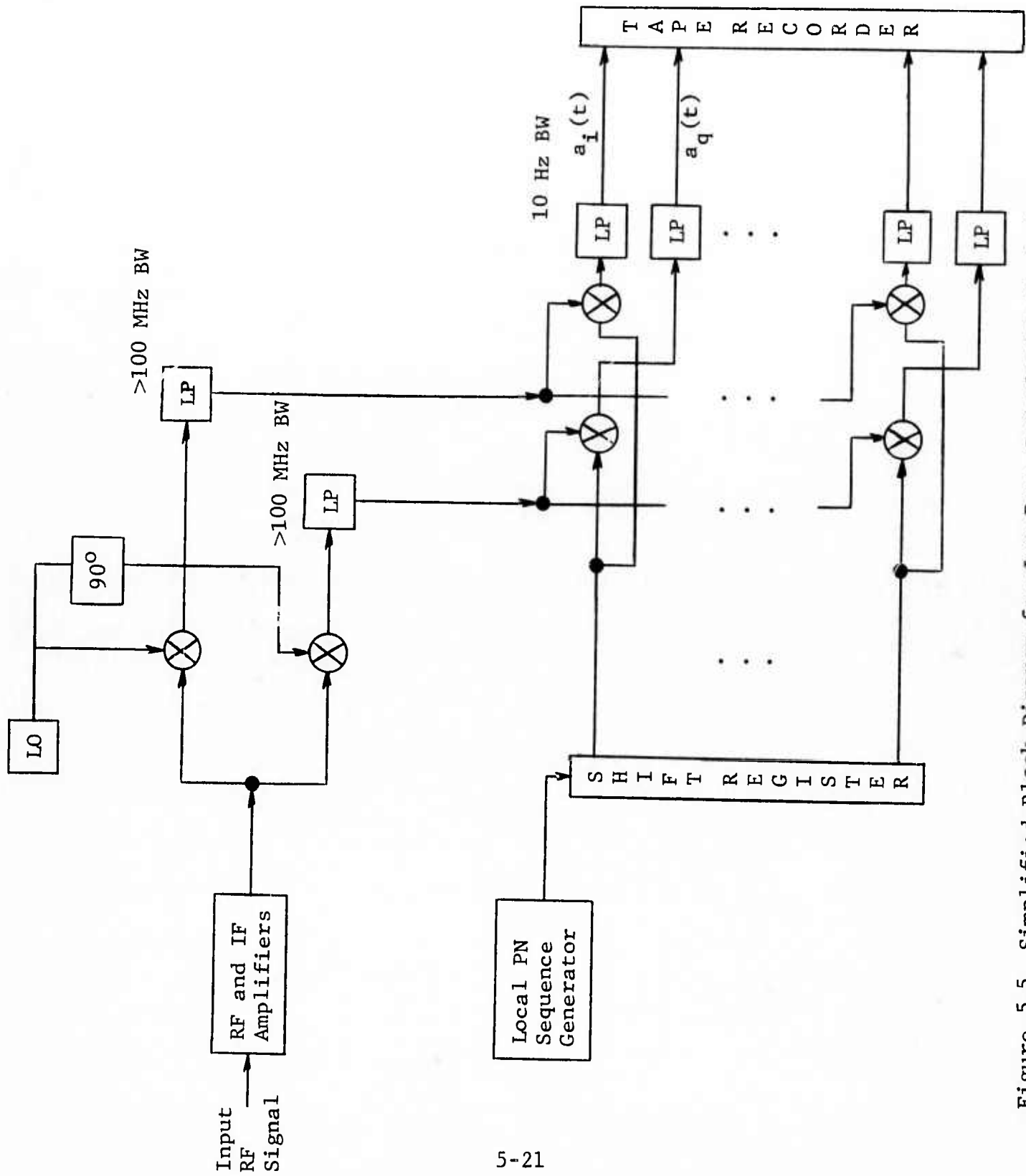


Figure 5.5 Simplified Block Diagram for Low Pass Correlation Technique

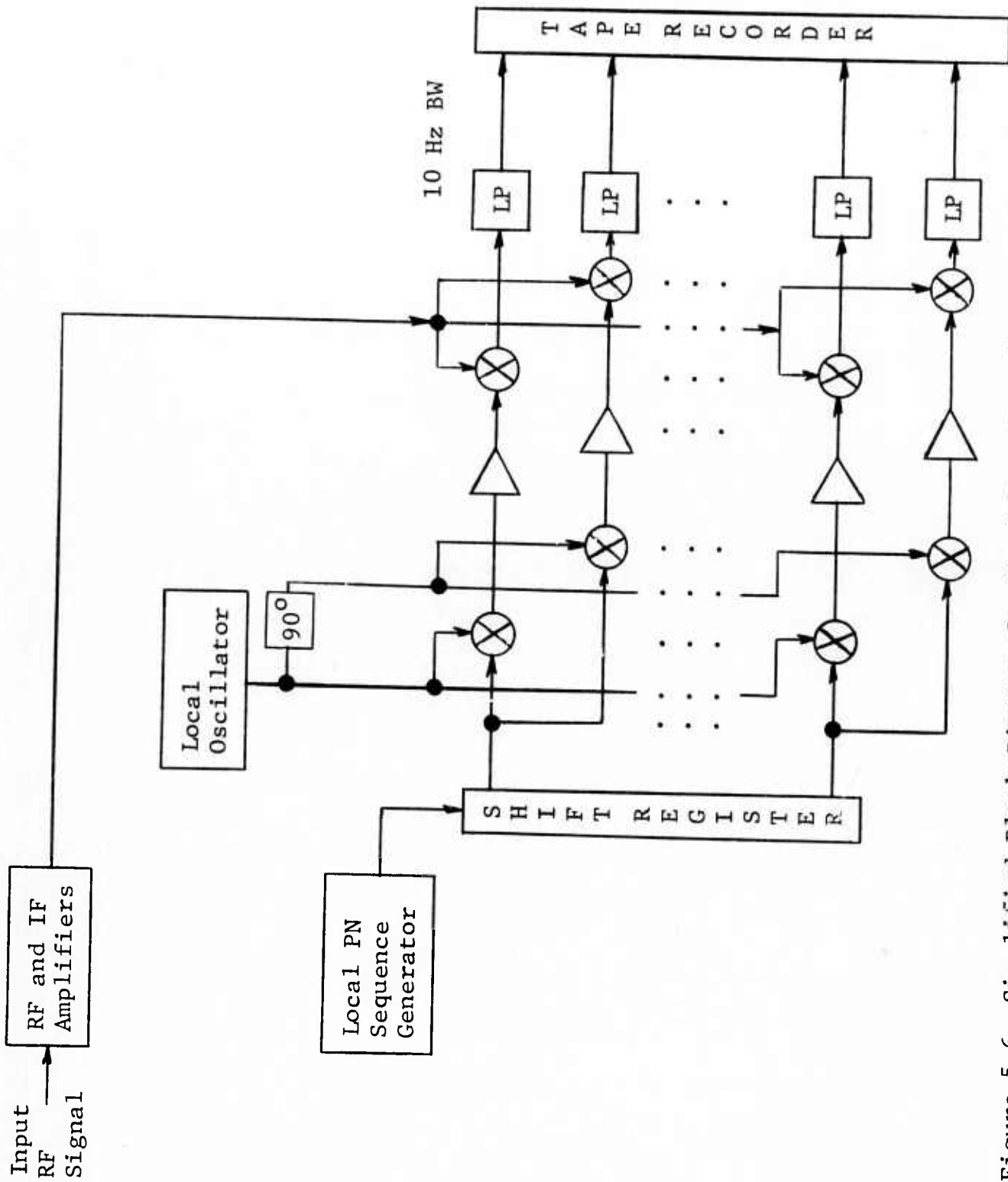


Figure 5.6 Simplified Block Diagram for Band-Pass Correlation Technique

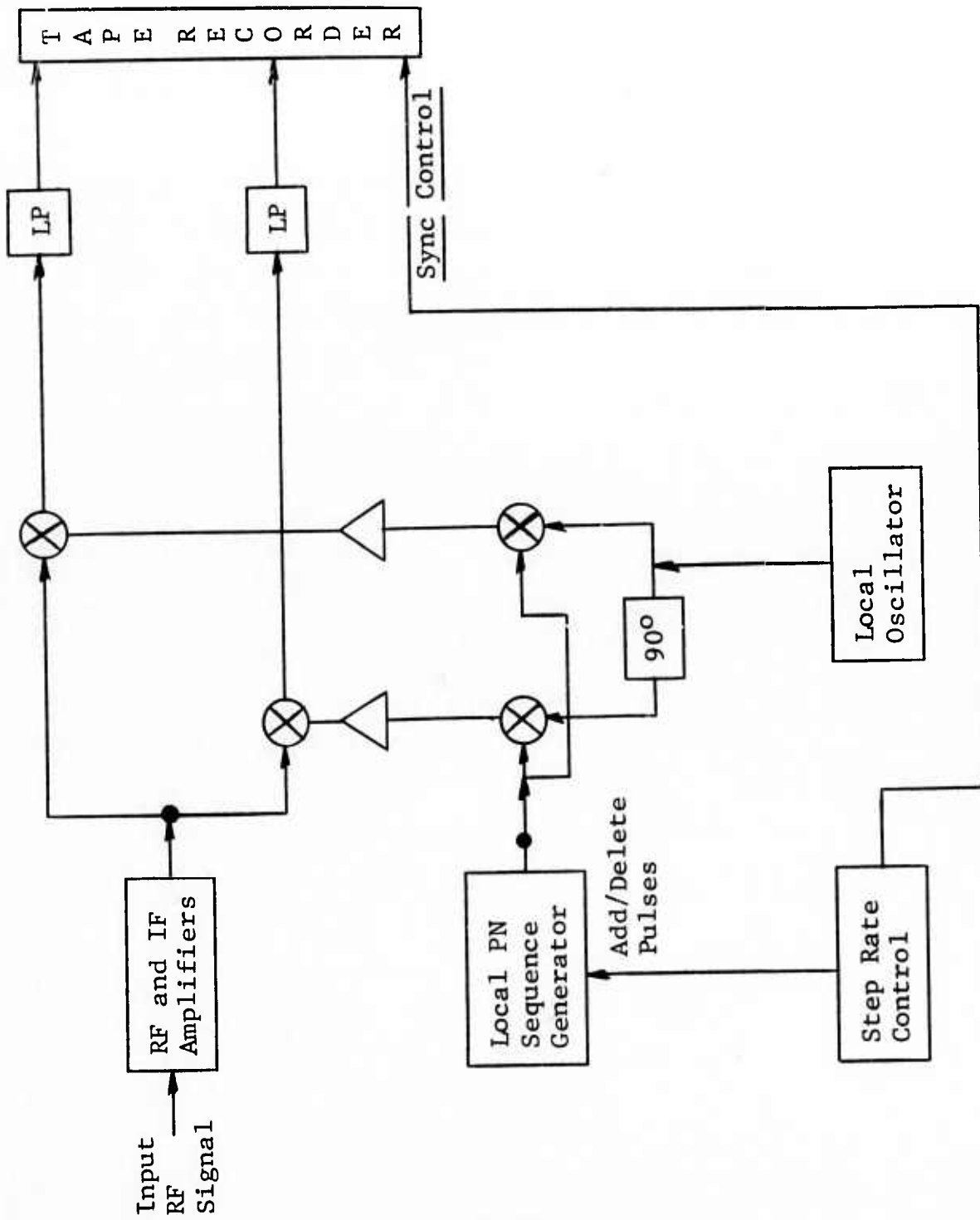


Figure 5.7 Simplified Block Diagram for Multiplexed Band-Pass Correlation Technique

successively stepped in time. This produces samples of (a_i, a_q) , (b_i, b_q) , etc., in succession eventually returning to (a_i, a_q) and repeating the process. The stepping can be produced by adding or deleting clock pulses. Control pulses obtained from the delay stepping electronics are applied to a separate track of the tape recorder. These would be used in demultiplexing the sampled $(a_i(t), a_q(t)), (b_i(t), b_q(t))$, etc. The simplicity of the receiver is evident in Fig. 5.7. As discussed in Appendix G, the only penalty in this system is a SNR loss at the output. However because of the very large processing gain of this system, it appears that trading reduced cost and complexity for reduced SNR makes sense. At any rate it should be noted that the system of Fig. 5.7 can be built to allow future up-dating to include parallel processing as in Fig. 5.6.

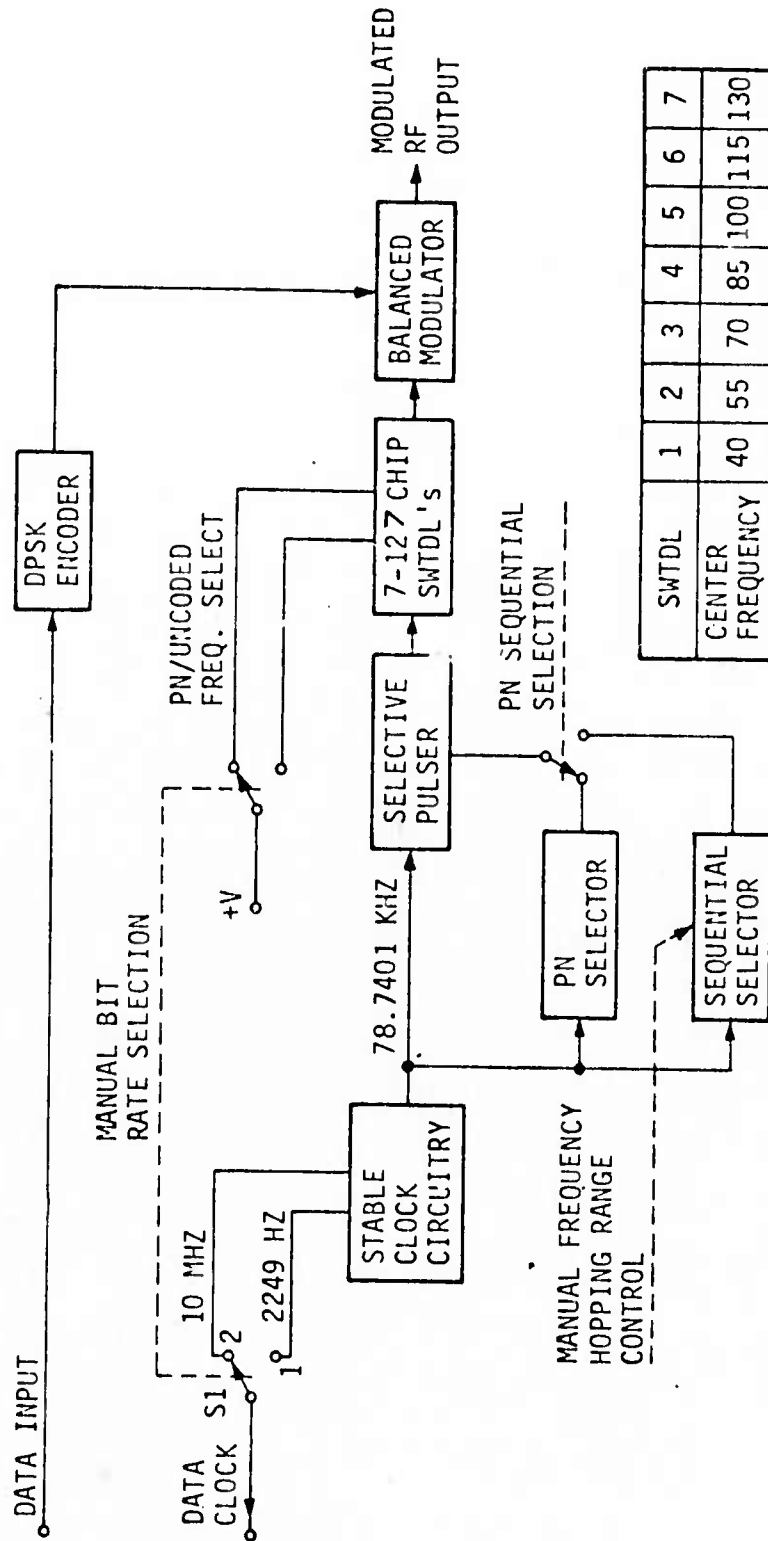
5.4 Use of Magnavox Frequency-Hopping PN Modem for Channel Probing

This section describes ways of using the Magnavox frequency-hopping PN modem in combination with a small amount of additional hardware for extracting useful channel parameter information. While both coherent and incoherent measurements will be discussed, the latter may be preferable because the proper operation of the coherent techniques depend rather critically upon the proper operation of the modem.

5.4.1 Description of Operating Modes to Use

We refer to Fig. 5.8* which describes the transmitter processing. Switch S_1 should be set to position 2, the manual frequency hopping range control should set the linear sequential hopping sequence to the 100 MHz bandwidth sweep (see Table 5-1 which indicates the set of IF frequencies for the frequency hops) and the data input should be set so that the balanced modulator output is unmodulated. When this is done the RF output consists of a sequence of RF pulses of 12.7 μ sec duration whose frequencies successively take on the values as indicated in Fig. 5.9, where f_0 is the RF center frequency (corresponding to the 85 MHz IF frequency). The method of design of the transmitter should produce coherent pulses at each frequency, so that, in principle, the complex amplitude of the channel transfer function can be measured at the receiver for each of the seven frequencies. Because the frequency hop waveforms are produced by pulsing IF filters with narrow video pulse, such coherence requires that the center frequencies of the filters be an integral multiple of the 78.7401 KHz pulsing rate. This is not exactly true for the center frequencies quoted by Magnavox (see Table 5-1). Nonetheless, it will be assumed that the center frequencies quoted are nominal values and that this integral relationship exists.

* Figures 5.8 and 5.10, and the information in Table 5-1 were obtained via private communication from RADC Project Engineer to CNR personnel.



SWTDL	1	2	3	4	5	6	7
CENTER FREQUENCY	40	55	70	85	100	115	130

Figure 5.8 Synthesizer Functional Diagram

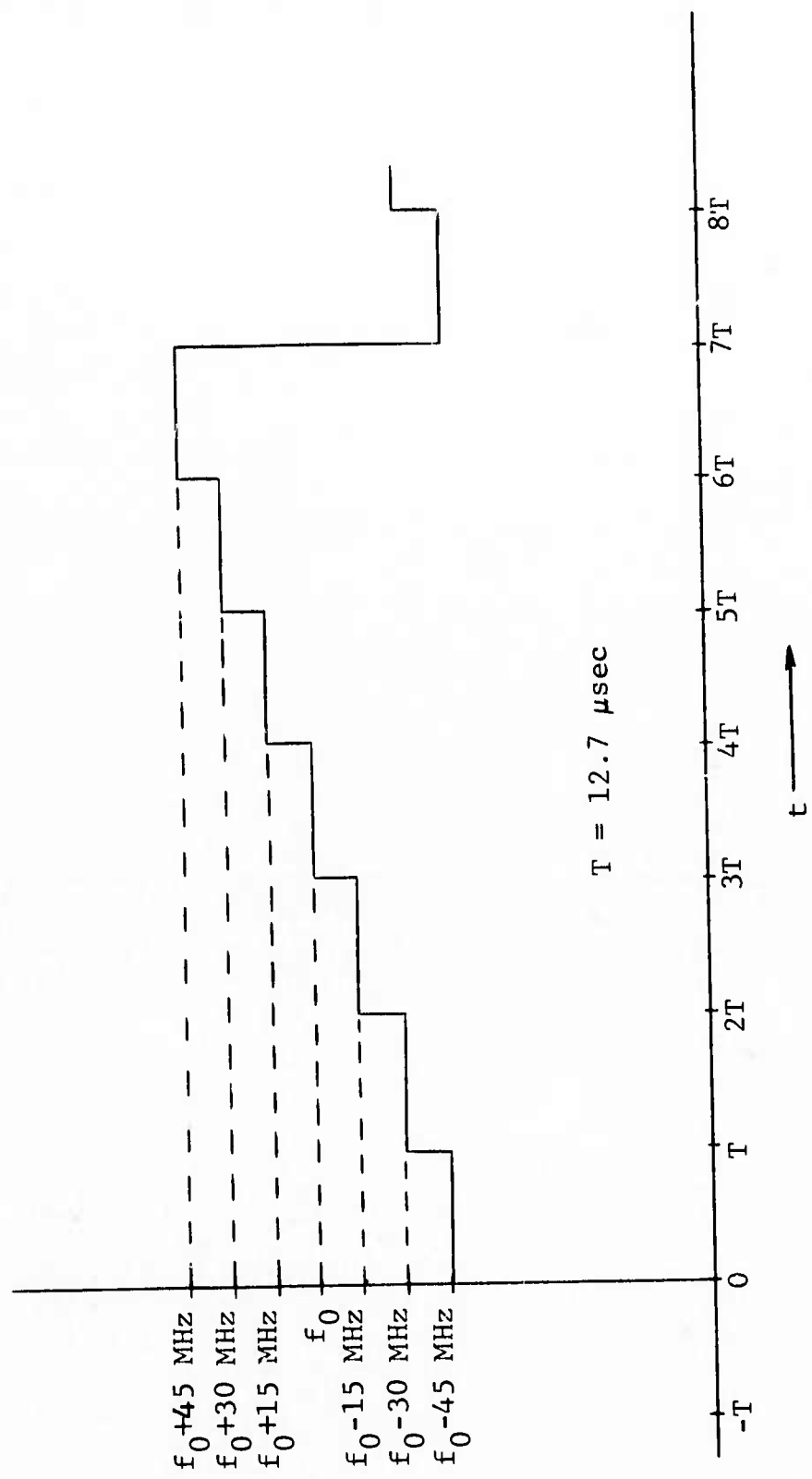


Figure 5.9 Frequency-Hopping Pattern For Probing Signal

Table 5-1
 SEQUENTIAL HOPPING SEQUENCES

<u>Output Signal Bandwidth*</u>	<u>Hop 1</u>	<u>Hop 2</u>	<u>Hop 3</u>	<u>Hop 4</u>	<u>Hop 5</u>	<u>Hop 6</u>	<u>Hop 7</u>	<u>Hop 8</u>
100 MHz	40 MHz	55 MHz	70 MHz	85 MHz	100 MHz	115 MHz	130 MHz	40 MHz
85 MHz	40 MHz	55 MHz	70 MHz	85 MHz	100 MHz	115 MHz	40 MHz	55 MHz
70 MHz	40 MHz	55 MHz	70 MHz	85 MHz	100 MHz	40 MHz	55 MHz	70 MHz
55 MHz	40 MHz	55 MHz	70 MHz	85 MHz	40 MHz	55 MHz	70 MHz	85 MHz
40 MHz	40 MHz	55 MHz	70 MHz	40 MHz	55 MHz	70 MHz	40 MHz	55 MHz
25 MHz	40 MHz	55 MHz	40 MHz	55 MHz	40 MHz	55 MHz	40 MHz	55 MHz
10 MHz	40 MHz	40 MHz	40 MHz	40 MHz	40 MHz	40 MHz	40 MHz	40 MHz

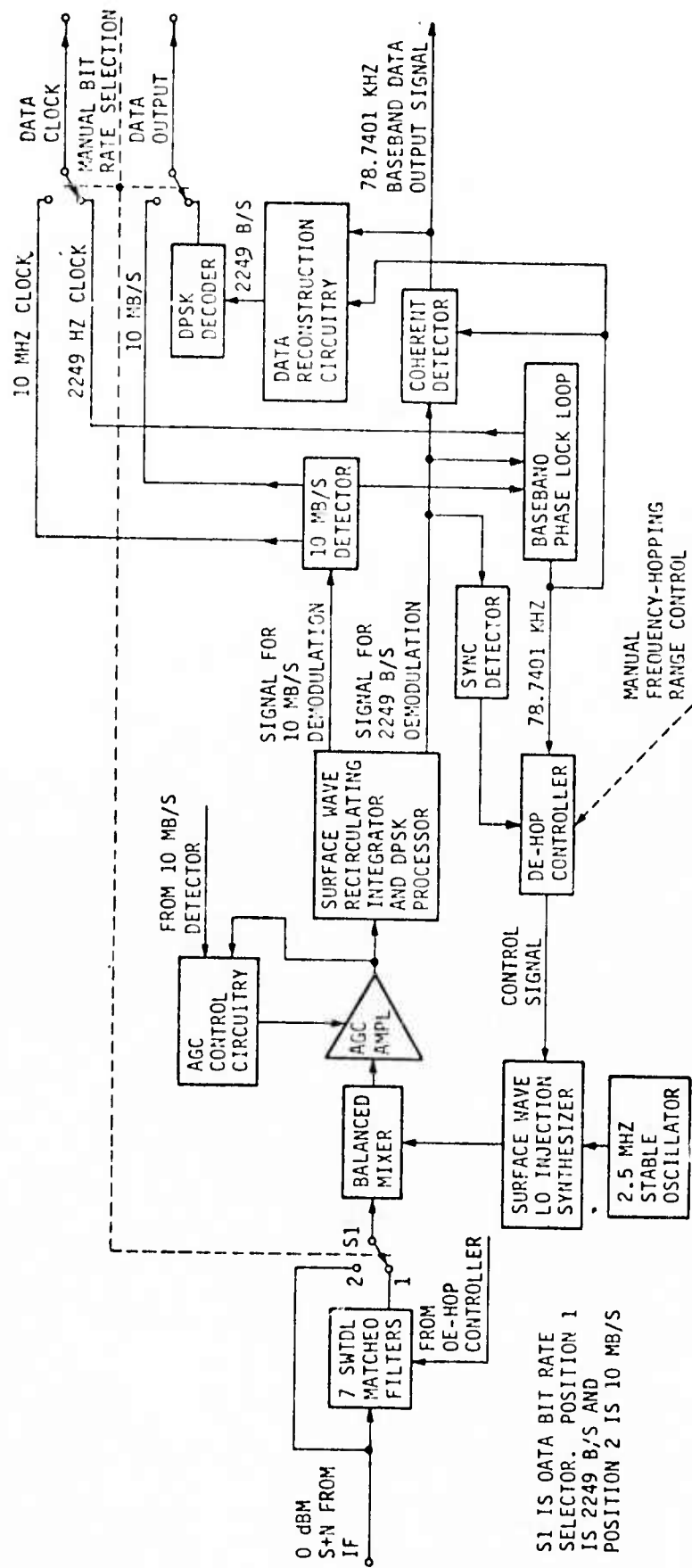
*The filters are pulsed phase-continuously, i.e., center frequency = integer x 78.7401.

We consider now the receiver operation. Figure 5.10 shows a block diagram of the receiver starting at IF (called the synchronizer). Again the switch S_1 is set at position 2. The frequency hopping is removed by means of the surface wave LO injection synthesizer/balanced mixer combination which sets the balanced mixer output to 85 MHz. If the frequency-hopping LO outputs are phased properly at each frequency, the balanced mixer output will be a sequence of 12.7 μ sec 85 MHz RF pulses whose complex amplitudes are the set of samples of the channel transfer function at the set of seven probed frequencies. If they are not phased properly, then at least the amplitude of the pulses will provide the correct amplitudes of the channel transfer function at these frequencies. Of course the AGC must be disabled to measure these amplitudes.

For coherent dehopping the IF frequencies used for dehopping to 85 MHz must be integral multiples of 78.7401 KHz. We shall assume nominal values for the frequencies quoted by Magnavox.

5.4.2 Channel Measurement and Recording

Figure 5.11 shows a portion of the receiver of Fig. 5.10 with some added processing indicated in dashed lines. The AGC amplifier output (gain manually set) is fed to an envelope detector whose output will be a nearly periodic pulse pattern with a shape dependent upon the degree of frequency selectivity and multipath spread of the channel. The rate of change will be very slow, say of the order of seconds. Figure 5.12 shows the



S1 IS DATA BIT RATE SELECTOR. POSITION 1 IS 2249 B/S AND POSITION 2 IS 10 MB/S

Figure 5.10 Synchronizer Functional Diagram

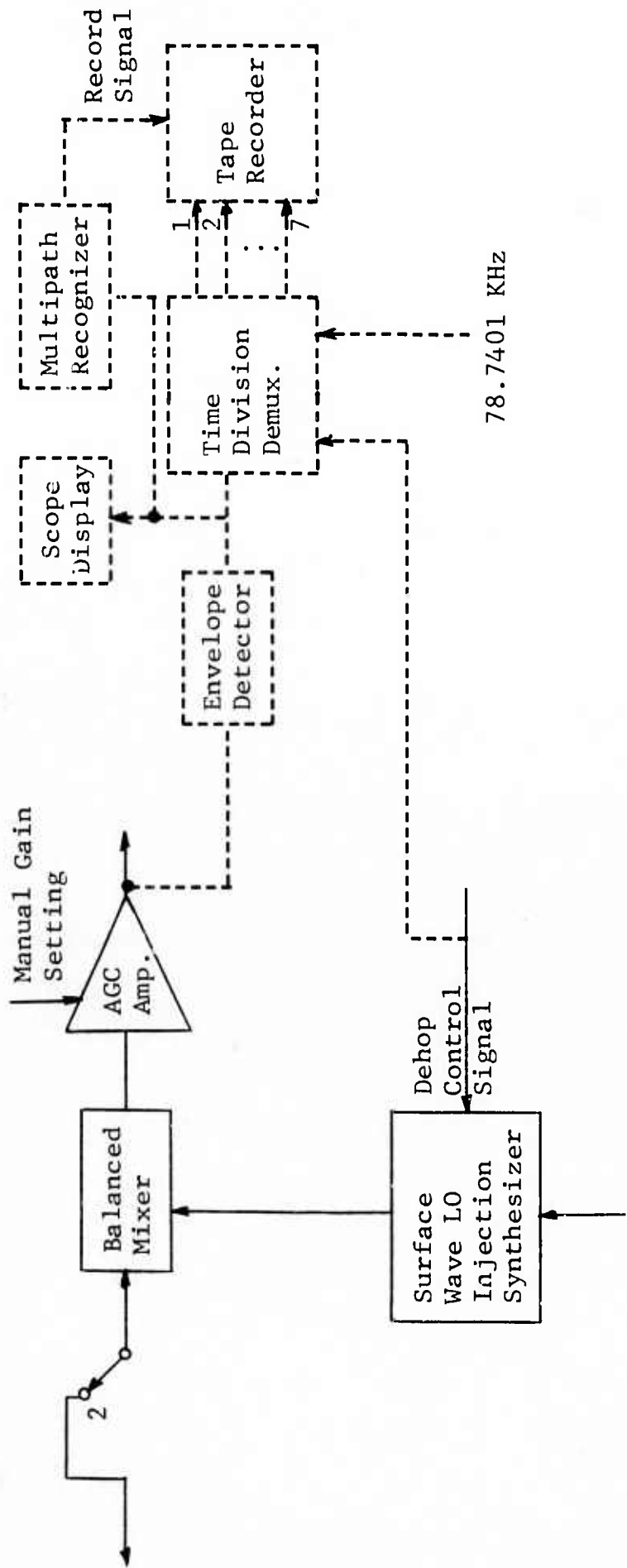
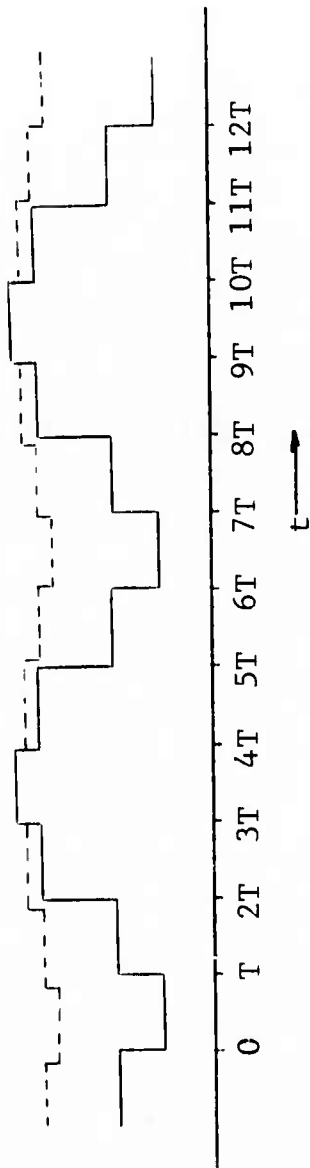


Figure 5.11 Measurement and Recording of Transfer Function Amplitude Samples

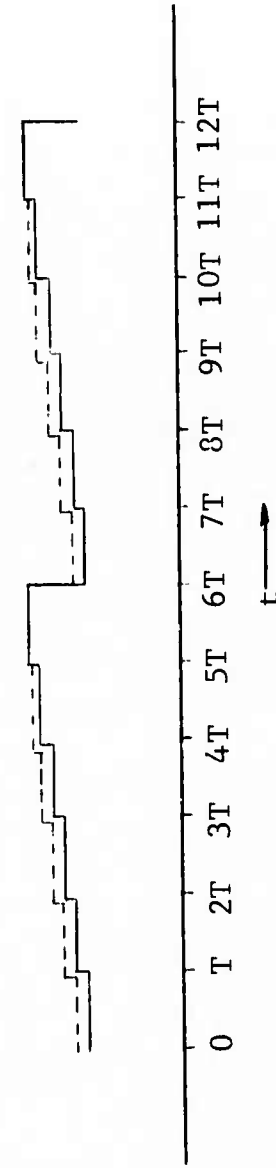
shape of the pattern for different two-path multipath spreads. In Fig. 5.12(a) the pattern corresponds to a two-path multipath condition producing nulls 100 MHz apart, which corresponds to a 10 ns delay between paths and nearly equal strength paths. The dashed line corresponds to the same multipath spread but with one path much bigger than the other. Fig. 5.12(b) corresponds to a multipath spread smaller than 10 ns.

The envelope detector output is fed to a time division demultiplexer which separately extracts and low pass filters the amplitude of each of the seven transfer function samples. The low-pass-filter bandwidth can be as low as 10 Hz because the channel is fading slowly. These seven slowly varying amplitudes can be fed to a seven track tape recorder. Alternatively one may remultiplex these seven channels into one TDM channel with a low switching rate of, say, 500 Hz. A third approach, which does not have the SNR improvement of the previous approaches and requires more tape for recording, is to record directly the output of the envelope detector containing the pulses occurring at 78.7401 KHz. A bandwidth of 150 Kc should probably be used in this application.

Because the phenomena of interest are expected to occur a small fraction of the time, a multipath recognizer is shown in Fig. 5.11 which recognizes the existence of frequency selective fading and starts the tape recorder. Algorithms for recognizing multipath and extracting channel parameter information are discussed in the following section.



(a) Two Paths
 Path Delay Difference = $\frac{1}{100 \text{ MHz}}$
 = 10 ns



(b) Multipath Spread < 10 ns

T = 12.7 μsec

Figure 5.12 Received Frequency Hop Patterns for Multipath Conditions

Coherent channel measurements would be undertaken through replacing the envelope detector by in-phase and quadrature coherent detectors, i.e., by two balanced mixers which are fed by a reconstructed 85 MHz carrier split into two 90° phase shifted components. (Hopefully this 85 MHz carrier is already present or readily derived in the receiver.) Because there are two detectors involved, there are two quasi-periodic sequences of $12.7 \mu\text{sec}$ pulses of period 7. The data acquisition and recording equipment must be modified in an obvious way to accommodate the two sequences.

5.4.3 Channel Parameter Extraction

Clearly more channel information can be extracted with the coherent approach and we consider this case first. If the equipment is working properly the tape recorded information supplies 7 uniformly spaced complex samples of the channel transfer function 15 MHz apart. From propagation studies it has become clear that the refractive anomalies producing the multipath condition lead to a discrete multipath condition with a few paths, usually two dominant paths. To estimate the detailed multipath structure two approaches may be used:

- a) Discrete Fourier transform of 7 complex samples with appropriate aperture weighting
- b) Least squares fitting of 7 complex samples to specific assumed multipath structures with unknown parameters.

The 15 MHz spacing between frequency samples implies that the impulse response to be measured (including terminal equipment filtering) should be less than $66 \frac{2}{3}$ nanoseconds long to prevent aliasing. The aperture weighting used on the samples

before the Fourier transform in a) should be designed to minimize the aliasing problem. A raised cosine aperture of 120 MHz width will result in a pulse of $16 \frac{2}{3}$ ns width for a single path.

With regard to b) we note that since there are 7 complex samples available, a multipath structure with 14 real parameters can be unambiguously estimated from the data. Thus up to a 5-path structure may be estimated (4 delays and 5 complex amplitudes) without ambiguity (paying due regard to the $66 \frac{2}{3}$ nano-second multipath restriction).

In the case of incoherent measurement only the magnitude of the channel transfer function samples is available. The Fourier transform of the squared magnitude of a transfer function is just the autocorrelation of the impulse response. Thus by applying the Fourier transform to the seven squared samples some multipath information can be gained. Least squares fitting for an assumed discrete impulse response autocorrelation function may also be tried. For example, for an assumed two-path structure one may estimate relative path strength and delay difference.

Simple measures of multipath spread or degree of frequency selectivity may be employed in order to recognize the existence of a multipath condition. A simple measure of degree of frequency selectivity is the average magnitude of the departure of the transfer function samples from the average magnitude of the transfer function. Thus let R_k equal the envelope at the k 'th frequency and

$$\overline{R(t)} = \frac{1}{7} \sum_{k=1}^7 R_k(t) \quad (5.1)$$

be the average transfer function amplitude over the seven frequencies. Then

$$A = \frac{\sum_{k=1}^7 |R_k(t) - \bar{R}(t)|}{\bar{R}(t)} \quad (5.2)$$

is a measure of frequency selectivity that is easily instrumented. When A exceeds some value (to be determined from the sensitivity of the system) a selective fading multipath condition may be assumed to exist.

When the multipath spread is sufficiently small, flat fading, i.e., non-selective fading, will occur. This condition may be identified by comparing $\bar{R}(t)$ to the values expected under normal propagation. Through this computation and the computation of A one may identify the three states: normal propagation, non-selective fading, frequency-selective fading.

SECTION 6
CONCLUSIONS AND RECOMMENDATIONS

As a result of this study the following conclusions have been reached:

- 1) No coherence bandwidth limitation exists in the 4 - 10 GHz band for the transmission of data with wide-band PN carriers. In contrast to conventional systems, performance improves as the PN carrier bandwidths become larger than the coherence bandwidth.
- 2) The most serious multipath threat to data transmission by PN carriers arises from refractive layers with steep negative gradients because this discrete multipath cannot be discriminated against by antennas. For ground-to-air links these layers must be tilted to produce multipath. Significant multipath is not likely to occur beyond elevation angles of $2 - 3^{\circ}$ in ground-air transmission.
- 3) When the discrete refractive multipath does occur, the multipath components can be delayed from a fraction of a nanosecond to tens of nanoseconds relative to the normal direct path. The multipath components are generally larger than the direct path. The PN carrier system may lock onto a stronger multipath component and then lose synchronization when the multipath component disappears due to the airplane moving into an interference-free region.
4. When two or more paths are being "tracked" by the PN carrier, severe fading of the output data signal will occur if the paths are of nearly equal strength. Addition of an extra PN carrier demodulator delayed less than a PN "chip" to obtain a multipath diversity channel can improve performance considerably.

- 5) A frequency-hopped PN carrier is subject to poor multipath resistance unless attention is given to adjust the probability distribution of frequency hops to produce a PN carrier autocorrelation function with low sidelobes.
- 6) Channel probing for characterization bandwidths less than 200 MHz should utilize a PN probing signal and a single time-multiplexed correlation demodulation, as discussed in Section 5.3. The resulting equipment is the most economical approach to meeting the twin goals of providing the essential data for channel parameter extraction and stored channel simulations.
- 7) The time and spatial, statistical nonstationarity of refractive multipath points to the need for a stored-channel simulation capability for development and comparative evaluation of modem concepts for RCV links.

As a result of these conclusions, the following recommendations for further work are presented to assure the effective development of RCV digital data modems for data transmission:

- a) Channel measurements should be conducted utilizing a suitable channel prober designed along the lines suggested in this study. Flight tests should be coordinated with synoptic measurements of refractive index. The channel measurements should be analyzed to validate the predicted multipath structures. In addition a playback unit should be fabricated to recreate the measured channels in the laboratory.
- b) An anti-multipath modem design study should be carried out. Not only the use of multipath diversity or Rake concepts should be considered, but also maximum likelihood and adaptive equalization approaches. Consideration should be given to the dynamic multipath "stealing" problem discussed in 3).

- c) The multipath fading will cause errors to occur in bursts. Error control procedures should be investigated to utilize decoding combined with channel measurements, since this combined approach is the most effective. Also the modem characteristics discussed in b) should be considered together with the coding-decoding and channel measurements for an overall optimization.
- d) The signal design problem for frequency hopping modems should be studied with a view to obtaining a PN autocorrelation function optimized for multipath rejection.

Appendix A
SYSTEM MODEL FOR LINEAR CHANNELS USING PN CARRIERS

The system to be analyzed is shown in Fig. A.1 where all indicated operations and signals are complex low-pass equivalent. The complex envelopes of the data, PN carrier, channel impulse response, input additive noise, input to low-pass filter, and output PN carrier demodulated signal are given by $d(t)$, $p(t)$, $g(t, \xi)$, $\eta(t)$, $u(t)$ and $v(t)$, respectively. Examination of Fig. A.1 shows that the input to the low-pass filter, $u(t)$, may be expressed as

$$u(t) = e^{j\psi} \int p^*(t-\tau)p(t-\xi)d(t-\xi)g(t, \xi) d\xi + \eta(t)p^*(t-\tau)e^{j\psi} \quad (\text{A.1})$$

where τ is slowly time varying due to a tracking loop and ψ is either a constant or slowly varying due to a tracking loop in a coherent system.

The product term $p^*(t-\tau)p(t-\xi)$ consists of a steady term plus a fluctuating wideband component. By averaging we determine that the steady component is given by

$$\overline{p^*(t-\tau)p(t-\xi)} = R(\tau-\xi) \quad (\text{A.2})$$

where $R(\tau)$ is the autocorrelation function of the probing signal.

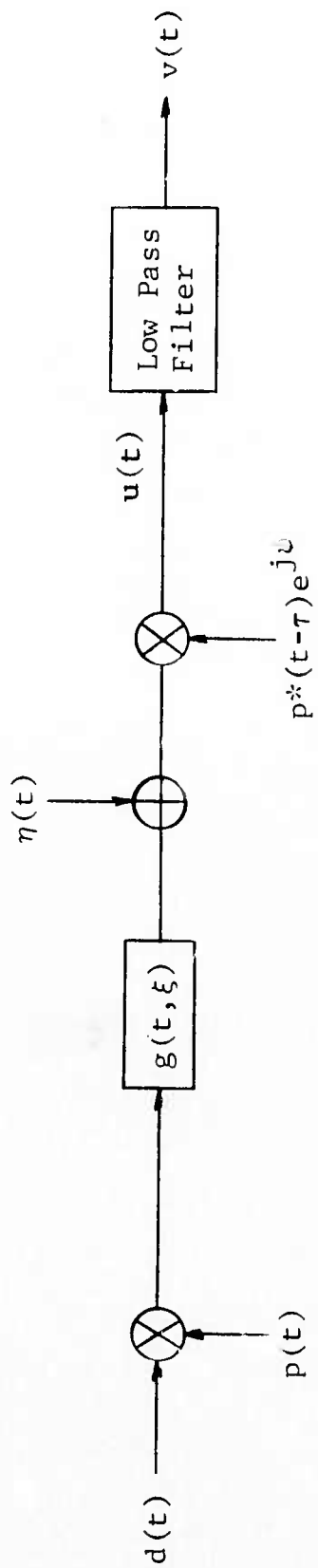


Figure A.1 Idealized Signal Processing Operations in a Linear Channel With PN Carrier Modulation and Demodulation

Letting

$$p^*(t-\tau)p(t-\xi) = R(\tau-\xi) + q(\tau, \xi, t) \quad (\text{A.3})$$

where $q(\tau, \xi)$ is the wideband fluctuating component, we find that (A.1) becomes

$$\begin{aligned} u(t) = & e^{j\psi} \int d(t-\xi)R(\tau-\xi)g(t, \xi) d\xi \\ & + e^{j\psi} \int q(\tau, \xi, t)d(t-\xi)g(t, \xi) d\xi \\ & + e^{j\psi}\eta(t)p^*(t-\tau) \end{aligned} \quad (\text{A.4})$$

The first term in (A.4) is the data signal term, the second is a self-noise term, and the third term is an additive noise term due to the external input additive noise $\eta(t)$. We consider each of these terms separately as far as their contribution to the output of the low-pass filter is concerned.

Note that the output data-signal term $s(t)$ is obtained by passing the input data signal $d(t)$ through an equivalent channel filter with impulse response equal to the product $R(\tau-\xi)g(t, \xi)$ in cascade with the low pass filter as shown in Fig. A.2.

When the frequency selectivity of the channel impulse response is small over the bandwidth of the input data signal, which will be true in the case of RCV links, it will also be small over the bandwidth of the equivalent filter impulse

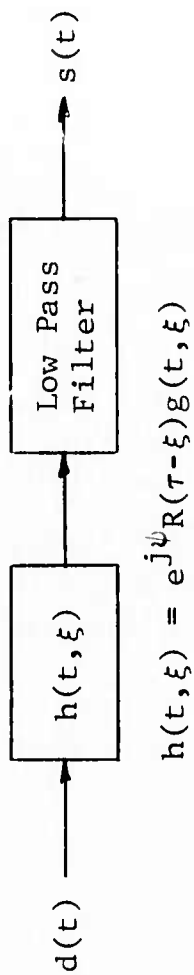


Figure A.2 Equivalent Channel Filter for Data Signal

response $h(t, \xi)$. Then the filter $h(t, \xi)$ may be replaced by a delay equal to the group delay at zero frequency (i.e., at carrier frequency in the real system) and a complex gain constant equal to the gain of $h(t, \xi)$ at zero frequency. The low pass filter will be transparent to the signal at the output of $h(t, \xi)$ in any case of practical interest because it is designed to pass $d(t)$ undistorted and the channel fading is slow enough not to significantly increase the bandwidth of its output signal. Thus with the above valid approximations the channel acts like a simple complex time-varying gain

$$s(t) = d(t - \tau_0) e^{j\psi} G(t, \tau) \quad (\text{A.5})$$

where

$$G(t, \tau) = \int R(\tau - \xi) g(t, \xi) d\xi \quad (\text{A.6})$$

Note that generally τ and ψ will be time-variant due to the action of tracking loops. This problem has been studied in Section 4.

The self noise term in (A.4) may be regarded as essentially white noise as far as the low-pass filter in Fig. A.1 is concerned. As long as the bandwidth of the low pass filter is very much smaller than that of the PN carrier, and the number of multipath components is small, which is true for RCV channels, the self noise may be shown to be negligible by comparison with the data signal.

The external additive noise term is white also and its output contribution is given by a noise of power-level $N_o B_N$ where N_o is the one-sided power density of the input additive noise, B_N is the noise-bandwidth of the low pass filter. In the previous statement the normalization

$$|p(t)|^2 = 1 \quad (A.7)$$

has been used.

Appendix B

EFFECT OF PROBABILITY DISTRIBUTION OF FREQUENCY HOPS ON CORRELATION FUNCTION OF PN CARRIER

The complex envelope of the transmitted signal corresponding to an M'ary frequency hopped N'ary PSK PN carrier may be expressed in the form

$$z(t) = \exp [j\phi(t)] \exp [j2\pi \int_0^t F(x) dx] \quad (\text{B.1})$$

where the first factor is the PN N'ary PSK modulation and the second factor is the PN FSK modulation. According to the definition of the autocorrelation function

$$R(\tau) = \overline{z^*(t)z(t+\tau)} \quad (\text{B.2})$$

Assuming that the PSK and FSK are statistically independent

$$R(\tau) = \overline{\langle \exp [j(\phi(t+\tau) - \phi(t))] \rangle} \cdot \overline{\langle \exp [j2\pi \int_t^{t+\tau} F(x) dx] \rangle} \quad (\text{B.3})$$

which is the product of the autocorrelation functions of each modulation considered separately. The overline indicates an ensemble average and the $\langle \rangle$ a time average.

We may express $\phi(t)$ and $F(t)$ in the form

$$\phi(t) = \sum_k \text{Rect} \left(\frac{t}{\Delta} - k \right) \phi_k \quad (\text{B.4})$$

$$F(t) = \sum_k \text{Rect} \left(\frac{t}{P\Delta} - k \right) F_k \quad (\text{B.5})$$

where

$$\text{Rect}(t) = \begin{cases} 1 & |t| < \frac{1}{2} \\ 0 & |t| \geq \frac{1}{2} \end{cases} \quad (\text{B.6})$$

is a rectangular pulse and ϕ_k , F_k are (pseudo) random phase shifts and frequency shifts (or hops), respectively, with the duration of a frequency hop equal to $P\Delta$ where Δ is the duration of a PSK bit.

Assuming that the phase shifts are selected so that no carrier component is present, i.e., that

$$\overline{\exp [j\phi_k]} = 0 \quad (\text{B.7})$$

the correlation function of the PSK signal is readily found to be the triangle

$$\overline{\langle \exp [j(\phi(t+\tau) - \phi(t))] \rangle} = \begin{cases} 1 - |\tau|/\Delta & ; \quad |\tau| < \Delta \\ 0 & ; \quad |\tau| \geq \Delta \end{cases} \quad (\text{B.8})$$

Because (B.8) is a factor in $R(\tau)$ (see (B.3)) it follows that the second average need only be evaluated for values of $|\tau| < \Delta$. We assume that $P \gg 1$. In this case the frequency is constant for many PSK bits and little error is incurred by using the approximation

$$\int_t^{t+\tau} F(x) dx \approx \tau F(x) \quad (\text{B.9})$$

Then

$$\begin{aligned} \overline{\langle \exp [j2\pi \int_t^{t+\tau} F(x) dx] \rangle} &\approx \overline{\exp [j2\pi F_k \tau]} ; \quad |\tau| < \Delta \\ &P \gg 1 \\ &= C(2\pi\tau) \quad (\text{B.10}) \end{aligned}$$

where

$$C(x) = \int W(F) e^{jFx} dF \quad (\text{B.11})$$

is the characteristic function of the probability distribution of frequency hops, $W(F)$.

Thus

$$R(\tau) = (1 - |\tau|/\Delta) C(2\pi\tau) \quad ; \quad |\tau| < \Delta, P \gg 1 \quad (\text{B.12})$$

We consider two examples

$$W_1(F) = \frac{1}{2P+1} \sum_{-P}^P \delta(F - \frac{P}{\Delta}) \quad (\text{B.13})$$

$$W_2(F) = \frac{1}{2P+1} \sum_{-P}^P (1 + \cos \pi \frac{P}{P}) \delta(F - \frac{P}{\Delta}) \quad (\text{B.14})$$

In these cases for $P \gg 1$

$$R_1(\tau) \approx (1 - |\tau|/\Delta) \text{sinc} [2P\tau/\Delta] \quad ; \quad P \gg 1 \quad (\text{B.15})$$

$$R_2(\tau) \approx (1 - |\tau|/\Delta) \text{sinc} [P\tau/\Delta] \left(\frac{\cos \pi P\tau/\Delta}{1 - 4P^2 \tau^2/\Delta^2} \right) \quad ; \quad P \gg 1 \quad (\text{B.16})$$

Note that while the tails of $R_1(\tau)$ drop to zero slowly, $R_2(\tau)$ is negligible for $|\tau| < \Delta/P$.

Appendix C

CALCULATIONS OF VARIANCES OF NOISE TERMS

The purpose of this appendix is to calculate the variances and correlation of the noise terms N_1 and N_2 appearing in the diversity channel outputs (Eqs. (4.36) and (4.37)). We assume white Gaussian noise at the receiver input. Therefore the noise $n(t)$ appearing at the detector is the result of passing white noise through the assumed Gaussian filter in the receiver front-end. Writing $n(t)$ in terms of co-phasal and quadrature components:

$$n(t) = n_c(t) \cos \omega_c t + n_s(t) \sin \omega_c t \quad (\text{C.1})$$

we have

$$S_{n_c}(\omega) = S_{n_s}(\omega) = |H(\omega)|^2 \frac{N_0}{2} \quad (\text{C.2})$$

The assumed filter transfer function (see Appendix M) gives

$$|H(\omega)|^2 = e^{-2\alpha\omega^2} \quad (\text{C.3})$$

so by transforming (C.2) we have

$$R_n(t) \triangleq R_{n_c}(t) = R_{n_s}(t) = \frac{N_0}{4\sqrt{2\pi\alpha}} e^{-t^2/8\alpha} \quad (\text{C.4})$$

Referring to Fig. 4.14 we see that the channel 1 noise term may be written as

$$\begin{aligned}
N_1 &= \frac{\cos \theta}{T} e \int_0^T x(t-t_e) n_c(t) dt \\
&+ \frac{\sin \theta}{T} e \int_0^T x(t-t_e) n_s(t) dt
\end{aligned} \tag{C.5}$$

Writing the first term as N_{1c} and the second as N_{1s} it is simple to show that

$$\overline{N_{1c} N_{1s}} = 0 \tag{C.6}$$

$$\overline{N_{1c}^2} = \frac{\cos^2 \theta}{T^2} e \int_0^T dt \int_0^T ds R_x(t-s) R_n(t-s) \tag{C.7}$$

and

$$\overline{N_{1s}^2} = \frac{\sin^2 \theta}{T^2} e \int_0^T dt \int_0^T ds R_x(t-s) R_n(t-s) \tag{C.8}$$

where $R_x(t)$ is the correlation function of the unfiltered PN sequence. Hence,

$$\overline{N_1^2} = \overline{(N_{1c} + N_{1s})^2} = \frac{1}{T^2} \int_0^T dt \int_0^T ds R_x(t-s) R_n(t-s) \tag{C.9}$$

Similarly, the channel 2 output may be written as

$$N_2 = N_{2c} + N_{2s} \quad (C.10)$$

where

$$N_{2c} = \frac{\cos \theta \Delta}{T} \int_0^T x(t-t_e-\Delta)n_c(t) dt \quad (C.11)$$

$$N_{2s} = \frac{\sin \theta \Delta}{T} \int_0^T x(t-t_e-\Delta)n_s(t) dt \quad (C.12)$$

and it may be shown that

$$\overline{N_2^2} = \frac{1}{T^2} \int_0^T dt \int_0^T ds R_x(t-s)R_n(t-s) \quad (C.13)$$

Finally, the cross-correlation term may be computed, giving

$$\overline{N_{1c}N_{2s}} = \overline{N_{1s}N_{2c}} = 0 \quad (C.14)$$

$$\overline{N_{1c}N_{2c}} = \frac{\cos \theta_e \cos \theta \Delta}{T^2} \int_0^T dt \int_0^T ds R_x(t-s+\Delta)R_n(t-s) \quad (C.15)$$

and

$$\overline{N_{1s}N_{2s}} = \frac{\sin \theta_e \sin \theta \Delta}{T^2} \int_0^T dt \int_0^T ds R_x(t-s+\Delta)R_n(t-s) \quad (C.16)$$

Combining these last three results gives

$$\overline{N_1 N_2} = \frac{\cos(\theta_e - \theta_\Delta)}{T^2} \int_0^T dt \int_0^T ds R_x(t-s+\Delta) R_n(t-s) \quad (C.17)$$

The preceding results may all be expressed in terms of one integral. That is,

$$\overline{N_1^2} = \overline{N_2^2} = f(0) \quad (C.18)$$

and

$$\rho = \frac{\overline{N_1 N_2}}{\sqrt{\overline{N_1^2} \overline{N_2^2}}} = \frac{f(\Delta)}{f(0)} \cos(\theta_e - \theta_\Delta) \quad (C.19)$$

where

$$f(\Delta) \triangleq \frac{1}{T^2} \int_0^T dt \int_0^T ds R_x(t-s+\Delta) R_n(t-s) \quad (C.20)$$

If we note that since the integrand is non-zero only for values of $|t-s|$ very much less than T , we may approximate this very accurately by the single integral

$$f(\Delta) = \frac{\sqrt{2}}{T} \int_{-\infty}^{\infty} R_x(u-\Delta) R_n(u) du \quad (C.21)$$

To evaluate this further we substitute the functional form of $R_x(t)$:

$$R_x(t) = \begin{cases} 1 - |t| & |t| \leq 1 \\ 0 & |t| > 1 \end{cases} \quad (C.22)$$

and the functional form of $R_n(t)$ from Eq. (C.4). Omitting the straightforward integration, the result is

$$\begin{aligned} f(\Delta) = & \frac{N_0}{2\sqrt{2} T} \left[2\Delta \operatorname{erfc} \left(\frac{\Delta}{2\sqrt{2\alpha}} \right) - (\Delta-1) \operatorname{erfc} \left(\frac{\Delta-1}{2\sqrt{2\alpha}} \right) \right. \\ & \left. - (\Delta+1) \operatorname{erfc} \left(\frac{\Delta+1}{2\sqrt{2\alpha}} \right) \right] \\ & + \frac{N_0}{T} \sqrt{\frac{\alpha}{\pi}} \left[e^{(\Delta-1)^2/8\alpha} - 2e^{-\Delta^2/8\alpha} + e^{-(\Delta+1)^2/8\alpha} \right] \quad (C.23) \end{aligned}$$

Appendix D
THE EQUATIONS OF GEOMETRIC OPTICS

Each component ψ of the transmitted field can be represented by the scalar wave equation

$$\nabla^2 \psi + k_0^2 n^2 \psi = 0 \quad (D.1)$$

where $k_0 = \frac{2\pi}{\lambda_0}$ is the free space wavenumber and n is the refractive index along the propagation path. Assuming ψ has amplitude A and phase $k_0 n S$, which are arbitrary real functions of position, i.e.,

$$A \exp(-jk_0 n S) \quad (D.2)$$

then substituting Eq. (D.2) into (D.1) yields the approximate formula

$$\left(\frac{\partial S}{\partial x}\right)^2 + \left(\frac{\partial S}{\partial y}\right)^2 + \left(\frac{\partial S}{\partial z}\right)^2 = n^2 \quad (D.3)$$

where x , y and z are the Cartesian coordinates of the communication link. Equation (D.3) is an approximation known as the equation of the eikonal, which is valid under the two conditions that, in a distance equal to the wavelength of radiation,

- (1) The index of refraction does not change appreciably
- (2) The fractional change in the spacing between adjacent rays must be small compared to unity.

The largest wavelength for the proposed RCV application is $\lambda = 7.5$ cm. ($f_0 = 4$ GHz). Using the steepest refractivity gradient given by Eq. (3.6) of Section 3.2.1.2, the percentage change in n over a distance equal to λ is $\approx 3 \times 10^{-6}$. Thus condition (1) is certainly satisfied in tropospheric links. Work done by Wong [3.5] indicates that in the presence of atmospheric layers, the rays travel in well defined bundles. Within each of these bundles, condition (2) is satisfied at all but a finite number of caustic points. At these caustics, which are formed by the intersection of adjacent rays, the ray theory can be slightly modified [3.41], [3.42] to provide approximate field intensity. In the other regions where the separate ray bundles intersect, the relative amplitudes and phases of each bundle can be calculated from ray theory, since each satisfies condition (2). These regions are known as multipath regions, interference regions, and radio anti-holes.

The differential equation which governs the ray trajectories can be derived from a simple geometric analysis and the eikonal equation [3.22]

$$\frac{d\hat{t}}{d\sigma} = \frac{\nabla n \cdot \hat{u}}{n} \hat{u} \quad (D.4)$$

where \hat{t} is a unit vector along the ray trajectory σ , and \hat{u} is a unit vector along the eikonal S . Note from (D.2) that an eikonal is simply a surface of constant phase. Now the rate of change of \hat{t} along σ is simply the reciprocal of the radius of curvature of the ray. Therefore (D.4) can be written as

$$\frac{1}{R} = \frac{-|\nabla n| \sin \gamma}{n} \quad (D.5)$$

where γ is the angle between \hat{t} and ∇n , and R is the local radius of curvature of the ray. For the RCV application considered here, the ray trajectories are nearly horizontal and the n -gradients are nearly vertical, therefore

$$\sin \gamma \approx 1 \quad \text{for RCV application} \quad (D.6)$$

It should also be noted that the refractive index is very nearly unity, i.e.,

$$n \approx 1 \quad (D.7)$$

Therefore, Eq. (D.5) can be very closely approximated by

$$\frac{1}{R} = -|\nabla n| \quad (D.8)$$

Thus for linear n -profiles in which ∇n is constant, the ray trajectories are circles. To a first approximation this linear model can be used to develop ray tracings in the troposphere. In this contract report, the linear profile was used exclusively, and in the later part of the study the multi-layer linear profile (i.e., piecewise linear) was used.

The delay that a signal experiences in traveling from point a to b is given by

$$\xi = \int_a^b \frac{d\sigma}{c} \quad (\text{D.9})$$

which can be written as

$$\xi = \frac{1}{c_0} \int_a^b n \, d\sigma \quad (\text{D.10})$$

since the refractive index is defined as the ratio of the speed of propagation in free space to that along the ray trajectory, i.e.,

$$n = \frac{c_0}{c} \quad (\text{D.11})$$

It is instructive to examine

$$\frac{d}{d\sigma} (n\hat{t}) = n \frac{d\hat{t}}{d\sigma} + \hat{t} \frac{dn}{d\sigma} \quad (\text{D.12})$$

Substituting Eq. (D.4) into (D.12) and noting that the gradient is defined by

$$\frac{dn}{d\sigma} = \nabla n \cdot \hat{t} \quad , \quad (\text{D.13})$$

we get

$$\frac{d}{d\sigma} (n\hat{t}) = (\nabla n \cdot \hat{u})\hat{u} + (\nabla n \cdot \hat{t})\hat{t} \quad (\text{D.14})$$

or

$$\frac{d}{d\sigma} (n\hat{t}) = \nabla n \quad (D.15)$$

From the calculus of variations, Eq. (D 15) is known as the Euler equation and is the condition necessary to minimize the integral (D.10). Thus, a ray trajectory can be interpreted as that path which locally minimizes the delay from transmitter to receiver. This is also known as Fermat's principle.

For the vertical gradient n-profiles used in this report, it can be shown that along any ray, Snell's law is satisfied. For a flat earth with a vertical gradient, this can be expressed as

$$n \sin \gamma = \text{constant} \quad (D.16)$$

whereas for a spherical earth with a radial gradient

$$nr \sin \gamma = \text{constant} \quad (D.17)$$

This second form of Snell's law is of course more useful for a stratified atmosphere over the spherical earth. However, by performing a convenient coordinate transformation which effectively flattens the earth and modifies the refractive index structure, one can use the form of Snell's law given by Eq. (D.16). This is discussed in Section 3.2.1.3.

Appendix E
THE DIRECT PATH

The direct path leaves the transmitter at an angle α_T and is received at an angle α_R (see Fig. E.1). The range L of the receiver is given by

$$L = R_0(\sin \alpha_T + \sin \alpha_R) \quad (\text{E.1})$$

and the difference in heights of R and T is given by

$$h_R - h_T = -R_0(\cos \alpha_T - \cos \alpha_R) \quad (\text{E.2})$$

Eliminating α_T from Eqs. (E.1) and (E.2) and solving for α_R , gives

$$\sin \alpha_R = \frac{L}{2R_0} \pm \frac{h_R - h_T}{2R_0} \sqrt{\left(\frac{2R_0}{S}\right)^2 - 1} \quad (\text{E.3})$$

where S is the slant range given by

$$S^2 = (h_R - h_T)^2 + L^2 \quad (\text{E.4})$$

Now when R_0 approaches $\pm\infty$, the direct path becomes a straight line and

$$\lim_{R_0 \rightarrow \pm\infty} \sin \alpha_R = -\frac{h_R - h_T}{S} \quad (\text{E.5})$$

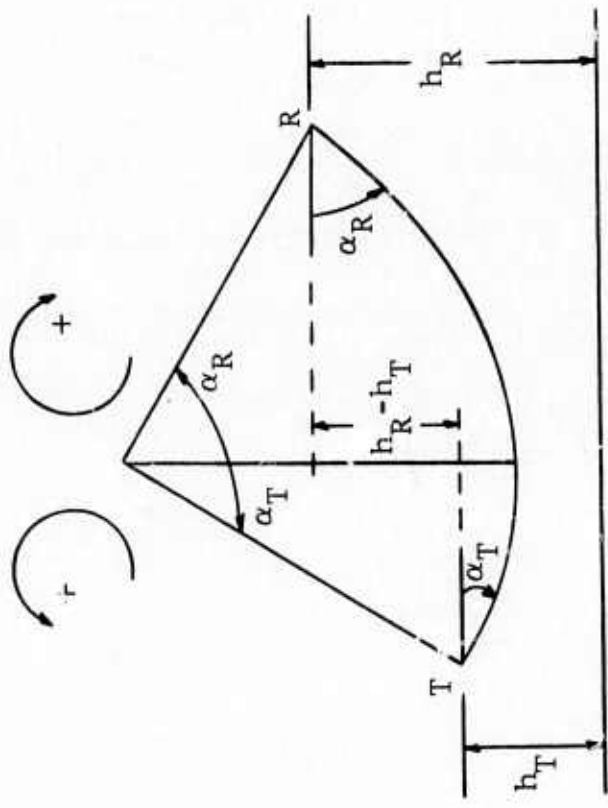


Figure E.1 The Direct Path

Taking the limit of Eq. (E.3) as $R_0 \rightarrow +\infty$, and comparing it to (E.5) indicates that the minus sign should be used in the evaluation of $\sin \alpha_R$, i.e.,

$$\sin \alpha_R = \frac{1}{2R_0} - \frac{h_R - h_T}{2R_0} \sqrt{\left(\frac{2R_0}{S}\right)^2 - 1} \quad (\text{E.6})$$

Substituting (E.6) into (E.1) gives α_T as

$$\sin \alpha_T = \frac{L}{2R_0} + \frac{h_R - h_T}{2R_0} \sqrt{\left(\frac{2R_0}{S}\right)^2 - 1} \quad (\text{E.7})$$

The normalized parameters k_T and k_R are given by

$$k_{T,R} = \frac{2R_0}{L} \sin \theta_{T,R} \quad (\text{E.8})$$

from which

$$k_T = 1 + \frac{h_R - h_T}{L} \sqrt{\left(\frac{2R_0}{S}\right)^2 - 1} \quad (\text{E.9})$$

$$k_R = 1 - \frac{h_R - h_T}{L} \sqrt{\left(\frac{2R_0}{S}\right)^2 - 1} \quad (\text{E.10})$$

Note that in order to have real solution for k_T and k_R it is necessary that the diameter of the ray trajectory be greater than the slant range,

$$2R_0 \geq S \quad (E.11)$$

This should be satisfied for all RCV applications.

Substituting Eqs. (E.9) and (E.10) into Eq. (3.23) gives the direct path delay

$$\xi_{\text{direct}} = \frac{L}{c_0} - \frac{L^3}{24R_0^2 c_0} \left\{ 1 + 3 \left(\frac{h_R - h_T}{L} \right)^2 \left[\left(\frac{2R_0}{S} \right)^2 - 1 \right] \right\} \quad (E.12)$$

The variation in the power of the direct path as a function of range L is given by Eq. (3.31) as

$$P_{\text{direct}} \sim \frac{I_{\text{direct}}}{I\Omega} \frac{1}{L \sin \theta^T} \frac{\partial \alpha^T}{\partial L} \quad (E.13)$$

This is easily evaluated from Eq. (E.7) as

$$P_{\text{direct}} \sim \frac{\frac{1}{2R_0} - \frac{(h_R - h_T)}{L^2}}{\frac{L^2}{2R_0} + (h_R - h_T)} \quad (E.14)$$

Note that when $R_0 \rightarrow \infty$, (i.e., free space) $P_{\text{direct}} \sim \frac{1}{L^2}$ as expected. Also, $P \sim \frac{1}{L^2}$ when $h_R = h_T$ or when $\frac{L^2}{2R_0} \gg (h_R - h_T)$.

Appendix F

CALCULATIONS FOR SINGLE STRATIFIED LAYER ABOVE TERMINALS

General Analysis

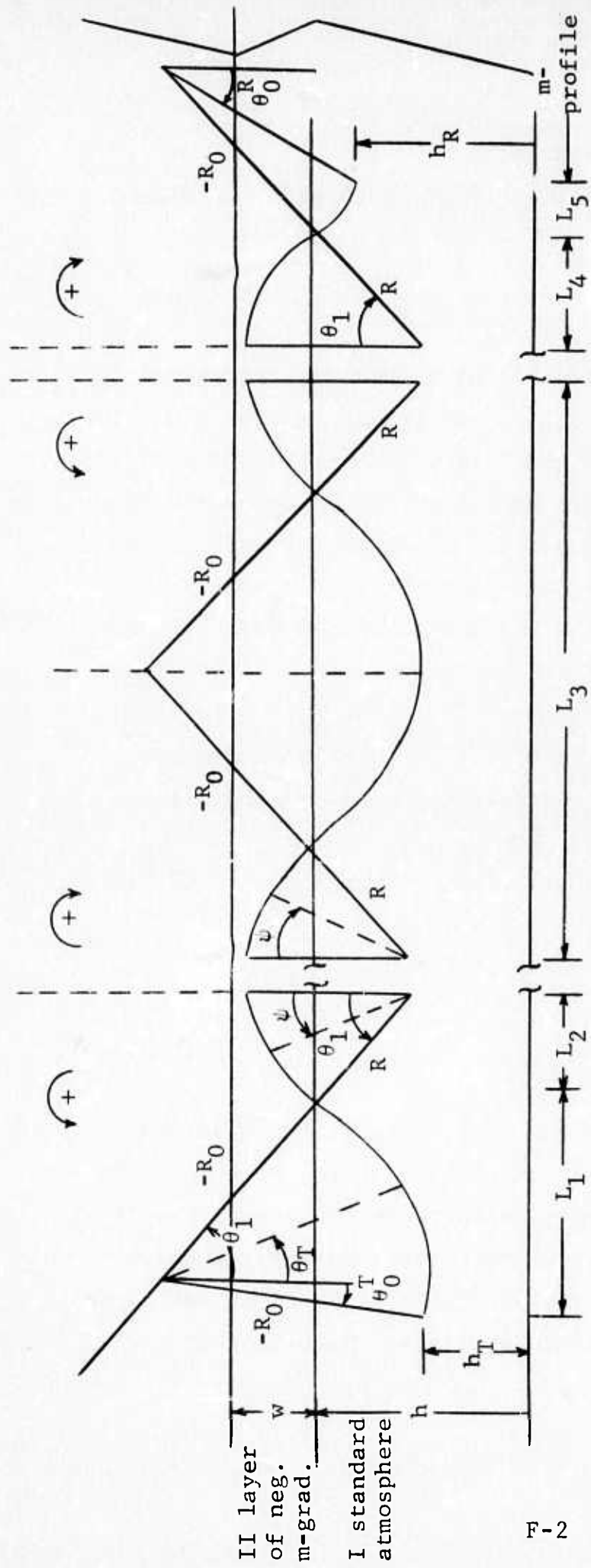
The transmitter T is located at h_T and the receiver R at h_R . The height of the layer is h and it has thickness w . The distance measured along the earth from T to R is L (see Fig. F.1). Angles associated with ascending trajectories are considered positive when measured CCW, while angles associated with descending trajectories are positive when measured CW. The coordinate transformation has been effected which results in a flat earth and a modified refractive index profile (see Fig. 3.6). Rays which bend toward the earth have a positive curvature and those bending away have a negative curvature. The radius of curvature of a ray is given by Eq. (3.19) as

$$R = -1 / \left(\frac{\partial m}{\partial z} \right) \quad (\text{F.1})$$

where

$$m = n(1+z/a) \approx n+z/a \quad (\text{F.2})$$

With the m -profile shown in Fig. F.1, rays in the layer are bent toward the earth, while outside the layer, rays are bent away from the earth. Any rays which reach the top of the layer escape and do not return to the receiver. Therefore, only those rays which are refracted back towards earth in the layer are considered in the multipath analysis. Note that it is



There may be n of these sections $n=0,1,2,\dots$

F-2

$$L_1 = R_0 (\sin \theta_0^f - \sin \theta_1)$$

$$L_2 = R \sin \theta_1$$

$$L_3 = 2(R-R_0) \sin \theta_1$$

$$L_4 = R \sin \theta_1$$

$$L_5 = R_0 (\sin \theta_0^R - \sin \theta_1)$$

Figure F.1 Geometry of Single Stratified Layer Above Terminals

possible for a ray to be continually refracted between regions I and II a total of n times ($n = 0, 1, \dots$) in traveling from T to R. This is illustrated in Fig. F.1 by a single section of length L_3 .

In the region I below the layer, the (modified) refractive index will be assumed linear with a positive slope g_0 ,

$$m = m_0 + g_0 z \quad (\text{F.3})$$

The actual index n has a nearly standard negative slope, however under the earth-flattening coordinate transformation the slope becomes positive. In region I, the height z along a ray can be expressed as

$$z = \begin{cases} h_T + R_0 (\cos \theta_T - \cos \theta_0^T) & \text{at transmitter side} \\ h_R + R_0 (\cos \theta_T - \cos \theta_0^R) & \text{at receiver side} \end{cases} \quad (\text{F.4})$$

where θ_0^T and θ_0^R are the take-off and arrival angles of the ray, and the angular displacement of a ray is measured by θ_T . The elemental path length from T toward R is

$$d\sigma = \begin{cases} -R_0 d\theta^T & \text{at T side} \\ R_0 d\theta^R & \text{at R side} \end{cases} \quad (\text{F.5})$$

where from Eq. (F.1),

$$R_0 = -1/g_0 \quad (F.6)$$

Substituting (F.4), and (F.6) into (F.3), gives

$$m = m_0 - \cos \theta_T + \cos \theta_0^{T,R} + g_0 h_{T,R} \quad (F.7)$$

where the T and R refer to whether the path is on the transmitter or receiver side.

In a similar manner, the modified refractive index in the region II within the layer can be evaluated as

$$m = m_0 - \cos \psi + \cos \theta_0^T + g_0 h_T \quad (F.8)$$

where the angular displacement of a ray is measured by ψ , and the elemental path length is

$$d\sigma = \pm R d\psi \quad (F.9)$$

Now the total path delay from T to R was derived in Appendix D as

$$\xi = \frac{1}{c_0} \int_{\text{along ray}} m d\sigma \quad (F.10)$$

Substituting the expressions for m and $d\sigma$ into (F.10) and performing the indicated integration, we get

$$\begin{aligned}
\xi = & \frac{(n+1)}{c_0} [(m_0 + g_0 h_T + \cos \theta_0^T) \theta_1 - \sin \theta_1] (R-R_0) \\
& + \frac{R_0}{c_0} (m_0 + g_0 h_T + \cos \theta_0^T) \theta_0^T - \frac{R_0}{c} \sin \theta_0^T \\
& + \frac{(n+1)}{c_0} [(m_0 + g_0 h_R + \cos \theta_0^R) \theta_1 - \sin \theta_1] (R-R_0) \\
& + \frac{R_0}{c_0} (m_0 + g_0 h_R + \cos \theta_0^R) \theta_0^R - \frac{R_0}{c} \sin \theta_0^R \quad (F.11)
\end{aligned}$$

where θ_1 is the angle at which the ray enters (and leaves) the layer. In order for the rays to intersect at L, we require that the total path length as a function of the angles equals L, i.e.,

$$\begin{aligned}
R_0(\sin \theta_0^T - \sin \theta_1) + R \sin \theta_1 + 2n(R-R_0) \sin \theta_1 + R \sin \theta_1 \\
+ R_0(\sin \theta_0^R - \sin \theta_1) = L \quad (F.12)
\end{aligned}$$

which can be rewritten as

$$\sin \theta_1 = \frac{(k-1)L}{2(n+1)(R_0-R)} \quad (F.13)$$

where

$$k = \frac{k_T + k_R}{2} \quad (F.14)$$

$$k_T = \frac{2R_0}{L} \sin \theta_0^T \quad (F.15)$$

$$k_R = \frac{2R_0}{L} \sin \theta_0^R \quad (\text{F.16})$$

Since the angles are small, we have

$$\sin \theta_0^T = \theta_0^T - \frac{1}{6} \sin^3 \theta_0^T \quad (\text{F.17})$$

Substituting (F.15) into (F.17) we get

$$\theta_0^T = \left(\frac{k_T L}{2R_0}\right) + \frac{1}{6} \left(\frac{k_T L}{2R_0}\right)^3 \quad (\text{F.18})$$

and likewise

$$\theta_0^R = \left(\frac{k_R L}{2R_0}\right) + \frac{1}{6} \left(\frac{k_R L}{2R_0}\right)^3 \quad (\text{F.19})$$

Similarly

$$\cos \theta_0^{T,R} = 1 - \frac{1}{2} \left(\frac{k^{T,R} L}{2R_0}\right)^2 \quad (\text{F.20})$$

In a like manner, from Eq. (F.13), assuming θ_1 is small

$$\theta_1 = \frac{(k-1)L}{2(n+1)(R_0-R)} + \frac{1}{6} \left[\frac{(k-1)L}{2(n+1)(R_0-R)}\right]^3 \quad (\text{F.21})$$

$$\cos \theta_1 = 1 - \frac{1}{2} \left[\frac{(k-1)L}{2(n+1)(R_0-R)}\right]^2 \quad (\text{F.22})$$

Substituting (F.13) - (F.22) into (F.11) gives

$$\xi = \frac{L}{c_0} + \frac{L^3}{24R_0^2 c_0} \left[\frac{3k(k_T^2 + k_R^2) - (k_T^3 + k_R^3)}{2} - \frac{2(k-1)^3}{(n+1)^2 (1-R/R_0)^2} - \frac{3(k_T^2 + k_R^2)}{2} \right] \quad (\text{F.23})$$

In the special case when $k_T = k_R = k$, $h_T = h_R$ and $n=0$. Eq. (F.23) becomes identical to a previous result derived by Ruthroff [3.15]. It should be noted, however, that Ruthroff's analysis assumes a flat earth without utilizing the modified index of refraction, and therefore, the modified radii, R_0 and R .

When the ray is at the interface between regions I and II, $\theta^T = \theta^R = \theta_1$, and $z=h$, thus from Eq. (F.4) we get the two auxiliary equations

$$h = h_T + R_0 (\cos \theta_1 - \cos \theta_0^T) \quad (F.24)$$

$$h = h_R + R_0 (\cos \theta_1 - \cos \theta_0^R) \quad (F.25)$$

Substituting Eqs. (F.20) and (F.22) into (F.24) and (F.25) gives

$$h = h_T + \frac{R_0}{2} \left\{ \left(\frac{k_T L}{2R_0} \right)^2 - \left[\frac{(k_T + k_R - 2)L^2}{4(n+1)(R_0 - R)} \right] \right\} \quad (F.26)$$

$$h = h_R + \frac{R_0}{2} \left\{ \left(\frac{k_R L}{2R_0} \right)^2 - \left[\frac{(k_T + k_R - 2)L^2}{4(n+1)(R_0 - R)} \right] \right\} \quad (F.27)$$

The simultaneous solution of Eqs. (F.26) and (F.27) give the values of k_T and k_R which can be inserted in Eq. (F.11) to give the total path delay ξ .

Solutions for k_T and k_R

The normalized parameters k_T and k_R needed in the evaluation of path delay are obtained from the simultaneous solution of Eqs. (F.26) and (F.27), which can be written as

$$A_T = k_T^2 - \frac{(k_T + k_R - 2)^2}{B} \quad (\text{F.28})$$

$$A_R = k_R^2 - \frac{(k_T + k_R - 2)^2}{B} \quad (\text{F.29})$$

where

$$A_T = 8R_0(h-h_T)/L^2 \quad (\text{F.30})$$

$$A_R = 8R_0(h-h_R)/L^2 \quad (\text{F.31})$$

$$B = 4(n+1)^2(1-R/R_0)^2 \quad (\text{F.32})$$

Subtracting Eq. (F.28) from (F.29) gives

$$\frac{k_R^2}{A} - \frac{k_T^2}{A} = 1 \quad (\text{F.33})$$

where

$$A = A_R - A_T = -8R_0(h_R - h_T)/L^2 \quad (\text{F.34})$$

Adding (F.28) and (F.29) gives

$$A_T + A_R = k_T^2 + k_R^2 - \frac{2}{B} (k_T + k_R - 2)^2 \quad (\text{F.35})$$

In the standard atmosphere R_0 is negative, so that for $h_R > h_T$, $A > 0$, and Eq. (F.33) describes a hyperbola with a minimum value of k_R given by

$$|k_{R_{\min}}| = \frac{\sqrt{-8R_0(h_R - h_T)}}{L} \quad (\text{F.36})$$

The asymptotes are 45° lines on a k_T - k_R plane (see Fig. F.2). The values of k_T and k_R which satisfy Eq. (F.33) are therefore constrained to lie along this hyperbola. To examine the nature of the quadratic curve described by Eq. (F.35), we shall perform a change of coordinates such that

$$x = [(k_T - t) + (k_R - r)]/2 \quad (\text{F.37})$$

$$y = [-(k_T - t) + (k_R - r)]/2 \quad (\text{F.38})$$

from which

$$k_T = x - y + t \quad (\text{F.39})$$

$$k_R = x + y + r \quad (\text{F.40})$$

Substituting (F.39) and (F.40) into (F.35), gives

$$\begin{aligned} A_T + A_R = & x^2 \left(2 - \frac{8}{B}\right) + y^2 (2) + x \left[2(t+r) - \frac{8(t+r-2)}{B}\right] \\ & + y [2(r-t)] + \left[t^2 + r^2 - \frac{2(t+r-2)^2}{B}\right] \end{aligned} \quad (\text{F.41})$$

In order to perform the coordinate transformations such that the cross terms disappear, then it is necessary from the coefficient of y that

$$r = t \quad (\text{F.42a})$$

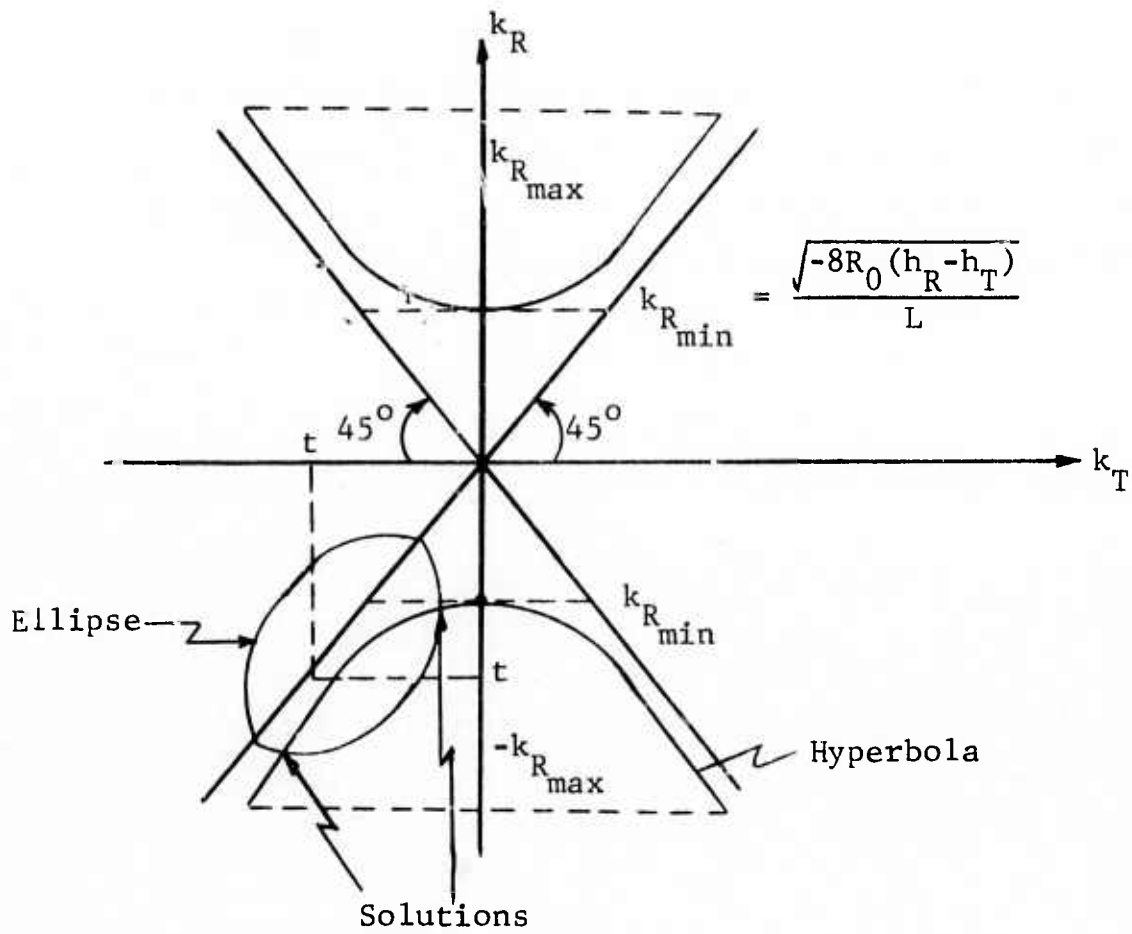


Figure F.2 Solutions for (k_T, k_R)

Substituting that into the x coefficient and requiring that it equal 0, we get

$$t = \frac{1}{1-B/4} \quad (\text{F.42 b})$$

Substituting (F.42a) and (F.42b) into (F.41) gives

$$x^2 \left[\frac{2 - \frac{8}{B}}{A_T + A_R - \frac{2}{1 - \frac{B}{4}}} \right] + y^2 \left[\frac{2}{A_T + A_R - \frac{2}{1 - \frac{B}{4}}} \right] = 1 \quad (\text{F.43})$$

Inserting the values of A_T , A_R and B yields

$$\frac{x^2}{a^2} + \frac{y^2}{b^2} = 1 \quad (\text{F.44})$$

where

$$a^2 = \frac{\left[\frac{4R_0(2h-h_R-h_T)}{L^2} - \frac{1}{1 - (n+1)^2(1-R/R_0)^2} \right]}{\left[1 - \frac{1}{(n+1)^2(1-R/R_0)^2} \right]} \quad n = 0, 1, 2, \dots \quad (\text{F.45})$$

$$b^2 = \left[\frac{4R_0(2h-h_R-h_T)}{L^2} - \frac{1}{1 - (n+1)^2(1-R/R_0)^2} \right]_{n = 0, 1, 2, \dots} \quad (\text{F.46})$$

Note that for x and y to have real solutions (i.e., for the equations to be valid) a^2 and b^2 must be positive. Note that Eq. (F.44) describes an ellipse with major and minor axes a and b . Since the coordinate transformation is only a rotation and translation of the k_T - k_R axes, the ellipse has the same shape on the k_T - k_R axes. The center of the ellipse is at $x=y=0$. Therefore, the center is at

$$0 = k_T^0 = k_R^0 - 2t \quad (\text{F.47})$$

$$0 = -k_T^0 + k_R^0 \quad (\text{F.48})$$

or

$$k_T^0 = k_R^0 = t = \frac{1}{1 - \frac{B}{4}} = \frac{1}{1 - (n+1)^2 (1-R/R_0)^2} \quad (\text{F.49})$$

Now the solutions for k_T and k_R must lie along this ellipse as well as the hyperbola shown in Fig. F.2. Thus, the intersections of the two give the desired solutions for k_T and k_R . By varying the system parameters (height of layer h , range L , etc.) the two curves change their relative size and location, such that they may intersect at two points, four points, or no points. The values of k_T and k_R at these intersection points can be determined graphically or numerically using standard techniques. If the layer were infinitely thick, the number of such intersections would equal to the number of refracted rays which reach the receiver in addition to the direct path ray.

However, due to the finite thickness of the layer, there is a maximum value of the angle at which a ray may enter or leave the layer without escaping into the upper atmosphere. This in turn dictates a maximum value for k_T and k_R . The maximum values of k_R occurs when a ray received at an angle θ_R , where

$$\sin \theta_R = \frac{k_R L}{2R_0} \quad (\text{F.50})$$

just grazes the top of the layer (see Fig. F.1). Any ray which is launched at an angle greater than θ , will escape the layer. If the layer has thickness ω , then from Fig. F.1, it is seen that

$$\cos \theta_{1_{\max}} = (R-\omega)/R = 1 - \frac{\omega}{R} \quad (\text{F.51})$$

Now

$$\cos \theta_R = \cos \theta_1 + \frac{h-h_R}{-R_0} \quad (\text{F.52})$$

so that

$$\cos \theta_{R_{\max}} = \cos \theta_{1_{\max}} - \frac{h-h_R}{R_0} = 1 - \left(\frac{\omega}{R} + \frac{h-h_R}{R_0} \right) \quad (\text{F.53})$$

The maximum value for k_R is given by

$$k_{R_{\max}} = \frac{2R_0}{L} \sin \theta_{R_{\max}} \quad (\text{F.54})$$

Determining $\sin \theta_{R_{\max}}$ from (F.53) and assuming that the layer thickness ω is much less than the radius R and that the vertical distance between the receiver and layer height is much less than the radius R_0 (both these conditions are virtually always satisfied), $k_{R_{\max}}$ becomes

$$k_{R_{\max}} = \frac{-2R_0}{L} \sqrt{2\left(\frac{\omega}{R} + \frac{h-h_R}{R_0}\right)} \quad (\text{F.55})$$

Thus, intersections of the ellipse and hyperbola in the k_T - k_R plane which lie within the region defined by

$$k_{R_{\min}} \leq k_R \leq k_{R_{\max}} \quad (\text{F.56})$$

define values of k_T and k_R which yield multipath on the particular link under study.

Appendix G

ANALYSIS OF MATCHED FILTER AND CORRELATION TECHNIQUES

In this appendix we will analyze the SNR performance and distortion characteristics of the matched filter and correlation techniques of channel measurement. The transmitted signal is assumed to be a large TW product pulse of high duty cycle repeated periodically. This signal may be formed by modulating a carrier with a baseband signal or by pulsing a band-pass filter and heterodyning.

In the former case the complex envelope of the transmitted signal $z(t)$ can be represented in the form

$$z(t) = \sum \mu(t-kT) \quad (G.1)$$

where $\mu(t)$ is a generally complex waveform representing the basic pulse shape. In the latter case the complex envelope would be represented by

$$z_1(t) = \sum \mu(t-kT)e^{-j2\pi f_1 kT} \quad (G.2)$$

where f_1 is the "center" frequency of the band-pass filter. The complex signal $z(t)$ in (G.1) is periodic with period T and has a line spectrum with harmonics at multiples of $1/T$ Hz. In general the signal $z_1(t)$ in (G.2) is not periodic. It has a line spectrum, however, whose frequency locations differ from that of (G.1) by a frequency shift of f_1 Hz. This may be seen from the identities

$$\Sigma \mu(t-kT) = \Sigma \delta(t-kT) \otimes \mu(t) \quad (G.3)$$

$$\Sigma \mu(t-kT)e^{-j2\pi f_1 kT} = \Sigma \delta(t-kT)e^{-j2\pi f_1 t} \otimes \mu(t) \quad (G.4)$$

where $\delta(\cdot)$ is the unit impulse and \otimes denotes convolution.

The impulse train has the spectral representation

$$\int e^{-j2\pi ft} (\Sigma \delta(t-kT)) dt = \frac{1}{T} \Sigma \delta(f - \frac{m}{T}) \quad (G.5)$$

Thus if $U(f)$, $Z(f)$, $Z_1(f)$ are the spectra of $\mu(t)$, $z(t)$, $z_1(t)$,

$$Z(f) = \frac{1}{T} U(f) \Sigma \delta(f - \frac{m}{T}) = \frac{1}{T} \Sigma U(\frac{m}{T}) \delta(f - \frac{m}{T}) \quad (G.6)$$

$$Z_1(f) = \frac{1}{T} U(f) \Sigma \delta(f + f_1 - \frac{m}{T}) = \frac{1}{T} \Sigma U(\frac{m}{T} - f_1) \delta(f + f_1 - \frac{m}{T}) \quad (G.7)$$

Only if f_1 is some harmonic of $1/T$ will $z(t) = z_1(t)$. Since the receiver processing involves coherent integration from received pulse to received pulse, the use of $z_1(t)$ would require some technique of cancelling the phase shift factor $\exp(-j2\pi f_1 kT)$ at the receiver. We assume from this point on that this complication may be avoided and a transmitted signal of the form (G.1) is used.

The LOS communications channel may be characterized with the aid of a complex time-variant impulse response $g(t, \xi)$ which relates the input complex envelope $z(t)$ to the output complex envelope $w(t)$ by the equation

$$w(t) = \int z(t-\xi)g(t, \xi) d\xi \quad (G.8)$$

One may incorporate the effects of the transmitter and receiver channelizing filters in $g(t, \xi)$ or one may incorporate these filters in the definition of the basic pulse $\mu(t)$. These alternatives may be seen from Fig. G.1. In Fig. G.1(a) the filters are shown as they occur in the channel. In Fig. G.1(b), the transmitter and receiver channelizing filters with impulse responses $h_T(t)$, $h_R(t)$, respectively, are shown incorporated into an "effective" propagation medium. Note that since the additive noise in this "effective" system occurs after $h_R(t)$, the additive noise of the actual system $\hat{\eta}(t)$ must be replaced by a filtered additive noise, $\eta(t) = \hat{\eta}(t) \otimes h_R(t)$. Figure G.1(c) shows the channelizing filters incorporated into an "effective" pulse generation filter. The transfer of the receiver filter from after the propagation medium to before the propagation medium is only valid when the fading time constant of the channel is very much larger than the time constant of the receiver filter, which is certainly true in the present case. Until the distinction is necessary, we shall proceed with our analysis without specifying whether the channelizing filters are included in $\mu(t)$ or $g(t, \xi)$.

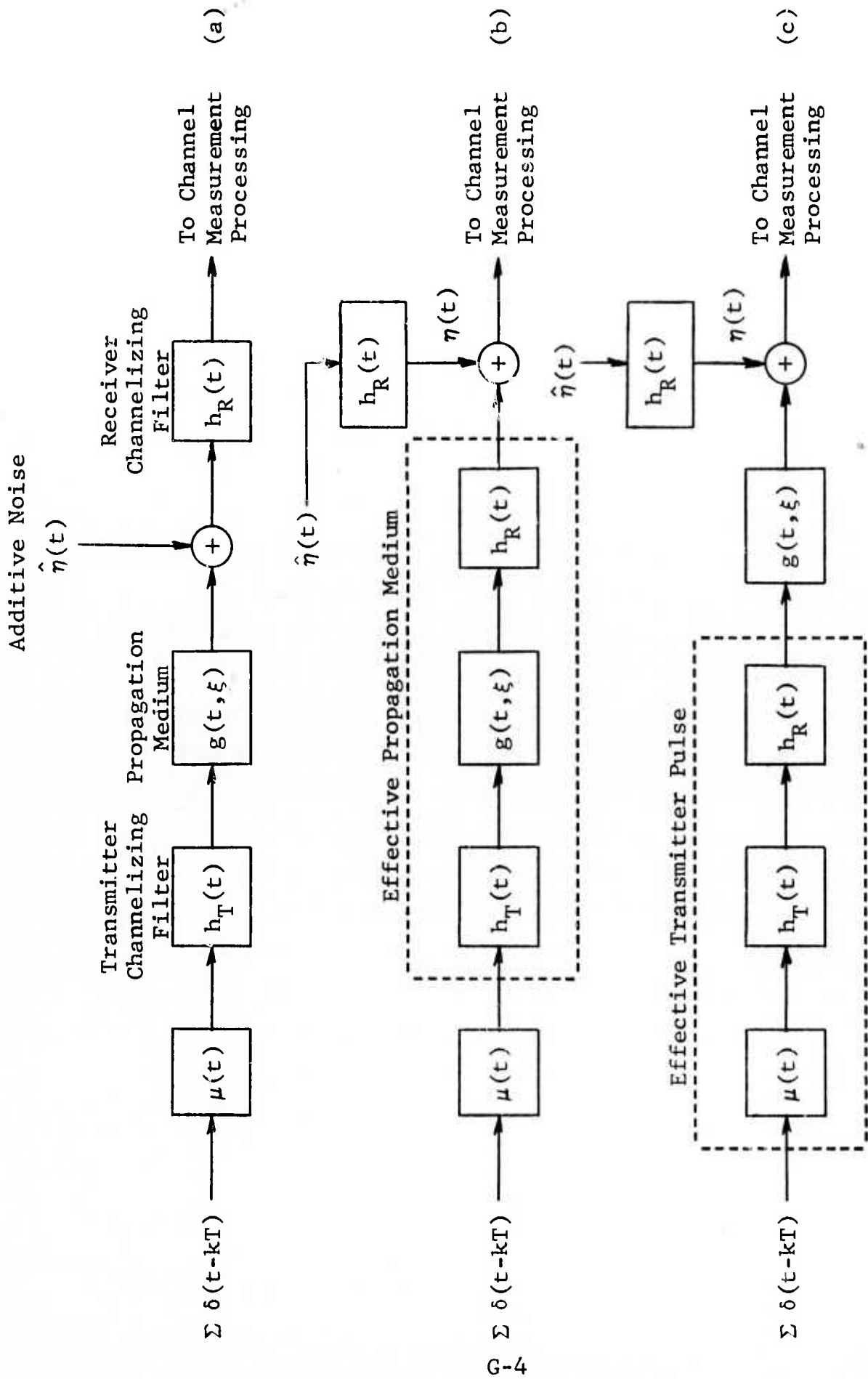


Figure G.1 Options for Incorporation of Terminal Filters

We now analyze the performance of the matched filter and correlation system block diagrammed in Figs. 5.1 - 5.6 of Section 5. In terms of complex envelope processing the basic elements of the two systems to be analyzed are shown in Figs. G.2(a) and (b).

The matched filter with impulse response $m^*(-t)$ is matched to a pulse $m(t)$ which ideally is equal to $\mu(t)$. However terminal equipment filtering and design limitations will prevent this equality. For simplified idealized calculations $\mu(t)$ and $m(t)$ would be set equal to one period of the maximal length shift register sequence of +1's and -1's modulated on rectangular pulses of duration Δ , i.e.,

$$\mu(t) = m(t) = \sum_{p=0}^{P-1} x_p q(t - p\Delta) \quad (\text{idealized}) \quad (\text{G.9})$$

where

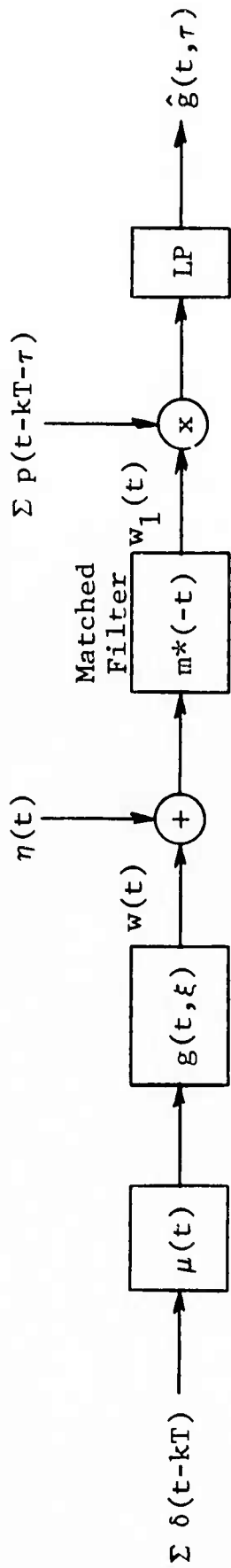
$$x_p = \pm 1 \quad (\text{G.10})$$

$$q(t) = \begin{cases} 0 & ; \quad t < 0, t > \Delta \\ 1 & ; \quad 0 \leq t \leq \Delta \end{cases} \quad (\text{G.11})$$

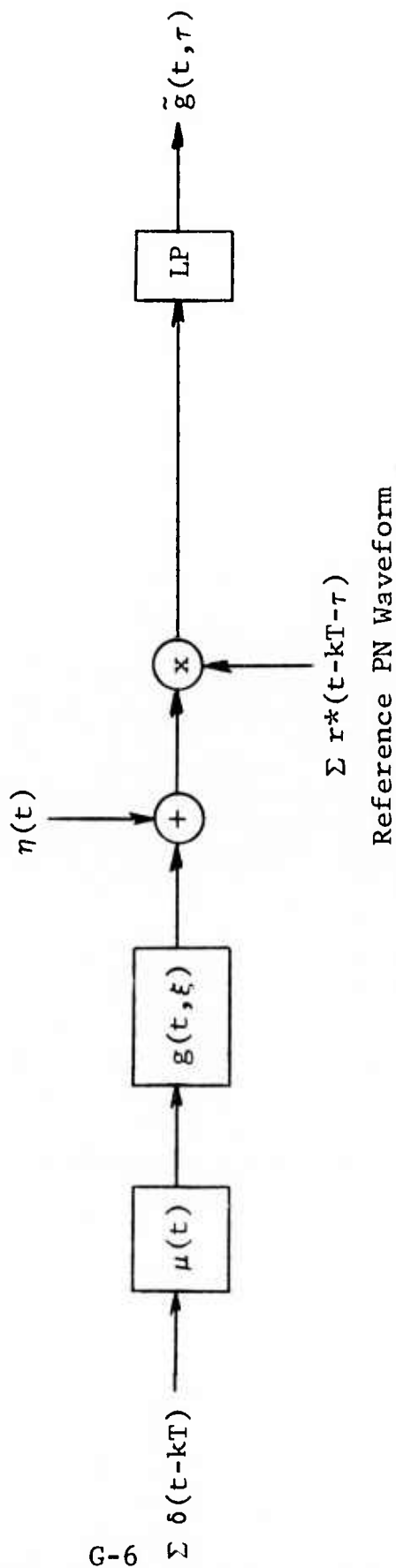
The duration T of the large TW product pulse $\mu(t)$ is related to the rectangular pulse duration Δ by

$$T = \Delta P \quad (\text{G.12})$$

Sampling Pulse Train



(a) Basic Elements of Matched Filter Processing



(b) Basic Elements of Correlator Processing

Figure G.2 Basic Elements of Channel Measurement for Matched Filter and Correlation Techniques

where P is the length of the maximal length shift register sequence. If the length of the shift register which can generate the maximal length sequence is L , then

$$P = 2^L - 1 \quad (G.13)$$

In Fig. G.2(a) the sampling process is shown as multiplication by a periodic narrow pulse train with period T . The sampling pulse $p(t)$ is frequently idealized to an impulse. After the sampling process a (complex) low pass filter with bandwidth less than half the sampling rate extracts $\hat{g}(t, \tau)$, an estimate of the complex amplitude channel impulse response at a fixed value of delay τ . Because the channel is time varying this complex amplitude is time varying. Depending on the value of τ selected $\hat{g}(t, \tau)$ is analogous to $a_i(t) + ja_q(t)$, or one of the other complex lettered pairs, discussed in Section 5. A discrete set of values of τ is chosen to adequately sample $\hat{g}(t, \tau)$ vs. τ .

The receiver processing with the correlation technique, Fig. G.2(b), is shown as multiplication by reference PN waveform $\sum r^*(t - kT + \tau)$. Since the balanced modulators realizing the multiplication process will be driven into saturation for practical reasons, one may assume that $r(t)$ takes the form of the sequence of rectangular pulses indicated in (G.9), i.e., one may assume

$$r(t) = \sum_{p=0}^{P-1} x_p q(t - p\Delta) \quad (G.14)$$

The low pass filters in G.2(a) and (b) are assumed identical.

The analysis to be given is carried out most simply with the aid of the time variant transfer function $T(f,t)$ which is the Fourier transform of $g(t,\xi)$ with respect to ξ ,

$$T(f,t) = \int g(t,\xi) e^{-j2\pi f \xi} d\xi \quad (G.15)$$

The input-output relationship utilizing $T(f,t)$ is given by

$$w(t) = \int Z(f) T(f,t) e^{j2\pi f t} df \quad (G.16)$$

Note that $T(f,t)$ is just the complex time varying modulation on a received carrier transmitted at the frequency f (actually f Hz from carrier frequency). For the LOS channel $T(f,t)$ varies very slowly with t (say a 1 Hz bandwidth).

We first consider the matched filter and correlator system outputs in the absence of additive noise. The input impulse train has the Fourier series representation

$$\sum_{-\infty}^{\infty} \delta(t-kT) = \frac{1}{T} \sum_{-\infty}^{\infty} e^{j \frac{m2\pi}{T} t} \quad (G.17)$$

which is consistent with the discrete spectrum (G.5). From (G.6) and (G.16) we see that the output of the propagation channel is given by

$$w(t) = \frac{1}{T} \sum_{-\infty}^{\infty} U\left(\frac{m}{T}\right) T\left(\frac{m}{T}, t\right) e^{j2\pi \frac{m}{T} t} \quad (C.18)$$

G.1 The Matched Filter Technique: No Additive Noise

We now focus our attention on the matched filter system. The input to the matched filter consists of a set of slowly fading tones separated in frequency by $1/T$ Hz. Since the time constant of the matched filter is negligible by comparison to the fading time constant, each tone is affected by the matched filter through multiplication by the transfer function of the matched filter at the tone's center frequency. The transfer function of the matched filter is given by $M^*(f)$, where

$$M(f) = \int m(t) e^{-j2\pi ft} df \quad (G.19)$$

Thus the signal component of the matched filter output is given by

$$w_1(t) = \frac{1}{T} \sum_{-\infty}^{\infty} U\left(\frac{m}{T}\right) M^*\left(\frac{m}{T}\right) I\left(\frac{m}{T}, t\right) e^{j \frac{2\pi m}{T} t} \quad (G.20)$$

The sampling pulse train can be expressed as the convolution

$$\sum p(t-kT-\tau) = \sum \delta(t-kT-\tau) \otimes p(t) \quad (G.21)$$

from which it may be seen that it has the Fourier series expansion

$$\sum p(t-kT-\tau) = \frac{1}{T} \sum P\left(\frac{n}{T}\right) e^{j2\pi \frac{n}{T} (t-\tau)} \quad (G.22)$$

The input to the low pass filter is the product

$$\begin{aligned}
 w_1(t) \sum p(t-kT+\tau) &= \frac{1}{T^2} \sum_m \sum_n U\left(\frac{m}{T}\right) M^*\left(\frac{m}{T}\right) P\left(\frac{n}{T}\right) T\left(\frac{m}{T}, t\right) e^{j2\pi\left(\frac{m+n}{T}\right)t} e^{-j2\pi\frac{n}{T}\tau} \\
 &= \sum_s g_s(t, \tau) e^{j2\pi\frac{s}{T}(t-\tau)} \quad (G.23)
 \end{aligned}$$

where

$$g_s(t, \tau) = \frac{1}{T^2} \sum U\left(\frac{m}{T}\right) M^*\left(\frac{m}{T}\right) P\left(\frac{s-m}{T}\right) T\left(\frac{m}{T}, t\right) e^{j2\pi\frac{m}{T}\tau} \quad (G.24)$$

The second expression in (G.23) represents the low pass filter as a set of zonal bands centered on the frequencies $\{s/T; s=0, \pm 1, \dots\}$. The low pass filter bandwidth and the frequency spacing $1/T$ is adjusted so that only the zone around zero Hz is passed. Thus

$$\hat{g}(t, \tau) = g_0(t, \tau) = \frac{1}{T^2} \sum U\left(\frac{m}{T}\right) M^*\left(\frac{m}{T}\right) P\left(-\frac{m}{T}\right) T\left(\frac{m}{T}, t\right) e^{j2\pi\frac{m}{T}\tau} \quad (G.25)$$

For the idealized case of impulse sampling, $P(\cdot) = 1$, and $m(t) = \mu(t)$, and (G.25) simplifies to

$$\hat{g}(t, \tau) = \frac{1}{T^2} \sum |U(\frac{m}{T})|^2 T(\frac{m}{T}, t) e^{j2\pi \frac{m}{T} \tau} \quad (G.26)$$

Utilizing the relationship

$$\int \sum \delta(f - \frac{m}{T}) A(\frac{m}{T}) B(f) df = \sum A(\frac{m}{T}) B(\frac{m}{T}) \quad (G.27)$$

we see that

$$\hat{g}(t, \tau) = \int \left\{ \frac{1}{T^2} \sum_m \delta(f - \frac{m}{T}) |U(\frac{m}{T})|^2 \right\} T(f, t) e^{j2\pi f \tau} df \quad (G.28)$$

The term in brackets in (G.28) may be shown to be equal to the power density spectrum of the periodic probing waveform $\sum \mu(t-kT)$. Thus if the autocorrelation function of this probing waveform is defined as $C(\tau)$,

$$\begin{aligned} C(\tau) &= \frac{1}{T} \int_0^T \sum_k \mu^*(t-kT) \sum_l \mu(t+\tau-lT) dt \\ &= \frac{1}{T} \int_0^T \mu^*(t) \sum_l \mu(t+\tau-lT) dt \\ &= \frac{1}{T^2} \sum |U(\frac{m}{T})|^2 e^{j2\pi \frac{m}{T} \tau} \end{aligned} \quad (G.29)$$

its Fourier transform is just the bracketed term in (G.28). Then changing the right-hand side of (G.28) into a convolution,

$$\hat{g}(t, \tau) = \int C(\tau - \xi) g(t, \xi) d\xi \quad (G.30)$$

Assuming the rectangular "chips" of (G.9) and a maximal length shift register sequence for the x_p 's, $C(\tau)$ may be represented as the sum of a constant component plus a periodic triangle, i.e.,

$$C(\tau) = -\frac{1}{P} + \left(1 + \frac{1}{P}\right) \sum_k \text{Tri} \left(\frac{\tau - kT}{\Delta}\right) \quad (G.31)$$

where

$$\text{Tri}(x) = \begin{cases} 1 - |x| & ; \quad |x| < 1 \\ 0 & ; \quad \text{elsewhere} \end{cases} \quad (G.32)$$

Using (G.31) in (G.30)

$$\begin{aligned} \hat{g}(t, \tau) = & -\frac{1}{P} \int g(t, \xi) d\xi + \left(1 + \frac{1}{P}\right) \int \text{Tri} \left(\frac{\tau - \xi}{\Delta}\right) g(t, \xi) d\xi \\ & + \left(1 + \frac{1}{P}\right) \sum_{k \neq 0} \int \text{Tri} \left(\frac{\tau - kT - \xi}{\Delta}\right) g(t, \xi) d\xi \end{aligned} \quad (G.33)$$

We assume that $g(t, \xi)$ is non-zero only for $0 < t < L_{\max} < T$ and that τ is selected in the interval $0 < \tau < T$. Then the third term in (G.33) vanishes. The first term in (G.33) is a

spurious term that can be made as small as desired by choosing P large enough. Thus if we assume $g(t, \xi)$ consists of discrete paths

$$g(t, \xi) = \sum_{k=1}^K G_k(t) \delta(\xi - \xi_k) \quad (G.34)$$

then (G.33) becomes

$$\hat{g}(t, \tau) = -\frac{1}{P} \sum_{k=1}^K G_k(t) + \left(1 + \frac{1}{P}\right) \sum_{k=1}^K G_k(t) \text{Tri} \left(\frac{\tau - \xi_k}{\Delta}\right) \quad (G.35)$$

If the paths are of equal strength but uniformly distributed independent random phases, the strength of the first term relative to the peak strength of any of the paths in the second term is just

$$\frac{K}{P^2(1 + 1/P)^2} \quad (G.36)$$

For four paths and $P = 255$ (8 stage shift register), (G.36) indicates that the spurious term is around 36 dB below any of the "peaks" in the second term.

Assuming P is large enough to make the first term in (G.35) negligible, and that T is bigger than L_{\max} , (the maximum multipath spread) we find that

$$\hat{g}(t, \tau) \approx \int \text{Tri} \left(\frac{\tau - \xi}{\Delta}\right) g(t, \xi) d\xi \quad (G.37)$$

when the idealized conditions (G.9) are assumed. In order to collect information sufficient for stored channel evaluation $\hat{g}(t, \tau)$ must be "sampled" as a function of τ with delay increments small enough to allow reconstruction of a transfer function which is identical to the channel transfer function over a limited bandwidth.

Consider first the case of infinitesimal delay increments which implies that $\hat{g}(t, \tau)$ is available as a function of τ . The transfer function corresponding to $\hat{g}(t, \tau)$, $\hat{T}(f, t)$, is obtained by Fourier transforming

$$\hat{T}(f, t) = \int \hat{g}(t, \tau) e^{-j2\pi f\tau} d\tau \quad (G.38)$$

which from (G.37) becomes

$$\hat{T}(f, t) = T(f, t) \Delta \text{sinc}^2 f\Delta \quad (G.39)$$

The $\text{sinc}^2(f\Delta)$ function has a broad maximum around $f=0$, so that in the vicinity of this maximum $\hat{T}(f, t)$ will differ from $T(f, t)$ only by a known constant.

Since the cost of the equipment is related to the number of samplers, one will have available only $\hat{g}(t, nT_0)$, $n = 0, 1, \dots, N$ where $NT_0 > L_{\max}$. The question of how small N may be made may be answered by examining the reconstructed transfer function corresponding to $\{\hat{g}(t, nT_0); n = 0, 1, \dots, N\}$. This transfer function is readily found by sampling theorems to be given by

$$\hat{T}_{\text{samp}}(f, t) \sim \sum T(f - \frac{m}{T_0}, t) \Delta \text{sinc}^2(f - \frac{m}{T_0})\Delta$$

(G.40)

To avoid aliasing in an interval about $f=0$ clearly requires that $1/T_0$ be large enough in relation to the "width" of the sinc function.

We now relax the idealized condition (G.9) and return to (G.25). In this more general case one may show that $\hat{T}(f, t)$, Eq. (G.39) becomes replaced by

$$\hat{T}(f, t) = T(f, t) \Delta \text{sinc}^2 f \Delta H_T(f) H_R(f) Q(f) P(-f)$$

(G.41)

where $H_T(f)$, $H_R(f)$ are the transfer functions of the transmitter and receiver filters, $Q(f)$ is a transfer function that accounts for the departure of the matched filter from ideal, and $P(f)$ is the sampling pulse transfer function. It is clear that various possibilities for equalization of the $\text{sinc}^2 f \Delta$ function exist through manipulating $H_T(f)$, $H_R(f)$, or even $P(f)$. Because of the finite delay T_0 between samples an aliasing problem exists. Given that a region W Hz wide is desired alias-free one may readily determine the restrictions on system parameters to accommodate this requirement.

G.2 The Correlation Technique; No Additive Noise

We turn now to an analysis of the low-pass filter output in Fig. G.2(b) which describes the correlation technique of channel measurement. The received signal at the channel output

$w(t)$ is given in Eq. (G.18). As mentioned previously, in complex notation the correlation operation involves low pass filtering the product

$$w(t) \sum r^*(t-kT-\tau) \quad (G.42)$$

where the sum defines the local PN sequence waveform (see (G.14), (G.10), (G.11)). This sum is a periodic function

$$\sum r^*(t-kT-\tau) = \frac{1}{T} \sum R^*\left(\frac{n}{T}\right) e^{-j2\pi \frac{n}{T} (t-\tau)} \quad (G.43)$$

Forming the product (G.42) with $w(t)$ represented by (G.18) we find that

$$\begin{aligned} w(t) \sum r^*(t-kT-\tau) &= \frac{1}{T^2} \sum \sum U\left(\frac{m}{T}\right) T\left(\frac{m}{T}, t\right) R^*\left(\frac{n}{T}\right) e^{j2\pi \left(\frac{m-n}{T}\right) t} e^{j2\pi \frac{n\tau}{T}} \\ &= \sum h_s(t, \tau) e^{j2\pi \frac{s}{T} (t-\tau)} \end{aligned} \quad (G.44)$$

where

$$H_s(t, \tau) = \frac{1}{T^2} \sum_m U\left(\frac{m}{T}\right) R^*\left(\frac{m-s}{T}\right) T\left(\frac{m}{T}, t\right) e^{j2\pi \frac{m}{T} \tau} \quad (G.45)$$

Equation (G.25) expresses the low pass filter output in terms of zonal bands located at harmonics of $1/T$. The low pass filter will select only the band around $f=0$. Thus the low pass filter output is given by

$$\tilde{g}(t, \tau) = h_0(t, \tau) = \frac{1}{T} \sum_m U\left(\frac{m}{T}\right) R^*\left(\frac{m}{T}\right) T\left(\frac{m}{T}, t\right) e^{j2\pi \frac{m}{T} t} \quad (G.46)$$

For the idealized case where $\mu(t) = r(t)$, (G.46) simplifies to

$$\tilde{g}(t, \tau) = \frac{1}{T} \sum_m |U\left(\frac{m}{T}\right)|^2 T\left(\frac{m}{T}\right) e^{j2\pi \frac{m}{T} \tau} \quad (G.47)$$

Comparison of Eq. (G.47) with Eq. (G.20) reveals that the low pass filter output for the idealized correlation technique becomes identical to that for the idealized matched filter technique. The discussion in the previous section concerning the sampling of $\hat{g}(t, \tau)$ vs. τ to allow reconstruction of a finite bandwidth portion of the time variant transfer function carries over directly to $\tilde{g}(t, \tau)$. When the transmitter and receiver filters are included, the reproduced transfer function takes the form

$$\tilde{T}(f, t) = T(f, t) \Delta \text{sinc}^2 f \Delta H_T(f) H_R(f) \quad (G.48)$$

when $\tilde{g}(t, \tau)$ is known for all τ . The aliasing problem resulting from the availability of only $\{\tilde{g}(t, nT_0); n=0, 1, \dots\}$ is identical to that described in the preceding section for $\hat{g}(t, nT_0)$.

G.3 Output Signal-to-Noise Ratios

In computing output SNR's there is little error introduced by the idealized filtering and sampling. The computation of output noise is facilitated by expressing the input noise in the form

$$\eta(t) = \sum \eta_m(t) e^{j2\pi \frac{m}{T} t} \quad (G.49)$$

where $\eta_m(t) e^{j2\pi \frac{m}{T} t}$ is the complex envelope of that part of the noise $\eta(t)$ which lies in the frequency band $(-\frac{1}{2T} + \frac{m}{T} < f < \frac{1}{2T} + \frac{m}{T})$. Note that these noises are statistically independent. The noise at the low pass filter input for the correlation technique is given by the product

$$\begin{aligned} \eta(t) \sum r^*(t-kT-\tau) &= (\sum \eta_m(t) e^{j2\pi \frac{m}{T} t}) (\frac{1}{T} \sum R^*(\frac{n}{T}) e^{-j2\pi \frac{n}{T} (t-\tau)}) \\ &= \frac{1}{T} \sum \sum \eta_m(t) R^*(\frac{n}{T}) e^{j2\pi (\frac{m-n}{T}) t} e^{j2\pi \frac{n}{T} \tau} \\ &= \sum \eta_s(t) e^{j2\pi \frac{s}{T} t} \quad (G.50) \end{aligned}$$

where

$$n_s(t) = \frac{1}{T} \sum \eta_m(t) R^*\left(\frac{m-s}{T}\right) e^{j2\pi\left(\frac{m-s}{T}\right)\tau} \quad (G.51)$$

Since $\eta_m(t)$, all m , occupies a band $-\frac{1}{2T} < f < \frac{1}{2T}$, $n_s(t)$ is confined to the same band. Thus the only part of the last summation which produces noise at the low pass filter output is the $s=0$ term,

$$n_0(t) = \frac{1}{T} \sum \eta_m(t) R^*\left(\frac{m}{T}\right) e^{j2\pi\frac{m}{T}\tau} \quad (G.52)$$

As far as the low pass filter is concerned this constitutes a complex white noise whose power spectral density is given by

$$\begin{aligned} \tilde{N}_0 &= 2N_0 \frac{1}{T^2} \sum |R\left(\frac{m}{T}\right)|^2 \\ &= 2N_0 C(0) \\ &= 2N_0 \end{aligned} \quad (G.53)$$

where $C(\tau)$ is the autocorrelation function of the probing waveform (G.29), N_0 is the one-sided power spectral density of the real noise and we have assumed the idealized waveform leading to (G.31) for $C(\tau)$.

Turning now to the matched filter technique, where we assume that $r(t) = \mu(t)$ in keeping with our idealized processing analysis, we see that the noise input to the sampler can be expressed in the form

$$\begin{aligned} \eta(t) \otimes r^*(-t) &= \Sigma \left\{ \eta_m(t) e^{j2\pi \frac{m}{T} t} \right\} \otimes r^*(-t) \\ &= \Sigma \left[\eta_m(t) \otimes \left\{ r^*(-t) e^{-j2\pi \frac{m}{T} t} \right\} \right] e^{j2\pi \frac{m}{T} t} \end{aligned} \quad (G.54)$$

Using the Fourier series representation of the sampler, the noise input to the low pass filter can be expressed in the zonal form

$$\begin{aligned} &\Sigma \delta(t-kT-\tau) \{ \eta(t) \otimes r^*(-t) \} \\ &= \Sigma_m \Sigma_n \left[\eta_m(t) \otimes \left\{ r^*(-t) e^{-j2\pi \frac{m}{T} t} \right\} \right] e^{j2\pi \frac{m}{T} t} \frac{1}{T} e^{j2\pi \frac{n}{T} (t-\tau)} \\ &= \Sigma_s m_s(t) e^{j2\pi \frac{s}{T} t} \end{aligned} \quad (G.55)$$

where

$$m_s(t) = \frac{1}{T} \Sigma_m \eta_m(t) \otimes \left\{ r^*(-t) e^{-j2\pi \frac{m}{T} t} \right\} e^{j2\pi \left(\frac{m-s}{T} \right) \tau} \quad (G.56)$$

As in the previous case only the $s=0$ term in (G.55) contributes noise to the low pass filter output. Thus the output noise is given by

$$m_0(t) = \frac{1}{T} \sum \eta_m(t) \otimes \left\{ r^*(-t) e^{-j2\pi \frac{m}{T} t} \right\} e^{j2\pi \frac{m}{T} \tau} \quad (\text{G.57})$$

The component noise terms in (G.57) are statistically independent with the m 'th term having power spectral density $2N_0 |R(f + \frac{m}{T})|^2 / T^2$, $|f| < 1/2T$. Thus the power spectrum of $m_0(t)$ is given by

$$\begin{aligned} P_{m_0}(f) &= 2N_0 \frac{1}{T^2} \sum |R(f + \frac{m}{T})|^2 \quad ; \quad |f| < 1/2T \\ &= 2N_0 C(0) \\ &= 2N_0 \end{aligned} \quad (\text{G.58})$$

as in the case of the correlation technique. Thus the noise outputs of the two techniques are identical.

In order to define input and output SNR it is necessary for us also to determine the strengths of the signal terms. We assume a channel consisting of a set of discrete paths. The received signal including additive noise is given by

$$w(t) = \sum_{k=1}^K G_k(t) z(t - \xi_k) + n(t) \quad (G.59)$$

where

$$|z(t)|^2 = 1 \quad (G.60)$$

and W , the bandwidth of $z(t)$ is of the order of $2/\Delta$, where Δ is the "chip" duration. The complex noise $\eta(t)$ has power spectral density $2N_0$, where N_0 is the one-sided density of the real noise.

The output signal from the low pass filter is, from (G.35), (assuming $P \gg 1$),

$$w_{\text{out}}(t) = \sum_{k=1}^K G_k(t) \text{Tri} \left(\frac{\tau - \xi_k}{\Delta} \right) + n_0(t) \otimes h_L(t) \quad (G.61)$$

where $n_0(t)$ also has power spectral density $2N_0$ and $h_L(t)$ is the impulse response of the low pass filter. The SNR in estimating the strength of the k 'th path is then

$$\rho_k = \frac{P_k}{2N_0 B_L} \quad (G.62)$$

where B_L is the (two-sided) noise bandwidth of the low pass filter, and

$$P_k = \overline{|G_k(t)|^2} \quad (G.63)$$

is the strength of the k'th path.

The input signal-power-to-noise power density P_0 is given by

$$P_0 = \frac{\sum p_k}{2N_0} \quad (G.64)$$

where we have assumed all paths to be fluctuating independently and to have zero mean. Thus the output SNR in terms of the input SNR is given by

$$\rho_k = \frac{P_0}{B_L} \frac{p_k}{\sum p_\ell} \quad (G.65)$$

In the case of the multiplexed correlation technique described in Section 5, Fig. 5.6, the output for a given value of τ is sampled with a rectangular pulse occurring at a certain duty cycle d . Ultimate recovery of the function $\tilde{g}(t, \tau)$ then requires a low pass filtering operation. It is trivial to show that the net SNR loss is just by a factor d . Thus

$$\rho_k = \frac{P_0}{B_L} \cdot \frac{p_k}{\sum p_\ell} \cdot d \quad (G.66)$$

for the multiplexed correlation technique.

Appendix H
CALCULATIONS FOR SINGLE STRATIFIED LAYER BELOW TERMINALS

General Analysis

When the layer is below the terminals, the analysis proceeds similarly to that given in Appendix F. The main distinction is that since the layer bends rays toward the earth, it acts to direct the signal away from the receiver, while the standard atmosphere below the layer turns rays away from the earth and toward the receiver. The geometry is shown in Fig. H.1a. If the origin of a Cartesian coordinate system is placed at the transmitter with the z-axis pointing downward, the geometry of the situation can be equivalently redrawn as shown in Fig. H.1b.

In a manner directly analogous to that presented in Appendix F, the following equations can be written

Region I:

$$m = m_0 + g_0 z \quad (g_0 < 0) \quad (\text{H.1})$$

$$z = \begin{cases} h_T + R_0(\cos \theta_T - \cos \theta_0^T) & \text{at transmitter side} \\ h_R + R_0(\cos \theta_T - \cos \theta_0^R) & \text{at receiver side} \end{cases} \quad (\text{H.2})$$

where θ_0^T and θ_0^R are the take-off and arrival angles of the ray, and θ_T measures the angular displacement along the path. The elemental path length from T toward R is

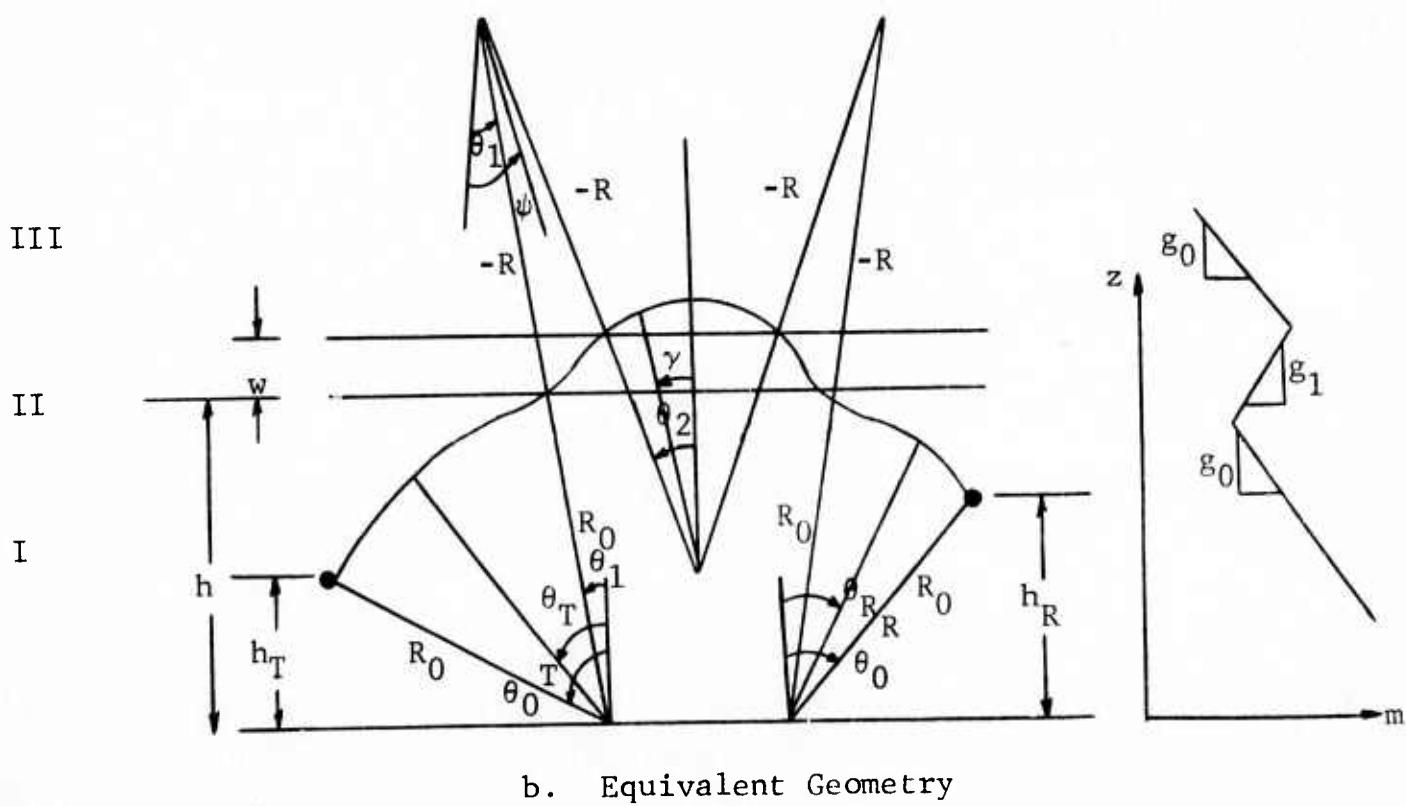
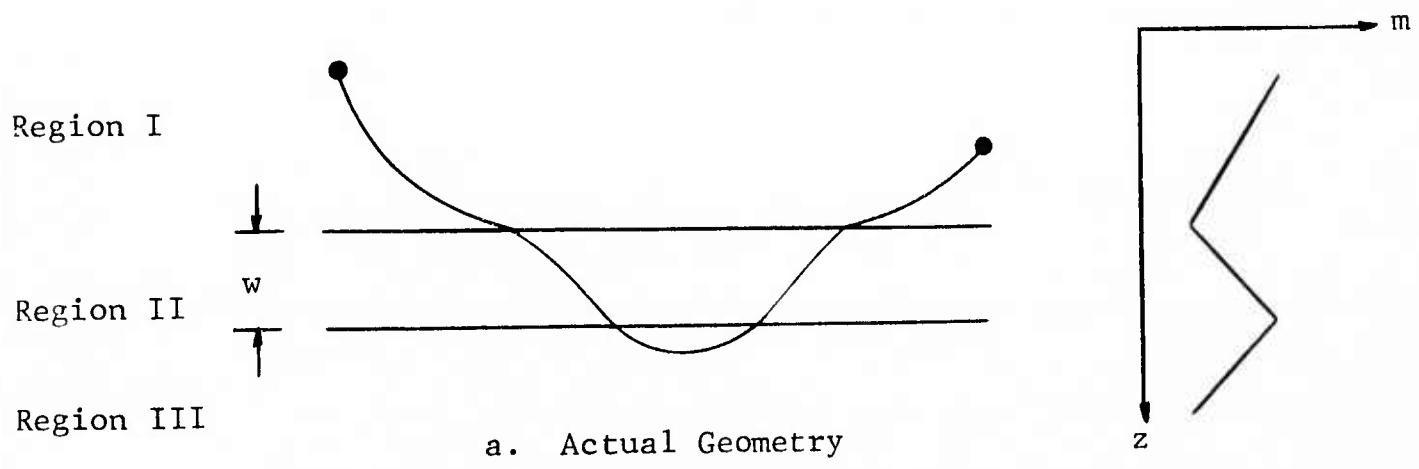


Figure H.1 System Geometry for Layer Below Terminals

$$d\sigma = \begin{cases} -R_0 d\theta_T & \text{at T side} \\ R_0 d\theta_R & \text{at R side} \end{cases} \quad (\text{H.3})$$

where in the equivalent geometry

$$R_0 = -1/g_0 \quad (\text{H.4})$$

has a positive value. Substituting (H.2) and (H.4) into (H.1) gives

$$m = m_0 + g_0 h_{T,R} - \cos \theta_T + \cos \theta_0^{T,R} \quad (\text{H.5})$$

where T,R refer to whether the path segment is on the transmitter or receiver side.

Region II:

In a similar manner, the modified refractive index in region II within the layer can be evaluated as

$$m = m_0 + g_0 h_{T,R} - \cos \psi + \cos \theta_0^{T,R} \quad (\text{H.6})$$

where the angular displacement of a ray is measured by ψ , and the elemental path length is

$$d\sigma = \pm R d\psi \quad (\text{H.7})$$

Region III:

It can similarly be shown that in region III

$$m = m_0 + g_0 h_{T,R} - \cos \gamma + \cos \theta_0^{T,R} \quad (\text{H.8})$$

where γ measures angular displacement, and

$$d\sigma = \pm R_0 d\gamma \quad (\text{H.9})$$

The total path length was derived in Appendix D as

$$\xi = \frac{1}{c_0} \int_{\text{along ray}} m d\sigma \quad (\text{H.10})$$

Substituting the expressions for m and $d\sigma$ into (H.10) and performing the indicated integration, gives

$$\begin{aligned} \xi = & \frac{R_0}{c_0} [(m_0 + \cos \theta_0^T)(\theta_0^T - \theta_1) - \sin \theta_0^T + \sin \theta_1] \\ & + \frac{R}{c_0} [(m_0 + \cos \theta_0^T)(\theta_1 - \theta_2) - \sin \theta_1 + \sin \theta_2] \\ & + \frac{R_0}{c_0} [(m_0 + \cos \theta_0^T)\theta_2 - \sin \theta_2] \\ & + \frac{R_0}{c_0} [(m_0 + \cos \theta_0^R)(\theta_0^R - \theta_1) - \sin \theta_0^R + \sin \theta_1] \\ & + \frac{R}{c_0} [(m_0 + \cos \theta_0^R)(\theta_1 - \theta_2) - \sin \theta_1 + \sin \theta_2] \\ & + \frac{R_0}{c_0} [(m_0 + \cos \theta_0^R)\theta_2 - \sin \theta_2] \end{aligned} \quad (\text{H.11})$$

where θ_1 and θ_2 are the angles of the ray trajectory at the bottom and top of the layer, respectively.

In order for the rays to intercept the receiver at a range L, it is required that the total path length equals L, i.e.,

$$R_0 \sin \theta_0^T - 2(R_0 - R)(\sin \theta_1 - \sin \theta_2) + R_0 \sin \theta_0^R = L \quad (\text{H.12})$$

The height of the layer above T,R and the thickness w of the layer are related to $\theta_0^{T,R}$, θ_1 , and θ_2 by

$$h - h_{T,R} = R_0(\cos \theta_1 - \cos \theta_0^{T,R}) \quad (\text{H.13})$$

$$w = R(\cos \theta_2 - \cos \theta_1) \quad (\text{H.14})$$

Appendix I
CALCULATIONS FOR MULTILAYER PROFILE

Refractive Index Profile

The (modified) refractive index profile is assumed to be layered with linear variation in each layer as a function of height, z . The slope of the profile in each region is specified by

$$\frac{\partial m}{\partial z} = g_i \quad \text{for} \quad z_i < z \leq z_{i+1} \quad i = 0, 1, 2, \dots \quad (\text{I.1})$$

where z_i and z_{i+1} are the altitudes of the lower and upper boundaries of the i 'th layer. A typical profile is shown in Fig. I.1.

Multipath in the i 'th Layer

A ray which enters the i 'th layer from below at an angle θ_i leaves it at an angle θ_{i+1} . The layer extends from a height Z_i to Z_{i+1} and the ray traverses a horizontal distance l_i . The (modified) refractive index within the layer is given by

$$m = m_i + g_i (z - Z_i) \quad (\text{I.2})$$

where m_i is the value of m at $z = Z_i$. The radius of curvature of the ray trajectory is

$$R_i = \frac{-1}{\partial m / \partial z} = -1/g_i \quad (\text{I.3})$$

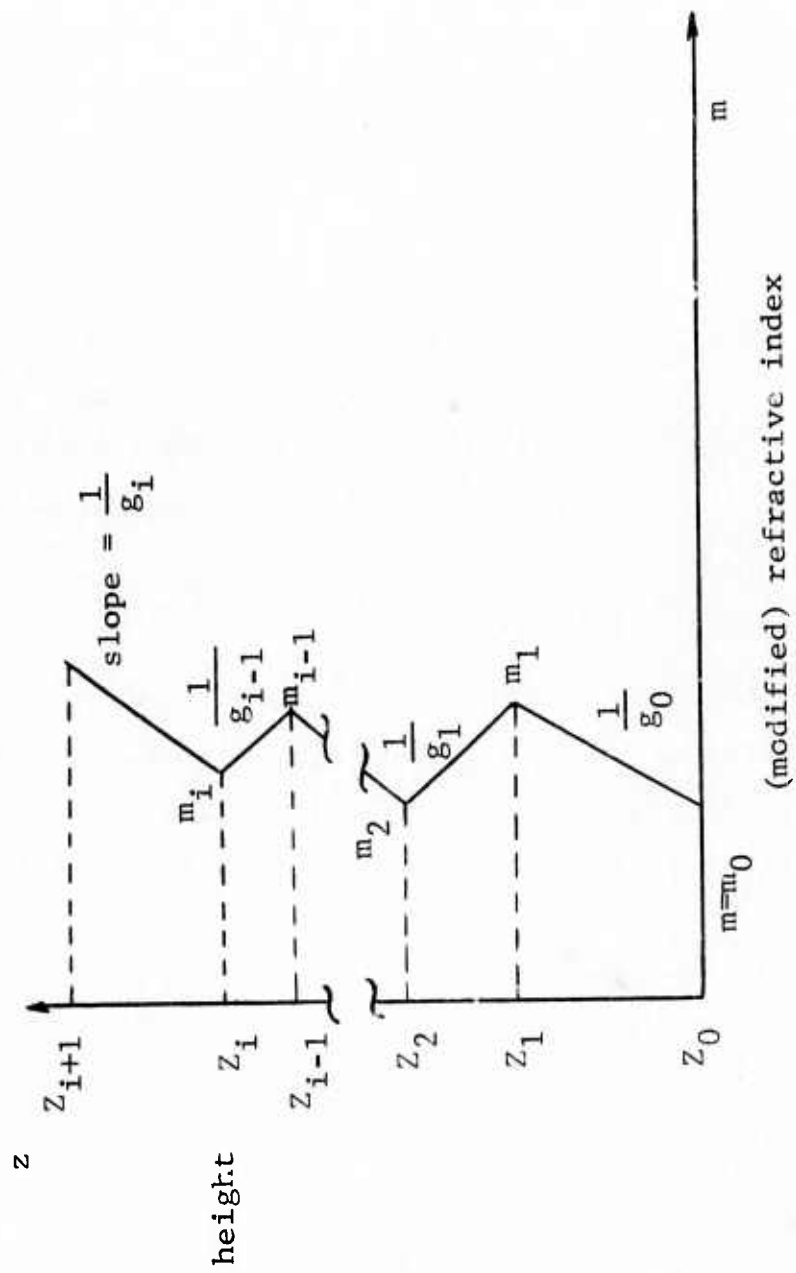


Figure I.1 Piecewise Linear m-Profile

The minus sign indicates that for a positive m-gradient, the ray curves away from the earth. These quantities are shown in Fig. I.2.

Since the ray trajectory is circular, the height of the path above Z_i can be expressed as

$$z - Z_i = -R_i (\cos \theta_i - \cos \psi_i) \quad (\text{I.4})$$

or

$$z - Z_i = \frac{1}{g_i} (\cos \theta_i - \cos \psi_i) \quad (\text{I.5})$$

and a differential line segment along the path as

$$d\sigma_i = -R_i d\psi_i = \frac{1}{g_i} d\psi_i \quad (\text{I.6})$$

The horizontal extent of the path is similarly given by

$$l_i = \frac{1}{g_i} (\sin \theta_{i+1} - \sin \theta_i) \quad (\text{I.7})$$

The time it takes for a signal to travel through the layer along the ray is shown in Appendix D to be given by the line integral

$$\xi_i = \frac{1}{c_0} \int_{\text{ray}} m d\sigma_i \quad (\text{I.8})$$

Substituting (I.2) - (I.6) into (I.8) gives

$$\xi_i = \frac{1}{c_0 g_i} \int_{\theta_i}^{\theta_{i+1}} (m_i + \cos \theta_i - \cos \psi_i) d\psi_i \quad (\text{I.9})$$

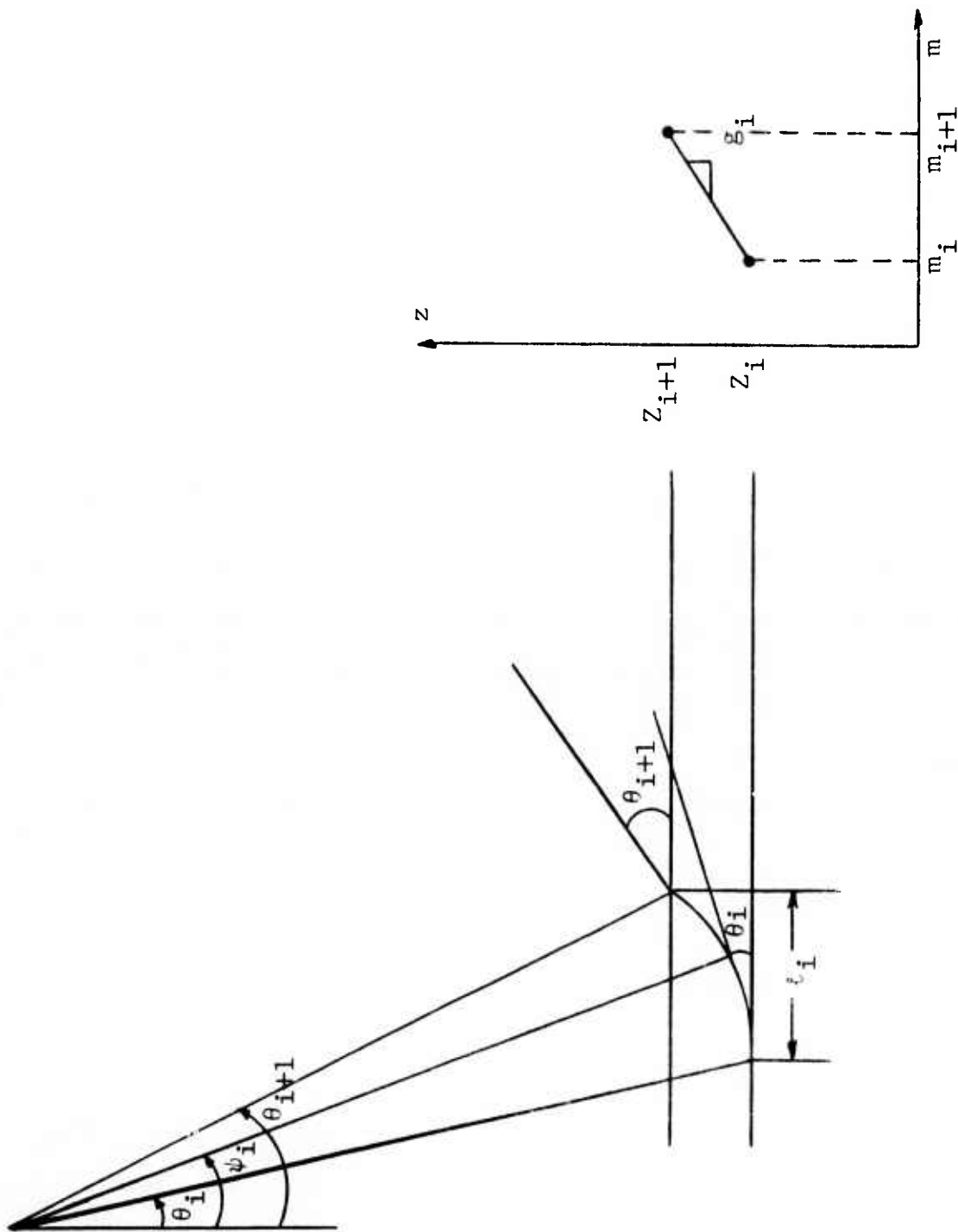


Figure I.2 Ray Trajectory in the i 'th Layer

which is easily evaluated

$$\xi_i = \frac{1}{c_0 g_i} [(m_i + \cos \theta_i)(\theta_{i+1} - \theta_i) - (\sin \theta_{i+1} - \sin \theta_i)] \quad (\text{I.10})$$

The time it takes for a signal to travel the distance l_i in free space is given by

$$T_i = l_i/c_0 = \frac{1}{c_0 g_i} (\sin \theta_{i+1} - \sin \theta_i) \quad (\text{I.11})$$

The delay difference between these two paths is defined by

$$\Delta \xi_i = \xi_i - T_i \quad (\text{I.12})$$

which becomes

$$\begin{aligned} \Delta \xi_i = \frac{1}{c_0 g_i} [(m_i + \cos \theta_i)(\theta_{i+1} - \theta_i) \\ - 2(\sin \theta_{i+1} - \sin \theta_i)] \end{aligned} \quad (\text{I.13})$$

The angles $\{\theta_i\}$ $i = 1, 2, 3$ can be computed in terms of the initial ray angle θ_0 from Snell's law

$$m_i \cos \theta_i = m_0 \cos \theta_0 \quad i = 1, 2, 3, \dots \quad (\text{I.14})$$

A ray which enters the i 'th layer from above at an angle θ_{i+1} leaves it at an angle θ_i . The delay a signal experiences

in passing through the layer on this descending trajectory is easily shown to be identical to that of the previous ascending trajectory.

If Snell's law (I.14) indicates $\cos \theta_i > 1$, the ray cannot penetrate the layer, and a turning point must therefore exist. At the turning point $\theta=0$. Thus, for an ascending trajectory

$$\Delta \xi_i = \frac{1}{c_0 g_i} [(m_i + \cos \theta_i)(-\theta_i) - 2 \sin \theta_i] \quad (\text{I.15})$$

while for a descending trajectory

$$\Delta \xi_i = \frac{1}{c_0 g_i} [(m_i + 1)(\theta_{i+1}) - 2 \sin \theta_{i+1}] \quad (\text{I.16})$$

These answers are identical to (I.13) with the angle for which $\cos \theta > 1$, set equal to zero. It is also easy to show that Eq. (I.13) is valid for negative as well as positive values of the slope g_i .

Total Path Delay at Range L (Relative to Free Space Delay to L)

The total delay difference between the signal which reaches a range L via the refracted path and that which would reach a range L in free space is given by

$$\Delta \xi = \frac{1}{c_0} \sum \left(\frac{m_i + \cos \theta_i}{g_i} \right) (\theta_{i+1} - \theta_i) - 2 \frac{(\sin \theta_{i+1} - \sin \theta_i)}{g_i} \quad (\text{I.17})$$

The range L is

$$L = \sum \frac{\sin \theta_{i+1} - \sin \theta_i}{g_i} \quad (\text{I.18})$$

If the initial ray angle θ_0 is specified, then the subsequent angles and turning points can be computed from Snell's law. The summations are then carried out over the ray trajectory. For positive initial angles, the subscript of each term in the summation increases by one until a turning point is reached, at which point the subscripts begin to decrease by one. Likewise, for negative initial angles, the subscripts decrease until a turning point is reached at which point they begin to increase. Equation (I.18) generates a θ vs. L diagram while (I.17) gives the corresponding delay profile.

Appendix J

DEFINITION OF SPECULAR AND DIFFUSE COMPONENTS

The time variant transfer function $H(f,t)$ is assumed to have a specular and diffuse component

$$H(f,t) = H_{\text{spec}}(f,t) + H_{\text{diff}}(f,t) \quad (\text{J.1})$$

where the specular component of $H(f,t)$ is given by the ensemble average

$$H_{\text{spec}}(f,t) = \langle H(f,t) \rangle \quad (\text{J.2})$$

The diffuse component therefore characterizes the zero mean fluctuations on the channel. The output signal over the channel can then be written as the sum of specular and diffuse components

$$w(t) = w_{\text{spec}}(t) + w_{\text{diff}}(t) \quad (\text{J.3})$$

where the specular component is given by

$$\langle w(t) \rangle = w_{\text{spec}}(t) = \int Z(f) H_{\text{spec}}(f,t) e^{j2\pi ft} df \quad (\text{J.4})$$

and the diffuse component by

$$w_{\text{diff}}(t) = \int Z(f) H_{\text{diff}}(f,t) e^{j2\pi ft} df \quad (\text{J.5})$$

These relations are shown in Fig. J.1.

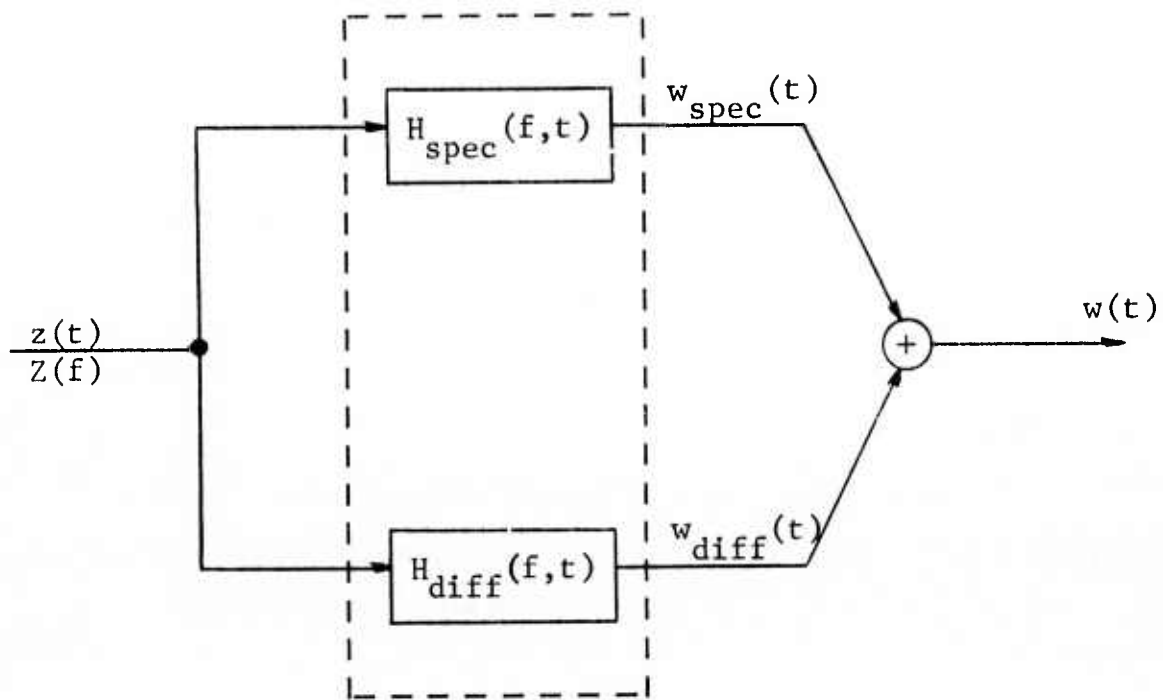


Figure J.1 The Specular and Diffuse Components

If $H_{\text{spec}}(f,t)$ has a constant magnitude and a linear phase variation as a function of f and t , then the specular component becomes a discrete specular component given by

$$H_{\text{spec}}(f,t) = H_{\text{ds}}(f,t) = C \exp(-j2\pi f \xi_s) \exp(j2\pi \nu_s t) \quad (\text{J.6})$$

where C is a complex constant and ξ_s and ν_s are the specular delay and Doppler frequency, respectively. Note from Eq. (J.4) that $H_{\text{spec}}(f,t)$ need only have a discrete nature over the bandwidth of the input signal and the duration of the output signal in order to produce a discrete specular output component. Substituting Eq. (J.6) into (J.4) gives this output as a near replica of the input, with a specular delay and Doppler shift, i.e.,

$$w_{\text{ds}}(t) = C z(t - \xi_s) e^{j2\pi \nu_s t} \quad (\text{J.7})$$

This is shown diagrammatically in Fig. J.2.

Another interpretation of the discrete specular component can be made by removing the specular point delay and Doppler from $H_{\text{spec}}(f,t)$ and expanding in a power series in t and f , i.e., let

$$G(f,t) = H_{\text{spec}}(f,t) \exp[j2\pi(f\xi_s - \nu_s t)] \quad (\text{J.8})$$

then

$$G(f,t) = \sum_{m=0}^{\infty} \sum_{n=0}^{\infty} G_{mn} f^m t^n \quad (\text{J.9})$$

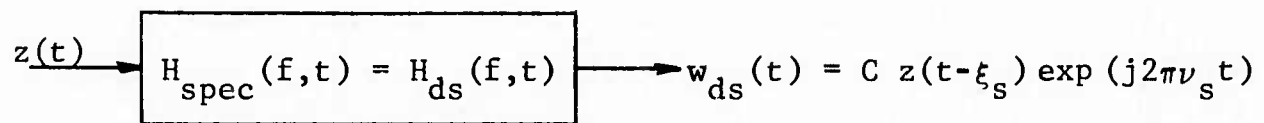


Figure J.2 The Discrete Specular Component

where

$$G_{mn} = \frac{1}{m!n!} \left[\frac{\partial^{m+n} G(f,t)}{\partial f^m \partial t^n} \right]_{\substack{f=0 \\ t=0}} \quad (J.10)$$

Note that we are assuming for simplicity that the signals are to be centered at $f=t=0$ about which $G(f,t)$ is expanded. The zero-order ($m=n=0$) term in this ft -power series representation of the system function is then observed to be the discrete specular component, i.e.,

$$H_{ds}(f,t) = G_{00} \exp [-j2\pi(f\xi_s - \nu_s t)] \quad (J.11)$$

The higher order terms which depend on the partial derivatives, determine the variation of $H_{spec}(f,t)$ with respect to f and t . Thus the discrete specular component is simply the first term in a power series expansion of $H_{spec}(f,t)$, and further, when the variation of $H_{spec}(f,t)$ across the bandwidth of the input signal and time duration of the output signal is negligible, the discrete specular component is the only appreciable specular component. Convergence properties of the expansion (J.9) as well as the significance of power series models has been discussed by Bello [3.29].

The remaining terms in the power series expansion could be defined as the continuous specular component. Similarly, discrete and continuous diffuse components could be defined by generating an ft -power series expansion of $H_{diff}(f,t)$. However, since only the discrete specular component is presently under study, these other components are now mentioned only for completeness.

Appendix K

INTEGRAL FORMULATION OF THE SPECULAR COMPONENT

The signal scattered from a rough surface can be computed from the modified Stratton-Chu integral (see DeRosa, Ref. [3.36], p. 70)

$$V = \frac{jK_R}{4\pi} \iint A_R(\vec{r}_{SR}) \hat{\rho}_R^* \cdot \left[-\sqrt{\frac{\mu_0}{\epsilon_0}} \hat{n} \times \vec{h} + (\hat{n} \times \vec{e}) \times \hat{\beta} + (\hat{n} \cdot \vec{e}) \hat{\beta} \right] \omega \, dA \quad (K.1)$$

where

$$\omega = [\exp(-jk \hat{\beta} \cdot \vec{r}_{SR})] / r_{SR} \quad (K.2)$$

\vec{e} and \vec{h} are the total fields just above the surface, A_R , $\hat{\rho}_R$, and K_R are the (voltage) gain pattern, the polarization, and a constant associated with receiving antenna, respectively.

\vec{r}_{SR} is the slant range from S to R, and \hat{n} and $\hat{\beta}$ are unit vectors normal to S and in \vec{r}_{SR} direction, respectively (see Fig. K.1). If the excitation were a unit cissoid, integral (K.1) would represent the time variant transfer function $H(f,t)$, i.e., when the incident electric field is given by

$$\vec{E}_i = \frac{K_T A_T(\vec{r}_{TS})}{\sqrt{4\pi} r_{TS}} \exp(-jk\hat{\alpha} \cdot \vec{r}_{TS}) \hat{\rho}_T \quad (K.3)$$

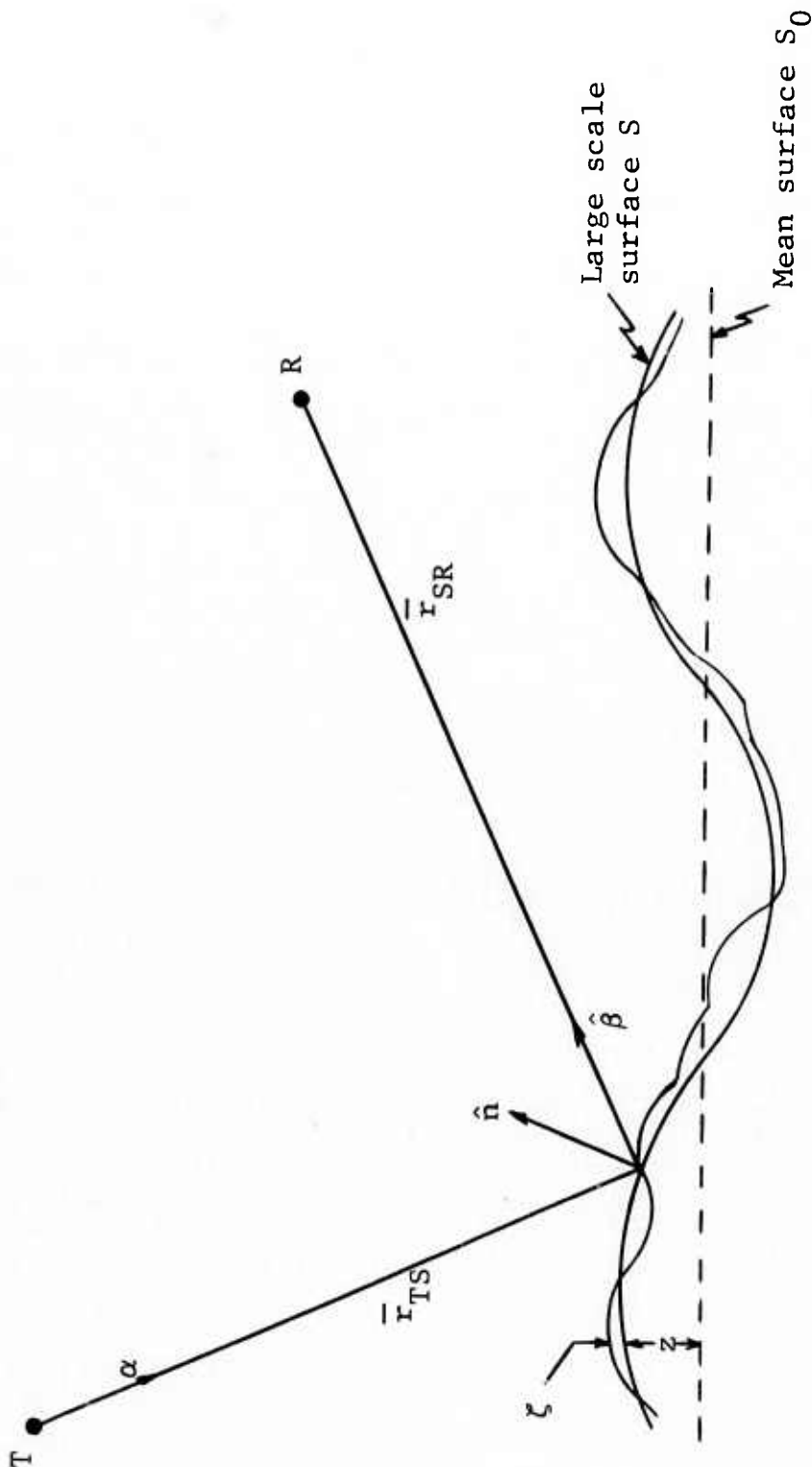


Figure K.1 Geometry of Surface Scattering

then

$$V = H(f, t) \quad (K.4)$$

Assuming that the surface has two discernable scales of roughness, such that the fields on the surface can be calculated by the Kirchoff method (for the large scale roughness) and the small perturbation method (for the small scale), then it can be shown that

$$\vec{e} = \vec{E}^0 + \vec{E} \quad (K.5)$$

$$\vec{h} = \vec{H}^0 + h \quad (K.6)$$

where the zero'th order fields are given by

$$\vec{E}^0 = \frac{2a_0}{a_0 + b_0} \vec{E}^i - \frac{2a_0(\epsilon_0 - \epsilon_1)}{\epsilon_0 b_0 + \epsilon_1 a_0} (\hat{n} \cdot \vec{E}^i) \left(\hat{n} + \frac{\hat{\alpha}}{a_0 + b_0} \right) \quad (K.7)$$

$$\vec{H}^0 = \frac{2a_0}{a_0 + b_0} \sqrt{\frac{\epsilon_0}{\mu_0}} \left[(\hat{\alpha} \times \vec{E}^i) + (a_0 - b_0) \hat{n} \times \vec{E}^i + \frac{(\epsilon_0 - \epsilon_1)(a_0 - b_0)}{\epsilon_0 b_0 + \epsilon_1 a_0} (\hat{n} \cdot \vec{E}^i) (\hat{\alpha} \times \hat{n}) \right] \quad (K.8)$$

in which

$$a_0 = -\hat{n} \cdot \hat{\alpha} \quad (K.9)$$

$$b_0 = \sqrt{\frac{\epsilon_1}{\epsilon_0} - 1 + a^2} \quad (\text{K.10})$$

The first order fields are given by

$$\begin{aligned} \vec{E} = \frac{1}{a\epsilon_1 + b\epsilon_0} & \left\{ \frac{\epsilon_1 - \epsilon_0}{a+b} [(\hat{\beta} \cdot \vec{J}_m)(\hat{n} \times \hat{\beta}) + \sqrt{\frac{\mu_0}{\epsilon_0}} \hat{\beta} \times (\hat{n} \times J_e)] \right. \\ & \left. + \frac{\epsilon_1}{\epsilon_0} (\hat{\beta} \cdot \vec{J}_m) + \epsilon_0 \sqrt{\frac{\mu_0}{\epsilon_0}} \hat{\beta} \times (\hat{\beta} \times J_e) \right\} \end{aligned} \quad (\text{K.11})$$

$$\vec{H} = \sqrt{\frac{\epsilon_0}{\mu_0}} \hat{\beta} \times \vec{E} \quad (\text{K.12})$$

in which the electric and magnetic current densities are given by

$$\vec{J}_e = jk \sqrt{\frac{\epsilon_0}{\mu_0}} \left(1 - \frac{\epsilon_0}{\epsilon_1}\right) \hat{n} \times (\vec{E}^0 \times \hat{n}) \zeta \quad (\text{K.13})$$

$$\vec{J}_m = \frac{\epsilon_1 - \epsilon_0}{\epsilon_0} (\hat{n} \cdot \vec{E}^0) \hat{n} \times \nabla \zeta \quad (\text{K.14})$$

and

$$a = \hat{n} \cdot \hat{\beta} \quad (\text{K.15})$$

$$b = \sqrt{\frac{\epsilon_1}{\epsilon_0} - 1 + a^2} \quad (\text{K.16})$$

It should be noted that \vec{E} and \vec{H} are linearly proportional to the small scale height, ζ , and slopes, $\nabla\zeta$. Since no other terms in the integrand of (K.1) are dependent on these random variables, when (K.1) is averaged over ζ and $\nabla\zeta$, the contribution from \vec{E} and \vec{H} will have a mean value equal to zero. Therefore when computing the specular component, only the large scale surface and related fields need be considered.

The integration in (K.1) is carried out over the rough surface, S . The differential area dA can be expressed in terms of the differential area element along the mean surface, i.e.,

$$dA = dA_{\text{mean}} / (\hat{n} \cdot \hat{m}) \quad (\text{K.17})$$

where

$$dA_{\text{mean}} = dx_1 dx_2 \quad (\text{K.18})$$

\hat{m} is the mean normal

$$\langle \hat{n} \rangle = \hat{m} \quad (\text{K.19})$$

Then the received voltage can be expressed as

$$V = \iint g(\hat{n}, x_1, x_2) e^{-jk(\hat{\alpha} \cdot \vec{r}_{TS} + \hat{\beta} \cdot \vec{r}_{SR})} dx_1 dx_2 \quad (\text{K.20})$$

where g is obtained by substituting (K.3) and (K.7) - (K.10) into (K.1)

$$g(\hat{n}, x_1, x_2) = \frac{j^k R_T}{(4\pi)^{1/2}} A_R A_T \dots \quad (K.21)$$

and the phase factor, referenced to the mean surface is

$$\hat{\alpha} \cdot \vec{r}_{TS} + \hat{\beta} \cdot \vec{r}_{SR} = r_{10} + r_{20} + (\hat{\alpha} - \hat{\beta}) \cdot \hat{a}_z Z \quad (K.22)$$

Since \hat{n} , and therefore g , vary only with the surface slopes, then g and the phase factor can be averaged separately (assuming the height Z and the surface slopes are independent). The average value of V can then be expressed as

$$\langle V \rangle = \iint \langle g(\hat{n}, x_1, x_2) \rangle C_Z [k(\alpha_z - \beta_z)] e^{-jk(r_{10} + r_{20})} dx_1 dx_2 \quad (K.23)$$

where C_Z is the characteristic function of the surface heights, i.e.,

$$C_Z(\omega) = \langle e^{j\omega Z} \rangle \quad (K.24)$$

The effect of averaging over the surface heights then is to modify the illumination $g(\hat{n}, x_1, x_2)$ by the characteristic function $C_Z[k(\alpha_z - \beta_z)]$ evaluated at each (x_1, x_2) point.

Note that g is not generally a linear function of \hat{n} . If it were, then the average value of V , could be computed from (K.23) by performing the integration with $\hat{n} = \hat{m}$. However, since it contains products of factors containing \hat{n} [e.g., $(\hat{n} \cdot \hat{\alpha})(\hat{n} \cdot \hat{\rho}_T)(\hat{n} \cdot \hat{\rho}_R)$], then in general

$$\langle g(\hat{n}, x_1, x_2) \rangle \neq g(\hat{m}, x_1, x_2) \quad (\text{K.25})$$

where \hat{m} is the mean normal. The important conclusion reached here is one that is not usually appreciated in calculating the specular component, and that is, the mean value of the scattered signal is not necessarily equal to the signal scattered from the mean surface (with the illumination modified by C_2).

When the surface is perfectly conducting, $\epsilon \rightarrow \infty$, and a straightforward calculation shows that

$$\lim_{\epsilon \rightarrow \infty} \langle g(\hat{n}, x_1, x_2) \rangle = g(\hat{m}, x_1, x_2) \quad (\text{K.26})$$

where again \hat{m} is the mean normal. Therefore, in the evaluation of the specular component of the received signal, the rough surface S may be replaced by the mean surface S_0 only when the surface is perfectly conducting. For finitely conducting calculations higher order moments of \hat{n} enter into the specular calculation.

It seems reasonable from intuition that for finitely conducting surfaces which are not very rough, the dispersion in \hat{n} may be negligible, so that \hat{n} may be replaced by the mean value \hat{m} in $g(\hat{n}, x_1, x_2)$. This heuristic argument was presented by

Beckmann [3.3] and is generally used for justification of specular calculations. The mathematical complexity of evaluation of the specular component for finitely conducting surfaces is presented in the Soviet literature, where a one-dimensional, first-order solution is given [3.37].

For present purposes, the specular component scattered from a perfectly conducting surface will be calculated, and the more complex problem associated with the finitely conducting surface will be deferred to a later research effort. Since more power is scattered from a perfectly conducting surface, the calculations represent worst-case multipath interference.

Appendix L

CALCULATIONS FOR SURFACE SCATTER AND REFLECTION CHANNEL

Specular Point Delay

The delay difference between the specularly reflected signal and the direct path signal is given by (see Fig. L.1)

$$\Delta\xi = \frac{1}{c} (r_1 + r_2 - r_{TR}) \quad (\text{L.1})$$

where

$$r_1 = a \sqrt{1 + (1+h_T/a)^2 - 2(1+h_T/a) \cos \theta_S} \quad (\text{L.2})$$

$$r_2 = a \sqrt{1 + (1+h_R/a)^2 - 2(1+h_R/a) \cos (\theta_R - \theta_S)} \quad (\text{L.3})$$

$$r_{TS} = a \sqrt{(1+h_T/a)^2 + (1+h_R/a)^2 - 2(1+h_T/a)(1+h_R/a) \cos \theta_R} \quad (\text{L.4})$$

The evaluation of (L.1) is simplified by expressing θ_S , $(\theta_R - \theta_S)$, and θ_R in terms of the arc lengths along the surface.

$$\theta_S = L_1/a \quad (\text{L.5})$$

$$\theta_R - \theta_S = L_2/a \quad (\text{L.6})$$

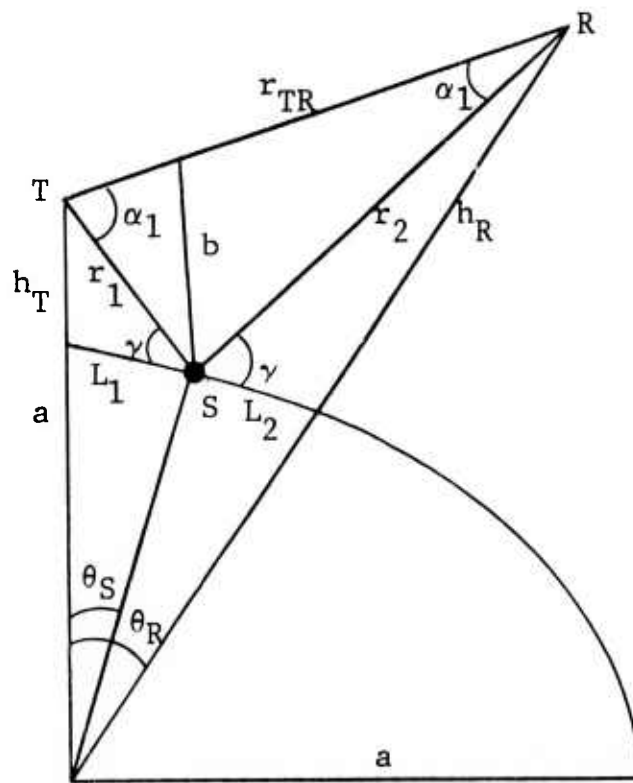


Figure L.1 Specular Point Geometry

$$\theta_R = L/a \quad (L.7)$$

where a is the earth's radius, and

$$L = L_1 + L_2 \quad (L.8)$$

is the range from T to R measured along the surface. When this distance L is much smaller than a , as it is in virtually all line-of-sight links, the angles can be approximated by their signs, such that

$$\cos \theta_S = \sqrt{1 - \sin^2 \theta_S} \approx \sqrt{1 - \left(\frac{L_1}{a}\right)^2} \approx 1 - \frac{1}{2} \left(\frac{L_1}{a}\right)^2 \quad (L.9)$$

and likewise

$$\cos (\theta_R - \theta_S) \approx 1 - \frac{1}{2} \left(\frac{L_2}{a}\right)^2 \quad (L.10)$$

$$\cos \theta_R \approx 1 - \frac{1}{2} \left(\frac{L}{a}\right)^2 \quad (L.11)$$

Substituting (L.9) - (L.11) into (L.2) - (L.4) gives

$$r_1 = \sqrt{h_T^2 + L_1^2 (1 + h_T/a)} \quad (L.12)$$

$$r_2 = \sqrt{h_R^2 + L_2^2 (1 + h_R/a)} \quad (L.13)$$

$$r_{TR} = \sqrt{(h_R - h_T)^2 + L^2 \left(1 + \frac{h_T + h_R}{a} + \frac{h_T h_R}{2a^2}\right)} \quad (L.14)$$

In tropospheric communication channels $h_T, h_R \ll a$, so that the slant ranges can well be approximated by

$$r_1 = \sqrt{h_T^2 + L_1^2} \quad (\text{L.15})$$

$$r_2 = \sqrt{h_R^2 + L_2^2} \quad (\text{L.16})$$

$$r_{TR} = \sqrt{(h_R - h_T)^2 + L^2} \quad (\text{L.17})$$

with the previously mentioned stipulations

$$h_T, h_R, L \ll a \quad (\text{L.18})$$

Equations (L.15) - (L.17) are identical to the slant ranges for a flat earth geometry as shown in Fig. L.2. Thus as long as the range from T to R and the heights of T and R are much smaller than the radius of the earth (using the 4/3 model), the flat earth approximation will yield reasonably accurate results for specular multipath calculations. The maximum error in the calculation of specular point delay difference is calculated below.

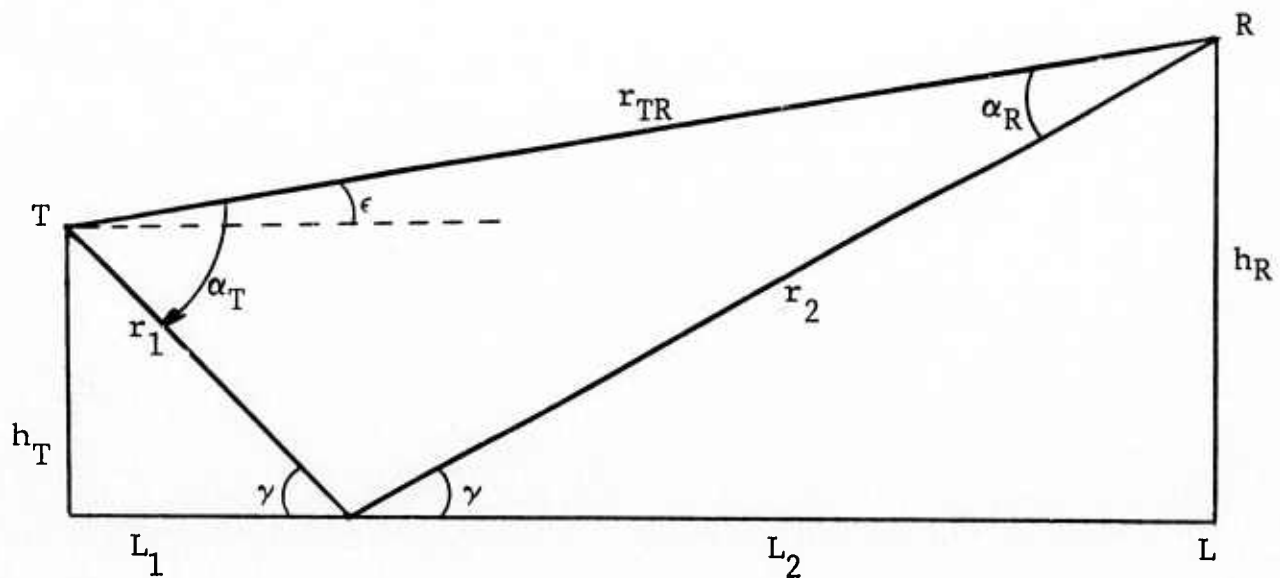


Figure L.2 Flat Earth Approximation

Error Bound for Specular Point Delay Difference

At small grazing angles, the slant ranges from T to S, S to R, and T to R, can be written as

$$r_1 = \sqrt{h_T^2 + L_1^2} \sqrt{1 + h_T L_1^2 / a (h_T^2 + L_1^2)} \quad (\text{L.19})$$

$$r_2 = \sqrt{h_R^2 + L_2^2} \sqrt{1 + h_R L_2^2 / a (h_R^2 + L_2^2)} \quad (\text{L.20})$$

$$r_{TR} = \sqrt{(h_R - h_T)^2 + L^2} \sqrt{1 + [h_T (1 + \frac{h_R}{a}) + h_R] L^2 / a [(h_R - h_T)^2 + L^2]} \quad (\text{L.21})$$

Noting that for a flat earth geometry (see Fig. L.2), the grazing angle γ and elevation angle ϵ are given by

$$\cos \gamma = L_1 / \sqrt{h_T^2 + L_1^2} = L_2 / \sqrt{h_R^2 + L_2^2} \quad (\text{L.22})$$

$$\cos \epsilon = L / \sqrt{(h_R - h_T)^2 + L^2} \quad (\text{L.23})$$

Substituting (L.22) and (L.23) into (L.19) - (L.21), and assuming that $h_T, h_R \ll a$, we get

$$r_1 = \sqrt{h_T^2 + L_1^2} \left(1 + \frac{1}{2} \frac{h_T}{a} \cos^2 \gamma\right) \quad (\text{L.24})$$

$$r_2 = \sqrt{h_R^2 + L_2^2} \left(1 + \frac{1}{2} \frac{h_R}{a} \cos^2 \gamma\right) \quad (\text{L.25})$$

$$r_{TR} = \sqrt{(h_R - h_T)^2 + L^2} \left[1 + \frac{1}{2} \frac{(h_T + h_R)}{a} \cos^2 \epsilon\right] \quad (\text{L.26})$$

The true range difference is given by

$$\Delta r = r_1 + r_2 - r_{TR} \quad (\text{L.27})$$

Note that if we estimated the slant ranges by the flat earth values,

$$\tilde{r}_1 = \sqrt{h_T^2 + L_1^2} \quad (\text{L.28})$$

$$\tilde{r}_2 = \sqrt{h_R^2 + L_2^2} \quad (\text{L.29})$$

$$\tilde{r}_{TR} = \sqrt{(h_R - h_T)^2 + L^2} \quad (\text{L.30})$$

then these estimates are each smaller than the true values given in (L.24) - (L.26). The (flat earth) estimate of range difference is given by

$$\Delta \tilde{r} = \tilde{r}_1 + \tilde{r}_2 - \tilde{r}_{TR} \quad (\text{L.31})$$

The error in this estimate is

$$E_{\Delta r} = (r_1 + R_2 - r_{TR}) - (\tilde{r}_1 + \tilde{r}_2 - \tilde{r}_{TR}) \quad (L.32)$$

$$= \left[\frac{\cos^2 \gamma}{2a} (h_R r_1 + h_R r_2) \right] - \left[\frac{\cos^2 \epsilon}{2a} (h_T + h_R) r_{TR} \right] \quad (L.33)$$

Now since

$$\begin{aligned} \cos^2 \gamma (h_T r_1 + h_R r_2) &\leq (h_T r_{TR} + h_R r_{TR}) \cos^2 \gamma \\ &\leq (h_T + h_R) r_{TR} \cos^2 \epsilon \end{aligned} \quad (L.34)$$

Then the magnitude of the maximum error in Δr is given by

$$|E_{\Delta r}|_{\max} = \frac{(h_T + h_R)}{2a} r_{TR} (\cos^2 \epsilon - \cos^2 \gamma) \quad (L.35)$$

Replacing $\cos \epsilon$ by its maximum value, we get

$$|E_{\Delta r}|_{\max} \leq \frac{h_T + h_R}{2a} r_{TR} \sin^2 \gamma \quad (L.36)$$

Then the maximum error in the delay calculation is given by

$$|E_{\Delta t}|_{\max} \leq \frac{1}{c} \left(\frac{h_T + h_R}{2} \right) \frac{r_{TR}}{a} \sin^2 \gamma \quad (L.37)$$

From a direct trigonometric analysis of the flat earth geometry, it can be shown that

$$L_1 = h_T L / (h_T + h_R) \quad (\text{L.38})$$

$$L_2 = h_R L / (h_T + h_R) \quad (\text{L.39})$$

Substituting Eq. (L.38) and (L.39) into (L.15) - (L.17) gives

$$r_1 = \frac{h_T L}{h_T + h_R} \sqrt{1 + \left(\frac{h_R + h_T}{L}\right)^2} \quad (\text{L.40})$$

$$r_2 = \frac{h_R L}{h_T + h_R} \sqrt{1 + \left(\frac{h_R + h_T}{L}\right)^2} \quad (\text{L.41})$$

$$r_{TR} = L \sqrt{1 + \left(\frac{h_R - h_T}{L}\right)^2} \quad (\text{L.42})$$

The range difference between the direct and reflected paths is given by

$$\Delta r = r_1 + r_2 - r_{TR} \quad (\text{L.43})$$

When the transmitter and receiver heights are much less than the range L, the square roots can well be approximated by the first two terms of their binomial series. This results in a delay difference of

$$\Delta\xi = \frac{\Delta r}{c} \approx 2h_T h_R / L \quad (\text{L.44})$$

A plot of this delay difference as a function of range with h_T and h_R as parameters is shown in Fig. 3.38.

The Specular Point Doppler

The maximum Doppler shift between the direct and reflected paths occurs when the aircraft is moving along one of the ray trajectories. The relative Doppler shifts induced by the motion of R and T are then given by

$$\Delta\nu_R = \frac{f_0 v_R}{c} (1 - \cos \alpha_R) \quad (\text{L.45})$$

$$\Delta\nu_T = \frac{f_0 v_T}{c} (1 - \cos \alpha_T) \quad (\text{L.46})$$

where v_R and v_T are the aircraft velocities, and α_R and α_T are the angles between the direct path and reflected path measured at R and T, respectively (see Fig. L.2).

The angles α_R and α_T are related to ϵ , the elevation angle of R with respect to T, by

$$\alpha_R = \gamma - \epsilon \quad (\text{L.47})$$

$$\alpha_T = \gamma + \epsilon \quad (\text{L.48})$$

Therefore

$$\tan \alpha_R = \tan (\gamma - \epsilon) = (\tan \gamma - \tan \epsilon) / (1 + \tan \gamma \tan \epsilon) \quad (\text{L.49})$$

and

$$\tan \alpha_R = (\tan \gamma + \tan \epsilon) / (1 - \tan \gamma \tan \epsilon) \quad (\text{L.50})$$

Now

$$\tan \gamma = (h_R + h_T) / L \quad (\text{L.51})$$

and

$$\tan \epsilon = (h_R - h_T) / L \quad (\text{L.52})$$

so that

$$\tan \alpha_R = (2h_T / L) / (1 + \frac{h_R^2 - h_T^2}{L^2}) \quad (\text{L.53})$$

$$\tan \alpha_T = (2h_R / L) / (1 - \frac{h_R^2 - h_T^2}{L^2}) \quad (\text{L.54})$$

For the low grazing angle cases of interest here $h_T, h_R \ll L$. This results in the close approximations

$$\tan \alpha_R = 2h_T / L \quad (\text{L.55})$$

$$\tan \alpha_T = 2h_R / L \quad (\text{L.56})$$

The angles α_R , α_T and γ are plotted as a function of receiver height, transmitter height, and range in Fig. 3.39. A plot of the maximum Doppler difference normalized to the direct path

Doppler is shown in Fig. 3.40 as a function of h_T , h_R and L .

Antenna Discrimination

In order for the antennas to successfully discriminate against specular multipath, the specular point must not lie in the common region illuminated by the transmitting and receiving antennas. In the previous section, it was shown that the specular point subtends angles α_R and α_T with respect to the direct path ray, where

$$\tan \alpha_R = 2h_T/L \quad (L.57)$$

$$\tan \alpha_T = 2h_R/L \quad (L.58)$$

For the cases of interest, α_R and α_T are small angles so that the tangents are approximately equal to the angles. In order to discriminate against specular multipath, one of the antennas must have a beamwidth which satisfies

$$\frac{B_R}{2} < 2h_T/L \text{ radians} \quad (L.59)$$

$$\frac{B_T}{2} < 2h_R/L \text{ radians} \quad (L.60)$$

where B_R and B_T are the receiving and transmitting antenna elevation angle beamwidths, respectively. A graph of α_T and α_R is shown in Fig. 3.39 of Section 3.5.2. It is seen that for an aircraft at a range of 200 miles, and a height of 10,000 feet, the ground terminal would need a beamwidth less

than 2° to discriminate against the specular multipath. The specular delay difference under these conditions is seen from Fig.3.38 to be about 0.2 nanosecond (assuming $h_T = 100$ feet). As the aircraft altitude is decreased, a still smaller beamwidth is needed to successfully discriminate against this specular component.

The necessary size of the antennas can be related to the multipath geometry by examining the half-power beamwidth of an antenna with a uniform current distribution [3.39].

$$B = 50.8 \lambda / \ell \text{ degrees} \quad (\text{L.61})$$

where λ is the wavelength and ℓ is the length of the aperture (in the vertical direction). Equation (L.61) is also approximately valid for a parabolic antenna with a uniform distribution. Comparison of (L.61) with (L.59) and (L.60) indicates that in order to discriminate multipath, the approximate sizes of the antennas are constrained by

$$\ell_T > 0.443 \lambda L / h_R \quad (\text{L.62})$$

$$\ell_R > 0.443 \lambda L / h_T \quad (\text{L.63})$$

The largest wavelength for the proposed system is about 7.5 cm (0.25 feet), so that

$$\ell_T > 288 L / h_R \text{ feet} \quad (\text{L.64})$$

$$\ell_R > 288 L / h_T \text{ feet} \quad (\text{L.65})$$

where the units of L are miles and the units of h_T , h_R are feet. Thus for an aircraft at a 200 mile range and a 10,000 foot altitude, the ground antenna (T) would need to be larger than about 5.8 feet in order to discriminate against the specular component. Because the ground antenna is at a much smaller height, the size of the aircraft antenna l_R would need to be prohibitively large to provide this discrimination.

It should be noted that antenna side lobes have been ignored in this analysis. However, it should be mentioned in passing that if the side lobe level is large in the direction of the specular point, significant multipath could be coupled into the receiver via this side lobe even though the main beamwidth is small enough to provide discrimination. Thus care must be taken in designing the antennas to prevent appreciable side lobe levels in the specular direction.

Appendix M

CALCULATION OF CORRELATION FUNCTIONS

The detailed behavior of the carrier tracking loop in a PN receiver is determined by the correlation function $R(t)$ of the received PN sequence and the locally generated replica. Similarly, the behavior of the code tracking loop is determined by the correlation function $S(t)$ of the received sequence and the output of the split-gate circuit. In this appendix we calculate these correlation functions for the case in which the received sequence has been passed through a linear filter with a Gaussian transfer function.

The receiver waveforms $x(t)$ and $y(t)$ are shown in Fig. M.1; $x(t)$ is the PN output waveform and $y(t)$ is the split-gate output waveform. The waveform $r(t)$ of the received sequence is the result of passing $x(t)$ through a linear filter with impulse response $h(t)$; that is,

$$r(t) = x(t) * h(t) . \quad (M.1)$$

where

$$h(t) = \frac{1}{2\sqrt{\pi\alpha}} e^{-t^2/4\alpha} . \quad (M.2)$$

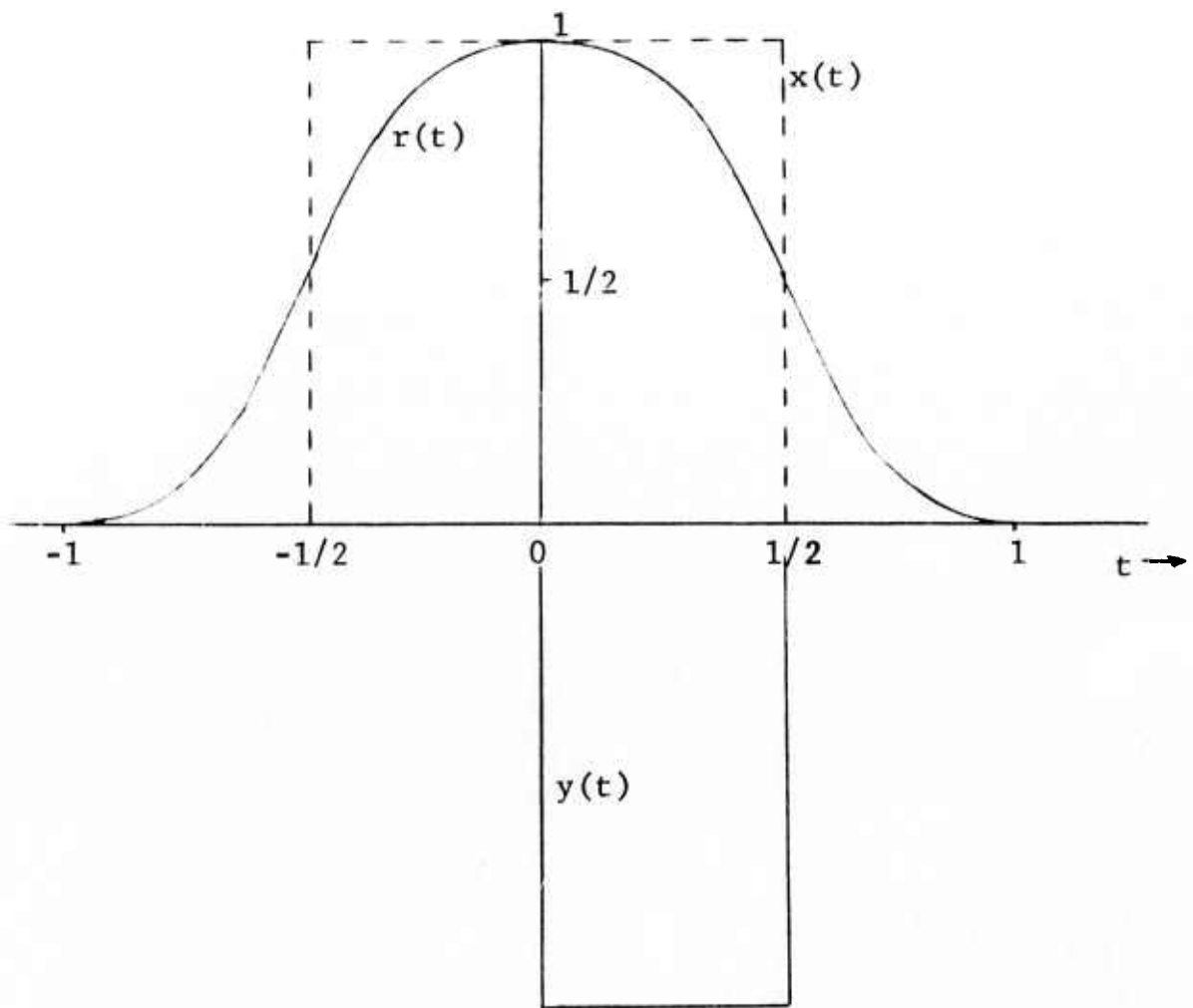


Figure M.1 Receiver Pulse Shapes

The transform* of $h(t)$ is given by

$$H(\omega) = e^{-\alpha\omega^2} \quad (\text{M.3})$$

The parameter α may be expressed in terms of the transfer function's 3 dB point:

$$\alpha = \frac{\log_e 2}{2\omega_{3 \text{ dB}}^2} \quad (\text{M.4})$$

Substituting the transfer function of (M.3) into Eq. (M.1) it is readily found that

$$r(t) = \frac{1}{2} \left[\text{erfc} \left(\frac{t-1/2}{2\sqrt{\alpha}} \right) - \text{erfc} \left(\frac{t+1/2}{2\sqrt{\alpha}} \right) \right] \quad (\text{M.5})$$

where the complementary error function is defined by

$$\text{erfc } x = 1 - \text{erf } (x) \quad (\text{M.6})$$

*To make this transfer function approximately realizable, a factor $e^{-j\omega t_0}$, corresponding to a delay t_0 could be inserted in Eq. (M.3); this modification would simply result in a time shift of all the functions to be calculated.

where

$$\operatorname{erf}(x) = \frac{2}{\sqrt{\pi}} \int_0^x e^{-t^2} dt \quad (\text{M.7})$$

and

$$\operatorname{erf}(-x) = -\operatorname{erf}(x) \quad (\text{M.8})$$

The desired correlation functions are given by

$$R(t) = x(t) * r(t) \quad (\text{M.9})$$

and

$$S(t) = y(t) * r(t) \quad (\text{M.10})$$

Both of these may be evaluated by substituting the appropriate waveforms and carrying out the indicated convolution. The laborious details will not be presented; the results are:

$$\begin{aligned}
R(t) = & t \operatorname{erfc} \left(\frac{t}{2\sqrt{\alpha}} \right) - \left(\frac{t-1}{2} \right) \operatorname{erfc} \left(\frac{t-1}{2\sqrt{\alpha}} \right) \\
& - \left(\frac{t+1}{2} \right) \operatorname{erfc} \left(\frac{t+1}{2\sqrt{\alpha}} \right) - \sqrt{\frac{\alpha}{\pi}} \left[2e^{-t^2/4\alpha} - e^{-(t-1)^2/4\alpha} - e^{-(t+1)^2/4\alpha} \right]
\end{aligned}
\tag{M.11}$$

$$\begin{aligned}
S(t) = & (t+1/2) \operatorname{erfc} \left(\frac{t+1/2}{2\sqrt{\alpha}} \right) - (t-1/2) \operatorname{erfc} \left(\frac{t-1/2}{2\sqrt{\alpha}} \right) \\
& + \left(\frac{t-1}{2} \right) \operatorname{erfc} \left(\frac{t-1}{2\sqrt{\alpha}} \right) - \left(\frac{t+1}{2} \right) \operatorname{erfc} \left(\frac{t+1}{2\sqrt{\alpha}} \right) \\
& - \sqrt{\frac{\alpha}{\pi}} \left[2e^{-(t+1/2)^2/4\alpha} - 2e^{-(t-1/2)^2/4\alpha} + e^{-(t-1)^2/4\alpha} - e^{-(t+1)^2/4\alpha} \right]
\end{aligned}
\tag{M.12}$$

(These results are plotted in Figs. M.2 and M.3.)

In order to apply the Newton-Raphson technique to solving the simultaneous loop equations, expressions for the derivatives of these functions will be required. These are readily obtained by differentiating; the results are

$$R'(t) = \operatorname{erfc} \left(\frac{t}{2\sqrt{\alpha}} \right) - \frac{1}{2} \operatorname{erfc} \left(\frac{t-1}{2\sqrt{\alpha}} \right) - \frac{1}{2} \operatorname{erfc} \left(\frac{t+1}{2\sqrt{\alpha}} \right)
\tag{M.13}$$

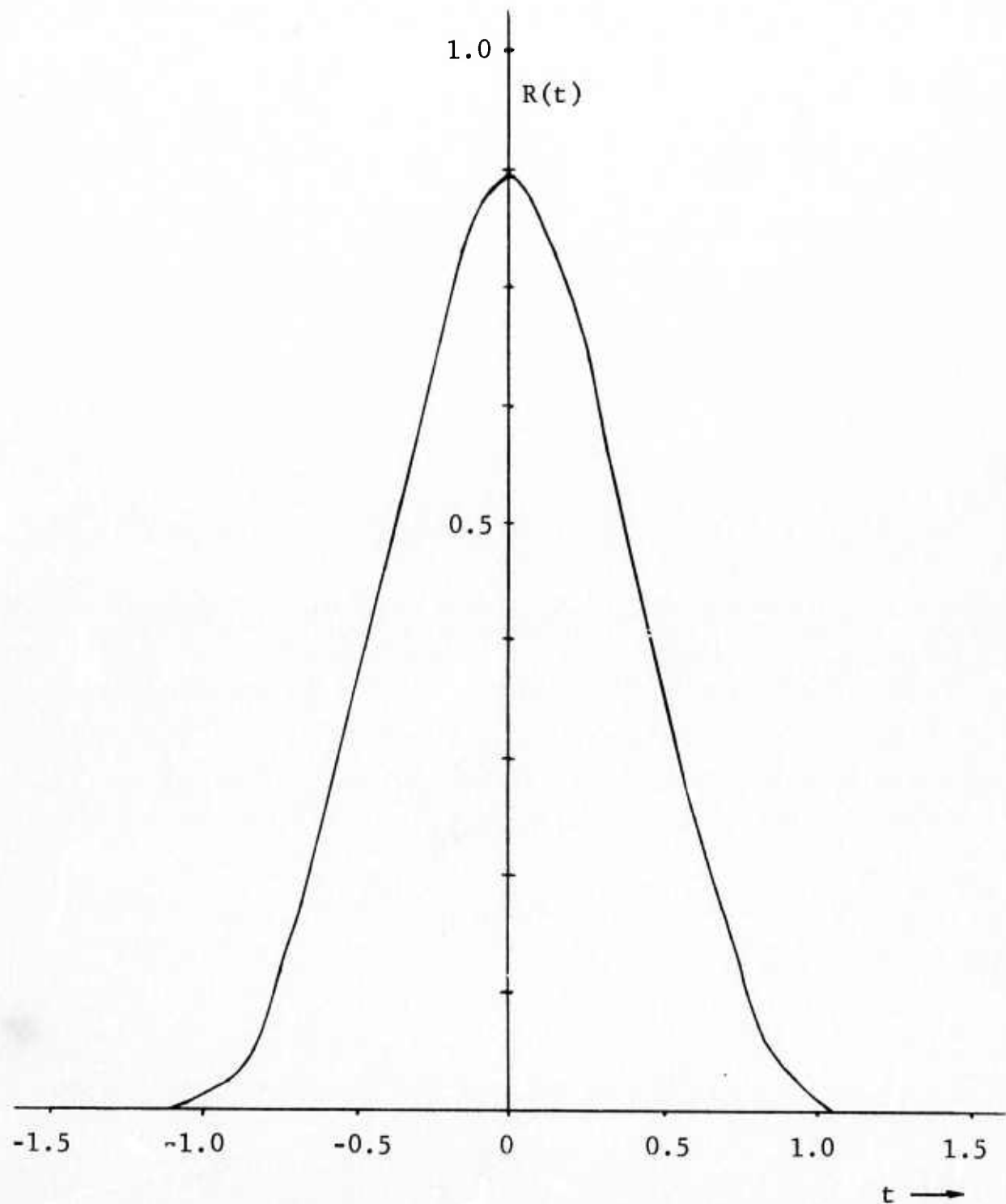


Figure M.2 The Correlation Function $R(t)$
M-6

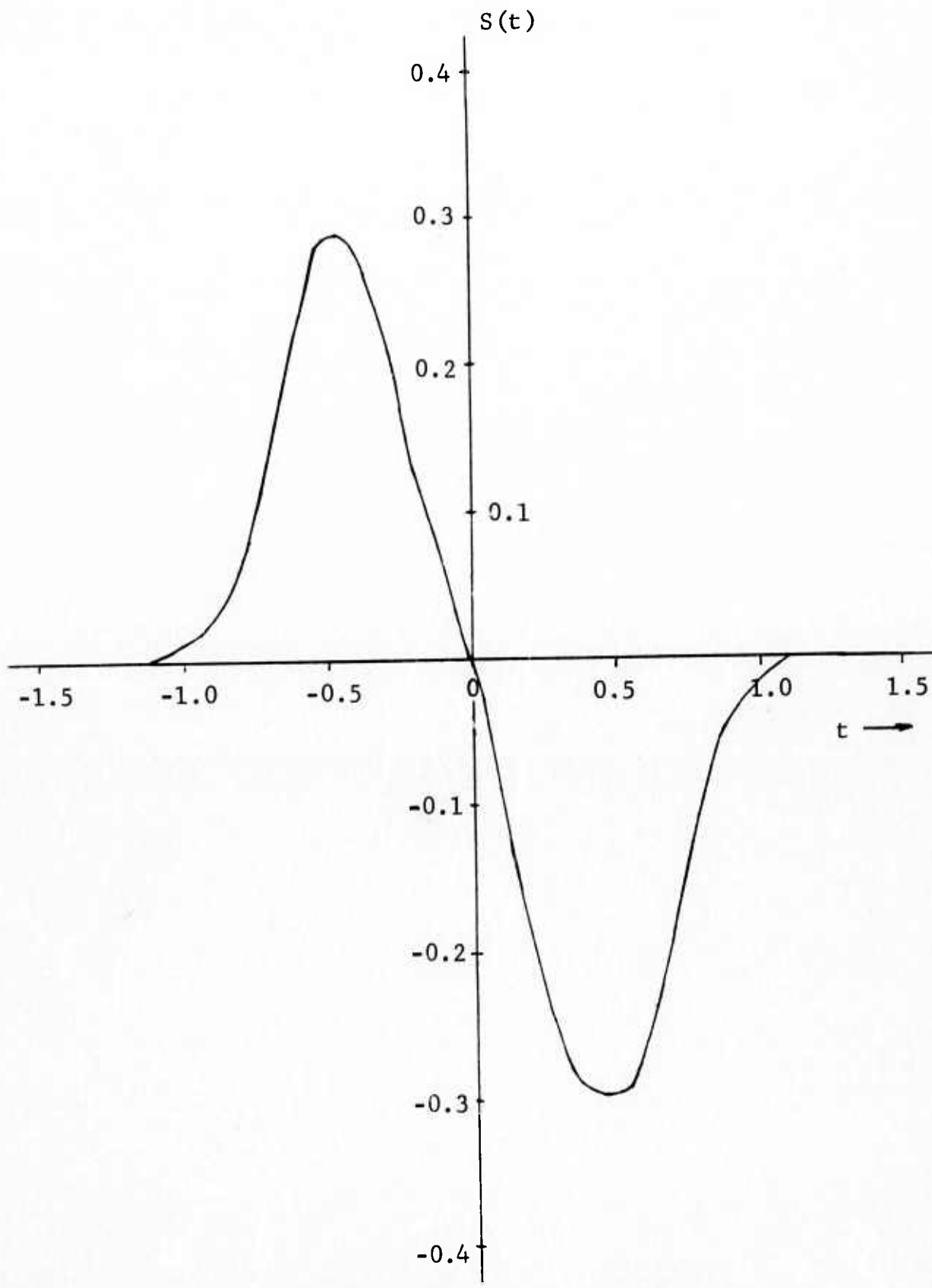


Figure M.3 The Correlation Function $S(t)$

and

$$S'(t) = \operatorname{erfc} \left(\frac{t+1/2}{2\sqrt{\alpha}} \right) - \operatorname{erfc} \left(\frac{t-1/2}{2\sqrt{\alpha}} \right) + \frac{1}{2} \operatorname{erfc} \left(\frac{t-1}{2\sqrt{\alpha}} \right) - \frac{1}{2} \operatorname{erfc} \left(\frac{t+1}{2\sqrt{\alpha}} \right)$$

(M.14)